UNIVERSITÀ DEGLI STUDI DI PALERMO

Dottorato in Ingegneria dell'Innovazione tecnologica

Dipartimento dell'Innovazione Industriale e Digitale (DIID)

Ingegneria Chimica, Gestionale, Informatica, Meccanica

Settore Scientifico Disciplinare ING-IND/26

Circular approach for the valorisation of industrial waste heat and industrial effluents

IL DOTTORE

Ing. Vassallo Fabrizio

IL TUTOR

Prof. Ing. Giorgio Micale

IL COORDINATORE:

Prof. Ing. Salvatore Gaglio

CO-TUTORS

Prof. Ing. Andrea Cipollina

CICLO XXXIII

ANNO CONSEGUIMENTO TITOLO 2021

CONTENTS

Introduction

The continuous increase of urbanization and population in the world results in an increase in the demand for primary resources such as food, energy, water, and minerals. This has led to an increase in the exploitation of natural resources in a way no longer sustainable. Referring to energy and desalination industrial sectors, the adoption of fossil fuels, with the consequent release of thousands of tons of CO_2 into the atmosphere, and the release of millions of cubic meters of brine concentrated in the receiving water bodies are causing an important climate change due to environmental pollution. Therefore, these aspects are leading to revise the economic model on which the industrial sectors are based to make them more sustainable from an environmental point of view. In fact, in recent years we are witnessing the transition from a linear to a circular economic model. This is pushing academic and industrial researchers to consider industrial effluents, such as waste heat and industrial waste brines, as an additional resource to produce electricity, water and minerals. By doing so, the industrial process becomes more profitable, and, at the same time, more environmentally friendly.

Regarding the valorisation of waste heat, it is important to stress that in any industrial sector that uses fossil fuels, an amount ranging between 20-50% of the consumed energy is lost as waste heat dissipated via exiting hot streams. Technologies for the recovery of waste heat at high and medium temperature are already present in the market, while the recovery of waste heat at low temperature (below 150 ° C) is limited due to the lack of technologies capable of converting this efficiently into other useful forms, such as electricity or water. Recently, thermolytic salts solution have been proposed as salts in the salinity gradient closed-loop processes to convert low-temperature waste heat into electricity (*Salinity Gradient Power Heat Engine*, SGP-HE) or freshwater (*Forward Osmosis Thermally Re-generable Drawing solution*, FO-TRD). These technologies consist of: (i) *a generation unit* where the salinity gradient of the two salty solutions is exploited to produce electrical energy (SGP-HE) or fresh water (FO-TRD), and (ii) a *regeneration unit* where the low grade heat is used to restore the initial salinity gradient of the feed solutions. The peculiarity of thermolytic salts solutions, such as ammonium bicarbonate (NH_4HCO_3) solution, is that their ionic solutes (e.g. NH_4^+ and HCO_3^-) undergo a degradation process into gaseous species (CO_2 and NH_3) when the temperature is increased over a certain value, typically ranging between 40 and 60°C.

In the first section of the present PhD thesis, two different regeneration unit, based on the air stripping and vapour stripping process, for the regeneration of thermolytic salts solutions are

investigated. Then, a simulation platform of the two regeneration systems has been developed, using the process simulator Aspen Plus®, and fully validated against experimental results. Once validated, the models have been used to assess which of the two regeneration systems is more suitable for closed loop applications. From this analysis, it emerged that the regeneration unit based on vapour stripping is the only one that can allow the complete regeneration of thermolytic salts solutions. Then, a mathematical model of the thermolytic RED-HE was developed by coupling the Aspen Plus® process model of the vapour stripping regeneration to a validated RED process model and used to perform a sensitivity analysis.
Furthermore, a widely experimental campaign was carried out with the first thermolytic RED-HE prototype, demonstrating the feasibility and robustness of the process.
Finally, a theoretical analysis was carried out for two thermolytic salts based closed-loop applications, i.e. SGP-HE and FO-TRD.
Regarding the valorisation of industrial waste brine, it is worth noting that huge amounts of concentrated brines are nowadays generated (as an example, the seawater desalination leads already to the production of more than 100M m^3/day of disposed brine), which are directly, or after appropriate treatment, discharged in a receiver water bodies. However, these strategies for the disposal of the waster brine are often unsustainable due to (i) high capital cost and (ii) high environmental impact. Thus, a valuable alternative to the direct disposal is the minimization of the brine volume carried out by means of two classes of technologies, *i.e.* thermal evaporative and membrane separation, which allow to avoid the direct disposal and to recover useful minerals and salts mixtures, following the Zero Liquid Discharge (ZLD) concept. Nowadays, researchers focus their attention in order to exploit industrial waste brines as a new source of minerals for their valorisation. In particular, the recovery of magnesium from brines is strategic due to the high risk of supply in European countries, as indicated by the fact that it has been identified by the European Commission, among the 30 critical raw materials (CRW) for EU.
The second section of this PhD thesis aims at the development of technologies for the recovery of minerals, such as magnesium and calcium, from industrial brine effluents, through a circular approach.
Therefore, the main goal of this second section is the design and construction of a pilot scale innovative crystallizer (Multiple Feed Plug Flow Reactor, MF-PFR) for the recovery of magnesium and calcium hydroxide at high purity from industrial waste brines. Both minerals

are recovered by a chemical crystallization in which an alkaline reactant, *i.e.* sodium hydroxide, is mixed with the brine.

Firstly, preliminary laboratory tests were carried out in order to assess the possibility to recover magnesium and calcium, separately, by means of accurate control of pH. Afterwards, the MF-PFR pilot was designed and assembled. Thus, an ah-doc experimental campaign was carried out in order to assess the quality and filterability of the produced magnesium hydroxide at different sodium hydroxide concentrations and two different operational configurations. Subsequently, the pilot plant was shipped to the industrial site at the premised of Plant One B.V. (Botlek, Rotterdam, the Netherlands) and installed within a treatment chain with the aims to valorise a real spent brine from an ion- exchange resins plant for water softening operated by Evides Industriewater B.V., in Rotterdam (The Netherlands). A wide experimental campaign was carried out in order to assess the stability and robustness of the MF-PFR pilot plant. The plant performance was assessed in terms of recovery efficiency and purity of magnesium and calcium hydroxide precipitated.

In addition, two experimental campaigns were carried out at the University o Palermo using artificial brine mimicking the concentration of the brines tested in Plant One. In the second experimental campaign, a pre-treatment step for the removal of bicarbonate/carbonate ions was implemented in order to minimise the effects of co-precipitation of calcium carbonates during the Mg-recovery step, actually leading to a higher purity of magnesium hydroxide recovered. Finally, several tests were carried out using waste brine from saltworks with a concentration in magnesium from 10 to 25 times higher than ones tested in Plant One, in order to assess the capability of the pilot crystalliser to process highly concentrated brines (e.g. >20 gMg^{2+}/L).

Following the division in the two sections, as described above, the contents of the present PhD thesis are organised as detailed the following.

Section 1 Reverse electrodialysis heat engine: from waste heat to electrical energy.

Chapter 1 presents an overview of waste heat availability and of available technologies for the conversion of waste heat into electrical energy, with a deep analysis on closed loop systems based on the use of thermolytic salts, looking also at the technologies leading to the production of freshwater.

Chapter 2 focuses on the development of a simulation platform for the thermolytic Reverse ElectroDialysis Heat Engine (RED-HE), describing briefly the 1D mathematical model used for the RED and in more details the models for the regeneration units implemented on the process simulator Aspen Plus®.

In ***Chapter 3*** the validation of the previously mentioned models with experimental data is reported, along with the results a wide experimental campaign of the first thermolytic RED Heat Engine (*RED-HE)* pilot unit.

Chapter 4 presents a perspective analysis of closed-loop systems for the production of electrical energy (looking at both RED-HE and PRO-HE) and for the production of freshwater (Forward Osmosis Thermally Regenerable Drawing solution, FO-TRD).

Section 2. Minerals recovery from waste industrial brine.

Chapter 5. presents an overview of availability of industrial waste brines, along with the strategies so far proposed to manage them, focusing on the recovery of minerals, such as magnesium and calcium in the form of hydroxides ($Mg(OH)_2$(s) and $Ca(OH)_2$(s)).

Chapter 6 focuses on the development and construction of the reactive crystallisation MF-PFR pilot unit.

Chapter 7 presents the experimental activity carried out at the Brine Excellence Center (BEC) of the University of Palermo, using two different kinds of brine, *i.e.* a synthetic brine and a real industrial waste brine produced in saltworks.

Chapter 8 covers the wide experimental activity carried out at the at Plant One B.V. in Botlek (Rotterdam, the Netherlands) using real industrial waste brine and where the MF-PFR pilot unit was integrated with in a larger treatment chain for the full valorisation of spent regeneration brine from IEX softening plant. This activity was performed during a 6 months internship under the co-supervision of prof. Henri Spanjers (Delft University of Technology)

Section 1

Reverse electrodialysis heat engine: from waste heat to electrical energy.

Abstract

A huge amount of thermal energy generated by human activities is directly released in the environment in the form of hot flue gas, hot water, etc.., causing a serious environmental impact, due to the release of CO_2 and temperature pollution. As an opposite approach, valorisation and reuse of such waste thermal energy (waste heat) allows increasing the thermal efficiency of industrial plants along with the reduction of CO_2 emissions. Currently, available technologies allow the valorisation of waste heat at high-grade (above 500 ° C) and medium-grade temperature (from 100°C to 400 ° C) converting it into mechanical or electrical energy. However, a huge part of the produced waste heat is available at a temperature below 100°C. Thus, closed-loop salinity gradient technologies represent an innovative and promising alternative to convert low-grade waste heat into power in the uncovered range of low and very-low temperatures. Examples are Salinity Gradient Heat Engines, such as the Reverse Electrodialysis Heat Engine (RED-HE) or Thermally Regenerable Drawing agent Forward Osmosis (FO-TRD) for desalination of saline streams.

In this Section, a model for the whole RED-HE based on the use of thermolytic salts solutions is presented. An existing and validated mathematical model for the RED process, based on NaCl-water solutions, was adapted in order to describe the unit behaviour with thermolytic solutions. On the other side, two different regeneration processes for the thermolytic salts solutions have been considered: (i) air stripping/absorption-condensation process and (ii) vapour stripping/absorption -condensation. In particular, each proposed regeneration process has been modelled using Aspen Plus®. Both regeneration options have been investigated by means of lab scale prototypes and the obtained results have been used to validate the process models. These have been used to carry out a sensitivity analysis to investigate the performance of the two-regeneration units, which highlighted advantages and disadvantages of the two regeneration processes and the important limitations of the air stripping/absorption-condensation for actual applications. Finally, a theoretical analysis of the whole RED-HE has been carried out to investigate the influence of operating conditions and process configurations, indicating that an exergy efficiency of almost 5% can be achieved with state-of-the-art units, while a value close to 10% could be achieved adopting optimised membranes.

A full experimental campaign has been also carried out on a prototype RED-HE, representing the first-world example of such prototype units and previously developed within

the RED-Heat-to-Power EU project. Long-run experiments were fundamental to demonstrate the feasibility and stability of the process, while performance analysis has shown a maximum exergy efficiency experimentally obtained about 1%.

Finally, a theoretical analysis of the application of thermolytic salts regeneration strategies to the Forward Osmosis process for saline waters desalination has been conducted.

1. Valorisation of low-temperature waste heat via the thermolytic solutions closed-loop applications

1.1 Waste heat availability

The valorisation and reuse of waste heat is an interesting perspective because it would allow increasing industrial plant energy efficiency along with reducing CO_2 emissions and the energy cost. Referring to the industrial sector, a large amount of energy input, between 20-50% [1], is lost as waste heat as hot water, hot flue gas, etc.. However, the waste heat release in the environment as a "waste" stream that can be potentially recovered or converted in other useful forms, such as electrical power, or be used to produce fresh water.

Numerous studies focus on the availability of waste heat. In 2015 Gingerich et al [2] highlighted that about 38 billions of GJ of carbon, natural gas and nuclear energy were converted in 12.3 billions GJ of electrical energy with an average conversion efficiency about 32%, releasing in the environment about 18.9 billions of GJ of thermal energy. Another study carried out in the same year by Mirò et al focused on the investigation about the worldwide production of industrial waste heat, see *Figure 1.1* [3].

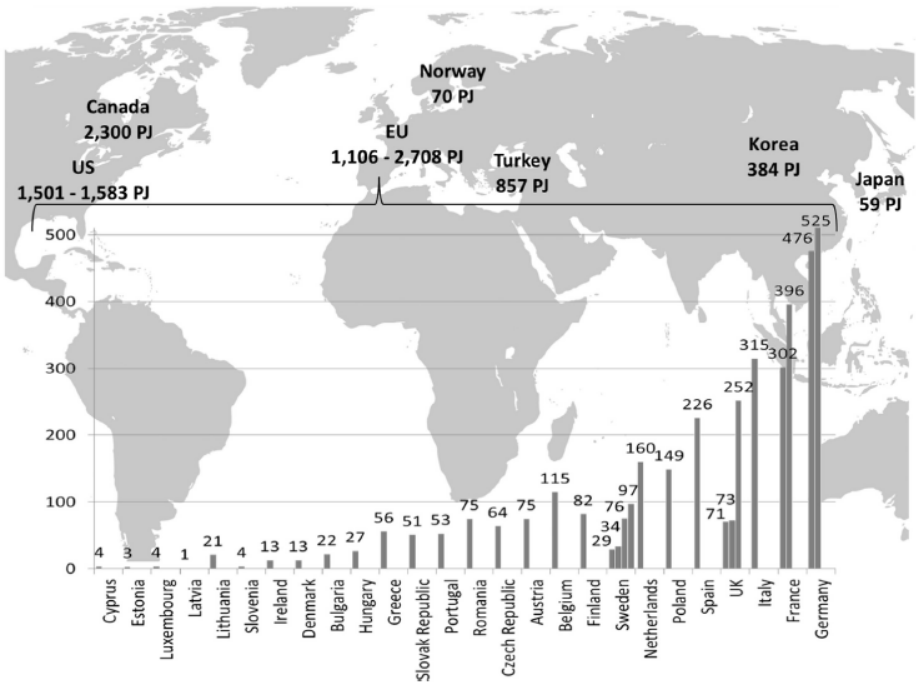

Figure 1.1. Yearly industrial waste heat potential in some of the most industrialised countries in the world (in PJ, PetaJoule), with a detailed break-down for European countries [3]

The total amount of waste heat shown in *Figure 1.1* does not take into account the amount of waste heat produced by China. Due to its fast growing, it became the largest consumer of energy in the world. In fact, about 10-50% of the total fuel consumption in different industry sectors is converted into waste heat. Just as an example, in 2010 Chinese ammonia industry released about 850 PJ of waste heat, *i.e.* 29 million tonnes of coal equivalent [4]. As regard the European countries, the total amount of waste heat produced was between 1106 and 2780 PJ per year (see *Figure 1.1*). In 2016, Law et al [5] evaluated the annual availability of waste heat in the UK industrial sector. They estimated that a total amount of about 14.4 TWh (about 4% of the total energy used) has been released in the environment. The authors assessed that the recovery of such waste heat would allow saving about 200-300 million £ per years along with the reduction of thousand ton of CO_2 released in the atmosphere, that in this case is about of 2039 tktCO_2 per years. Recently, Papapetrou et al [6] carried out a compressive analysis of the yearly production of waste heat available in the European countries per

industrial sectors referring to 2015, see *Figure 1.2*. Authors evaluated a potential waste heat equal to 304.13 TWh per year and about 40% of total waste heat is available at a temperature below 200°C.

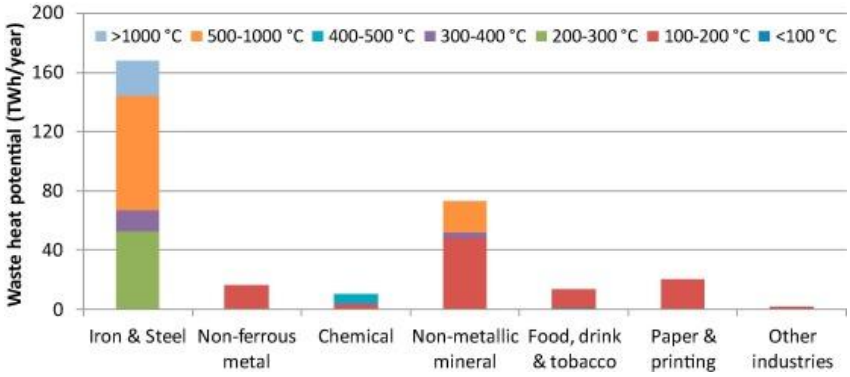

Figure 1.2.Yearly production of Waste heat per industrial sector and temperature level for EU industry in 2015 [6].

The temperature of waste heat released is the most important parameter in order to choose the appropriate technologies in order to convert it in other useful forms. Based on the temperature, the waste heat can be classified in three different levels: (i) *high temperature waste heat* (T>400°C), (ii) *medium temperature* (100°C<T<400°C) and (iii) *low temperature* (T<100°C).

A more detailed classification of the waste heat sources is reported in *Table 1.1* [7].

When the waste heat is at high temperature, it is easy to exploit it inside the same production process itself, as an example, according to the temperature, it can be used for the production of steam at medium or low pressure, to preheating streams etc. Whereas for the conversion of waste heat at low temperature there aren't available technologies in the market to exploit the exergy in an efficient way. In this context, this PhD work focus on the development of new technology and knowledge to use low-temperature waste heat for the production of electrical energy and fresh water.

Table 1.1.Classification of waste heat sources per industrial process and exhausted gas temperature [7].

Temperature level	Industrial Process	Exhausted gas temp (°C)
HT	Iron- and steelmaking	1450–1550
HT	Nickel refining furnace	1370–1650
HT	Steel electric arc furnace	1370–1650
HT	Glass melting furnace	1300–1540
HT	Basic oxygen furnace	1200
HT	Aluminium reverberatory furnace	1100–1200
HT	Steel heating furnace	1450–1550
HT	Copper reverberatory furnace	900–1090
HT	Glass oven without regenerator	900–1300
HT	Iron cupola	820–980
HT	Cooper refining furnace	760–820
HT	Reheating furnace without regenerator	700–1200
HT	Hydrogen plants	650–980
HT	Fume incinerators	650–1430
HT	Coke oven	650–1000
HT	Glass oven with regenerator	600–800
HT	Cement kiln	450–620
HT	Heat treating furnace	430–650
HT, MT	Melting oven	400–700
HT, MT	Gas turbine exhaust	370–540
HT, MT	Reciprocating engine exhaust	320–590
HT, MT	Reheating furnace with regenerator	300–600
MT	Blast furnace stoves	250–300
HT, MT	Drying and baking ovens	230–590
HT, MT	Steam boiler exhaust	230–480
HT, MT	Finishing soaking pit reheat furnace	200–600
MT	Steam boiler	200–300
MT	Coke oven	190
MT	Stack gas	160–200
MT	Container glass melting	140–160
MT	Flat glass melting	160–200
HT, MT	Ceramic kiln	150–1000
LT, MT	Drying, baking, and curing ovens	90–230
LT, MT	Cooling water from annealing furnaces	70–230
LT, MT	Cooling water from internal combustion engines	70–120
LT, MT	Exhaust gases exiting recovery devices in gas-fired boilers, ethylene furnaces	70–230
LT, MT	Conventional hot water boiler Process	60–230
LT	Process steam condensate	50–90
LT	Condensing hot water boiler	40–50
LT, MT	Hot processed liquids/solids	40–230
LT	Cooling water from air conditioning and refrigeration condensers	30–40
LT	Cooling water from air compressors	30–50
LT	Cooling water from furnace doors	30–50

1.2 Heat engines for the conversion of waste heat into electrical energy

Several technologies can be employed for the conversion of waste heat in another form of energy. In particular, these technologies can be classified into two main class: (i) actives and

(ii) passives. The passives technologies are based on re-use the waste heat in order to pre-heat or heat streams within the same process. The main technologies used are heat-exchanger used for thermal integration. On the other side, active technologies are based on the conversion of waste heat into another form of energy or heat at a higher temperature. In particular, the active technologies can be classified in: (i) waste heat to heat, (ii) waste heat to cold and (iii) waste heat to power. For this latter case, some of the conventional technologies used in the industrial for the valorisation of the waste heat are:

- *Steam Rankine Cycle (SRC)*, it bases on a classical Rankine cycle in which the heat is converted in electrical power by mean of steam. Therefore, the minimum temperature allowable for the process is about 340-370°C. For this reason, the SRC is adopted in the industry for the recovery of hot gas at high or medium temperature range (350-500°C) [8];
- *Organic Rankine Cycle (ORC)*, it bases on classical Rankine Cycle with a different working fluid, *i.e.* an organic fluid with a low boiling point. Due to the lower boiling point then water, the ORC can be used for the conversion of waste heat at medium temperature (from 100°C up to 300°C) [8];
- *Kaline Cycle (KC).* On the contrary of SRC and ORC, the KC exploit a binary mixture of water and ammonia, that brings about a non-constant evaporation temperature and makes a good thermal match between the sensible heat source and the working fluid temperature profiles, reducing the irreversibility during the waste heat recovery process. Moreover, the KC is suitable for the recover waste heat at medium temperature (from 100°C up to 300°C) [9].

Recently, different and innovative technologies have been developed in order to convert directly the waste heat into electrical energy. Some of them are very promising option of the recovery of waste heat at medium and low temperature. However, these technologies are affected by low efficiency conversion and high capital cost. Some of these technologies proposed for the conversion of waste heat are listed following:

- *Thermoelectric generation (TEG).* This technology exploits semiconductor materials able to convert waste heat into electrical energy. The TEG technology does not require moving part or working fluid [10].
- *Piezoelectric power generation with waste heat-powered expansion/compression cycle (PEPG).* This technology allows converting waste heat at a temperature

between 100 and 150°C into electricity. This device allows converting the thermal energy into electrical one exploiting the oscillation of a piezoelectric membrane due to the expansion of a gas [11].

- *Carbon carrier Cycle (CC).* This technology based on a modification of Rankine Cycle instead of using a condenser, a CO2 chemical absorption process is used to create the pressure reduction downstream of the turbine. This technology can convert into electricity waste heat at temperature until 150°C [12].
- *Salinity gradient closed loop technologies.* This technology allows converting waste heat at low temperature (below 100°C) into other useful forms, such as electrical energy, freshwater and hydrogen [13–20], exploiting the salinity gradient of two solutions.

Focusing on the *Salinity gradient closed loop technologies*, among the different working salts used for the preparation of solution proposed in the literature, the thermolytic salts appear very promising due to their chemical property. The thermolytic salts undergo a degradation process into gaseous species when the temperature is increased above a certain limit. Such degradation occurs also when the salts are dissolved in water solutions, making it possible to remove the salts by mean of thermal process. The most common thermolytic salts consist of NH_3-CO_2 based compounds, such as ammonium bicarbonate (NH_3HCO_3), ammonium carbamate ($NH_4NH_2CO_2$) and ammonium carbonate ($(NH_3)_2CO_3$). All of them decompose into NH_3 and CO_2 at a temperature between 35-60°C (at the atmospheric pressure). Independently the form of initial thermolytic salt, thermodynamic equilibria will lead a solution composition in which NH_4^+ and HCO_3^- ions are predominant, thus allowing considering ammonium bicarbonate (NH_3HCO_3) salts used in these technologies.

1.3 Thermolytic salts application in closed loop

As previously reported, the *Salinity gradient closed loop technologies* based on the thermolytic salts solution can be exploited to produce electrical energy, namely *Salinity Gradient Power Heat Engine (SGP-HE)*, hydrogen production, and *Forward Osmosis* for the desalination process with *thermally re-generable using agent (*FO-TRD) have been proposed recently in the literature. All of them consist of:

- *Generation unit* where the salinity gradient is exploited to produce electrical energy in the case of SGP-HE [13–16], directly into hydrogen [17–19] or into fresh-water in the case of FO-TRD [20];
- *Regeneration unit* where the waste heat at low temperature is used to restore the initial salinity of the two thermolytic solution.

Several works about thermolytic closed loop applications, are reported in literature about Forward Osmosis process and Salinity Gradient closed-loop system. Thermolytic Forward Osmosis is the most studied process, the NH_4HCO_3-water solutions are adopted as thermally re-generable draw agent to produce fresh water from saline solutions (see *Figure 1.3-a*). A FO closed-loop system consists of two sections: (i) a forward osmosis unit, in which the osmotic pressure gradient between feed (i.e. sea or brackish water) and draw solutions generates a water flux through the membrane from the feed to the drawing loop and (ii) a regeneration unit where low-temperature heat (about 60 °C) is used to remove the salt (NH_4HCO_3) from the excess diluted draw solution through a stripping process in order to remove two gaseous compounds, *i.e.* NH_3 and CO_2. The gases are separated and recovered in a distillation/stripping column, thus obtaining desalinated water and the gaseous compounds to regenerate the draw solution. The idea of using thermolytic salts solutions as draw agent in FO applications was proposed for the first time by Neff in 1964 with the patent "solvent extractor" [21]. Since then, a several studies were carried out both via theoretical analysis and experimental investigation.

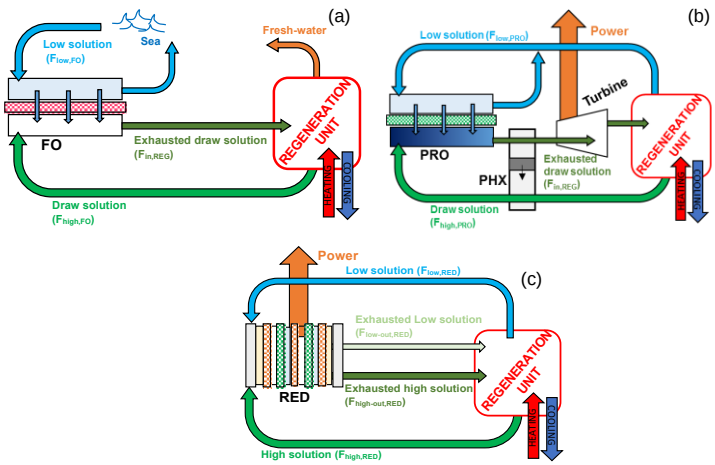

Figure 1.3.Schematic representations of the RED–HE (a), PRO-HE (b) and FO–TRD (c).

As regards the theoretical analysis about FO-TRD systems, McCutcheon et al. in 2005 [22] and McGinnis et al. in 2007 [23] have given more insight about the process. In particular, McCutcheon et al [22] described a forward osmosis process for seawater desalination, using ammonium bicarbonate solution to extract water from a saline stream through a semipermeable osmotic membrane. However, the regeneration step was described only qualitatively assuming the operation of a distillation column using waste heat. In 2007, McGinnis and Elimelech [23] continued the work, developing a simplified theoretical energetic analysis implemented on Aspen Hysys® calculating the energetic duty for the regeneration step. The authors proposed two different layouts for the regeneration unit: one using a single distillation column and the other using several distillation columns connected in series. The appropriate regeneration layout was chosen on the basis of the available waste heat temperature. In particular, using very low-grade heat, a single distillation column, operating under vacuum, is used; on the contrary, with heat temperature higher than 40°C, the multiple columns layout resulted into a higher thermal efficiency. In 2015, Zhou et al [24] carried out another modelling analysis for a closed loop FO process. They compared three different regeneration units: (i) distillation, (ii) stripping with steam, (iii) stripping with air. The analysis was carried out by using Aspen Plus®, adopting Electrolyte Non Random Two Liquid Redlich-Kwong (E-NRTL-RK) [25] as a thermodynamic package. Based on authors' results, the distillation system represents the best choice. In fact, (i) the air stripping requires a higher thermal energy demand and a larger column to achieve the same target purity, while

(ii) the stripping with steam, notwithstanding requiring a thermal duty similar to the distillation process, but requiring an additional compressor, the overall cost increases.

Moreover, several experimental investigations were performed, presenting some preliminary results on the FO-TRD system performance. In 2013, McGinnis et al [26] reported the first results of a pilot scale investigation on a NH_3-CO_2 FO desalination unit, using distillation as regeneration process. The pilot was tested for the desalination of water from a natural gas production in the Marcellus shale. Feed recovery higher than 60% was reported for the desalination of high salinity stream (>70.000 mg/L TDS) with a thermal consumption of 275 kWh/m^3 and an electrical consumption of 8.5 kWh/m3 of water produced. In the same year, Shim et al. [27] carried out experiments for NH_4HCO_3 separation using a Vacuum Membrane Distillation (MD) process. Results highlighted that the achieved salt removal efficiency was about 95% and 99% when the MD module is fed by solutions at 50 °C and 60° C, respectively. On the contrary, feeding the MD unit with a solution at 40°C, a lower removal efficiency of 85% was achieved. The separation efficiency was equal to 99.7% for NH_3 and 99.9 % for CO_2, while the thermal energy consumption to produce 1 m^3 of water ranged between 265 and 300 kWh. However, no data on power consumption were reported. In 2015, Kim et al [28] constructed and tested a 3 ton/day pilot plant for thermolytic-FO desalination. The system consisted of three units: (i) FO, (ii) thermolytic salt-water separation and (iii) draw solution regeneration. In particular, the two latter steps were integrated in a single column. The separation was carried out in a column filled with a structured packing operating at ambient pressure. The inlet solution was pre-heated with a solution extracted from the reboiler at temperatures up to 100 °C. In the same year, Boo et al. [29] studied the potential of trimethylamine - carbon dioxide (TMA -CO_2) as draw solution for osmosis process, FO and PRO. Experimental results of water fluxes in FO and PRO applications were compared to those obtained by using NH_3–CO_2 and NaCl draw solutions, reporting for the TMA-CO_2 slightly low water fluxes compared to the other two draw solutions. Moreover, the thermal energy requirement for the separation of the two thermolytic draw solutions was evaluated by using Aspen HYSYS with OLI electrolyte fluid package. Results indicate that TMA–CO_2 draw solution could be separated and recovered at lower thermal energy consumption than NH_3–CO_2 using a low- temperature, vacuum distillation column. However, TMA-CO2 may be harmful for human health and the environment.

Regarding the SGP-HE systems thermolytic salts based, low number of works are reported in the literature. The system consists of two units (see *Figure 1.3.b* and *c*): (i) a power unit

where the salinity gradient between two thermolytic salt solutions is exploited to produce electrical energy; (ii) a regeneration unit where low temperature waste heat is used to restore the initial salinity of the two feed solutions. Mainly, two different technology were studied: (i) Reverse Electro-Dialysis Heat Engine (RED-HE) and (ii) Osmotic Heat Engine (OHE).

This idea was proposed for the first time by Loeb in 1973 who patented an heat engine based on the closed-loop Pressure Retarded Osmosis (PRO) concept and in 1978 on the Reverse ElectroDialysis (RED) one [30,31]. Also for SGP-HE, some theoretical and experimental investigations were carried out and presented in the literature. As far, the main efforts of the experimental study about the SGP-HEs unit fed by thermolytic solution reported in the literature have been mainly focused on the generation unit. As regard the Reverse Electro-Dialysis Heat Engine (RED-HE) (i), in 2012 Luo et al [32] analysed the potential of a RED unit fed with aqueous NH_4HCO_3 solutions. They obtained a power density of 0.33 W/m^2 of membrane area, at optimized feed solutions concentrations (concentrate solution 1.5 M - dilute solution 0.02 M). Likewise, Cusick et al [33] in 2012 experimentally studied the use a microbial RED unit driven by ammonium bicarbonate, reporting a maximum power density of 2.1 W/m^2 produced by RED unit and 3.3 W/m^2 from the substrate oxidation. In the same year, Nam et al [34] investigated a microbial reverse electrodialysis fed by ammonium bicarbonate salts solution operating in closed loop. The system was effective in the organic matter removal and hydrogen production. As regeneration unit for the ammonium bicarbonate solutions, the authors proposed a distillation technology.

In 2014, Haztell et al [35] experimentally investigated the potential for directly converting the salinity gradient between ammonium bicarbonate solution in hydrogen in a closed loop RED. Based on the experimental results, the authors estimated that the energy captured through hydrogen in a RED stack made of 100 cell pair may reach values around 118 Wh/m^3.

In 2015, Kwon et al [36] carried out an experimental characterization of the RED process, investigating the effect on process performance of various parameters such as: inlet flow rates and concentrations, membrane type and compartment thickness. The best result was an optimised maximum power density of 0.77 W/m^2 of membrane area.

In 2016, Bevacqua et al [37] performed another extensive experimental analysis on a RED system fed with NH_4HCO_3 solutions. Results showed that maximum amount of power production was obtained at 2M-0.02M concentration set, achieving a power density of 1.2 W/m^2 of membrane.

In 2020 Tian et al [38] developed a novel hybrid system named PRC by combining a photocatalytic fuel cell (PFC) and a reverse electrodialysis operating in closed loop. The system was able to convert solar energy and salinity gradient energy into electricity and, at the same time, to degrade organic pollutants in the anode chamber and to produce hydrogen peroxide in the cathode chamber. Within the RED system ammonium bicarbonate solutions were used as working solutions, reusable in the process after a regeneration step by using a distillation process powered by low-grade waste heat. Results showed peak power density o 1.5 W/m^2 of cathode area and energy efficiency of the PRC system around 4%.

In 2017 Kim et al [39] developed an experimentally validated model to evaluate the performance of a RED unit fed by ammonium bicarbonate solutions. Results showed a maximum net power density of 0.84 W/m^2 membrane obtained with concentrations of 2 M-0.01 M. In the same year, Bevacqua et al [40] carried out a theoretically assessment of the performance of RED-HE fed by ammonium bicarbonate solutions using an air stripping column. The regeneration unit was modelled on Aspen Plus®. The results shown that the maximum exergy efficiency achieved was about 22%

As regards theoretical investigations on Osmotic Heat Engine (OHE) (ii), in 2007, McGinnis et al [41] performed a study on a PRO based heat engine where solutions of ammonium salts at high concentration (i.e. NH_4HCO_3 and NH_4OH) were adopted as drawing agent. Simulations carried out with a simplified model obtaining a theoretical power density in the PRO unit higher than 200 W/m^2, operating the PRO unit with a draw solution side at about 100 atm. Such conditions, led to overall exergy efficiency up to 16%.

In 2020 Tong et al [42] reported a systematic investigation of the energy efficiency and exergy efficiency of a thermolytic Osmotic Heat Engine (OHE) fed by solutions of ammonium bicarbonate. The analysis was carried out fixing the electric power output at 1.4 kW and changing the concentration of the two solutions. Results have shown an overall energy efficiency of 4.61% corresponding to an exergy efficiency 17.9%. Moreover, the feasibility of the system to operate by using different heat sources, low-grade industrial waste heat and solar thermal energy, was analysed by evaluating and comparing the energy return on investment (EROI) for the two different sources.

The closed-loops based on thermolytic salts solutions were one of the very promising alternative solutions in order to convert very low-grade waste heat into fresh water and electrical energy. The application of these close-loop technologies can help to reduce/avoid thermal pollution of the environment making the industrial process environmentally and

economically more sustainable. However, the studies reported here focus mainly on the generation unit and very few works on the regeneration unit. In particular, very few works have experimentally analysed the applicability of thermolytic salts as thermally re-generable agent leaving a total gap of an experimentally validated mathematical model able to reliably evaluate the performance of real potential of closed-loop systems, i.e. SGP and FO. Thus, one of the goals of this thesis is to fill totally this gap developing a validated mathematical model, that allows converting low-grade heat into electrical energy, opening the way for further development and possible industrial application.

1.4 Motivation and goal of this work

Over the past two decades, the *Salinity gradient closed-loop technologies* gained raising interest among the researchers due to the increasing knowledge of these technologies for the conversion of waste heat at low temperature in useful forms, such as electricity (SGP-HE) or freshwater (FO-TRD). Different theoretical and experimental studied have been carried out for the generation unit, while very few information is reported regarding the behaviour of the regeneration unit. Furthermore, no real demonstration of the process feasibility has been reported in the literature so far due to the significant efforts to operate a fully integrated SGP-HE system.

The activities of this section are carried out within the European project *RED Heat to Power*, funded by the European Union's Horizon 2020. The aims this project are to study and develop the first prototypes for the conversion of low-grade waste heat into electricity through a closed-loop reverse electrodialysis.

The main goal of this thesis is the study of the regeneration unit followed by the realization of a pilot unit for the valorisation of waste heat to produce electrical energy by means of an innovative RED-HE. To this goal, both modelling and experimental activity has been carried out. In specific:

- Modelling activities focused on the development of two simulation platforms of two different regeneration units validated against experimental results, in order to predict the behaviour and performance of the two closed loop systems¸ *i.e.* SGP-HE and FO-TRD.
- Experimental activities focused on the construction and testing of the first thermolytic RED-HE prototype, demonstrating the possibility to convert waste heat at low temperature (around 80°C) into electrical energy.

2. Simulation platform for RED-HE

Capther Outline

Part of this chapter has been published in:

F. Giacalone, **F. Vassallo**, L. Griffina,, , M.C. Ferrari, G. Micale, F. Scargiali, A. Tamburini, A.Cipollina," Thermolytic reverse electrodialysis heat engine: model development,integration and performance analysis", Energy Conversion and Management, Volume 189, 1 June 2019, Pages 1-13, doi: 10.1016/j.enconman.2019.03.045

2.1 Reverse electro dialysis mathematical model

The mathematical model used to describe the behaviour of *RED* process with NaCl-water solutions was adapted in order to describe the same process with NH_4HCO_3-water solutions [43].

In particular, the concentration and the flow-rate variation along the channels was taken into account by using a mono-dimensional approach. In fact, the unit, consisting in a given number of cell-pair (*i.e.* N_{cp}), was discretized in N_k calculation elements along the flow direction (see *Figure 2.1*).

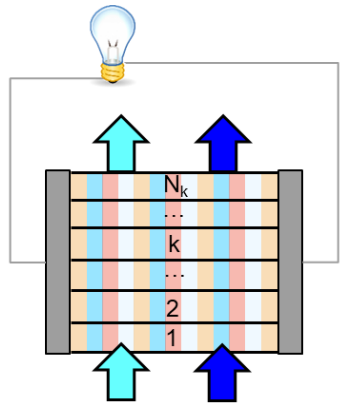

Figure 2.1. Discretization scheme of the RED unit.

Each calculation element represents a branch of an equivalent circuit, where passive (i.e. resistances) and active (i.e. generator) elements are present. Full details are reported in [43], as reported in *Figure 2.2*.

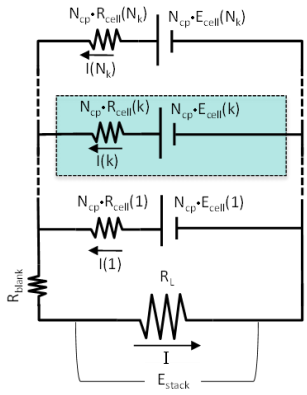

Figure 2.2. Equivalent electric scheme of RED unit.

Firstly, the main electric equation used in the model are follow reported.

The electric voltage (E_{cell}) generated in each branch, *i.e.* in a generic kth element of a cell pair, is computed according to Nerst's equation:

$$E_{cell}(k) = 2\alpha_{av}(k)\frac{RT}{zF}\ln\left(\frac{m_H(k)\gamma_H(k)}{m_L(k)\gamma_L(k)}\right) \qquad (2.1)$$

where, α_{av} is the average membranes permselectivity of the two *IEMs* (ionic exchange membranes), γ_H and γ_L are the activity coefficients of the two solutions, m_H and m_L are the molality of the solutions, F is the Faraday's constant, R is the universal gas constant and T is the absolute temperature (T=298K).

The resistance of the kth element of the cell pair (R_{cell}) was calculated as the sum of 4 resistances in series as follow:

$$R_{cell}(k) = [R_H(k) + R_L(k) + R_{CEM}(k) + R_{AEM}(k)] \qquad (2.2)$$

where R_{CEM} and R_{AEM} are the membranes resistance of the two membranes and R_H and R_L the electrical resistances of the solutions flowing in the two channels. Thus, the electric current (i) circulating in the kth branch is calculated using the following equation:

$$i(k) = \frac{E_{cell}(k) - (E_{stack} + R_{blank} * I_{stack})}{R_{cell}(k)} \qquad (2.3)$$

where E_{stack} is the electric voltage generated by the RED unit and R_{blank} is the resistance of the electrodic compartments, which is negligible for high cell pairs number (e.g. larger than 100 cell pair). The electric current circulating on the external load (I_{stack}) is the sum of the currents circulating in each "k^{th}" branch (Kirchhoff's junction rule).

$$I_{stack} = \sum_{k}^{N_k} I(k) \quad (2.4)$$

The closing equation, obtained by the Ohm's law on the external load, is the following:

$$E_{stack} = R_E * I_{stack} \quad (2.5)$$

where R_E is the resistance of the external load.
Finally, the gross power (P_{RED}) and the gross power density (P_d) are calculated as follows:

$$P_{RED} = N_{cp} * E_{stack} * I_{stack} \quad (2.6)$$

$$P_d = \frac{P_{RED}}{N_{cp} * A_{cp}} \quad (2.7)$$

where A_{cp} is the area of a cell pair.
In order to compute the variation of concentrations and flow-rates along channels, salt and global mass balance equations in each compartment (dilute and concentrate) were applied in order to compute the exiting concentration and flow-rate from each computational domain.
Considering a co-current arrangement, the salt and global mass balance equations can be written as follow:

$$C_{out}(k+1)Q_{out}(k+1) = C_{in}(k) * Q_{in}(k) \pm J_s(k) b \Delta x \quad (2.8)$$

$$\rho_{out}(k+1)Q_{out}(k+1) = \rho_{in}(k)Q_{in}(k) \pm J_w(k) * b\Delta x \frac{\rho_w}{M_w} \pm J_s(k) b \Delta x M_s \quad (2.9)$$

where the subscript *out*, *in*, *w* and *s* refer to the outlet section, inlet section, water and salt, respectively. The *C* is the molar concentration of the solution [mol/l] flowing in channels

(dilute or concentrate), b is the membrane width [m], Q is the flow rate and J_w and J_s are water and salt flux respectively.

In particular, the salt flux (J_s) was computed as follow:

$$J_{salt}(k) = J_{mig}(k) + J_{diff}(k) = \frac{i(k)}{zF} + 2 * \frac{P_{salt}}{\delta_m}(C_H(k) - C_L(k)) \qquad (2.10)$$

where *i* is the current density or current for unit of membrane area, δ_m is the thickness of the membrane (assumed equal for both IEM$_s$ membranes), P_{salt} is the salt permeability of the membrane (assumed equal for both IEM$_s$ membranes) and $C_H(k)$ and $C_L(k)$ are the concentration of the high and low solution. In particular, the salt flux is the sum of two term. The first is the *migrative flux (J_{mig})*, which gives the sat transferred with the counter ions across the *AEM* and *CEM* and the latter is *diffusive flux (J_{diff})*, refers to the diffusion of the co-ions. Factor 2 multiplying the diffusion flux take into account the two IEM$_s$ membranes in contact with the two channels.

As regard the water flux, it was computed by the following equation:

$$J_w(k) = J_{osm}(k) + J_{eosm}(k) = \\ -2\nu RTP_w\left(C_H(k)\phi_H(k) - C_L(k)\phi_L(k)\right) + n_{hy}J_{salt}(k)\frac{M_w}{1000*\varrho_w} \qquad (2.11)$$

where P_w is the average water permeability of the *IEMs* membrane, ϕ is the osmotic coefficient and n is the is the hydration number equal to 7.

In order to take into account the variation of the solution properties of ammonium bicarbonate along the channels, molality-dependent correlations were used. In particular:

(i) activity and osmotic coefficients of NH_4HCO_3 in water solution are estimated by mean of Pitzer's model [44];

(ii) density of the solutions was computed as a linear function of the molar concentration using literature data to obtain the fitting coefficients [45];

(iii) salt-solution conductivity is calculated using the Jone and Dole's equation with experimentally fitting parameters [46].

Moreover, the variation of the permselectivity and the resistance of the membranes along the stack channels were take into account adopting concentration-dependent correlation provided

by the manufacturer, while the water and salt permeability were considered constant (see *Table 2.1*)

Obviously, for the validation of the mathematical model, the operating and geometrical properties of the RED unit was purposely set according to the experimental RED features.

Table 2.1. Ion exchange membrane, i.e. cation and anion, properties adopted in the model.

Properties	
Permselectivity [%]	$0.8924 \cdot C_H^{-0.069}$
Resistance [Ωm^2]	$2.027 \cdot 10^{-4} \cdot C_L^{-0.236}$
Water permeability [ml/(bar·h·m^2)]	6 (*)
Salt Permeability [m^2/s]	$4.5\ 10^{-12}$ (*)
δ_m [m]	$1.25 \cdot 10^{-4}$

(*)Assumed constant in whole range of concentration

2.2 Regeneration unit

Based on the authors' knowledge, all the process schemes, theoretical analyses, experimental results reported in the literature on regeneration units for thermolytic solutions, two different regeneration processes were taken into account:

- Air stripping process;
- Vapour stripping process.

In particular, this section is devoted to present a model platform developed in Aspen Plus® in order simulate the behaviour of the two proposed regeneration systems.

2.2.1 Model Platform for the regeneration units

In order to describe the behaviour of the regeneration unit, a simulation platform was implemented in Aspen Plus® in order to simulate the behaviour of the two different regeneration processes.

The main chemical equilibrium reactions involved in ammonium bicarbonate-water solutions [33,34] are reported below:

$$NH_4HCO_3 \leftrightarrow NH_4^+ + HCO_3^- \quad (2.12)$$

$$H_2O \leftrightarrow H^+ + OH^- \quad (2.13)$$

$$NH_3 + H_2O \leftrightarrow NH_4^+ + OH^- \quad (2.14)$$

$$CO_2(g) + H_2O \leftrightarrow HCO_3^- + H^+ \quad (2.15)$$

$$NH_3 + HCO_3^- \leftrightarrow NH_2COO^- + H_2O \quad (2.16)$$

$$HCO_3^- \leftrightarrow CO_3^{2-} + H^+ \quad (2.17)$$

A lot of reactions occurred inside the solution involving both charged and uncharged species in solution making the solution system not easy to describe. Thus, it is fundamental to validate the thermodynamic model with experimental results to demonstrate its reliability to describe the system behaviour. During the implementation of the process simulator, it was important to select the right thermodynamic package through which the interactions between all species are described.

Based on literature, some researchers have focused their attention toward two thermodynamic models, *i.e.* Electrolyte – Non-Random Two Liquid (E-NRTL) and *OLI*

System. In particular, Que et al [25] suggested adopting the *E-NRTL* model to describe the liquid-gas equilibrium of the NH_3-CO_2-H_2O system due to the good match between the model results with the experimental one.

Zhou et al [24] adopted the *E-NRT-RK* thermodynamic model to compute the energy consumption for three different regeneration unit (*i.e.* ari stripping, steam stripping and distillation column) in *FO* application. Likewise, McGinnis et al [23] exploited *OLI System* to compute the energy consumption of the distillation column used as regeneration system for a *FO* desalination process.

A first evaluation between the model results with the experimental one of a regeneration unit of thermolytic draw solution was given by Kim et al [28], reporting an important under-estimation of the thermal energy for the pilot system (about 50% less than experimental result). The experimental thermal power needs to produce 1 m^3 of fresh water (about 100 TDS) was about 300kWh.

In this thesis, vapour stripping and air stripping regeneration units were implemented in Aspen Plus® to simulate the behaviour of the column using the Rad Frac block, which adopts a rigorous stage-by-stage approach for modelling distillation, absorption and stripping processes allowing simulation, sizing, and rating of tray or packed columns.

Two different thermodynamic models, *i.e. OLI® and E-NRTL-RK,* were used in the process simulator. *OLI*® was used to estimate the solution properties and the electrical conductivity of each liquid streams. While, *E-NRTL-RK* [25], that predicts very well the liquid-gas equilibrium, was adopted to model the stripping column. The flowsheet of the two stripping processes are displayed in Figure 2.3.

Moreover, a *rate-based* model was chosen for the simulation in order to take into account the physical and chemical phenomena within the stripping column, such as energy and mass transfer phenomena, hydrodynamic, thermodynamic and chemical reaction features. Conversely, the humidification column was set in equilibrium mode.

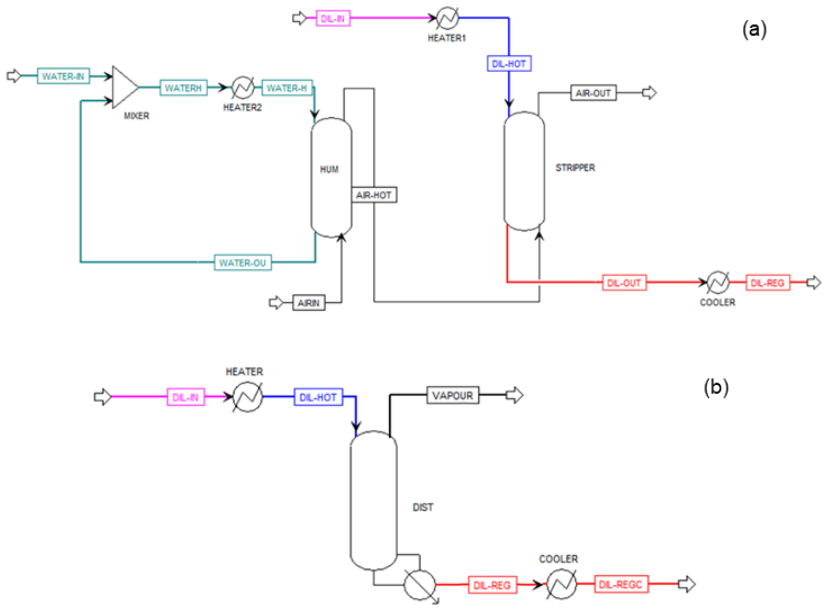

Figure 2.3. Aspen Plus® flowsheet of the experimental set-up: (a) air stripping column and (b) vapour stripping column.

After fixing the thermodynamic condition of the inlet streams along with the operating condition of the equipment, the process simulator computes the thermodynamic properties and electrical conductivity of the outlet streams and, furthermore, the thermal power (Q_{tot}) together with stripping steam/air flow-rate.

In order to evaluate the performance of the stripping column, some performance parameters were defined:

- Specific Thermal Consumption (*STC*) [kWh/m^3], defined as the amount of thermal energy consumed (Q_{tot} in kW) to produce a regenerated low solution ($F_{low,REG}$) at a fixed concentration:

$$STC = \frac{Q_{tot}}{F_{low,REG}} \qquad (2.18)$$

  This parameter is strongly dependent on the severity of the regeneration. In particular, the STC depends on the concentration of the solution fed into the stripping tower ($C_{in,REG}$) and the desired outlet concentration ($C_{low,REG}$). The outlet

concentration of the regenerated stream was computed as the sum of the species concentration remaining in solution.

- Removal efficiency (%R) defined by equation 2.19:

$$\%R = \frac{\sigma_{in,REG} - \sigma_{low,REG}}{\sigma_{in,REG}} \qquad (2.19)$$

where $\sigma_{in,REG}$ and $\sigma_{low,REG}$ are the conductivities of the inlet exhausted solution and the regenerated low solutions, respectively.

Obviously, for the validation of both process models, the operating and geometrical properties of the two columns were purposely set according to the experimental columns features.

3. Experimental investigation of RED-HE closed loop with thermolytic salts

. Chapter Outline

Part of this chapter has been published in:

F. Giacalone, **F. Vassallo**, L. Griffina,, , M.C. Ferrari, G. Micale, F. Scargiali, A. Tamburini, A.Cipollina," Thermolytic reverse electrodialysis heat engine: model development,integration and performance analysis", Energy Conversion and Management, Volume 189, 1 June 2019, Pages 1-13, doi: 10.1016/j.enconman.2019.03.045

F. Giacalone, **F. Vassallo**, F. Scargiali, A. Tamburini, A. Cipollina , G. Micale , "The first operating thermolytic reverse electrodialysis heat engine", Journal of Membrane Science, Volume 595, 1 February 2020, Article number 117522,doi: 10.1016/j.memsci.2019.117522.

F. Vassallo, F. Giacalone, F. Scargiali, A. Cipollina, G. Micale," Regeneration Units for Thermolytic salts applications in water & power production: State of art, Experimental and Modelling assessments", Desalination, Volume 504, 15 May 2021, https://doi.org/10.1016/j.desal.2021.114965

3.1 Reverse electrodialysis

The mono-dimensional *RED* model was validated at two different salinity gradients (*i.e.* 0.6-0.05M and 1.6-0.05M and considering the solutions velocity equal to 0.5 m/s.

A comparison of the experimental trend of power (P_{RED}) and stack voltage (E_{stack}) as a function of stack current (I_{stack}) is reported in *Figure 3.1*. Simulations were carried out using a longer RED stack (50 cell pairs 0.1x0.4 m^2 equipped with Fujifilm type 10 membranes provided by 0.155 µm spacer).

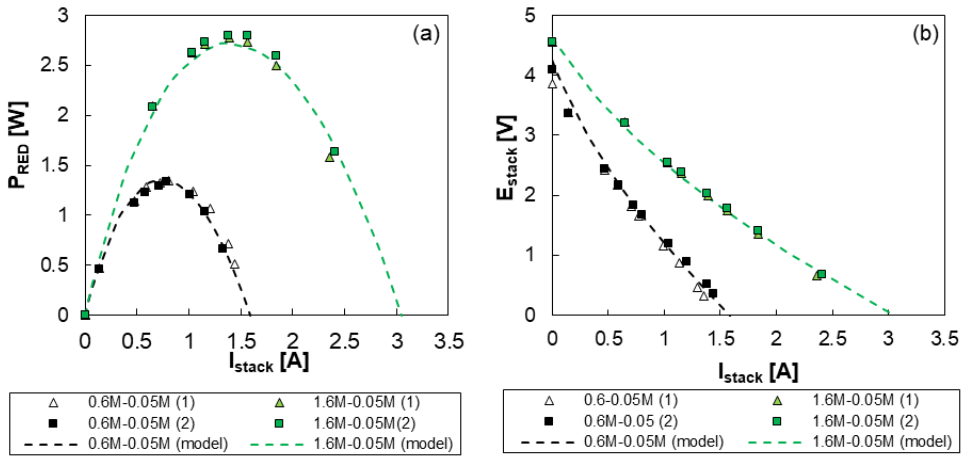

Figure 3.1. Power against electrical current (a) and electrical potential against the electrical current (b) in a RED stack fed by NH_4HCO_3 solution at solutions velocity 0.5 m/s. The RED stack had 50 cell pairs (0.1x0.4m^2).

The model predictions overlap very well the experimental results demonstrating the trustworthiness of the model in the range of conditions tested. Moreover, the maximum deviation between the electrical powers computed by model with the experimental one was around 10%.

Furthermore, the model was validating considering different salt-water solutions, such as NaCl-water solution, velocity and stack dimension giving a good match [43].

3.2 Lab-scale regeneration unit

As already presented in the previous section, in a closed-loop application based on the thermolytic-salts solution, the regeneration unit requires a "stripping step" in order to remove the salts and regenerate an exhausted dilute solutions (*i.e.* production of drinkable water for the case of *FO* application or low concentrate solution for *SGP-HE* application) and coupled with an "absorption step" in order to absorb stripped salts and regenerate the concentrate (draw) solution.

As already mention above, the main stripping process proposed in literature for the regeneration unit are: (i) air stripping, (ii) vapour stripping and distillation column. In particular, this chapter focus on the regeneration unit based on air and vapour stripping process. Two lab-scale prototype was developed and tested in order to validate the platform model implemented in *Aspen Plus*®.

3.2.1 Regeneration process conceptual schemes

Conceptual schemes of the two regeneration units, *i.e.* air stripping/absorption process and vapour stripping/absorption one, are reported in *Figure 3.2*.

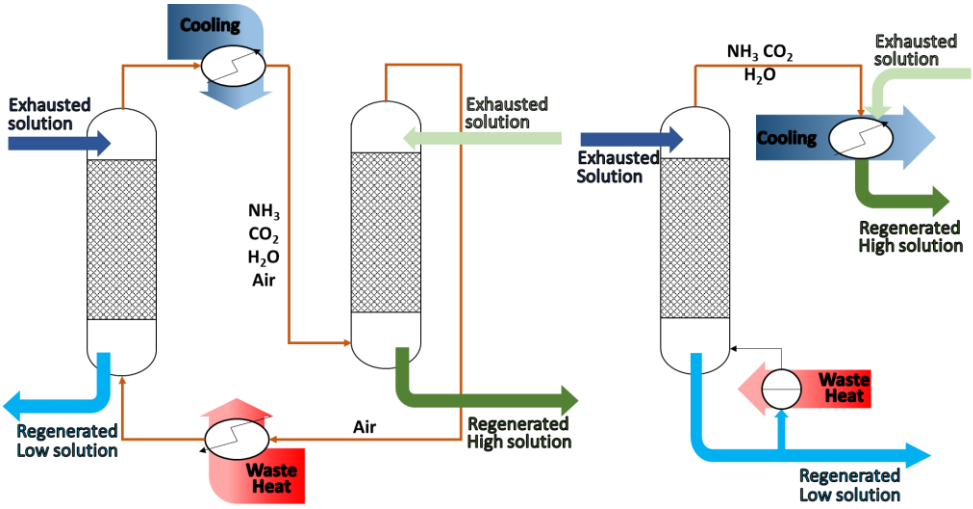

Figure 3.2. Conceptual schemes of the two lab-scale regeneration units: (a) air stripping/absorption unit and (b) vapour stripping/absorption unit.

As regard the air stripping/absorption process (see *Figure 3.2-a*), air is used to as a stripping agent to promote the realise of ammonia and carbon dioxide from the exhausted solution coming from the generation unit and to produce a "a regenerated low solution" with low concentration of thermolytic salts for (SGP systems), while, for the case of FO process, is the fresh water. The air entering in the stripping column is saturated by vaporizing a part of the exhausted solution, avoiding losses of efficiency in the stripping column due to sudden water evaporation causing a relevant drop in temperature. Thus, the hot air enriched in ammonia and carbon dioxide is cooled and fed into the absorption column, where the carbon dioxide, ammonia and part of water are condensed and absorbed in a portion of exhausted solution (*i.e.* the exhausted high solution in the case of SGP-HE). The air exiting from the absorption column is heated again and humidified and re-fed inside the stripping column for a new regeneration cycle.

In the case of regeneration unit based on vapour stripping/absorption-condensation process (*Figure 3.2-b*), the stripping agent is the steam produced by partial vaporization of the exhausted solution in a reboiler. The vapour, rising up in the column, allow the stripping of ammonia and carbon dioxide from exhausted solution generating a "regenerated low solution" with low concentration of thermolytic salts (SGP-HE process), while, for the case of FO process, is fresh water. Subsequently, the stripped gas along with the vapour are condensed and adsorbed in the exhausted solution (*i.e.* the exhausted high solution in the case of SGP-HE). coming from "generation unit", restoring the initial concentration of high solution.

In the case of forward osmosis, a draw solution rich in ammonium bicarbonate salts is used to extract water from a natural stream (e.g. seawater), resulting in a diluted draw solution, i.e. the exhausted solution of *Figure 3.2-a & b*. This solution is in part sent to a stripping unit for producing freshwater by removing the thermolytic salts, and in part sent to the absorption-condensation unit for resolubilize the thermolytic salts, regenerating the draw solution ($F_{high,\ FO}$, *Figure 1.3-a*). The freshwater produced within the stripping column must have a total concentration of N-compounds lower than 1 ppm, thus requiring very effective and energy-demanding separation.

In the case of PRO and RED, the salinity gradient between two ammonium bicarbonate solutions is consumed in the generation process to produce electricity, resulting in exhausted solutions, a dilute and a high concentration one.

In the case of PRO, only the high concentration solution, i.e. the draw solution, is fed into the regeneration following a process similar to the one reported for the FO: part is sent to the stripping unit to produce a low concentrated solution and part to the absorption-condensation unit to regenerate the high solution ($F_{high,\ PRO}$, *Figure 1.3-b*). The low solution is then added to the exhausted low solution exiting from the power unit, restoring the original concentration of the low solution ($F_{low,\ PRO}$, *Figure 1.3-b*). Part of the exhausted low solution may be mixed to the exhausted "high" solution in order to manage possible issues of salt accumulation in the "low" solution loop.

In the case of RED, both solutions are fed into the regeneration unit. In particular, the low exhausted solution ($F_{low\text{-}out,\ RED}$, *Figure 1.3-c*) is fed into the stripping unit to restore the original low solution ($F_{low,\ RED}$, *Figure 1.3-c*), while the exhausted high solution ($F_{high\text{-}out,\ RED}$, *Figure 1.3-c*) is fed into the absorption-condensation unit to resolubilize the gases and restore the original concentration of the high solution ($F_{high,\ RED}$, *Figure 1.3-c*). Also in this case part of the exhausted high solution may be added to the exhausted low solution in order to manage eventually solvent accumulation in the concentrated loop.

For both processes, stripping towers were built and tested and specific model for the global regeneration unit were developed and validated, as reported in the following.

3.2.2 Air stripping experimental set-up and experimental procedure

In *Figure 3.3*, the schematic representation of the lab-scale air stripping set-up is described. The exhausted diluted solution, store inside the plastic tank (1), is fed in a stainless-steel coil tube sited inside a thermal bath (3) by means of a peristaltic pump (SEKO, mod. Kronos 50). The thermal bath is filled with deionized water, which is heated up in the range 60-80°C. Thus, the exhausted diluted solution is heated up to the degradation temperature of salt.
The heated exhausted dilute solution is fed to the top of the stripping column (6), where it is spread over the packing material and enters in contact with the rising hot saturated air. In the stripping column, the degradation of the thermolytic salts is completed and then, the produced gases are stripped. The gaseous stream of ammonia, carbon dioxide, vapour and air leaves from the top of stripping column, while the regenerated dilute solution is extracted from the bottom of the column and store inside the plastic tank (9).
It is important to note that air must be heated and humidified before to be fed in the stripping column. As matter of fact, a hot dry air directly fed to the stripping column leads to rapid evaporation of the water causing a cooling of the air and solution in the bottom of the column. The saturation and heating of the air is achieved inside the humidification column (5). The compressor (ABAC mod. PRO B6000 500 T7.5) furnishes dry air. The air flow rate is measured by a rotameter (8) (KEI INSTRUMENTS) and, fed to the saturation column (5) from the bottom. Hot deionized water is fed to the top of the column from thermal bath via a membrane pump (SHURFLO, mod. SLV 10AA41) (4). The hot deionized water allows heating and saturating the rising dry air. Finally, the hot saturated air is fed to the bottom of the stripping column, while the deionized water is sent back into the thermal bath.

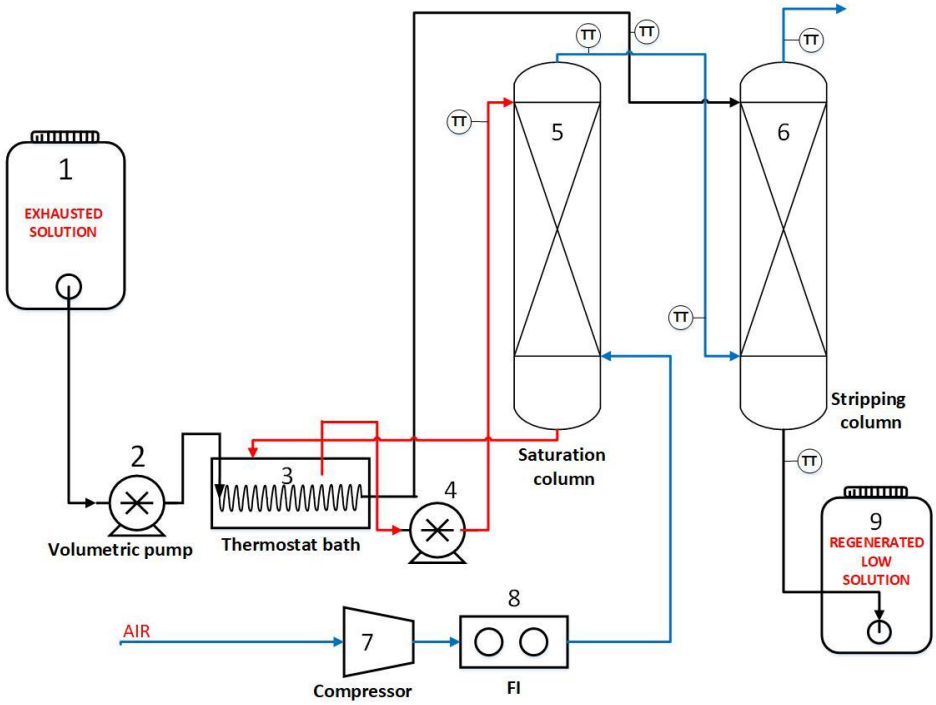

Figure 3.3. Lab-scale air stripping process. System components: (1) and (9) tank, (2) volumentric pump, (3) thermal bath, (4) membrane pump, (5) humidification column, (6) stripping column, (7) air compressor and (8) air flow-meter.

The saturation column is a Plexiglas tube with an inner diameter of 0.05 m and a height of 2 m. The column is filled with plastic Rasching rings (ID 0.01 m) for a height equal to 1.6 m. The air and deionized water are fed inside the column by means of distributor located at the bottom and at the top of the column, respectively. Along the packing height, O-Rings are placed and used as liquid distributor to avoid/reduce wall and channelling effects.

On the other hand, the stripping column is a Plexiglas tube with the same size of the saturation one. During the experiment, two different packing materials were tested in the stripping column: (i) metal Rasching rings (ID 0.01m) and (ii) Flexipac 700Y structured packing. The structured packing was provided by *Koch-Glitsch*®. It consists of corrugated stainless-steel sheets arranged in a crisscross configuration with a nominal inclination equal to 45°. Also in this case, the stripping column was filled for a height equal to 1.6 m and O-Rings was placed within the column.

The temperature of the air and liquid streams are measured by means of 6 T-type thermocouples, which are placed close to the inlets and outlets of the columns. The thermocouples are connected to National Instrument data acquisition device. The lab-scale air stripping regeneration unit in shown in *Figure 3.4.*

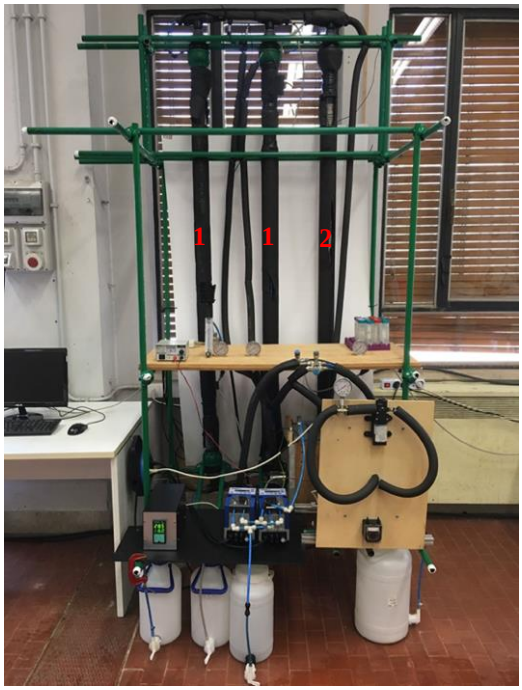

Figure 3.4. Lab-scale air stripping unit for the regeneration of thermolytic salts solution. Saturation column (1) filled with plastic Raschig rings, stripping column (2) filled with metal structured packing.

A wide experimental campaign was carried out. In particular, the influence of the flow rate and concentration of the inlet solution, air flow rate, operating temperature and packing material (*Table 3.1*) on the regeneration performance was examined.

The exhausted dilute solution (*i.e.* feed solutions) were prepared dissolving ammonium bicarbonate salts (Carlo Erba®, purity>99.5%) into deionized water.

In all test, the operative temperature of the stripping column (T_{sol}) was set equal to the temperature of saturated air (T_{air}). After reaching the stationary condition, four different samples of the regenerate dilute solution were taken every 10 min. The samples were cooled

down to 25°C and measured the electrical conductivity by means of conduct-meter (WTW, mod. 3320).

Table 3.1.Operative condition of the air stripping (Air flow rate (F_{air}), temperature of the inlet solution (T_{sol}), temperature of the inlet air (T_{air}), inlet flow rate of solution ($F_{in,REG}$) inlet concentration of solution ($C_{in,REG}$).

Packing	F_{air} [l/min]	T_{sol} [°C]	T_{air} [°C]	$F_{in,REG}$ [l/min]				$C_{in,REG}$ [mol/l] ($\sigma_{in,REG}$ [mS/cm])			
Raschig rings	35	60	60	0.1	0.15	0.2	0.25	0.21 (18)	0.50(39)	0.98 (69)	1.42 (94)
		70	70		0.15			0.21 (18)	0.50 (39)	0.98 (69)	1.42 (94)
Flexipac	35	60	60	0.1	0.15	0.2	0.25	0.21 (18)	0.50 (39)	0.98 (69)	1.42 (94)
		70	70		0.15			0.21 (18)	0.50 (39)	0.98 (69)	1.42 (94)
	70	60	60	0.15	0.2	0.25	0.3	0.2 (18)	0.5 (39)	0.98 (69)	1.42 (94)

3.2.3 Vapour stripping experimental set-up and experimental procedure.

In *Figure 3.5.* Lab-scale vapour regeneration unit. System components: (1) feed tank, (2) feed pump, (3) thermal bath, (4) stripping column, (5) reboiler, (6) regenerated solution pump, (7) regenerated low tank, (8) thermal bath, (9) concentrate tank, (10) Venturi pump, (11) Venturi ejector., the schematic representation of the lab-scale vapour stripping process is reported. The NH_4HCO_3 solution stored in a plastic tank (1) is fed to the top of the stripping column (4) by means of a peristaltic pump (2) (Cellai, mod. 503). Before feeding the solution into the column, the feed solution is heated via a thermal bath (3), which allows heating the inlet solution up to the desired temperature (T_{in} = *70°C*). The ammonium salts solution is fed to the top of the vapour stripping column, then, it falls through the packing material encountering the rising vapour. The rising vapour is produced in the reboiler, placed at the bottom of the column, vaporizing a part of the feed solution (5). The rising vapour encountering the hot feed solution in counter-current guarantees the continuous stripping of the thermolytic salts as ammonia and carbon dioxide extracted from top of the stripping tower. The stripping column, and also the reboiler, works under vacuum conditions in order

to allow the boiling of the feed solution at a temperature below 100°C. The vacuum condition is generated and maintained by mean of Venturi system (11) fed by a concentrate ammonium bicarbonate solution.

Moreover, the Venturi system allows the mixing/absorption of the stripped gases inside the concentrate solution tank (9). The concentrate solution is fed to the Venturi system by means of membrane pump (SHURFLO, mod. SH-4111-035) (10).

The condensation/absorption step involves exothermic reactions, thus required a thermal bath (8) to condense the extracted gases, which are absorbed in the concentrate solution.

The regenerate low solution is withdrawn from the reboiler via a magnetic gear pump (fluid-o-tech, mod. FG204) (6) and collected in a plastic tank (7).

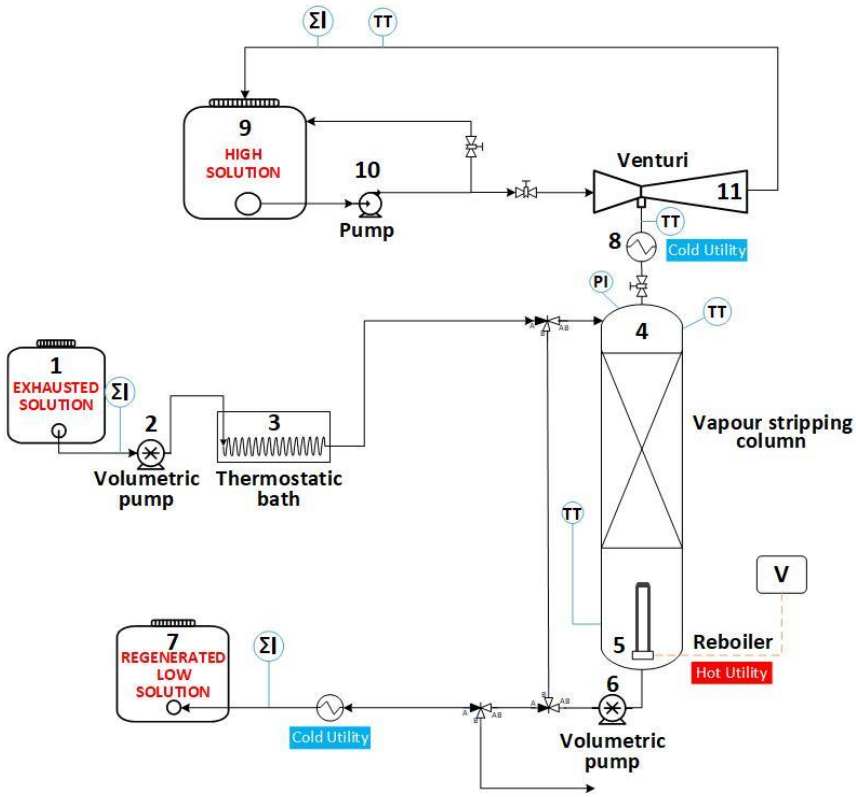

Figure 3.5. Lab-scale vapour regeneration unit. System components: (1) feed tank, (2) feed pump, (3) thermal bath, (4) stripping column, (5) reboiler, (6) regenerated solution pump, (7) regenerated low tank, (8) thermal bath, (9) concentrate tank, (10) Venturi pump, (11) Venturi ejector.

The stripping column is made up of a 2 m Plexiglas tube with an internal diameter equal to 0.05m, filled with a structured metal packing material *Flexipac /00Y (Koch-Glitch)* for a height of 1.6m. A liquid distributor allows the good distribution of the solution over the packing material. The reboiler consists of a Plexiglas tube (ID 0.1m) equipped with a regulating electrical resistance with a nominal power of 2kW. In order to monitor the boiling temperature, a T-type thermocouple is installed.

Also in this case, the temperature of the gas and liquid stream are measure with a four thermocouple. The pressure of the stripping column is monitored by an absolute pressure transducer.

A wide experimental campaign was carried out in order to test the experimental set-up under different condition (see *Table 3.2*).

The tests were performed at a fixed inlet flow rate ($F_{in,REG}$) of 0.215 l/min and inlet solution temperature ($T_{in,REG}$) equal to 70°C. In particular, regenerate low concentration (or conductivity) was monitored varying the inlet concentration (form 0.22M up to 0.61M) and the thermal power supplied to the reboiler (from 710 W up to 1050 W). The thermal power was regulated by varying the electrical current provided to the electrical resistance. After reaching the stationary condition, four samples were taken every 10 min. The samples were cooled down to 25°C and measured the solution conductivity by conductivity-meter (WTW, mod. 3320)

Table 3.2. Experimental condition of the regeneration vapour stripping unit. (inlet flow rate of solution ($F_{in,REG}$), temperature of inlet solution ($T_{in,REG}$), concentration of inlet solution ($C_{in,REG}$), temperature of reboiler ($T_{reboiler}$).

Packing	$F_{in,REG}$ [l/min]	$T_{,in,REG}$ [°C]	$C_{in,REG}$ ($\sigma_{in,REG}$) [mol/l] ([mS/cm])	Thermal power [W]			$T_{reboiler}$ [°C]		
Flexipac 700 Y	0.215	70	0.22 (18.6)	750	950		76	79	
			0.31 (25.5)	710	940	1050	76	78	80
			0.61 (46.4)	760	930	1020	77	79	80

3.2.4 Results and model validation of the model

This section is devoted to present the experimental results under different operating conditions of the two stripping towers previously presented. Moreover, the experimental results have been compared with the predictions of the process simulator in order to validate the modelling tool. Due to the complexity of the system under study, the validation of the model was carried out taking into account the electrical conductivity of the solutions (instead of the ion concentrations), simplifying and fasting the analysis of the samples. In particular, for given operative condition (*i.e.* temperature, packing material, air and inlet solution flow rate, thermal power, etc.) and inlet concentration, *i.e.* inlet conductivity at 25°C ($\sigma_{in,REG}$), the experimental conductivity of the regenerated low solution was evaluated at 25°C ($\sigma_{low,REG}$) and, then, compared with model results predicted by Aspen.

Air Stripping

The different operative conditions tested in the air stripping column are listed in the *Table 3.1*. Firstly, the effects of the packing material (*Aluminium Raschig rings and Flexipac 700Y structured packing*) was investigated, followed by effects due to the variation of the regeneration temperature (60°C and 70°C), of the air flow rate (35-70 l/minTable 3.1) and, eventually, of the inlet solution concentration (*i.e.* from 0.21M up to 1.42M corresponding to 18 mS/cm and 94 mS/cm)

Figure 3.6 a and *b* display the comparison between the outlet conductivities predicted by Aspen model with the experimental one as a function of the inlet solution conductivities ($\sigma_{in,REG}$) for the two packing materials. It is important to highlight that the model results are very close to the experimental one for both cases. As shown in *Figure 3.6*, the structured packing allows obtaining a removal efficiency higher than that obtained by Rasching rings packing. Thus, the finding average removal efficiency was equal to 44% with the structured packing, while 40% for the Rasching rings. Based on obtained results, in the following test, only structured packing was used.

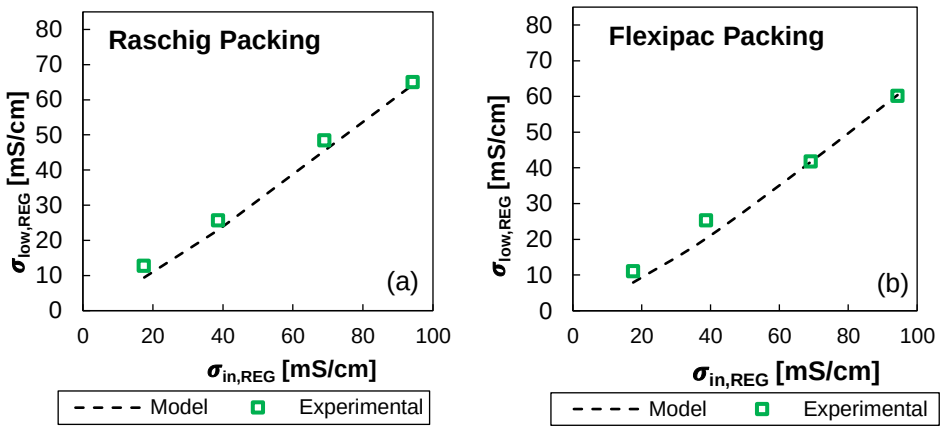

Figure 3.6. Comparison between the experimental outlet solution conductivity and the Aspen® model results for air stripping column equipped with (a) Rasching rings (b) Flexipac® structured packing as a function of inlet solution conductivity. The tests were run at given $F_{in,REG}$= 0.15 l/min, $T_{in,REG}$=60°C and F_{air} = 35 l/min

Another operating parameter affects the removal efficiency is the T_{in}. As shown *Figure 3.7*, also in this case, the Aspen model predictions are very close to the experimental highlighting the capability of the process simulator to predict very well the influence of the variation of the regeneration temperature.

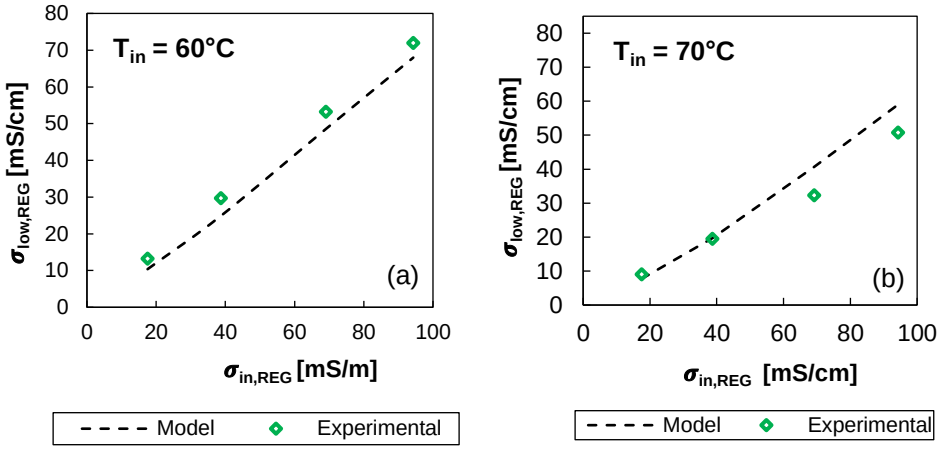

Figure 3.7. Comparison between the experimental outlet solution conductivity and the Aspen® model results for air stripping column at two different regeneration temperature (a) 60°C and (b) 70°C as a function of inlet solution conductivity. The tests were run at given $F_{in,REG}$= 0.1 l/min, F_{air} = 35 l/min and Flexipac® structured packing.

As expected, the amount the stripped increases at the increase of the regeneration temperature. The average removal efficiency ranged from an average value of 35% (regeneration temperature 60°C) up to 45% (regeneration temperature 70°C) with a peak of 56% for the lowest inlet conductivity.

Finally, the effect of the air flow-rate on the performance of the air stripping column was studied. In particular, two different air flow-rate (*i.e.* 35 l/min and 70 l/min) are investigated, fixing the flow-rate of the inlet solution ($F_{in,REG}$) equal to 0.25 l/min. As shown in *Figure 3.8*, an increase of the air flow-rate allows an increase of the amount of salts stripped from the solution. As matter of fact, the average removal efficiency increases from 27% (air flow-rate 35 l/min) up to 35% (air flow-rate 70 l/min).

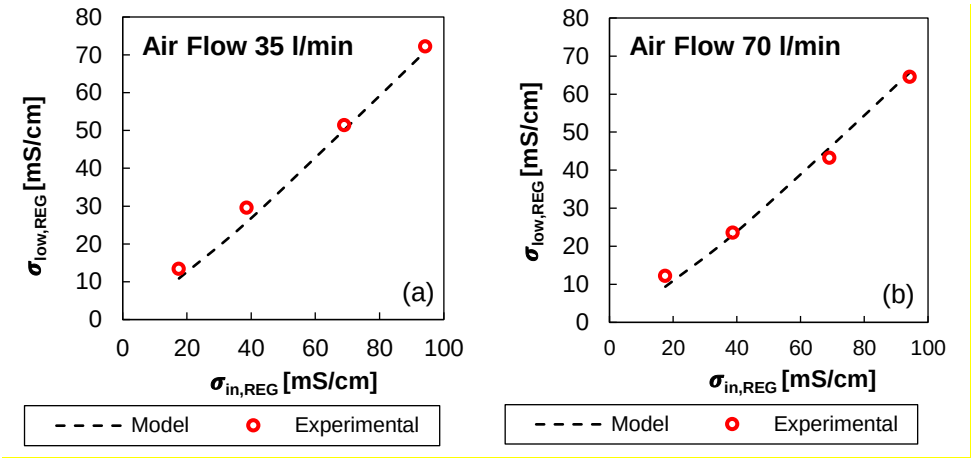

Figure 3.8. Comparison of the Aspen® model outlet conductivity with the experimental one for the air stripping column at two different air flow-rate: (a) F_{air} = 35 l/min and (b) F_{air} = 70 l/min, as a function of the inlet conductivity. The tests were run at given $F_{in,REG}$= 0.25 l/min, T_{in} = 60°C and Flexipac® structured packing.

On overall, the outlet conductivities predicted by Aspen® model and the experimental one are very close highlighting the capability of the model to predict the behaviour of the air stripping column. Moreover, the average outlet conductivities deviation between predictions by customize model (*OLI and E-NRTL-RK*) and experimental measurements is about 11%, with a maximum deviation is around 30% obtained for the lowest conductivity.

Vapour Stripping

The operative conditions investigated for the vapour stripping column are reported in Table 3.2. For these experiments, the column has been equipped with Felixipac® structure packing. Moreover, for all experiments, feed flow rate ($F_{in,REG}$) was fixed equal to 0.215 l/min in order to operate in a suitable way the packing material. During the experiment, the outlet solution flow-rate ($F_{low,REG}$) was adjusted in order to have a stable level inside the reboiler avoiding malfunction condition.

As shown in *Figure 3.9* a-c, the model predictions overlap very well the experimental outlet conductivities ($\sigma_{low,REG}$) as a function of the thermal power furnished by the reboiler. The increase of the thermal power supplied by the reboiler allows increasing the stripping vapour

flow-rate allowing the thermolytic salt removal to be improved. Thus, the maximum removal efficiency was equal to 85%.

Moreover, in all cases, the modelling prediction and the experimental results are very close with an average deviation of around 5% with a maximum equal to 15%.

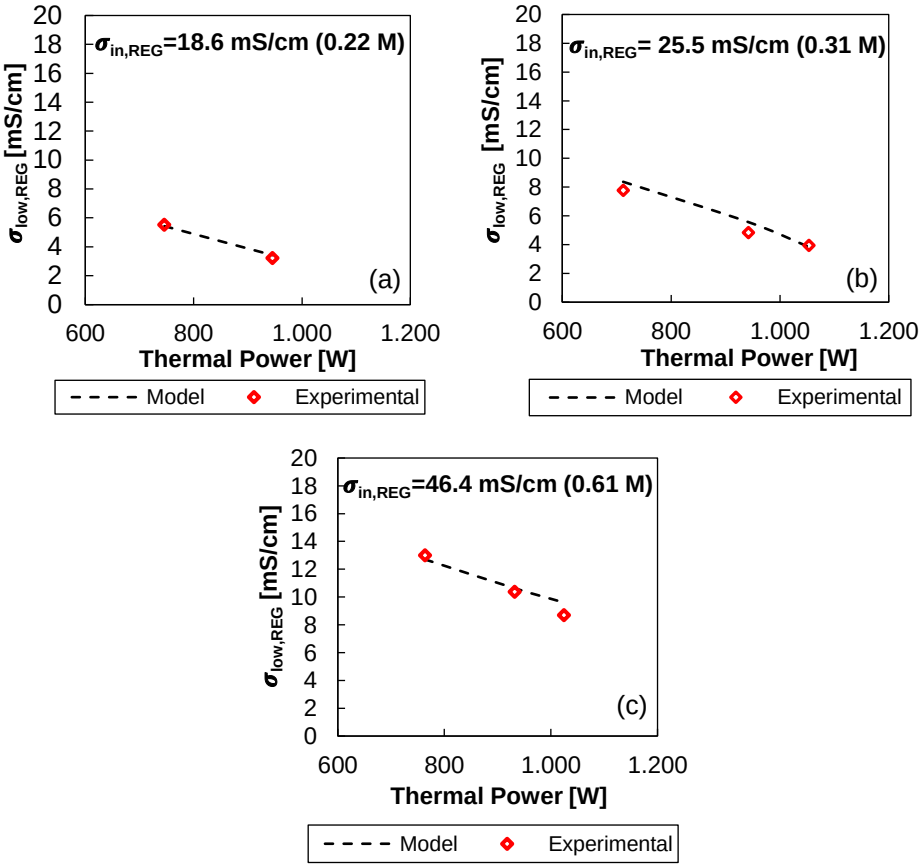

Figure 3.9. Aspen® model prediction of the outlet conductivity and experimental one form the vapour stripping column for three different inlet solution concentration ((a) 0.22M, (b)0.31M and (c) 0.61M) as function of thermal power supplied. Tests were run at $F_{in,REG}$=0.215 l/min and Flexipac® structured packing material.

3.3 Experimental investigation: First operating lab scale prototype RED-HE

This section is devoted to the present the first t-RED-HE prototype. In particular, the process scheme and the main feature of the prototype will be presented and, also, the adopted experimental procedure and the first results of the experiments.

3.3.1 Process Description

The t-RED-HE prototype consists of two main units: (i) a RED unit or *"power unit"*, where the electrical power is produced by exploiting the salinity gradient of two ammonia bicarbonate solutions, (ii) *regeneration unit*, where the low temperature waste heat is used in order to restore the initial salinity of the two ammonia bicarbonate solutions. A schematic representation of the closed-loop t-RED-HE is displayed in *Figure 3.10.*

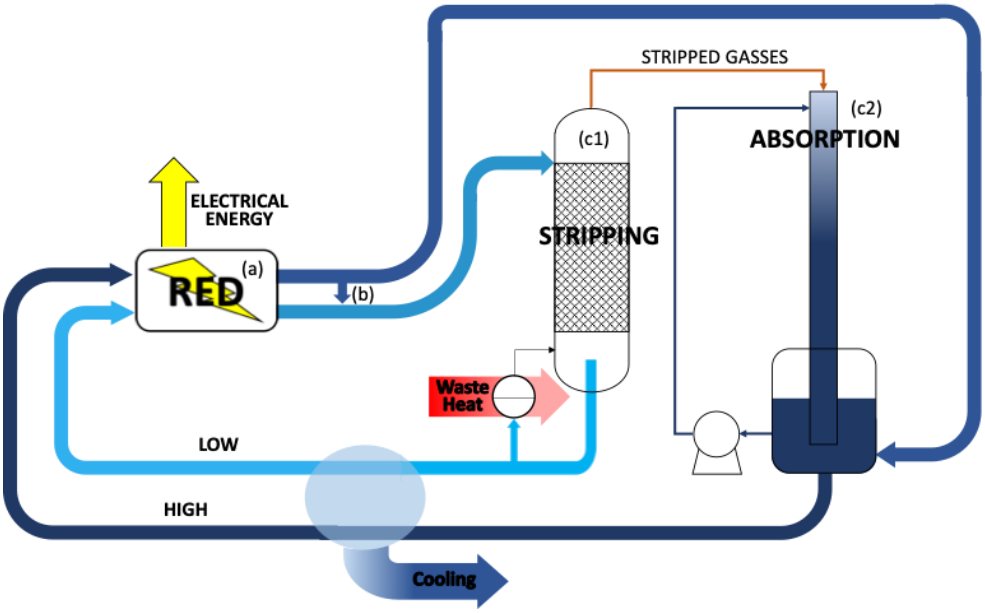

Figure 3.10. Conceptual scheme of t-RED-HE. (a) Power unit (RED unit), (b)water rebalance, (c1) stripping unit and (c2) condensation/absorption unit.

As shown in *Figure 3.10*, the Thermolytic RED-HE prototype contains the following components:

(a) Power Unit. Two different thermolytic salts solution concentrations, *i.e.* dilute (LOW) and concentrate (HIGH), are fed to the RED unit, in which the salinity gradient is converted into electrical energy as a result of a controlled mixing process thanks to the cation and the ion exchange membranes. Due to the presence of water flux and salt one, the two flowrates and the compositions of both streams change along the channels. In particular, part of the salts contained in the HIGH solution move towards the LOW solution, and, due to the osmotic flux, water is transferred from the LOW towards the HIGH. Thus, in order to restore the initial condition of both solutions, the salts and water must be moved in the opposite direction in the regeneration unit.

(b) Water rebalancing. Before to feed the solution in the vapour stripping column, it is important to restore the water content in the LOW moving part of exhausted High solution from HIGH circuit to LOW one balancing the water losses due to the osmotic flux in the RED unit and the evaporation inside the stripping column. Moreover, the direct mixing of the two streams is a source of irreversibility due to the dissipation of a part of chemical energy of the two streams causing a reduction of the overall energy efficiency.

(c) Regeneration unit. The regeneration of the two salts solutions is achieved by mean of two steps: (c1) stripping of thermolytic salts from LOW solution and (c2) condensation/absorption of the exiting gases from the top of the column in the HIGH solution. After the water rebalancing step, the LOW solution is pre-heated and fed into the top of the vapour stripping column. The exhausted Low solution is spread over the structured packing material by mean of a liquid distributor. The fallen solution through the packing materials is put in contact with the rising vapour in counter-current. The stripping vapour is produced by vaporizing of a part of the solution in a reboiler, which is placed on the bottom of the column. The rising hot vapour promotes the thermolytic salts degradation and the stripping of ammonia (NH_3) and carbon dioxide (CO_2) reducing the ions concentration (*i.e.* $NH_4^+, CO_3^-, CO_3^{2-}$, and $NH_2CO_3^-$) in the solution. The regenerated LOW solution withdrawn from the reboiler is cooled down to 25°C, collected in a LOW solution plastic tank and eventually refed to the RED unit. Whereas, the stripped gases, which are rich in water, ammonia and carbon dioxide, exits from the top of the column and reaches the barometric condenser. Before reaching the barometric condenser, the gases are cooled down to 25°C in order to condense the water and promote the absorption of the ammonia and carbon dioxide. In order to promote the adsorption of the stripped gases in the HIGH solution, the barometric column produces the needed vacuum to vaporize the LOW solution at low temperature

(T<100°C). The barometric column operates recirculating the HIGH solution from the reservoir to the top of the column. Moreover, the recirculating HIGH solution in the barometric column is mixed with the exhausted HIGH solution exiting from the RED unit. The regenerated HIGH solution withdrawn from the bottom of the barometric column is cooled down and, thus, recirculated to the RED unit.

3.3.2 Prototype description.

In *Figure 3.11*, the simplified *P&ID* diagram is displayed. The RED unit was furnished by REDstack BV (The Netherlands) consists of 50 cell pairs with an active area equal to 0.1x0.44 m^2. Each cell pair consists of two stacked membranes, *i.e.*one cation and one anion exchange membrane (Type 10 - Fujifilm Manufacturing Europe BV -The Netherlands). Inside each compartment, *i.e.* LOW and HIGH compartment, a spacer of 155 µm thickness and with a porosity equal to 79% (Deukum GmbH, Germany) is placed. The RED unit and the vapour stripping one are fed by means of gear pump (fluid-o-tech FG204). An electrolyte rinse solution (ERS) with a reversible redox couple $[Fe(CN)_6]^{4-}/[Fe(CN)_6]^{3-}$ is recirculated in the electrode compartments in order to convert the ionic current into the electric current. In order to minimize the osmotic flux from/to electrode compartments a proper supporter electrolyte (NH_4HCO_3) was added in the ERS. Moreover, different membrane (*i.e.* Fumasep F-10150-PF, Fumatech GmbH, Germany) was used to for the electrode compartment because it minimized the passage of the iron species at high concentration in the ERS.

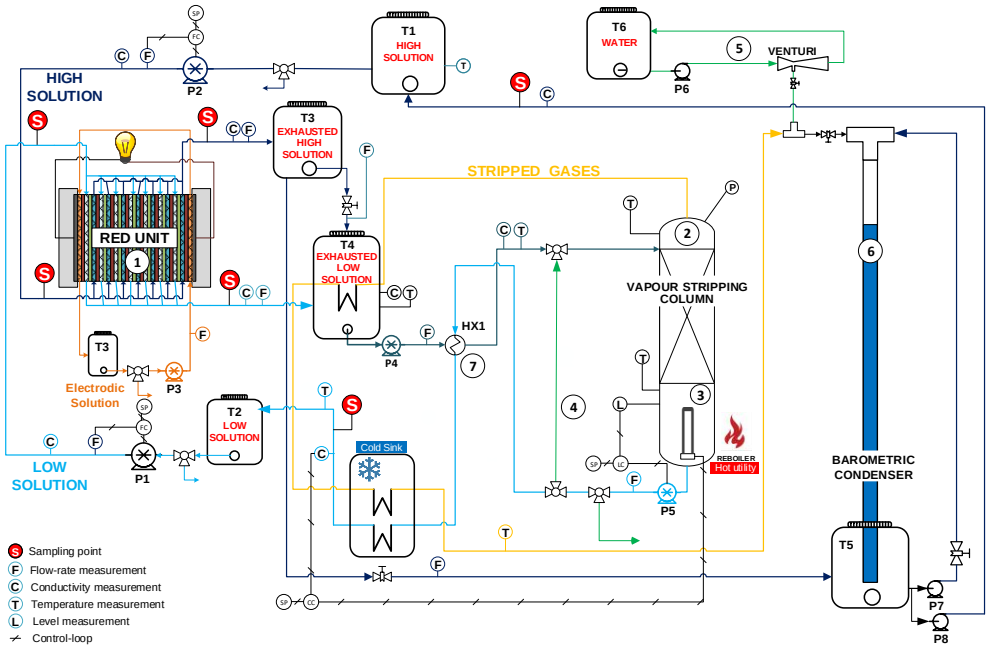

Figure 3.11. Simplified P&ID diagram of the thermolytic RED-HE prototype. The main items are: (1) RED unit, (2) Vapour stripping column, (3) Reboiler, (4) auxiliary circuit, (5) Venturi system, (6) barometric column, (7) thermal integration exchange, (S) sampling point.

The main properties of the IEM membrane are listed in *Table 2.1*, while the properties of the end membrane are reported in *Table 3.3*.

Table 3.3. Main properties of the end ion exchange membrane.

IEM	Thickness [μm]	Electrical resistance [Ω/cm^2]	Permselectivity [%]	Water permeability [g/(hr bar m^2)]
Fumasep F. 10150 PF	140-150	1.8-2.9[(a)]	94-98%[(b)]	n. a.

[a] NaCl at 25°C

[b] 0.1/0.5 mol/kg KCl at T=25°C

The vapour stripping column (2) is a Plexiglas tube of a height of 2 m and an internal diameter of 50 mm, filled with a structured packing material (*Flexipac® 700Y, Koch-Glitsch*). The packing material height is equal to 1.6 m. The bottom of the vapour stripping column is connected to a reboiler (3), where a part of LOW solution is vaporized to produce the

stripping vapour. The low-grade heat source has been simulated by means of an electrical resistance placed inside the reboiler. The heat supplied by electrical resistance is fixed regulating the intensity of the electrical current. The temperature of the solution in the reboiler is monitored by means of a T-type thermocouple.

Pressure and temperature of the column are monitored by an absolute pressure transducer (VEGA - VEGAbar 14) and a T-type thermocouple placed in the top of the column, respectively.

The barometric condenser (6) is made up of a 15 m tube (inner diameter of ½") with the bottom end immersed *HIGH solution tank* (T5).

The hot gases exiting from the top of the column is used to pre-heat the exhausted LOW solution by means of a stainless (AISI 316) coil tube submerged in the tank (T4) recovering part of the heat.

Moreover, a hair-pin exchange (7) is used for the thermal integration to recover a part of the heat exiting with the *regenerated LOW solution* from the bottom of the column and to pre-heat the solution fed in the vapour stripping column. It is made up of stainless steel (AISI 316) tube with an internal diameter of 6 mm and thickness 1.5 mm inserted in a Plexiglas tube (ID 12mm, thickness 2mm). The cold LOW solution flowed in the annular section and the regenerated Low solution in the internal tube. In order to reduce the thermal dissipation of hair-pin exchange, the Plexiglas tube is inserted inside an insulating tube of expanded neoprene.

The water rebalance is achieved by mixing a part of the exhausted HIGH solution with the exhausted LOW solution inside the tank T4. The amount of the exhausted HIGH solution to mix with the exhausted low solution was chosen in order to achieve the desiderate concentration (*i.e.* conductivity). This is evaluated for each operative condition by means of using the RED model along with the process simulator performing the mass balance. The exhausted HIGH solution tank is placed on the top of the prototype, while the exhausted LOW solution tank is placed on the bottom. This allows a natural flowing of the exhausted HIGH solution into the exhausted LOW solution tank. The control of flow rate is achieved by opening a needle vale placed along the line of exhausted HIGH solution.

The conductivity, temperature and flow rate of the streams in the RED unit and Regeneration one are monitored by using online sensors. The specification of the sensors installed in the prototype are listed in *Table 3.4*.

All sensors in the RED-HE prototype have been electrically connected with chassis produced by *National Instrument*. Afterwards, the computer was linked with the chassis by means of software *NI Measurement & Automation Explorer (MAX)*. Eventually, an interface panel has been implemented in the software LabVIEW in order to monitor and control the desiderate parameters of the prototype.

Table 3.4. Specification of the sensors installed in the prototype.

Component	Specification
Pressure transducer	VEGA-14 range: 0-100kPa accuracy: 0.3% FS
Thermocouple	TC direct mineral insulated thermocouple, range:200-400 accuracy: ± 1°C
Conductivity meter	WTW 3320 pH/Cond; range: 0.000-1000 mS/cm, accuracy ± 0.5% FS and ± 1LSD
Multimeters	FLUKE 175 True RMS, range:0.1mV-1000V and 0.01 mA-10A, accuracy: V DC ±(0.15% + 2 counts) A DC ± (.0% + 3 counts).
Data logger for Thermocouples	TC resolution: 0.1°C accuracy:0.1 % of reading
Flowmeters	Riels VMZ 030 DN 3, Range: 0.05-2 l/min accuracy:1% reading
Reboiler level sensors	VEGADIF 65 Range: 0-10 kPa accuracy ±0,065% FS

As seen *Figure 3.11*, four control-loop have been implemented in the prototype in order to control the flow-rate of LOW and HIGH solution feeding in the RED unit, the concentration of regenerated LOW solution from the bottom of the column (varying the electrical current supplied to electrical resistance), and the liquid level inside the reboiler (varying the flow rate of the regenerate LOW solution withdrawn from the bottom of the column).

Six different sampling point (S) are used to measure the electrical conductivity by means of laboratory conductivity-meter (WTW, mod. 3320) of the solutions. Two sampling points are placed at the inlet of the RED unit, another two at the outlet of RED unit, and the last two points are placed in the bottom of stripping and barometric column.

Moreover, a thermal bath is used as cold seek to cool down to 25°C the regenerate LOW solution after thermal integration and to condense the stripped gases.

During the start-up, an auxiliary circuit (4) is used to recirculate the hot solution form the bottom to the top in order to speed up the heating-up of the packing material. Moreover, also a Ventury ejector system (5) is used to evacuate air from the stripping column.

A picture of the RED-HE prototype is shown in *Figure 3.12*.

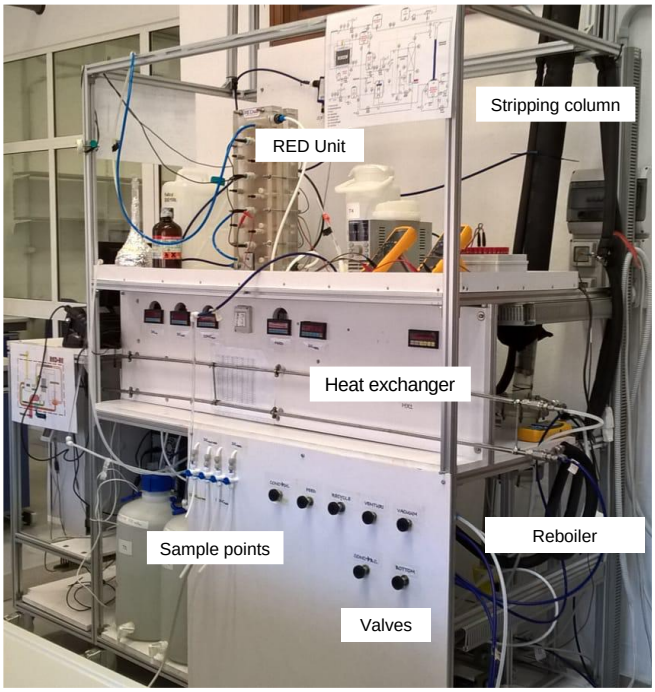

Figure 3.12. The t-RED-HE prototype.

3.3.3 Experimental procedure

The two feed solutions are prepared dissolving anhydrous high grade ammonium bicarbonate salt (Carlo Erba®, purity > 99,5%) into deionized water. The electrode rinse solution is prepared dissolving 0.1 mol/l of $K_3Fe(CN)_6$ and 0.1 mol/l $K_4Fe(CN)_6 \cdot 3H_2O$ in deionized water and adding an amount of ammonium bicarbonate equal to the average concentration of the two feed solutions.

An experimental calibration was carried out to link the measured conductivity (at 25°C) to the molar concentration of dissolved salt as follow:

$$\sigma = \Lambda \cdot C \qquad (3.1)$$

where σ is the solution conductivity (mS/cm), Λ is the specific molar conductivity (mS $cm^{-1}mol^{-1}l$)) and C is the molar concentration. The specific conductivity (mS l $cm^{-1}mol^{-1}$)) of ammonium bicarbonate solution is computed as follow:

$$\Lambda = \Lambda_0 - \frac{A_\Lambda C^{\frac{1}{2}}}{1+B_\Lambda C^{\frac{1}{2}}} \qquad (3.2)$$

where Λ_0 is the equivalent conductivity of salt at infinite dilution, A_Λ, B_Λ and C_Λ are fitting parameters, and C is the molar concentration. The fitting coefficients for NH_4HCO_3 at 298K have been obtained by fitting experimental data leading to: Λ_0= 101.88 A_Λ= 30.32, B_Λ= C_Λ= 0. In particular, both literature data [47] and original experiments were used in order to double check the consistency of the equation with the real behaviour of solutions.

For the aim of this work, the inlet flow rates in the RED unit are set equal to 0.215 l/min corresponding at a velocity inside the RED compartments of 0.5 cm/s. This value of both flow rates allows obtaining a good compromise between the RED unit and the regeneration unit operability.

During test, The RED unit is connected with a fixed external load. The value of the external load is chosen to operate around the maximum power condition. During continuous operation, the characteristic power behaviour was also evaluated at different operating time to valuate possible variations in the RED unit performance. In order to evaluate the power curve of the RED. Thus, the external load was changed from open-circuit (OC) to short-cut (SC) condition, measuring the stack voltage (V_{stack}) and the stack current (I_{stack}) by two multimeters (FLUKE 175). The electrical power (P_{RED}) produced by the RED unit is evaluated by the eq 2.6.

Typically, the performance of the RED unit is evaluated in term of maximum power production generated per unit of cell pair

$$P_{d,max} = \frac{P_{RED,max}}{A_m N_{cp}} \qquad (3.3)$$

where $P_{d,max}$ is the maximum power generated by the RED unit, A_m is the is the active air of the membrane (*i.e.* 0.1x0.44 m^2) and N_{cp} is the number of cell pairs (*i.e.* N_{cp} = 50).

The solution exiting from the regeneration unit are cooled down around 23-27°C in order to guarantee constant operating temperature of the RED unit. As matter of fact, a higher temperature condition may increase the RED power production due to the reduction of the stack resistance [48], but causing a possible formation of gas bubble inside the stack due to the salt degradation.

The operative pressure of the stripping column varies between 0.41-0.56 bar, whereas the reboiler temperature is in the rage 78-85°C. A start-up period of about 30 minutes is needed to heat-up the column and to reach the stationary condition.

In all experimental tests, the thermal duty was set in order to obtain the initial conductivity, *i.e.* concentration, of the solution fed into the RED unit. A solid-state relay was utilized in order to control the current provided to the electrical resistance (in the range 0-10 A) by using a voltage input between 0-10 V. The voltage supplied to the electrical resistance was kept equal to the main voltage (around 226 V). Thus, the thermal duty supplied to the reboiler was computed by measuring the voltage and the electrical current by mean of TRUE RMS multimeter.

The prototype was tested for more than 50h, to assess the robustness of the whole system subjected to a constant external load. In particular, the operation was performed in two/three days using the same solution inside the unit. In the first day, the operation continuously flows from 8 to 12 hours. Thus, it was turned-off and started again in the subsequent day, simulating the possible on/off operating cycles of the system when used as an energy storage mode. Finally, in the last day the prototype was run continuously for about 24h.

In order to assess the operational stability, a non-dimensional parameter, *i.e.* N_{RED}^{C}, was defined as ratio between the duration of the test and the residence time inside the RED unit:

$$N_{RED}^{C} = \frac{t_{test}}{t_{RED}} \qquad (3.4)$$

where the t_{test} is the duration of the long run test [min], and t_{RED} (residence time inside the RED unit) is the ratio between the liquid hold-up inside the compartments (channels) and the volume flow rate (*i.e.* 0.215 l/min) [min].

The N_{RED}^{C} is the number of cycles that the feed solution (LOW or HIGH) undergoes during the closed-loop operation inside the RED. In particular, a value of N_{RED}^{C} around 2700 has been reached for a time duration of the long run test up to 55h.

Also for the regeneration unit, a non-dimensional parameter, *i.e.* N_{REG}^{C}, was defined in order to estimate the number of the cycles that the LOW solution was subjected during the closed-loop operation in the vapour stripping column. This parameter is computed as follow:

$$N_{REG}^{C} = \frac{t_{test}}{t_{REG}} \qquad (3.5)$$

where t_{REG} is computed as the ratio between the liquid old-up inside the vapour stripping column (estimated as the 10% of the column volume) and the inlet flow rate (*i.e.* 0.23 l/min). Another parameter used to evaluate the performance of the prototype is the thermal efficiency (η_{th}) computed as the ratio between the electrical power produced by the RED unit and the thermal duty (TD) of the vapour stripping column:

$$\eta_{th} = \frac{P_{RED}}{TD} \qquad (3.6)$$

Finally, the exergy efficiency of the whole prototype (η_{ex}) is calculated as the ratio between the thermal efficiency (η_{th}) and the ideal Carnot efficiency (η_C), operating at the same range of temperature:

$$\eta_{ex} = \frac{\eta_{th}}{\eta_C} \qquad (3.7)$$

Since an electrical heater was used as an external source, for simplicity the exergy efficiency was computed considering the Cannot efficiency. Although, the exergy efficiency of the whole closed loop can be computed by the electrical energy produced divided by the variation Gibbs free power of external heat source.

As regard the RED unit, further performance parameters have been defined to assess the performance of the RED unit. One of these parameters is the thermodynamic yield (Y), computed as the ration between the experimental electrical power (P_{RED}) produced and the Gibbs free power of the mixing ($\Delta\dot{G}_{mix}$):

$$Y = \frac{P_{RED}}{|\Delta\dot{G}_{mix}|} \qquad (3.8)$$

The Gibbs free power of mixing is an important thermodynamic figure of merit that allows computing the maximum amount of power to be harvested form the mixing of two solutions at different concentration. This thermodynamic figure is calculated as difference between the Gibbs free power of the mixed solution and the two original one ($\dot{G}_H + \dot{G}_L$):

$$\Delta\dot{G}_{mix} = \dot{G}_{mix} - (\dot{G}_H + \dot{G}_L) \qquad (3.9)$$

Moreover, the Gibbs free power of a generic streams ($\dot{G}_k$) is computed considering the contribution of the salt and the water:

$$\dot{G}_k = \dot{n}_k \mu_k = \dot{n}_{water,k} \mu_{water,k} + \dot{n}_{salt,k} \mu_{salt,k} \qquad (3.10)$$

where $\mu_{water,k}$ and $\mu_{salt,k}$ is the chemical potential of the salt and the water, respectively [43,49], $\dot{n}_{water,k}$ and $\dot{n}_{salt,k}$ is the mole flow-rate (mol/s) of the water and salt k^{th} stream. The molar flow rate of each strems is eavluated through the experimental measurement of the flow-rate assumg that the density (as well as conductivity) of the solution is one of an equvalent solution of ammonium bircabonate at a given molarity. The density of the solution is a linear function of the molar concentration [45].

Finally, the RED exergetic efficiency ($\eta_{ex,RED}$) represents the fraction of chemical energy converted into electrical energy in the RED unit. The RED exergetic efficiency is defined as follow [43]:

$$\eta_{ex,RED} = \frac{P_{RED}}{(\dot{G}_H + \dot{G}_L)_{in} - (\dot{G}_H + \dot{G}_L)_{out}} \qquad (3.11)$$

All performance parameters above reported refer to the gross values of generated power, not taking into account the power required by pumps in order to operate the RED-HE prototype.

3.3.3 Results and discussion

Long-run tests were carried out using four different salinity gradients at the inlet of the RED unit (see *Table 3.5*) analysing the behaviour of the RED-HE unit in terms of conductivity of the solutions and performance parameters, such as: power, specific thermal consumption, and exergy efficiency.

Table 3.5. Operating conditions, i.e. molarity, top column pressure and bottom temperature, and experimental time duration for the four investigated cases.

	High Solution	Low Solution	Duration	Column Conditions	
case	Molarity [M] (σ_{av} [mS/cm])	Molarity [M] (σ_{av} [mS/cm])	Time [h] (N_{RED}^{C})	P_{TOP} [bar]	T_{BOTTOM} [°C]
(A)	0.6 (45.9)	0.05 (4.9)	8 (360)	0.40	77.0
(B)	1.0 (72.8)	0.052 (5.2)	55 (2700)	0.43	78.0
(C)	1.45 (94.8)	0.05 (4.8)	9 (400)	0.49	81.7
(D)	1.9 (114)	0.052 (5.2)	55 (2700)	0.55	84.5

As reported in *Table 3.5*, the long-run tests were performed for 8h for case A and C, while for case B and D up to 55h. For case B and D, the test token several days, initially with an intermittent functioning (8-12h of operation alternated with 12-16h of stop) in order to simulate the use as an energy storage system, and finally it operated continuously for more than 24 h.

3.3.3.1 Analysis of the stability in long run operation

The RED-HE prototype was tested in order to study the behaviour and the stability of all components during the long-run tests. The time variation of the conductivities of the solutions at the inlet and outlet of the RED unit working close to the maximum electrical power production is displayed in *Figure 3.13* a and c for case B (*i.e.* 1.0 M and 0.052 M) and D (*i.e.* 1.9M-0.052M). Referring to case D (*Figure 3.13-c*), the concentration of the HIGH inlet solution is reduced from 1.9M (*i.e.* 114 mS/cm at 25°C) down to 1.43M (*i.e.* 93.8 mS/cm at 25°C). At the contrary, the LOW inlet solution increases from 0.05M (*i.e.* 5.2 mS/cm at 25°C) up to 0.38 (*i.e.* 31.7 mS/cm at 25°C). After the water rebalancing, the concentration of the LOW solution is further increased from 0.38 up to 0.54 (*i.e.* 42.6 mS/cm at 25°C). The initial concentration of the LOW and HIGH solutions was, finally, restored in the regeneration unit, where the ammonium bicarbonate underwent a thermal degradation and removed by the LOW solution as gaseous ammonia and carbon dioxide. The stripped gases, rich in vapour, ammonia and carbon dioxide, were condensed and absorbed in the HIGH solution inside the barometric column.

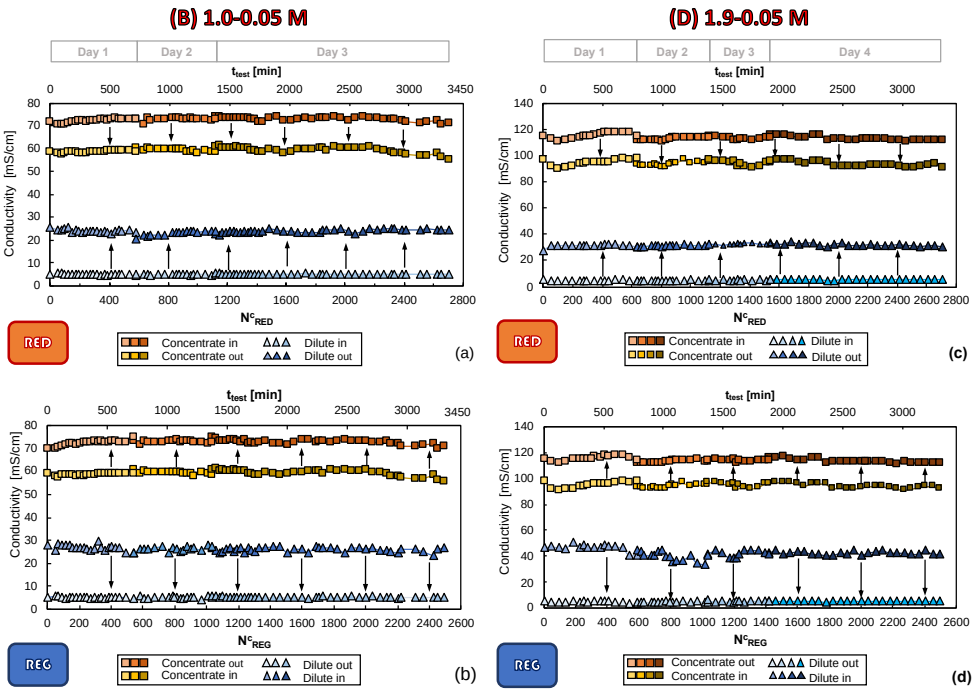

Figure 3.13. Time variation of the inlet/outlet conductivity of the solution in the RED unit (a and c) and the regeneration unit (b and d) for case B and D, respectively. The colour vertical bar in figure a and c denote when the power density curves were performed and reported in Figure 3.15.

The time variation of the conductivity of the regenerated solution is reported in *Figure 3.13 b* and *d* for case B (*i.e.* 1.0 M and 0.052 M) and D (*i.e.* 1.9 M-0.052 M), respectively. Regarding case D (*Figure 3.13-d*), the LOW conductivity solution is reduced from 0.54 M (*i.e.* 42.6 mS/cm at 25°C) down to 0.05 M (*i.e.* 5.2 mS/cm at 25°C), while the conductivity of the HIGH solution is increased from 1.43 M (*i.e.* 93.8 mS7cm at 25°C) up to 1.9 M (*i.e.* 114 mS/cm at 25°C), restoring the initial concentration (conductivity) of both solutions. Same consideration for the results of case B reported *Figure 3.13 a* and *b*.

The coloured vertical bars in *Figure 3.13 a* and *c* indicate when the power density measured was performed as reported in *Figure 3.15*.

Moreover, *Figure 3.13* shows that the conductivity of the solution was stable over the duration of the experiment highlighting the robustness of the prototype in continuous and intermitted operation (when the prototype was stopped and the solutions were store in the

buffer tanks for 12-16h), and, then, the potential use of RED-HE system for energy storage application.

In *Figure 3.14*, relevant results, such as specific thermal power, electrical power density and exergy efficiency, are reported for case B and D, respectively.

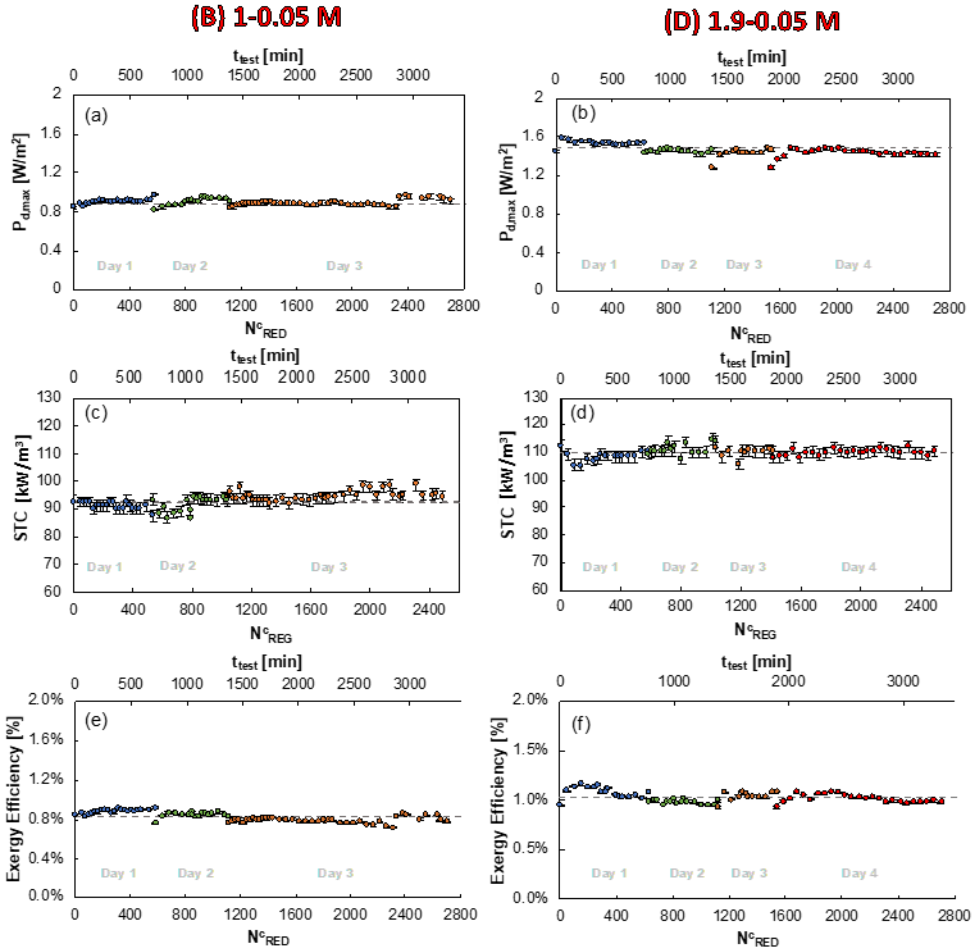

Figure 3.14. Time variation of the power density ($P_{d,max}$), Specific Thermal Consumption (STC) and exergy efficiency of the system for case B(a, c and e) and case D (b, d and f)

In all cases, the power density increases for about 10% in the first 1-2 h of the test until to reach the stationary condition. This behaviour may be due to the stabilization of the membrane along with the reduction of the electrical resistance of the RED unit. Only a small deviation (about 5%) form the average value are seen at the end of the operation (55 h or

2700 N_{RED}^{C}). The average value of harvested $P_{d,max}$ is equal to 1.5 W/m^2 for case D (1.9 M-0.0052 M) and 0.9 W/m^2 for case B (1 M - 0.0052 M). The increase of the HIGH concentration solution from 1.0 M up to 1.9 M results on an increase of the outlet LOW solution concentration from the RED unit. As matter of fact, the increase of the salinity gradient allows increasing both the migrative flux across the IEMs membrane (due to the increase of the electrical power production) and uncontrolled mixed phenomena (*i.e.* diffusive and osmotic salt and water flux, respectively).

Moreover, this causes an increase of the thermal power in the regeneration unit. In particular, the average STC of 93 kWh/m^3 for case B and 110 kWh/m^3 for case D (*Figure 3.14 c* and *d*). Also in this case, a small variation (about 5%) is observed at 55 h or 2500 N_{REG}^{C} of the operation.

Finally, the exergy efficiency of the system is shown in *Figure 3.14 e* and *f*. In particular, the average exergy efficiency is equal to 0.8%for case B and 1.1% for case D, with a small deviation in the first 1-2h and at 55h due to the variation of STC and P_d.

3.3.3.2 RED power generation for the four salinity gradients

The RED unit is an electric power generator, whose performance is typically evaluated by means of the so called “polarization curve”. The polarization curve consists in a plot of stack electrical voltage (V_{stack}) and generated power density ($P_{d,RED}$) as a function of the stack electrical current (I_{stack}) and voltage, respectively. Experimental results for the four tested different salinity gradients are reported in *Figure 3.15 a* and *b*.

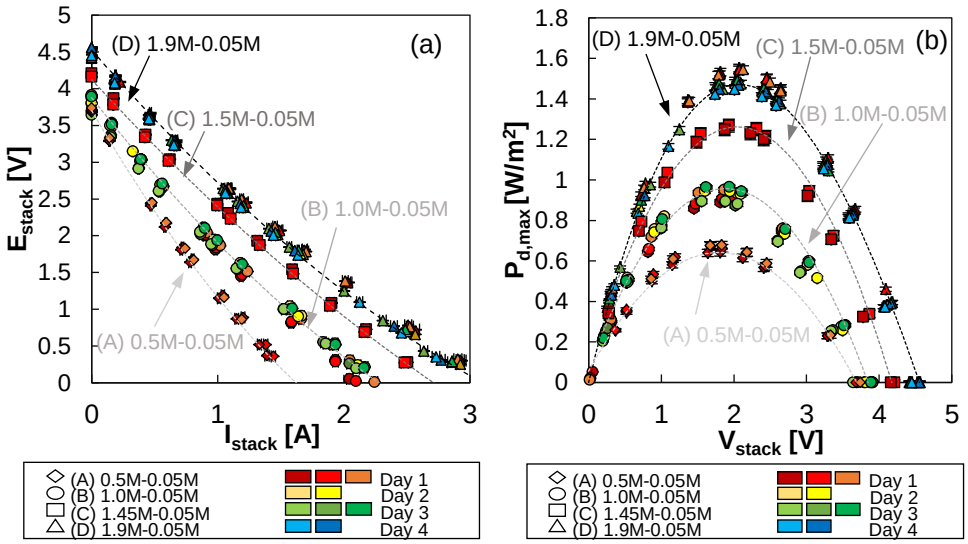

Figure 3.15.(a) Stack voltage as a function of stack current. (b) Power density generated as a function of stack voltage. Different series reported refers to the different salinity gradient tested performed at different number of cycles in the RED unit.

Note that for case A and C the polarization curves refer to one day (8-9h) of continuous operation, while for case B and D, different measurements were performed also in the day 3 and 4 of operation, as reported by the coloured rectangles in *Figure 3.15.*

Firstly, it is important to note that the stable behaviour of the power density generated by the RED unit in all reported cases, leading to good reproducibility of all power density curves (*Figure 3.15-b).* Moreover, the maximum power density value reported in *Figure 3.15-b* is achieved using different external load. In fact, for case A it ranged between 1.8 and 2.2 Ω, for cases B and C between 1.2 and 1.8 Ω, while for the last case D among 0.82 and 1. Ω, indicating a progressive reduction of the stack resistance at the increase of HIGH solution concentration.

Another significant result is the non-ohmic behaviour of the RED stack due to the non-linear relationship between the V_{stack} and I_{stack} as shown in *Figure 3.15-a.* As matter of fact, at increase of the electrical stack current, the internal resistance of the stack decreases due to the increase of the LOW solution concentration (*i.e.* conductivity). This effect is more evident due to the high residence time (*i.e.* low velocity of the solution along with long channels) used in this experimental campaign. Similar results were already reported in the literature by Vanoppen et al. [50]. Therefore, the maximum power density achieved in the experimental

campaign (about 1.5 W/m^2), using ammonium bicarbonate solutions of 1.9 M and 0.052 M, is lower than the highest power density reported in the literature (*i.e.* 2.42 W/m^2) up to now [37]. Conversely, the adoption of longe channels and low velocity allows a better exploiting of the salinity gradient.

Another two performance parameters of the RED units, *i.e.* thermodynamic yield (Y) and the exergetic efficiency, are reported in *Figure 3.16.*

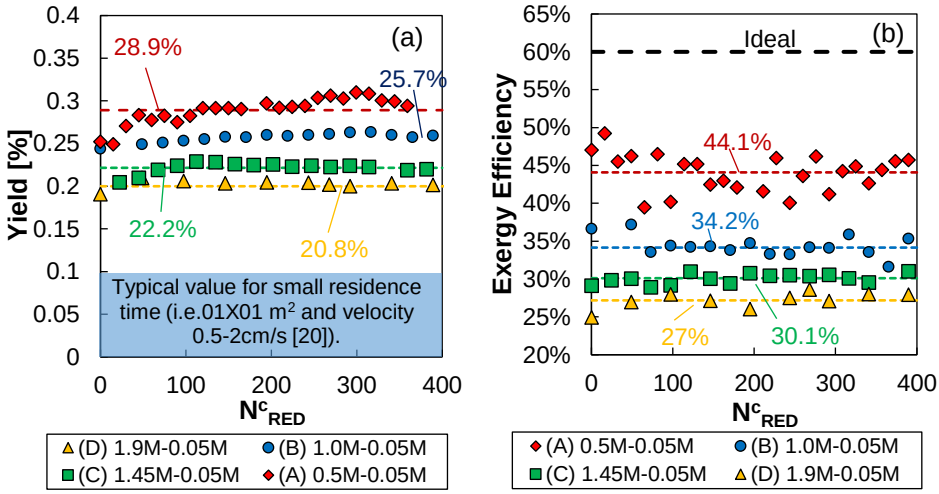

Figure 3.16.(a) Thermodynamic Yield vs the number of RED cycles: experimental value and typical value reported in the literature [37]. (b) the RED exergy efficiency vs number of RED cycles: experimental value and theoretical value for an ideal membrane (i.e. unitary permselectivity, null water flux and salt permeability)

An average thermodynamic yield of about 30% is achieved for case A, which goes down at an increase of the salinity gradient reaching a value of about 21% for case D *Figure 3.16-a*. As shown in *Figure 3.16-a*, the obtained value of average thermodynamic yield is five times higher than the values obtained in a laboratory RED unit (0.1x0.1 m^2) reported in the literature. In particular, the increase of the HIGH concentration solution reduces the thermodynamic yield due to the larger available Gibbs power that could be harvested (using longer RED channels to increase the residence time), but also the increase of the uncontrolled mixed phenomena [43], shown by the lower value of the exergy efficiency. In fact, the exergy efficiency decreases from 44% down to 27% when the concentration of the HIGH solution has been increased. Interestingly, the exergy efficiency of the system is comparable to the

maximum value obtained in a stack provided with ideal membranes (i.e. no water and salt flux and unitary permselectivity [43] operating with the same condition).

In fact, the maximum value of exergy efficiency reachable by the ideal stack is 60 $\pm$ 1% obtained considering four different tested salinity gradients. Thus, the exergy efficiency of the ideal stack is not affected by the variation of HIGH concentration solution due to the absence of uncontrolled mixing phenomena, such as salt and water flux across the membrane.

3.3.3.3 Influence of tested salinity gradients on overall prototype performances

An overall comparison of the system performance parameters is reported in *Figure 3.17*. The average values of maximum power density, specific thermal power and exergy efficiency obtained during the first 8 h of operation are plotted as a function of the HIGH solution concentration.

As expected, the maximum power density harvested by the RED unit increases at the increase of the HIGH solution concentration, due to the increase of the salinity gradient. In particular, a maximum power density of 1.5 W/m^2 was obtaines for case D. Thus, it decreases down to 1.2 W/m^2 for case C, 0.9 W/m^2 for case B and 0.63 W/m^2 for case A.

Conversely, the specific thermal power consumption in the vapour stripping column (*i.e.* the ratio between the *Thermal duty* and the *Inlet flow-rate*) for the regeneration of the LOW solution increases when the HIGH solution concentration increases. In particular, the STC increases from 77 kW/m^3 (case A) up to 110 kW/m^3 (case D).

Indeed, the exergy efficiency increases from 0.7% (case A) up to 1.1% (case D) at increasing the HIGH solution concentration.

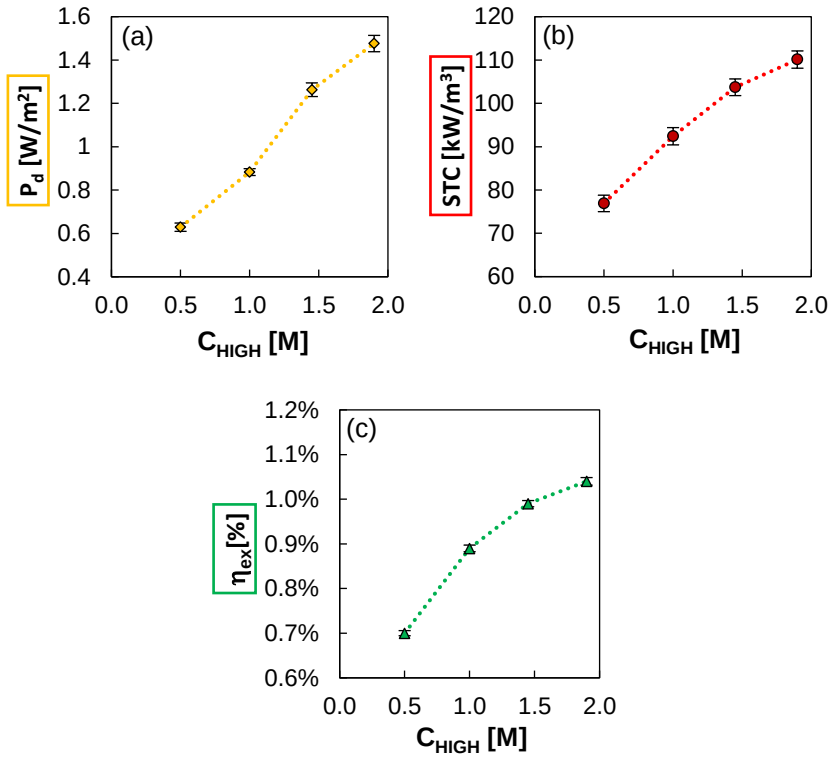

Figure 3.17.Average values (obtained in the first 8 h of operation) of (a) maximum power density ($P_{d,max}$), (b) specific thermal consumption (STC) and (c) exergy efficiency (η_{ex})of the t-RED-HE prototype as function of the HIGH concentration solution.

As shown in *Figure 3.17-c*, an increase of HIGH solution concentration could not result in a significant increase in overall exergy efficiency. As matter of fact, an increase of the HIGH solution concentration causes an increase of the concentration in the LOW solution, exiting from the RED and after water rebalancing step, leading to a release a large amount of gases in the stripping column, which could increase the operative pressure requiring a higher regeneration temperature. This phenomenon leads to requiring a heat source at a higher temperature causing an increase of maximum theoretical Carnot efficiency, thus maintaining the exergy efficiency almost constant.

However, working at HIGH solution concentration close to saturation could increase the risk of local salt precipitation in the high loop dramatically affecting the operation for long-term. It is important to stress that the proposed t-RED-HE is reported for the first time as a real implementation that was for the first time theorized by Loeb [31].

The low value of the exergy efficiency reported is due to the no-optimal operative condition of the system. However, a theoretical analysis of the whole RED-HE system is reported in Chapter 4, showing the possibility to increase until ten times higher exergy efficiencies by optimizing both RED and regeneration units.

3.3.4 Conclusion

In this chapter, the first experimental assessment of a thermolytic RED Heat Engine (RED HE) is presented. The RED-HE prototype was thoroughly tested in order to assess the real possibility to convert low-grade heat into electrical energy. It consists of two main units: (i) generation units consisting of a RED unit fed with ammonia bicarbonate solution and (ii) regeneration unit, *i.e.* a vapour stripping column, operating at a temperature below 90°C. The system was assessed in term of stability and performance parameters, such as STC, exergy, yield, efficiency, etc.., under different operating condition via long run tests (from 8 h up to 55 h). The highest values of yield and exergy conversion efficiency have been reported for the first time in the literature for RED units operating with thermolytic solutions. The highest exergy efficiency achieved was equal to 1.1% the largest salinity gradient (*i.e.* 1.9 M -0.05 M) of ammonia bicarbonate solutions. The obtained results showed very good stability of the process over the experimental time, in terms of solution conductivities, power generation and thermal power consumption. Moreover, the possibility to use the RED-HE for the energy storage has been assessed via intermittent operation performed in different days. The successful execution of RED-HE prototype allows demonstrating the real application of Loeb's idea, posing the first stone in order to exploit the low grade-heat to produce electrical energy, and, at the same time, reducing/avoiding the thermal environmental pollutant.

However, a room of improvement exists, including the developed exchange membranes suitable for the thermolytic solution (ammonium bicarbonate solution) in order to increase electrical production of RED unit because the used membranes give the maximum performance when NaCl solutions are adopted. Moreover, it is necessary to re-design the regeneration unit, i.e. the stripping tower and vacuum system, in order to better exploit the low-grade waste heat, improve the stripping of ammonia and carbon dioxide from solution reducing the thermal power consumption, and then increasing of thermal efficiency.

4 Perspective analysis

Chapter Outline

Part of this chapter has been published in:

F. Giacalone, **F. Vassallo**, L. Griffina,, , M.C. Ferrari, G. Micale, F. Scargiali, A. Tamburini, A.Cipollina," Thermolytic reverse electrodialysis heat engine: model development,integration and performance analysis", Energy Conversion and Management, Volume 189, 1 June 2019, Pages 1-13, doi: 10.1016/j.enconman.2019.03.045

F. Vassallo, F. Giacalone, F. Scargiali, A. Cipollina, G. Micale," Regeneration Units for Thermolytic salts applications in water & power production: State of art, Experimental and Modelling assessments", Desalination, Volume 504, 15 May 2021, https://doi.org/10.1016/j.desal.2021.114965

4.1 Theoretical analysis of the performance regeneration units

After the validation of the models, the simulation platforms developed in Aspen® were used in order to investigate and compare the performance of the two stripping processes (i.e. the air stripping column and the vapour one) for the design of the whole regeneration unit. Thus, sensitivity analyses were carried out to evaluate the air stripping column and vapour stripping column at a given separation. In fact, same targets and constrains (*i.e.* same waste heat temperature, inlet and outlet concentration of the solution, inlet flow-rate, etc.) were considered for both stripping columns. Operative conditions for air and vapour stripping columns are listed in *Table 4.1*.

Table 4.1. Simulation setting for the air and vapour stripping columns.

T_{wh} [°C]	F_{in} [l/min]	C_{in} [mol/l]	C_{low} [mg/l] (C_{low} [mmol/l])**							
85 105*	2	0.25	1000 (12.6)	500 (6.3)	100 (1.3)	50 (0.63)	25 (0.32)	10 (0.13)	5 (0.06)	1 (0.01)
		0.5	1000 (12.6)	500 (6.3)	100 (1.3)	50 (0.63)	25 (0.32)	10 (0.13)	5 (0.06)	1 (0.01)
		1	1000 (12.6)	500 (6.3)	100 (1.3)	50 (0.63)	25 (0.32)	10 (0.13)	5 (0.06)	1 (0.01)
		2	1000 (12.6)	500 (6.3)	100 (1.3)	50 (0.63)	25 (0.32)	10 (0.13)	5 (0.06)	1 (0.01)

*only for the vapour stripping column, to operate the tower at 1 atm.
**ammonium bicarbonate solutions equivalent concentration

The concentration values of the regenerated solution listed in *Table 4.1* refers to the sum of mg/l of nitrogen and carbon containing compounds in the solution, considering the ions ($NH_4^+, NH_2CO_2^-, HCO_3^-, CO_3^{2+}$) and the neutral species (NH_3 and CO_2).

The simulations were performed by setting the column as follow:

- The temperature of the waste heat used as hot utilities has been set equal to 85°C (or 105 for the vapour stripping column). A driving force equal to 5°C was considered for the heat exchangers. Therefore, waste heat is used to heat up to 80°C (T_{tower}) for the air stripping system, whereas for the vapour stripping system, the temperature of the reboiler is equal to 80°C and column operative pressure of 0.42 bar. In the case of a source of waste heat at 105°C, the column operative pressure is equal to 1 bar and the boiling solution is at 100°C.

- A design factor of 80% approach to flooding was chosen to compute the column diameter. Thus, the inlet flow rate was set equal to 2 l/min to obtain a reasonable ration between column diameter and packing diameter ($D_{column}/D_{packing}$ ~ 10). It is worth noting that the inlet flow rate has a low influence on the STC (specific thermal consumption), while the thermal power required for a given separation increases proportionally with the increase of the inlet flow rate, keeping constant other parameters.
- The height of the columns was set equal to 4m after studying its effect on the STC and selecting the lowest value which gives a good compromise between the column height and power consumption. *Figure 4.1-a* shows the influence of the height on the STC for the case of vapour stripping column to obtain an outlet concentration equal to 1 mg/l at fixed inlet concentration equal to 2M.

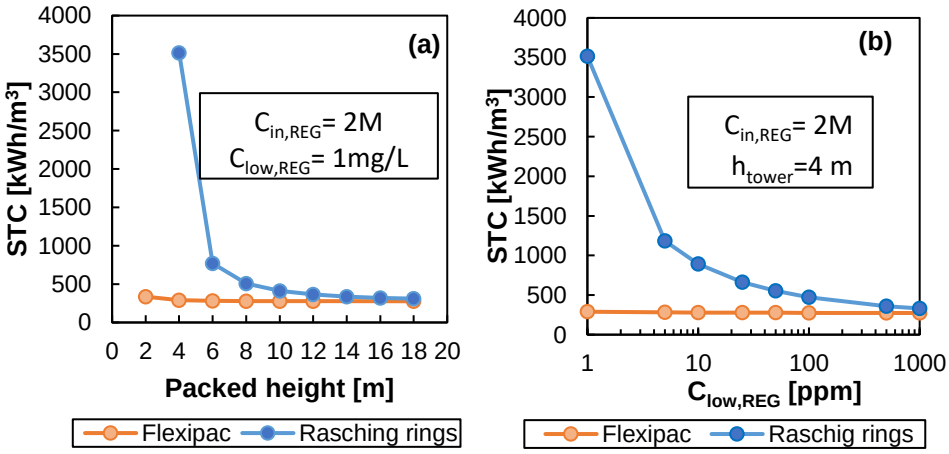

Figure 4.1.Specific thermal consumption of the vapour stripping column filled with Rasching ringa (blue line) and Flexipax 700Y (orange line) (a) as function of the packing height to regenerate a solution down to 1mg/l (C_{low}=1mg/L) and (b) as function of the regenerated low solution concentration at fixed packing height of 4m. T_{tower}=8°C, Q_{in}=2 l/min, C_{in}=2M.

The two analyses were carried out in order to analyse the influence of two different packing material (*i.e. Rasching ring and Flexipac 700Y*) on the STC. The former was performed at concentration equal to 2M, column outlet concentration at 1mg/l and varying the height of the column from 2 m up to 18 m (see *Figure 4.1–a*), while the latter was performed

considering the same inlet concentration, a packed height equal to 4 m and varying the outlet concentration from 1 mg/l up to 1000 mg/l (see *Figure 4.1–b*). Due to the lower specific area, the column filled with the *Rashing rings* requires a larger thermal power to reach the same regeneration. In fact, the lower the regenerated solution concentration, the larger is the difference in STC of the two systems. Indeed, when the outlet concentration of the regenerated solution is 1000 mg/l, similar performance of the two systems are predicted.
The Aspen® flowsheet of the two stripping processes are displayed in *Figure 4.2*.

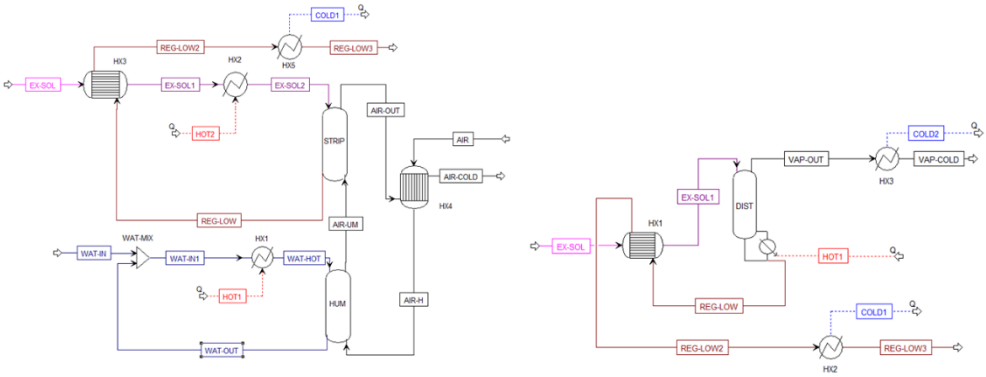

Figure 4.2. Aspen flowsheet of the two regeneration systems.

In the SGP closed-loop application, all outlet stream from the bottom of the column could be used as a dilute stream fed to the power generation unit. Therefore, an optimization analysis involving the power unit and the regeneration one is required in order to find the optimal operative condition. On the contrary, in the FO-closed loop application, the aim of the process is to produce fresh water, then, the dilute solution exiting from the bottom of the column must have a total concentration of N-containing compounds below than 1 mg/l [23].
The STC of the two stripping columns is shown in *Figure 4.3* as a function of the inlet molar concentration of the solution fed into the column (from 0.25M up to 2M) and the outlet concentration of the regenerated solution (from 1 mg/l up to 1000 mg/l). The STC is strongly affected by the amount of the thermolytic salt to remove in order to reach a given target. In fact, the higher the inlet concentration, the higher the specific thermal power consumption of the stripping unit.
In the case of air stripping, the STC is mainly due to the thermal power required for the vaporization of the water needed for the saturation of the stripping air, while only a small

fraction is used to heat up the inlet stream. Therefore, the thermal consumption depends on the air flow-rate needed to reach a given regeneration target and, then, at the severity of the separation. The needed air flow-rate for the separation increases at the increase of the amount of the gases to be stripped (see *Figure 4.4-a*). As an example, the required STC to reduce the composition of the thermolytic salts from 2M down to 1 mg/l of total dissolved species is equal to 215 kWh/m^3.

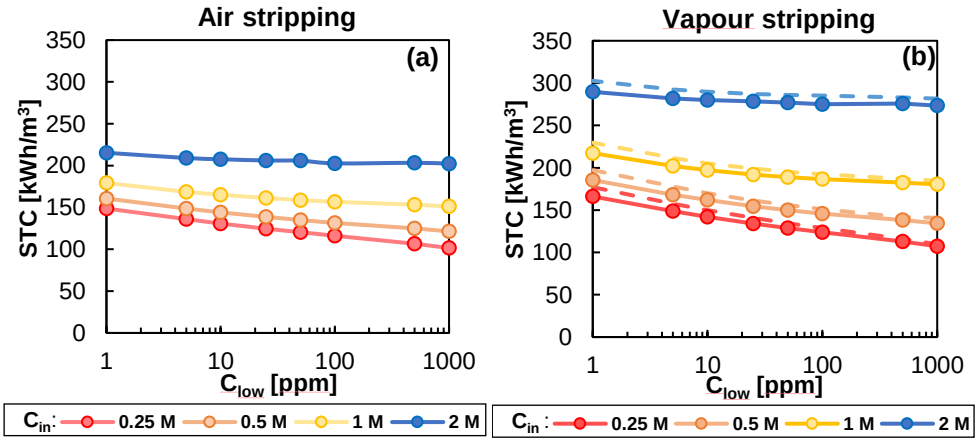

Figure 4.3. Specific thermal consumption of the two stripping columns as function of the inlet concentration solution (C_{in}) and the regenerated low solution concentration (C_{low}): (a) air stripping and (b) vapour stripping. T_{tower}=80°C, F_{in}=2 l/min. Dashed lines in figure b refers to the STC for T_{tower}=100°C

Otherwise from vapour stripping process, in the air stripping process, the flow-rate of the regenerated solution exiting from the column is equal to the inlet one, thus the recovery ratio (%R) (*i.e.* the ratio between the outlet regenerated flow rate and the inlet one in the column) is equal to 100%.

In case of vapour stripping unit, the STC is due to the thermal consumption required to generate the stripping vapour by partial vaporization of the inlet solution into the column. Also in this case, at more severity of the separation, the higher STC of the system and higher the amount vapour generated for the stripping. As an example, the needed STC to decrease the inlet concentration solution from 2M down to 1 mg/l is equal to 290 kWh/m^3, while is equal to 166 kWh/m^3 when the concentration of the regenerated solution is reduced from

0.25M down to 1 mg/l. Moreover, the outlet flow-rate of the regenerated depends on the inlet concentration solution (C_{in}).

In *Figure 4.4-b*, the outlet flow-rate of the regenerated low solution and the recovery ratio (%R) are reported as a function of the inlet low concentration (C_{in}) and regenerated outlet solution concentration (C_{low}). As an example, considering the reduction of the concentration of a thermolytic solution from 2M down to 1 mg/l of total dissolved species, the inlet flow rate is reduced from 2 l/min down to 1.4 l/min with a %R equal to 72% (see *Figure 4.4-b*).

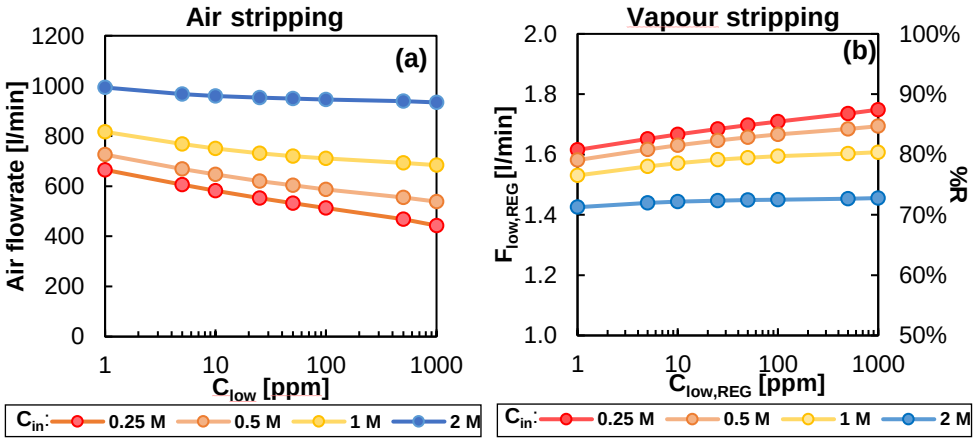

Figure 4.4. (a) Air flow rate required to reach the desiderate separation as function of the inlet and outlet concentration in the air stripping unit. (b)Regenerated low solution flow-rate and recovery ration (%R) as function of the inlet low concentration (C_{in}) and regenerated lo solution concentration (C_{low}) in the vapour stripping unit. T_{tower}=80°C, F_{in}=2 l/min.

Worth noting that similar performance has been obtained by operating the vapour stripping column at 1 bar. As highlighted by the dashed line in *Figure 4.3-b*, the STC is slightly higher than in the case of 80°C. However, the high temperature of the source of waste heat (T<100°C) is needed to power the reboiler of the vapour stripping column.

Another important aspect related to the regeneration process is the distribution of the species in the regenerated solution. A summary of the species distribution of the inlet solution concentration for the different cases understudy is reported in *Figure 4.5*. In particular, the inlet concentration solutions are mainly constituted by HCO_3^- and NH_4^+ ions, with a significant amount of $NH_{3(l)}$ and $CO_{2(l)}$. The regenerated solutions are mainly constituted by

HCO_3^-, NH_3 and NH_4^+. The concentration of the latter two species is important for the case of FO-Desalination water, because very low concentrations are tolerable in the fresh water production.

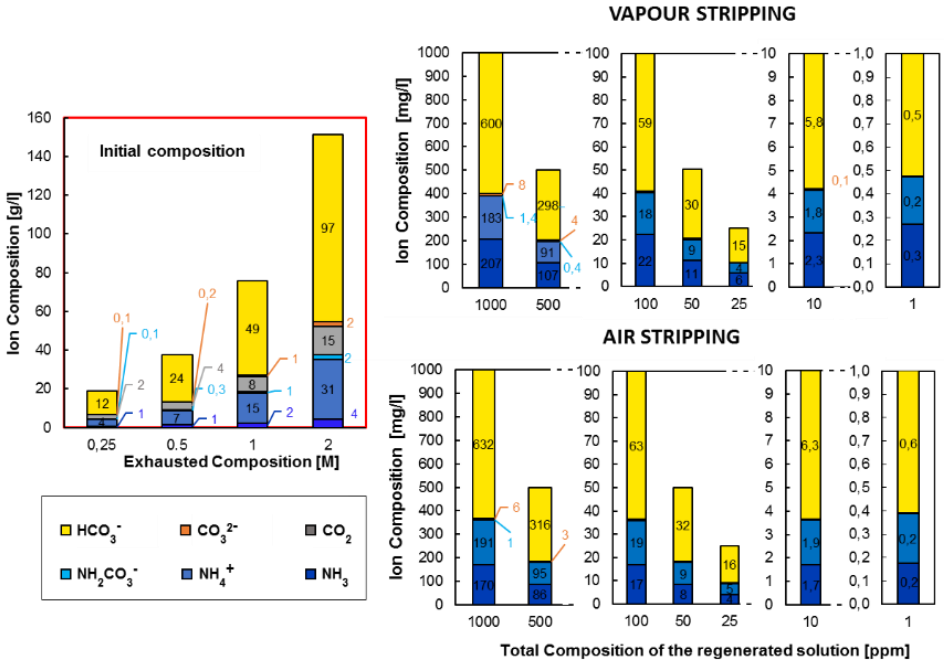

Figure 4.5.Composition of the inlet low solution concentration fed to the columns (on the left) and the composition of the regenerated low solution exiting from the column: vapour stripping (above) and air stripping(below). T_{tower}=80°C, F_{in}=2 L/min and Flexipac® 700Y

The validated models were adopted to carry out a conceptual design of the regeneration unit, including the absorption step where the stripped gases are condensed/absorbed in the exhausted concentrate solution.

In the case of air stripping/absorption process, the stripped gases (*i.e.* $CO_{2(g)}$, $NH_{3(g)}$) are cooled down to 25°C and sent to the bottom of the absorption column. The exhausted concentrate solution is fed to on the top of the absorber in order to absorb the stripped gases. In the air absorption column part of the water contained in the air is also condensed due to the cooling. After the absorption step, the air exiting from the top of the absorption column at 25°C may be heated up to the working temperature (80°C) and saturated again adding a fraction of the exhausted concentrate solution exiting from the power generation unit (water-rebalance process), before to enter into the column. In this case, the air saturation process at

80°C may be performed directly inside the stripping column, avoiding the use of humidification column by mean of the partial vaporization of the solution to regenerate. Thus, a part of exhausted high solution is added to exhausted low one (see MIX-1) in order to provide the amount of water lost in the stripping tower (see *Figure 4.6*).

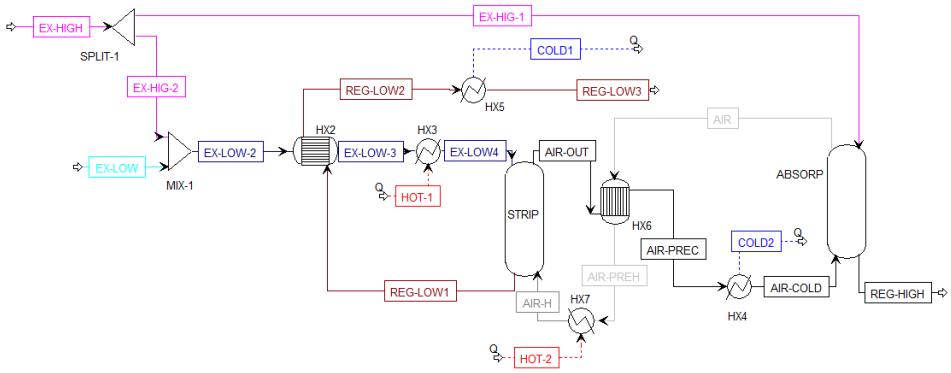

Figure 4.6. Aspen flowsheet of the regeneration unit based on the air stripping column. The main equipment are: HX heat exchange, STRIP air stripping tower, ABSORPT absorption tower, MIX-1 mixer and SPLIT-1 splitter.

As regards the vapour-stripping/absorption process, the stripped gases are cooled down to 25°C and condensed by a condenser/absorber, where are mixed with the exhausted concentrate solution. As an example, a barometric column, as used in the experimental RED-HE prototype described previously, may be used as condenser/absorber. Also on this case, the process was modelled in the Aspen® by considering a condenser followed by a mixer (see *Figure 4.7*).

The water rebalancing process may be required in order to provide to the regenerated solution (dilute stream) the water lost for the production of the vapour stripping in the reboiler. Therefore, par to the exhausted concentrate stream is mixed to the inlet dilute one (see MIX1 *Figure 4.7*) in order to restore the initial flow-rate of the regenerated dilute stream (water rebalancing).

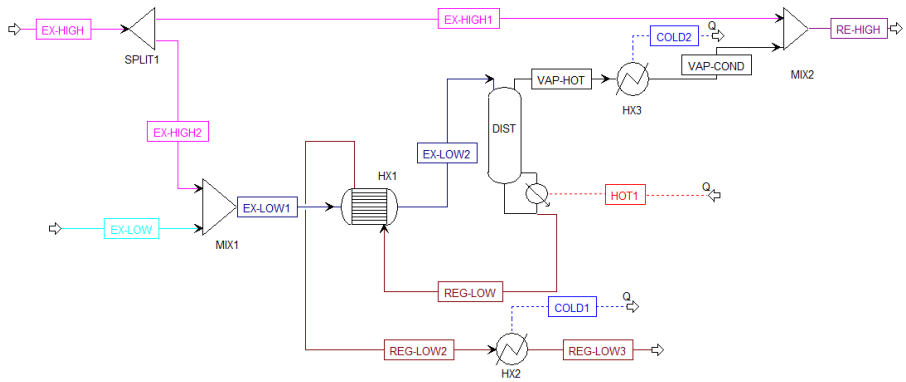

Figure 4.7. Aspen flowsheet of the regeneration unit based on the vapour stripping process. The main equipment are: HX heat exchange, DIST vapour stripping tower, MIX1abd MIX2 mixers and SPLIT1 splitter

The results of the modelling analysis of the whole regeneration units showed that the regeneration of the ammonium bicarbonate solutions is possible only with the vapour-stripping/absorption process, due to the limitation found in the air stripping/absorption process. As matter of fact, the use of large air flow-rate for the stripping process (see *Figure 4.4-a*) leads to a low partial pressure of $NH_{3(g)}$ and $CO_{2(g)}$ in the air affecting the absorption process. The low partial pressure of $NH_{3(g)}$ and $CO_{2(g)}$ makes difficulty the absorption and, then, to reach a given regeneration of the concentrate solution. In the worst case, the absorption of the species in the exhausted solution with a high concentration of thermolytic salts may be impossible and, then, the air continues the stripping of the thermolytic compound in the absorption column. Additionally, two different gases species $NH_{3(g)}$ and $CO_{2(g)}$ have very different vapour-liquid equilibrium condition. The NH_3 is hard to strip from the solution due to its high solubility in water, while the CO_2 is very ease to strip. At the contrary, the absorption of the $CO_{2(g)}$ is very hard than $NH_{3(g)}$. The dilution due to the air and the different vapour-liquid equilibrium rises the difficulty of the regeneration step leading to an accumulation of the $NH_{3(g)}$ in the dilute solution and of $CO_{2(g)}$ in the air.

At the contrary, in the case of vapour-stripping/absorption regeneration unit, the use of vapour as stripping agent makes the regeneration easier. As matter of fact, the vapour and ammonia are condensed and at the same time and the carbon dioxide is chemically absorbed, regenerating the exhausted concentrate stream at a given concentration.

For this reason, the vapour stripping/absorption process has been adopted in order to carry out a theoretical investigation of the RED-HE closed-loop system.

4.2 Description of the integrated model

The RED-He model consists of two main unit: (i) a RED unit, in which the salinity gradient between two ammonium bicarbonate solutions is exploited to produce electrical power as a power generation unit, (ii) a thermal regeneration unit, in which the low-grade waste heat (T<100°C) is used to restore the initial conditions of the two streams exiting from the power generation unit. A schematic representation of the RED-HE system is reported in *Figure 4.8.* The two NH_4HCO_3 solutions, concentrate and dilute, are fed to the RED unit in order to produce the electrical power by exploiting the salinity gradient. Inside the RED unit, part of the salt content in the concentrate solution moves to the dilute stream, whereas part of the water content in the dilute solution is transferred on the concentrate solution due to the osmotic flux.

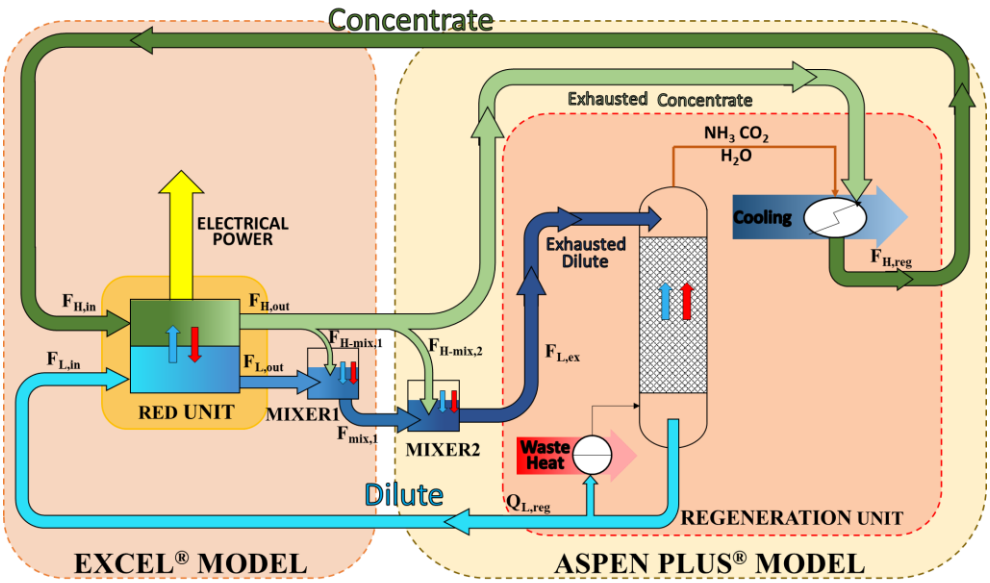

Figure 4.8. Conceptual scheme of the t-RED-HE process simulator. The red and blue arrows refer to the flux direction of the salt and water, respectively. The light red box refers to the RED model implemented in EXCEL®, while the light orange box for REGENRATION model implemented in ASPEN PLUS(R).

In order to restore the initial condition of both solutions, water and salts have to move in the opposite direction in the regeneration unit.

Following the exiting from the RED unit, a part of the exhausted concentrate solution is mixed to the exhausted dilute solution in mixer 1, in order to restore the water content in the dilute solution. In particular, this step is important to restore the flow-rate of the two solutions because the system works in closed-loop mode. After the first mixing, the exhausted dilute solution is again mixed to a part of exhausted concentrate solution restoring the amount of the water lost inside the vapour stripping column due to the partial vaporization of the dilute stream for the production of the needed steam for the stripping. From a practical point of view, water rebalancing can be carried out using just one mixer. But, from the model point of view, two different mixer are taken into account because RED-HE is divided in two sub-models (*i.e.* one for the RED unit (light red box *Figure 4.8*), and the other one for the regeneration unit (light orange box *Figure 4.8*)) developed in two different software and each of them contains a mixer. In the regeneration unit, the NH_4HCO_3 undergoes a thermal degradation into two gaseous species, *i.e.* ammonia and carbon dioxide. These two gaseous species are stripped by mean of vapour produced by partial vaporization of the dilute solution in the rebolier. In order to vaporize part of the dilute stream, low-grade waste heat (T<100°C) is used as thermal source to supply the reboiler. The stripped gases, exiting from the top of the column, are cooled down to 25°C and, then, absorbed in the exhausted concentrate solution to restore the initial concentration.

Finally, the two regenerated streams are fed again to the RED unit, where the restored salinity gradient is used again to produce electrical power.

The model of the RED-HE consists of two validated models:

1. The RED model, containing the mixer 1, has been implemented in Excel®;
2. The regeneration model, containing the mixer 2, has been implemented in Aspen Plus®.

4.2.1 Mass balance in the mixers

The RED sub-model is closed by mass balances in the mixer 1 in order to restore the initial water content in the two streams due to the osmotic flux occurred inside the RED unit. The mass balance used in the Mixer 1 are as follow:

$$\dot{F}_{mix,1} \cdot \rho_{mix,1} = \dot{F}_{L,out} \cdot \rho_{L,out} + \dot{F}_{H-mix,1} \cdot \rho_{H-mix,1} \quad (4.1)$$

$$\dot{F}_{mix,1} \cdot C_{mix,1} = \dot{F}_{L,out} \cdot C_{L,out} + \dot{F}_{H-mix,1} \cdot C_{H-mix,1} \quad (4.2)$$

where $\dot{F}_k$, ρ_k and C_k are the volumetric flow rate, density and concentration of the k^{th} generic streams. The subscript *L, out, mix,1* and *H-mix,1* refers to the dilute stream leaving the RED, the stream exiting from the Mixer 1 and part of the exhausted concentrate stream exiting from the RED sent into the Mixer 1, respectively. The amount of the concentrate stream to add in the Mixer 1 has been computed taking into account the amount of water moved from dilute to concentrate solution inside the RED by mean of Eq. (4.3):

$$\dot{F}_{H-mix1} = \frac{\dot{F}_{H,in}(\rho_{H,in} - C_{H,in} M_{Wsalt}) - \dot{F}_{H,out}(\rho_{H,out} - C_{H,out} M_{salt})}{\rho_{H,out} - C_{H,out} MW_{salt}} \quad (4.3)$$

where M_{salt} is the molecular weight of the NH_4HCO_3. The subscripts *in* and *out* refer to the inlet and outlet streams in the RED unit.

The flow rate ($\dot{F}_{mix,1}$) and molar concentration ($C_{mix,1}$) exiting from the Mixer 1 is used as input for the regeneration unit implemented in Aspen Plus®.

As regards Mixer 2, the mass balances have been implemented in the Aspen flow-sheet. The amount of exhausted concentrate stream to add in the Mixer 2 in order to rebalance the water lost in the column as stripping vapour is evaluated by means of *design spec* tool of Aspen Plus®. This tool is a goal seek with the aim to compute the amount of concentrate stream having the same water content lost in the stripping to add to the dilute stream. Moreover, the thermal duty required for a given regeneration is computed by means of second *design spec* (operating along with the previous one) which regulates the thermal power value in order to reach the desired regenerated dilute solution concentration.

4.2.2 Simulation settings

The simulations were carried out considering a RED unit equipped with 1000 cell pairs with an active area equal to 0.5x0.5 m^2 and 155 µm spacer thickness. Two different scenarios were studied: (i) current scenario in which the RED unit was equipped with the current membranes (Fujifilm Type 10 membranes) and (ii) a future scenario in which the RED unit is equipped with the future membranes. The properties of the current and future membranes are listed in *Table 4.2.*

Table 4.2. Main properties of the current and future IX membranes used for the analysis.

Properties	Current	Future
Water Permeability [ml/(bar·h·m^2]	6[(2)]	1.5[(2)]
Permselectivity [%]	85.1[(1)]	95[(2)]
Salt permeability [m^2/s]	4.5 10^{-12}[(2)]	1.13 10^{-12}[(2)]
Resistance [Ω·m^2]	6.01 10^{-04}[(1)]	1.50 10^{-04}[(1)]

[(1)]*reference concentration of 2 M-0.01 M NH_4HCO_3 water solutions. Property functions of solutions concentration using correlation reported in Chapter 2.*
[(2)]*assumed constant in the whole range of concentrations*

As described by Ashu et al [51] for the NaCl-water solutions, the properties of the future IX membrane are not far from the current membrane.
As regards the regeneration unit, the operating and geometrical properties of the stripping column were set as follow:

- Rashing rings with a diameter equal to 15 mm were adopted as packing material;
- A design factor equal to 80% approach flooding was chosen to compute the column diameter;
- Column height was set equal to 4 m.

4.3 Results and discussion of theoretical investigation of the closed loop Integrated model t-RED-HE

The global performance of the RED-HE was evaluated in term of thermal and exergy efficiency investigating the effect of the inlet flow-rate and inlet concentration of both

solutions fed in the RED unit. Moreover, the effect on the thermal and exergy efficiency using a multi-column configuration for the regeneration was evaluated.

Influence of the inlet concentration on the RED-HE system

Firstly, the influence of the inlet concentration on the global performance parameter of the RED-HE system was evaluated. In order to carry out this first theoretical analysis, the velocity of the two solutions inside the channels were set equal to 1 m/s (typical value used in the RED unit). The influence of the inlet solution concentration on the maximum power density ($P_{d,max}$) is shown in *Figure 4.9*. As shown in *Figure 4.9*, the $P_{d,max}$ harvested from the RED unit increases at the increase of the salinity gradient between the two inlet solution. Moreover, the $P_{d,max}$ depends on the residence time. In fact considering a larger residence time (*i.e.* larger stack) as in this case, the negative effect due to the resistance dilute solution is less important. At the contrary considering a low residence time (*i.e.* short stack), the electrical resistance of the dilute solution is the controlling factor affecting the $P_{d,max}$ [52]. Considering the current scenario, the highest $P_{d,max}$ is equal to 2 W/m^2, while for case of future scenario it is 4.25 W/m^2. Worth noting that the heighest $P_{d,max}$ in the future scenario is twice than current one, highlighting that reduction of the irreversibility phenomena occurring in the RED unit is responsible of the reduction of the $P_{d,max}$ [43].

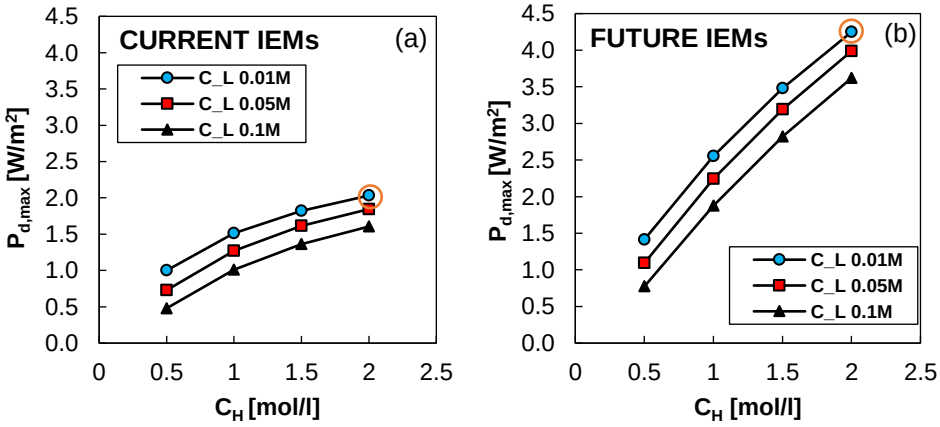

Figure 4.9. Maximum power density ($P_{d,max}$) of the RED unit as a function of the inlet concentration of both solution for the current (a) and future scenario (b).The RED unit

equipped with 1000 cell pairs (0.5x0.5 m^2) and inlet velocity of 1 m/s. Orange cycle indicates the maximum power density reached in the two scenarios.

Moreover, the effect of the inlet concentration in the RED unit on the TPC (thermal power consumption) of the vapour stripping column is reported in *Figure 4.10 a* and *b* for the current and future scenario, respectively.

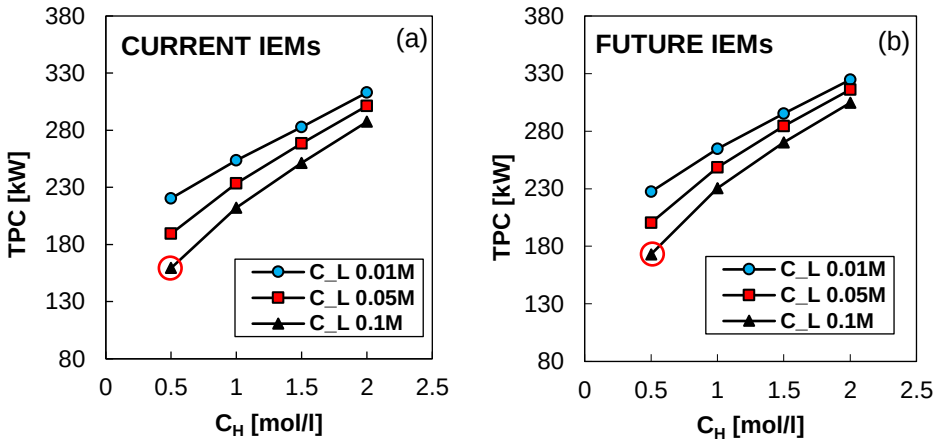

Figure 4.10. TPC as a function of inlet solution concentrations in the RED unit for current (a) and future (b) scenarios. RED unit equipped with 1000 cell pairs (0.5x0.5 m^2), inlet velocity equal to 1 cm/s. The temperature of waste heat ($T_{waste\text{-}heat}$) 80°C. Red cycle indicates the best performance for the two scenarios.

In particular, the higher power density harvested by the RED unit, the higher salinity gradient used, and then, the higher STC in the vapour stripping column to restore the initial condition of the two solutions. While, the lowest STC (160 kW) is obtained for the lower salinity gradient analysed (*i.e.* 0.5M-0.1M). As regards the future scenario, similar STC values are obtained due to the influence of the Mixer1. It is important to highlight that the two out-coming streams from the RED unit have a different concentration for the current and future scenarios respectively. While the concentration of the two solutions fed into the vapour stripping column are very similar for the current and future scenario due to the water-rebalancing performed by the Mixer1.

Finally, a global perform parameter, *i.e.* thermal efficiency (computed as the ratio between the gross electrical power generated by the RED and the TPC of the regeneration unit), has

been used in order to analyse the performance of the whole RED-HE system. *Figure 4.11* a and *b* display the effect of inlet concentration of the two solutions on the thermal and exergy efficiencies for the current and future scenarios, respectively.

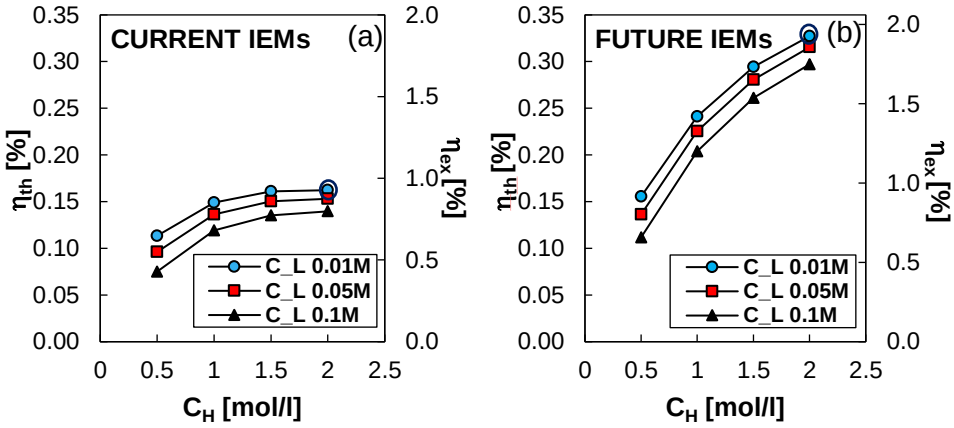

Figure 4.11.Thermal (η_{th}) and exergy (η_{ex}) efficiencies as a function on the inlet concentration for current (a) and future (b) scenarios. RED unit equipped with 1000 cell pairs (0.5x0.5 m^2), inlet velocity equal to 1 cm/s. The temperature of waste heat ($T_{waste\text{-}heat}$) 80°C. Blue cycle indicates the best performance for the two scenarios.

As seen in *Figure 4.11*, the higher values of the thermal and exergy efficiencies for both scenarios are obtained for the largest salinity gradient analysed (*i.e.* 2M-0.01M) because the salinity gradient strongly affects the electrical power obtained by the RED than the TPC.
In fact, taking into account the current scenario and concentration of the low solution equal to 0.01M, at the increasing of the concentration of the high solution from 0.5M up to 2M the power density increases from 1 W/m^2 up to 2 W/m^2, while the STC increases around 50%. Indeed for the future scenario, the power density increases almost three times (from 1.5 W/m^2 up to 4.25 W/m^2), while the STC is very similar to the one in the current scenario. In particular, the maximum thermal efficiency in the current scenario is equal to 0.16% (0.9% exergy efficiency), whereas is equal to 0.32% (1.93% exergy efficiency) in the future scenario.

Influence of the aqueous streams linear velocities on the RED-HE system

The following analysis takes in to account to the effect of the velocities of both solutions on the global performance of the RED-HE. In order to perform the analysis, the inlet concentration of the two solutions into the RED unit was fixed to the values which give the highest thermal (exergy) efficiency in the previous analysis, *i.e.* 2M for the high solution and 0.01M for the low.

In *Figure 4.12*, the influence of the velocities of the two inlet solutions on the $P_{d,max}$ is reported.

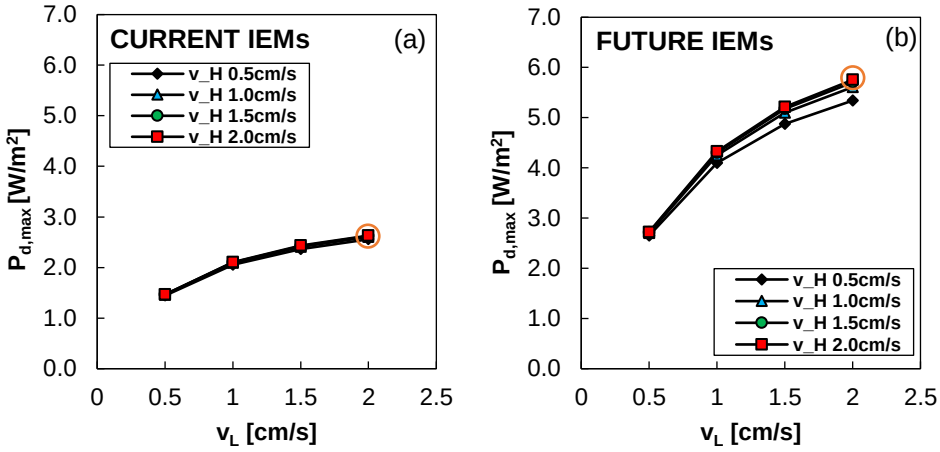

Figure 4.12. Maximum power density ($P_{d,max}$) of the RED unit as a function of the inlet velocities of both solution for the current (a) and future scenario (b).The RED unit equipped with 1000 cell pairs (0.5x0.5 m^2) and inlet concentrations equal to C_L=001 and C_H=2M. Orange cycle indicates the maximum power density reached in the two scenarios.

As shown in *Figure 4.12*, the $P_{d,max}$ increases at the increase the velocities of the solutions. In particular, the $P_{d,max}$ is mostly affected by the velocity of the low solution than the high one, reaching the highest value equal to 2.6 W/m^2 in the current scenario. As regards the future scenario, the maximum $P_{d,max}$ is 5.7 W/m^2 about twice than the lowest one. The influence of the inlet velocities of the two solutions on the TPC is reported in *Figure 4.13 a* and *b* for the current and future scenarios, respectively.

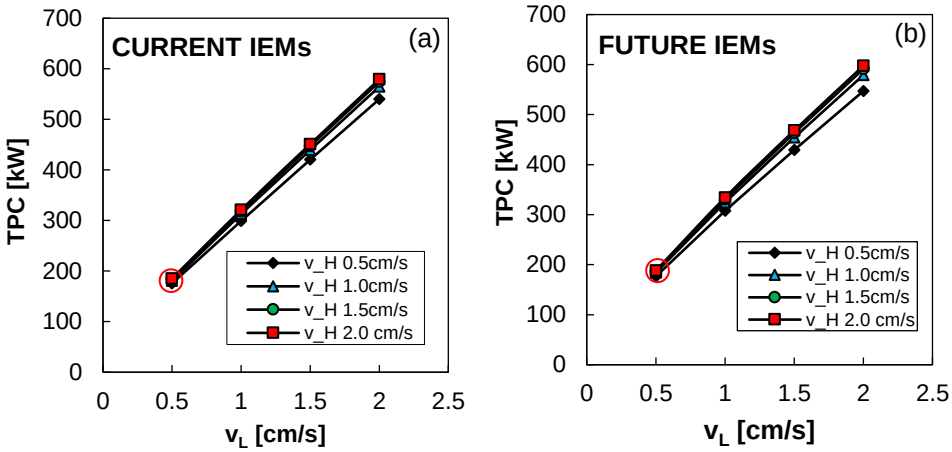

Figure 4.13. TPC as a function of inlet velocities of both solution in the RED unit for current (a) and future (b) scenarios. RED unit equipped with 1000 cell pairs (0.5x0.5 m^2), and inlet concentrations equal to C_L=001 and C_H=2M. The temperature of waste heat ($T_{waste\text{-}heat}$) 80°C. Red cycle indicates the best performance for the two scenarios.

As shown in *Figure 4.13*, the TPC linearly increases with the velocity of the low solution. In fact, the higher velocity inside the RED (*i.e.* high inlet flow-are), the higher dilute flow rate sent to the vapour stripping column, and then, the higher amount of the stripping vapour is required to achieve the desiderate separation in the regeneration unit. At the contrary, the TCP is slightly affected by the velocity of the high solution for current and future scenarios. Thus, the lowest TPC (around 180 kW) is obtained for the velocity of the dilute solution equal to 0.5 m/s for both scenarios. Finally, the influence of the inlet velocities of the two solutions on the thermal and exergy efficiencies are reported in *Figure 4.14 a* and *b* for the current and future scenarios, respectively. In both scenarios, the thermal and exergy efficiencies decrease at the increase with the increase of the velocities, highlighting that efficiency mainly depends on the influences of the velocity on TPC. Thus, the maximum value of thermal (exergy) efficiency is achieved at the lowest TPC value, which is obtained at the lowest velocities (0.5 m/s for both solutions). In particular, the maximum thermal (exergy) efficiency values is equal to 0.2% (1.1%) for the current scenario, while it increases up to 0.36% (2.1%) for the future scenario.

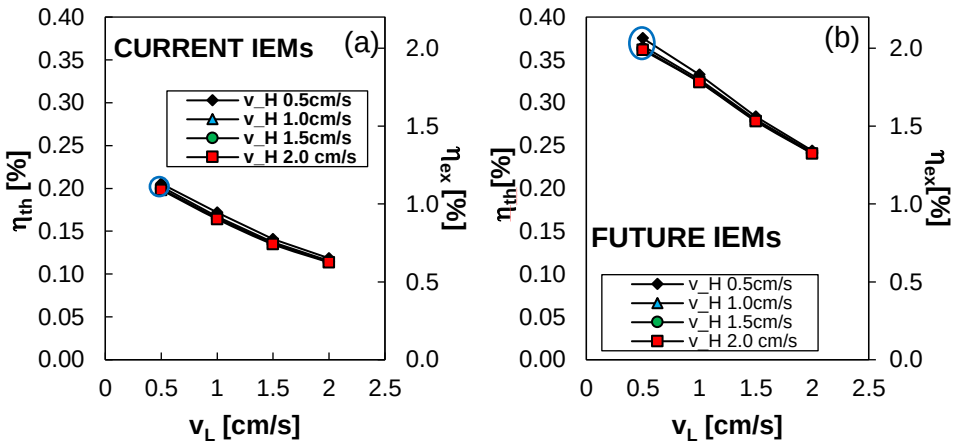

Figure 4.14. Thermal (η_{th}) and exergy (η_{ex}) efficiencies as a function on the inlet concentration for current (a) and future (b) scenarios. RED unit equipped with 1000 cell pairs (0.5x0.5 m^2), and inlet concentrations equal to C_L=001 and C_H=2M. The temperature of waste heat ($T_{waste\text{-}heat}$) 80°C. Blue cycle indicates the best performance for the two scenarios.

Multi-column configuration for the regeneration unit

The theoretical analysis on the RED-HE carried out far now has highlighted that in all investigated conditions the limiting factor is the thermal power consumption of the vapour stripping column determining a low thermal (exergy) efficiency of the whole process in both studied scenarios. The large TPC required by the column is due to the partial vaporization of the low solution in order to produce the needed stripping vapour. However, only a little portion of the heat contained in the steam is used to strip the gases, while the remaining part of the heat exits from the top of the column and it is discharged in the condenser. In order to increase the thermal (exergy) efficiency of the process, this discharged heat can be recovered and supplied within the following stripping column.

An alternative configuration of regeneration unit has already been proposed by McGinnins et al [23] for forward osmosis (FO) applications, the regeneration unit consists in a multi-column arrangement, in which the columns are fed in parallel while enthalpy of condensation is recovered and exploited as an energy source for the following column operating a low pressure. The multi-column configuration is very similar to the MED configuration. Regarding the multi-column configuration for the regeneration unit, the exhausted low solution exiting from the Mixer1 is split and sent in parallel into the columns. External low-

grade heat source is supplied into the first column, while the following column uses the heat obtained by the vapour condensation of the previous column as displayed in *Figure 4.15*.

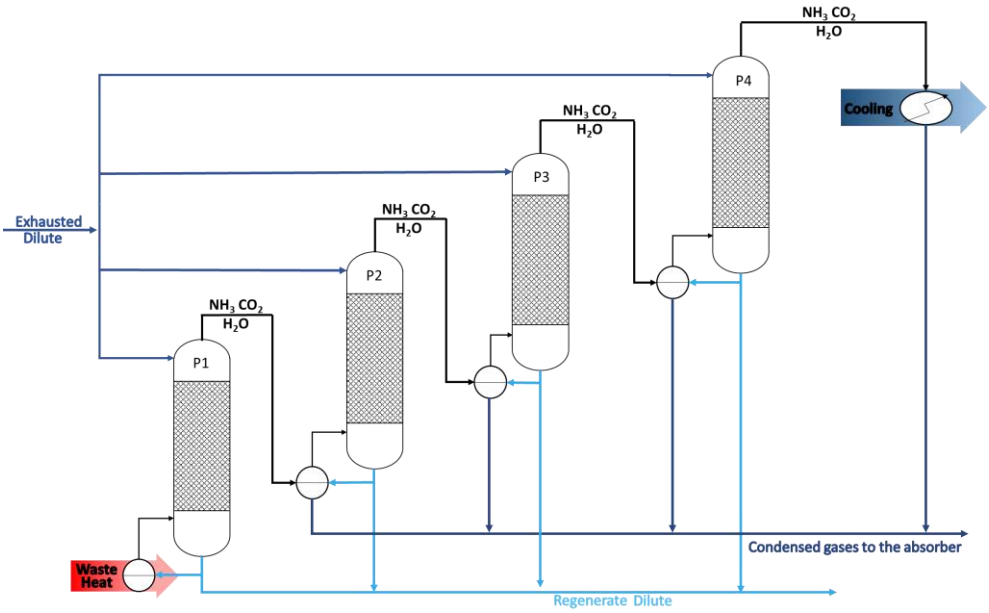

Figure 4.15. Schematic representation of a multi columns configuration with four vapour stripping column. Operative pressure P1>P2>P3>P4.

The absorption step of the condensed gaseous species is performed in the same way of single column configuration.

As the MED system, in which the thermal (exergy) efficiency increases with the increase of the number of effects, also in multi-columns configuration the thermal (exergy) efficiency increases at increasing the number of the columns. However, the maximum number of the vapour stripping is limited by the multicomponent nature of the condensing gases. As matter of fact, the condensation step takes place in a range of temperature between 4-8°C, diminishing quickly the available temperature difference between the first and the last column. Considering a temperature of the first column equal to 80°C (operating pressure of 0.4 bar) and the lowest temperature equal to 30°C (operating pressure 0.05 bar), the maximum number of column is equal to 5.

The influence of the number of the column of the thermal and exergy efficiencies of the RED-HE system fed by a low-grade (80°C) waste-heat are reported *Figure 4.16 a* and *b* for current

and future scenarios, respectively. The operative conditions of the RED unit were fixed equal to those which allowed reaching the highest value of thermal (exergy) efficiency, (*i.e.* inlet velocities of both solution equal to 0.5 m/s and molar concentrations equal to 2M and 0.01M).

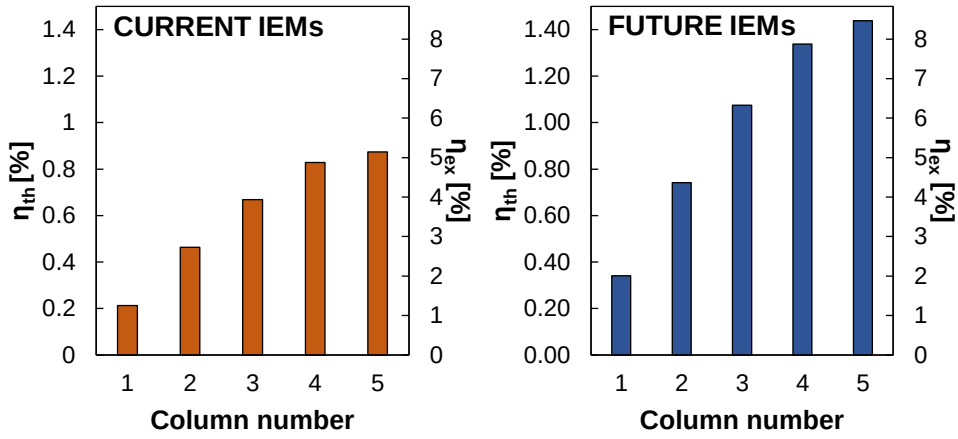

Figure 4.16.Effect of the number of the vapour stripping column used in the regeneration unit on the thermal (η_{th}) and exergy (η_{ex}) efficiencies for current (a) and future (b) scenarios. RED unit equipped with 1000 cell pairs (0.5x0.5m^2), inlet velocities of both solution of 0.5 m/s, C_H=2M and C_L=0.01M, $T_{waste-heat} = 80°C$ and $T_{bottom}^{last} = 30°C$.

As seen in *Figure 4.16*, the thermal and exergy efficiencies do not increase linearly with the increase of the number of the vapour stripping column. Regarding the current scenario, the efficiency increase more than double from 1 up 2 column, *i.e.* from η_{th} = 0.2% (η_{ex}=1.3%) up to η_{th} = 0.46% (η_{ex}=2.7%), while about four times higher for case of 5 columns η_{th} = 0.87% (η_{ex}=5.1%). In case of the future scenario, the thermal and exergy efficiencies for 5 columns configuration are 1.4% and 8.5%, respectively.

Worth to noting that the temperature of the waste heat supplied into the first column determines the maximum number of the column that could be used in the regeneration unit. In fact, the lower temperature of the waste heat supplied into the stripping column, the fewer number columns that could be used in the multi-column configuration and, than, the lower thermal (exergy) efficiency of the whole process. Moreover, an increase of the temperature of the waste heat could increase the thermal (exergy) efficiency, but it is useful to increase the driving force for the heat in order to reduce the heat exchanger area and the capital cost.

4.4 Theoretical analysis of the performance regeneration unit coupled with SGP or FO unit

Another example of the use of the validated simulation platform for the regeneration systems is reported in this chapter. The regeneration platform model was further used in order to predict the performance of three application based on the use of the thermolytic salts solutions. In particular, the case of Salinity Gradient Heat Engine (SGP-HE) and the Forward Osmosis (FO) unit for the desalination were analysed. In order to perfume this, simplified models for the SGP (both reverse electrodialysis, RED, and pressure retarded osmosis, PRO) and FO process were developed.

FO-Desalination

In the FO closed-loop system the osmotic pressure different between a draw solution and feed solution from a natural resource (e.g. seawater, brackish water) is exploited to produce drinkable water. The draw solution, consisting of water solution of ammonium bicarbonate, circulates continuously from the FO module and the regeneration unit. In this latter unit, the water recovered in the FO process is extracted from the exhausted draw solution by removing the thermolytic salts and at the same time, restoring the original condition of the draw solution. A schematic representation of the global process is reported in *Figure 4.17*.

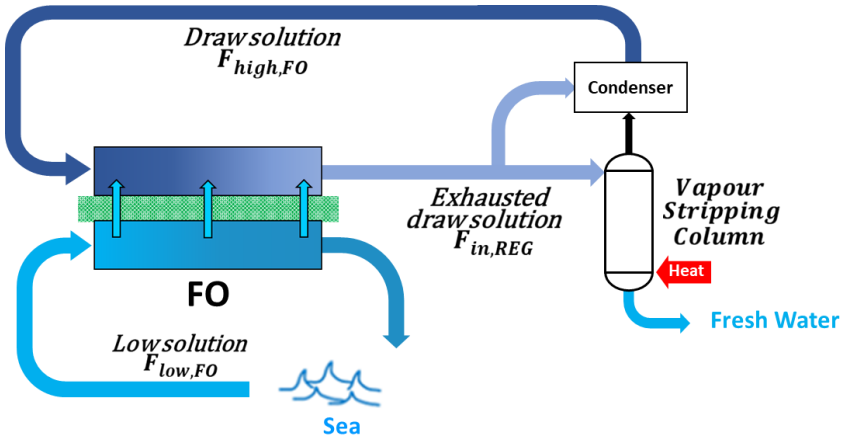

Figure 4.17.Schematic representation of the closed-loop-FO system. The main units are: (i) membrane process, i.e. Forward Osmosis unit and (ii) thermal process, Vapour stripping column to regenerate the draw solution and produce fresh water.

In FO process, the amount of recovered water depends on the concentration difference between the draw solution and the feed solution. Thus, the analysis of the closed-loop FO was performed by fixing a residual osmotic pressure difference between the two streams at the outlet of the FO module ($\Delta\pi_{out}$), in co-current and counter-current arrangement, and evaluating, for each residual pressure, the specific thermal consumption and the recovery ratio (*RR*), *i.e.* the ratio between the flowrate of produced fresh water and the feed solution, by applying trivial mass balances.

Figure 4.18 a and *b* report the RR ratio and the STC as a function of the inlet concentration of the feed-solution (from 0.1M up to 0.6 M) and of $\Delta\pi_{out}$, by fixing the concentration of the draw solution at 2M. The analysis was performed by considering 3 values of $\Delta\pi_{out}$ 10, 12 and 14 bar and by fixing the flow-rate of both solutions, feed and draw solutions, equal to 1 m^3/s. As expected, an increase of the feed solution concentration produces a decrease of the *RR*, due to the reduction of the driving force, and an increase of the *STC*, due to the increase of the exhausted draw solution concentration. In particular, the *RR* decreased from 86% (92% for the case of counter current) down to 40 % (50% in counter current) when the inlet concentration is increased from 0.1 M (brackish-water) up to 0.6M (seawater), while STC is increased from 225 kWh/m^3 (220 kWh/m^3 in counter current) up to 250 kWh/m^3(240 kWh/m^3 in counter current). Similarly, the influence of the draw solution concentration (i.e. 1, 1.5 and

2 M) on the performances of the system is reported in *Figure 4.18 c-d*, for the case of $\Delta\pi_{out}$ at 10 bar.

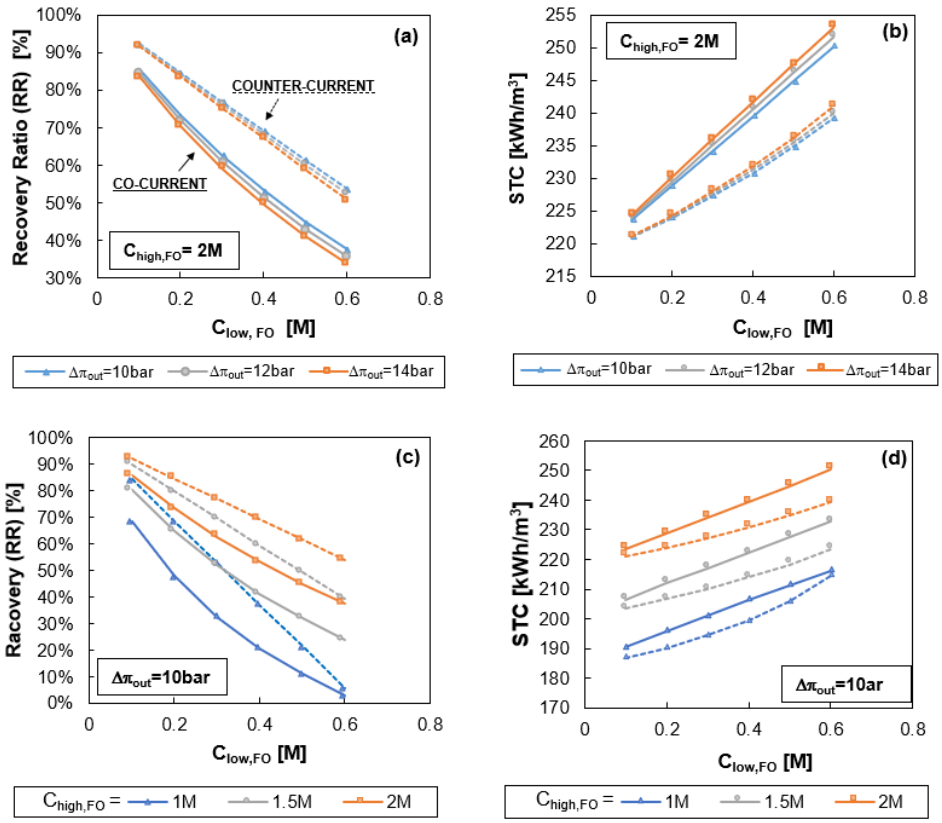

Figure 4.18. Recovery Ratio (a and b) and STC (c and d) as a function of concentration of the feed-solution and of the osmotic pressure different at the outlet of the FO system. Solid lines indicate co-current configuration, while dashed line counter-current one.

SGP - HE

The mixing of the two solutions at different concentration consume part of the original Gibbs free power of the two-streams due to an increase of the entropy of the system. Part of this power could be harvested by performing a controlled mixing process by adopting an SGP technology. The Gibbs free power of mixing (ΔG_{mix}) represents the maximum theoretical work which can be recovered when the two salt solutions are totally mixed together [53,54],

given by the difference between the Gibbs free energy of the mixed solution (G_{mix}) and the one of the initial streams (G_{low}+ G_{high}) as computed by Eq. 3.9-3.10.

The corresponding Gibbs free power of mixing ($\Delta\dot{G}_{mix}$) can be computed from Eq. 3.10 considering the molar flow rate (mol/s) instead of the moles of each species.

The performances of the two SGP units, *i.e.* PRO and RED, are evaluated by computing the amount of water (for the case of PRO) or salt (for the case of RED), to be exchanged between the two solutions in order to produce a certain percentage of the maximum theoretical work and ($\%\Delta G_{mix}$) evaluating the amount of water or salt exchanged between the two thermolytic solutions within the specific membrane process. Trivial mass balances are solved in order to determine the inlet solutions of the regeneration unit and thus, to evaluate the *STC* and the efficiency of the systems.

A schematic representation of the whole RED-HE is reported in *Figure 4.19*. Exiting from the power unit, the exhausted solutions are partially mixed in order compensate the loss of water in the dilute stream due to the production of stripping vapour. This causes an increase of both concentration and flowrate of the inlet solution in the regeneration, increasing the thermal power requirement.

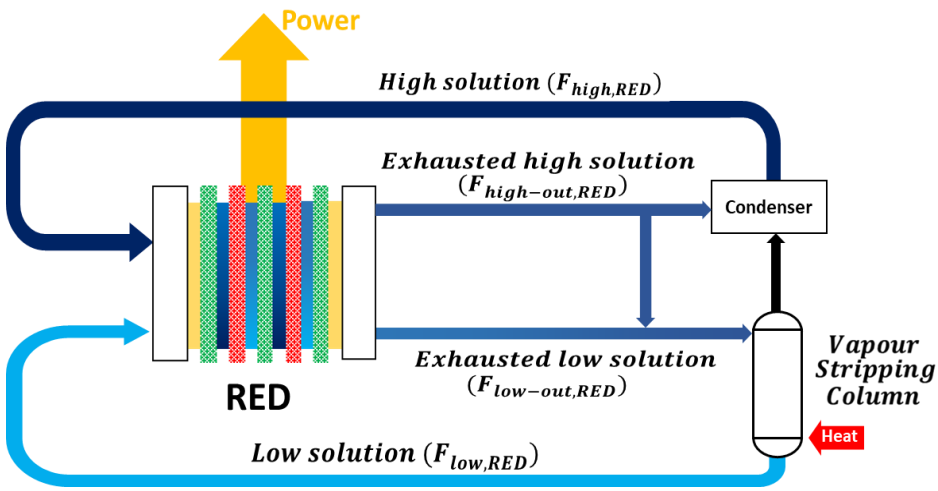

Figure 4.19.Scematic representation of closed loop RED-HE. The main units of the RED-HE are: (i) generation unit, RED for electrical production and (ii) regeneration unit, vapour stripping unit to restore the initial salinity gradient.

Figure 4.20-a repots the thermal efficiency of the global RED-HE as a function of the $\%\Delta G_{MIX}$ (from 10% up to 100%) and of the inlet low solution concentration, fixing the high solution concentration at 2M. The analysis was performed considering four value of low solution concentration entering the RED unit ($C_{low,RED}$), *i.e.* 1, 100, 500, 4000 mg/l and by fixing the value of the flow-rates of the solution fed into the RED unit equal to 1 m^3/s. As expected, an increase of the recovery of the ΔG_{MIX} produce an increase of the thermal efficiency due to the increase of the electrical energy harvested by the RED, despite an increase of the STC and thermal power duty due to the increase of concentration and the amount of the exhausted low solution. In particular, the thermal efficiency increase reaching a maximum value equal to 0.83% (exergy 4.55%), for $\%\Delta G_{MIX}$=90% and a minimum value equal to 0.1% (exergy 0.5%) for $\%\Delta G_{MIX}$ = 10%. The maximum value of efficiency is obtained for $C_{high,RED}$ equal to 500 mg/l as a compromise of the trend of mixing Gibbs free energy and of the thermal power consumption. Moreover, *Figure 4.20-b* reports the influence of the high solution concentration entering the RED unit ($C_{high,RED}$) on the efficiency of the whole RED-HE, fixing $C_{low,RED}$ at 500 mg/l. The analyses were performed by considering four value of $C_{high,RED}$ equal to 0.5, 1, 1.5 and 2 M.

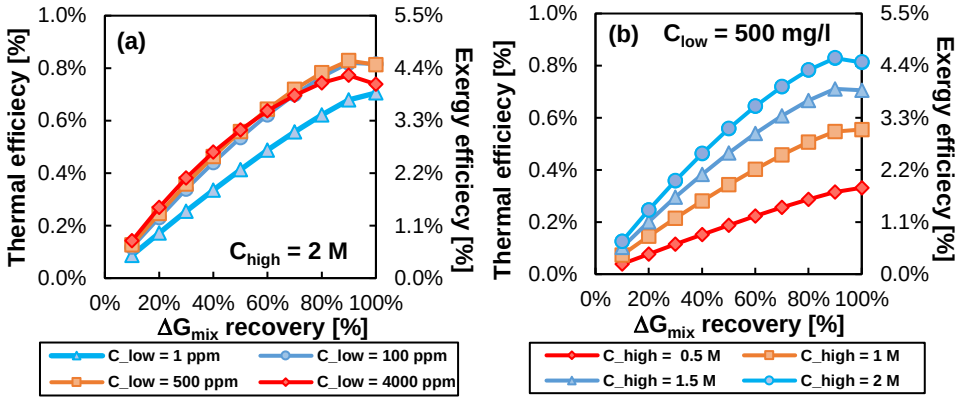

Figure 4.20. Thermal and exergy efficiency of the RED-HE as a function of the $\%\Delta G_{MIX}$ and $C_{low,PRO}$, fixing $C_{high,PRO}$=2M(a) and as a function $C_{high,PRO}$ fixing $C_{low,PRO}$=500 mg/l(b).

A schematic representation of the whole PRO-HE is reported in *Figure 4.21*. Exiting from the power unit, part of the exhausted dilute solution is added to the concentrated one in order to avoid salt accumulation in the dilute loop. Indeed, within the FO module only water is transferred, preserving the salt amount in the two streams, thus the residual amount of salt in

the dilute regenerated solution (1 mg/l) produce an accumulation in the dilute loop and a depletion in the concentrated loop. This causes a decreasing of the concentration and an increase of the flowrate of the inlet solution in the regeneration, resulting in an increase of the thermal power requirement.

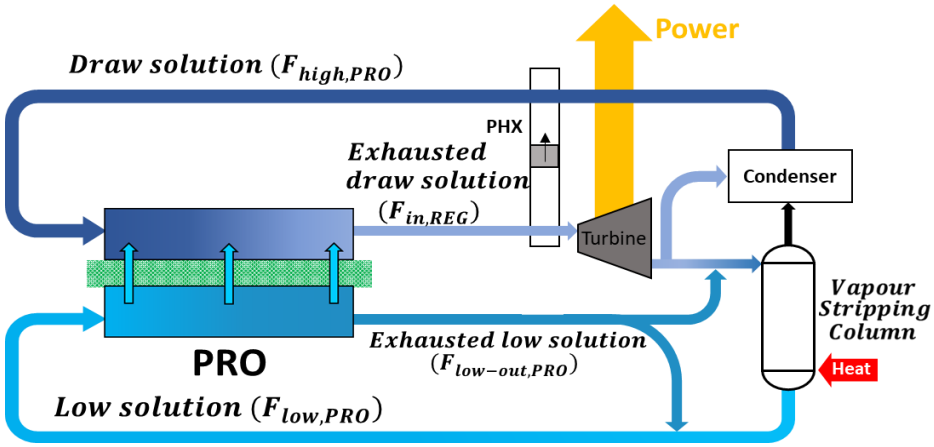

Figure 4.21.Scematic representation of whole PRO-HE. The main units are: (i) generation unit, Pressure Retarded Osmosis and a turbine to produce electrical energy (ii) regeneration unit, vapour stripping for the regeneration of initial salinity gradient.

Figure 4.22-a repots the thermal efficiency as a function of the $\%\Delta G_{MIX}$ (from 10% up to 90%) and of the inlet low solution concentration, fixing the $C_{high,PRO}$ = 2M. The analysis was performed considering three value of $C_{low,PRO}$ = 100, 500 and 4000 mg/l and fixing the inlet flow rates in the PRO unit, at 1 m^3/s. Differently from RED-HE, in this case, the thermal efficiency is marginally affected by $\%\Delta G_{MIX}$ ranging from 0.67% (3.68% of exergy efficiency) up to 0.74% (4.1% of exergy efficiency). This can be explained by the fact that, in the PRO-HE, both generated power and thermal power consumptions increase almost proportionally with $\%\Delta G_{MIX}$, while, in the case of RED-HE, thermal power requirements for regeneration are almost constant in the whole investigated range.

Finally, *Figure 4.22-b* reports the influence of $C_{high,PRO}$ on the thermal and exergy efficiency of the PRO-HE, fixing the $C_{low,PRO}$ at 500 ppm. Results show that the thermal efficiency dramatically decreases when decreasing $C_{high,PRO}$ from 2 to 0.5 M, passing from a maximum of 0.74% (4,1% of exergy efficiency) at 2M and $\%\Delta G_{MIX}$ of 10%, down to a minimum of 0.25% (1.4% of exergy efficiency) at 0.5M and $\%\Delta G_{MIX}$ of 90%. This can also be explained

by looking at the balance between power production and regeneration thermal requirements, these latter being practically independent on $C_{high,PRO}$, while energy generation in PRO is dramatically reduced by its decrease

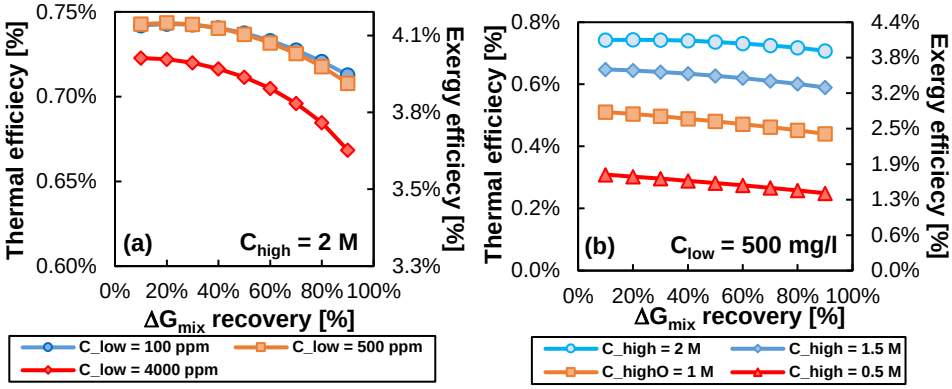

Figure 4.22.Thermal and exergy efficiency of the RED-HE as a function of $\%\Delta G_{MIX}$ and $C_{low,PRO}$, fixing $C_{high,PRO}$=2M(a) and as a function of $\%\Delta G_{MIX}$ and $C_{high,PRO}$, fixing $C_{low,PRO}$=500 mg/l(b).

Conclusions of Section 1

Thermolytic salts solutions are a promising working solution for FO closed loop and SGP-HE applications. In **Section 1**, two different regeneration unit for the regeneration of the initial salinity gradient of the thermolytic salts solution were investigated. The two stripping processes investigated are air stripping and vapour stripping along with absorber was studied. I particular, a simulation platform for the two regeneration processes was implemented in the process simulator Aspen Plus®. The two simulation platforms were validated against experimental results at different operating condition. In addition, an already existing 1D Excel® model of the RED unit, appropriately modified for the thermolytic solutions, was validated against the experimental results.

Subsequently, the first thermolytic RED-HE prototype was designed, assembled, and tested. The RED-HE prototype consists of two main units: (i) lab scale of RED unit and (ii) thermally-drive regeneration unit based on vapour stripping coupled with a barometric condenser. The stability and robustness of the prototype under different operating condition, *i.e.* four different salinity gradients, was assessed via long-run test up to 55 hours. The experimental outcomes highlighted a very good stability along with very good robustness of the process in term of power generation, reproducibility of polarization curves, solution properties and thermal power consumption. In particular, the highest exergy efficiency reached by the prototype was about 1.1% for the case of 1.9M-0.05M ammonium bicarbonate solutions.

Moreover, a perspective analysis was carried out using the two validated regeneration models. Results show that the specific thermal power consumption required for the regeneration of the inlet solution depends on the inlet thermolytic salts concentration. As regards of the air stripping, the specific thermal power consumption increases from 150 kWh/m^3 up to 215 kWh/m^3 when the inlet concentration increased from 0.25M up to 2M, fixing the outlet concentration equal to 1 mg/l. Whereas, in the case of vapour stripping, the specific thermal consumption increases from 166 kWh/m^3 up to 290 kWh/m^3 in the same condition. Although the air stripping unit allows a lower thermal consumption than the vapour stripping, in a closed loop application including the absorption process, the air stripping/absorption process is not suitable. This is due to the low partial pressure of ammonia and carbon dioxide in the air, reducing the efficiency of the absorption process. At the contrary, the vapour stripping/absorption process is the appropriate process for the

regeneration of thermolytic salts solutions due to the total condensation of the ammonia and of vapour stripping with the consequent chemical absorption of carbon dioxide.

Subsequently, a theoretical analysis of the RED-HE system was carried out coupling the validated Excel® model of the RED unit with the Aspen Plus® simulation platform of the vapour stripping/absorption regeneration unit. In particular, this analysis aimed to analyse the performance of the RED-HE system at different operative conditions. Thus, two different scenarios were taken into account: (i) current scenario and (ii) future one. In particular, in the current scenario, current membrane properties (Fujifilm Type 10 IEMs) were account, whereas, in the future one, enhancement membrane properties were taken into account. Regarding the current scenario, the highest exergy efficiency was equal to 1.25%, whereas, in the future scenario, the highest exergy efficiency achieved was equal to 2%. Both results were obtained fixing the concentration of the two solutions equal to 2M for the high solution and 0.01M for the low one with a velocity of low solution equal to 0.5 cm/s.

Moreover, a high exergy efficiency can be reached by using a multi-vapour stripping column configuration in the regeneration unit. As matter of fact, the exergy efficiency of the system increases from 1.25% up to 5.2% using 5 columns, in the current scenario. While, in the future scenario, the exergy efficiency increased up to 8.5%.

Finally, a theoretical analysis was carried out considering the three closed-loop applications, *i.e.* Forward Osmosis desalination of brackish and seawater, Reverse Electrodialysis Heat Engine and Pressure Retarded Osmosis Heat Engine. In all cases, the regeneration unit consisted of a vapour stripping/absorption process. The theoretical analysis was carried out looking at the performance of the system at different operating conditions such as the recovery ratio in FO and of the percentage of Gibbs free energy of mixing recovered.

As regards the FO processes, the results highlighted that high recovery ratio can be achieved, up to about 90% at 0.1M, *i.e.* brackish water is considered as feed solution, while between 50-54% when seawater is considered. Considering a waste heat at 85-90°C, specific thermal consumption resulted in the range of 180-250 kWh/m^3, and the lowest value was achieved for case of brackish water desalination.

As regards RED-HE, the highest overall thermal efficiency achieved was about 1% (exergy about 4.5%) obtained using a single column configuration. Interestingly, such values of thermal (exergy) efficiency are in line with the values obtained with the accurate simulation of RED-HE for the future scenarios. In fact, an efficiency between 1 and 2% was found for systems operating under real and future conditions, while values close to 5% were found in

ideal conditions such as those considered in the present analysis. Worth noting that, the implementation of a multi-column system with thermal integration can lead to exergy efficiency (as reported above, for the future scenarios the exergy efficiency can be improved up to 9%). Higher values of exergy efficiency published in [13,40] were obtained by applying very optimistic simplifying assumptions related to specific energy consumptions of the regeneration system, which were confuted in the present analysis and cannot be considered as a realistic target for thermolytic RED-HE technology, while they are still feasible in other implementation of RED-HE schemes (e.g. MED-RED heat engine) [15].

As regards PRO-HE, the highest overall thermal efficiency achieved was about 0.74% (exergy about 4.1%) obtained using a single column configuration.

Comparing with previously published values of exergy efficiency around 15% simulated for CO_2-NH_3 solutions [41], these findings indicate a still low performance of the PRO-HE. Nevertheless, it is worth noting that the mentioned work analysed the performance of a PRO system with 5.5M draw solution and operating pressures well above 150 bar, which is unfeasible with current state-of-the-art membranes and devices.

However, also in this case, the use of multi-column systems and thermal integration could lead to a 3-4 folds increase in the exergy efficiency with more interesting potentials for future implementation of this new technology.

Section 2

Minerals recovery from industrial waste brine

Abstract

A rising interest has been recently focused on the valorisation of waste brines from industrial processes, such as desalination plants, softening water industry, saltworks, etc.. In most cases, waste brines are disposed directly, or after being treated, into water bodies, causing environmental concerns and, more importantly, renouncing to the possibility of using such a waste as a source of valuable raw materials. In particular, the recovery of magnesium is of strategic importance for the European Union, as it has been defined as a critical raw material (CRW)by the European Commission.

The following Section is devoted to present the design, assembling and testing of an unconventional continuous pilot unit crystallizer for the recovery of magnesium from waste brines, namely the Multiple Feed Plug Flow Reactor (MF-PFR), aiming at the recovery of magnesium and calcium hydroxides at purity higher than 90%.

The MF-PFR pilot unit has been firstly constructed and tested in the Brine Excellence Center (BEC) satellite laboratory of UNIPA. The experimental campaign carried out with synthetic and real brines highlighted the best conditions to achieve a high solids filterability and control the target purity, which achieved a purity between 90% and 98% depending on the calcium and bicarbonates contents of the feed brine.

The effect of a pre-treatment aiming at removing quantitatively the bicarbonates content of the brine (by means of the vapour stripping column presented in Section 1) was investigated too, showing purity of magnesium hydroxide can increase from 95% (without pre-treatment) up to 99%, thanks to the minimisation of calcium carbonates precipitation.

In a second phase, the MF-PFR pilot unit was shipped to a real environment installation site (Botlek, Rotterdam, The Netherlands) and tested feeding a real spent brine from the industrial water softening plant of Evides Industriewater B.V. (Rotterdam, The Netherlands). Selective precipitation and recovery of magnesium and calcium hydroxide was successfully confirmed and the pilot plant performance was assessed in terms of recovery efficiency and purity of produced crystals, which were found to be, in most investigated cases, above 96% and 90%, respectively.

5. Industrial brines: from waste to resource for minerals mining

5.1 Worldwide sources of industrial brines

The rising water demand along with growing global population, associated with the increasing water consumption and the diminishing water supply are aggravating the water scarcity in many world regions. This has pushed to find alternative sources to satisfy the increasing demand for water, such as the desalination of seawater [55]. The desalination is a process that allows removing salts from seawater in order to produce a water meeting the quality, *i.e.* salinity, required of different human uses. In particular, the desalination process separates the intake seawater in two streams, one is the freshwater and the latter is a concentrate stream or industrial waste brine. Two classes of desalination processes are currently employed: (i) thermal-based processes and (ii) membraned-based processes. Nowadays, the membrane-based processes, such as reverse osmosis (RO), are the most widely used due to their higher efficiency compared to the other thermal-based technologies [56].

In 2019, Jones et all [57] carried out a comprehensive analysis about the state of desalination and brine production in the world. The authors taken into account 15906 desalination plants located in 177 countries and territories across the world regions. The total production capacity of the desalinations plant under analysis is approximately 95.37 Mm^3/day (34.81 billion m^3/year), which is increase of about 10 times over the last 40 years, in fact the capacity in 1975 was below 10 million m^3 per day. *Figure 5.1-a* displays the installed capacity of the desalination plant from 1960 up to 2020.

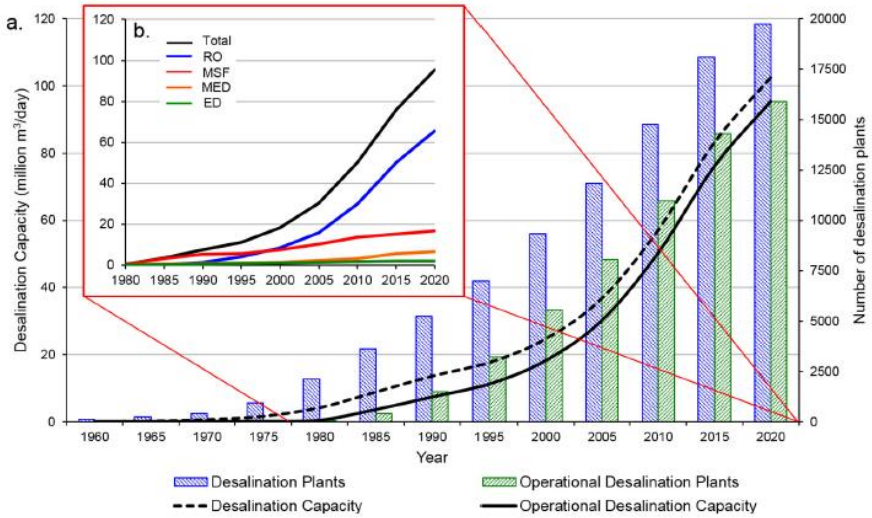

Figure 5.1. Trend of desalination plant, (a) number and capacity of total and operational desalination plant and (b) desalination technologies used [56].

As shown in *Figure 5.1-b,* it is possible to understand how the technologies used for the desalination are changed from 1980 up to 2020. In particular, in the last 15 years, the membrane processes, such as reverse osmosis (RO), are become the dominant technologies for the desalination, with a fresh water production of 65.5 million m^3 per day, about the 69% of the total fresh water production considered. As said before, the production of fresh water is linked to the production of the waste brine, which is about 141.5 million m^3/day about 50% higher than total fresh water production. Going to analysed the geographical distribution of the desalination plant, *Figure 5.2* reports the global distribution of desalination plants.

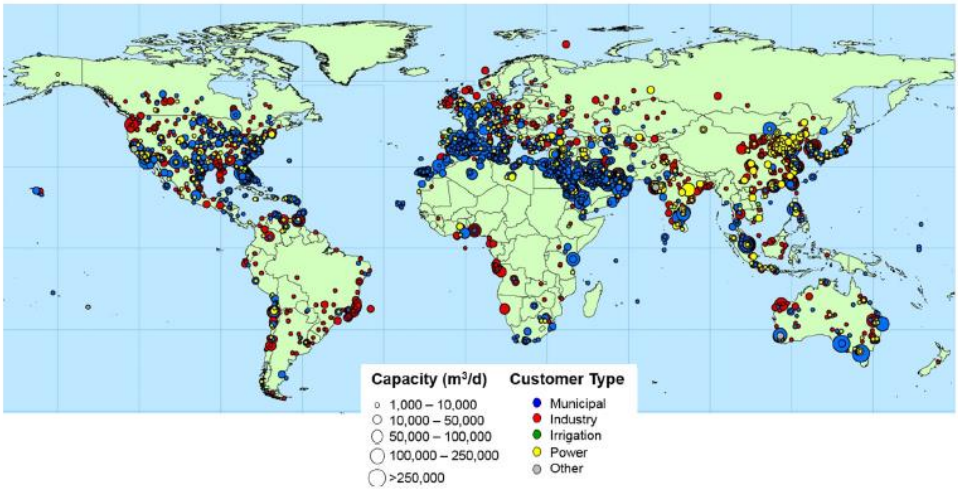

Figure 5.2. Global distribution of desalination plants with capacity higher than 1000 m^3 per day by sector user of produced water [56].

As shown in *Figure 5.2*, it is clear that the largest number of desalination plants are installed in the Middle East and North Africa with a desalination capacity equal to 48% of the total one. As regards, Europe, desalination capacity equal to 9.2% of the total one is installed, and of 9.2%, 5.7% is installed in Spain. From this outcome, it is clear that about 50% of the total desalination capacity is installed in the Mediterranean basin, releasing about 50% of the total produced brine. The release of brines in the sea causes an enormous negative environmental impact, changing the habitat of the flora and fauna of the sea [58,59]. Therefore, improved brine management strategies are required in order to reduce the environmental impact of the release of the produced brines. Considering that brines have a concentration of dissolved minerals 1.5-2 time higher than seawater, these can be considered as new source to extract al lot of minerals. At the light of this consideration, the European regions can become the new mines for the extraction of minerals, such as magnesium due to the high risk of supply and its high economical relevance.

5.2 Manage of the industrial/natural waste brine

In the past, the produced industrial waste brines were directly, or after appropriate treatment, discharged in a receiver water bodies. Different strategies were used to manage the produced waste brines based on the location of the desalination plant. Commonly, desalination plants are located near the sea, so the direct discharge of such brines in receiving water bodies (e.g. seas and oceans) is presently the most common disposal strategy. In order to reduce the environmental impact, different mitigation strategies have been considered, e.g.: (i) Discharge mixed with power plant cooling water [60,61], (ii) Single pipe discharge to deep water [61], (iii) discharge pipe equipped with diffusers [62], and (iv) discharge to beach and offshore galleries and trenches [62].

On the contrary in the case of inland industrial process, the option of disposal directly to the sea is not feasible, thus some other disposal strategies have been studied, namely: (i) deep well injection [63–65], (ii) disposal into surface water bodies [66], (iii) irrigation of plants tolerant high salinity [67,68], (v) disposal to municipal sewers [69], and (vi) evaporative ponds [70]. All disposal methods presented are feasible for low production and without the presence of any hazardous chemical content, although they are subject to restrictions dictated by climatic conditions, seasonal demand, land availability and groundwater conditions. However, these strategies for the disposal of the waster brine are often unsustainable due to (i) high capital cost, ranging from 5% to 33% of the total cost of the process, and (ii) environmental impact [71]. A valuable alternative to the direct disposal is the minimization of the brine volume. The minimization methods based on the membrane process technologies are the followings: (i) electro dialysis reversal (EDR) [72], (ii) forward osmosis (FO)[73,74], (iii) Vibratory shear enhanced processing (VSEP) [75]. On the other side, the thermal-based technology used for the minimization are the followings: (i) Wind Aided Intensified eVaporation (WAIV) [76,76,77], (ii) membrane distillation (MD) [78,79], (iii) multi stage flash (MSF) and multi-effect distillation (MED) [80–82], (iv) brine evaporator cooler/concentrator (BECC) [83]. However, a combination of minimization and evaporative techniques, e.g. evaporative ponds, allows to avoid the direct disposal of waste brine and to recover useful salts mixtures, following the Zero Liquid Discharge (ZLD) concept [84,85]. In general, these brines are typically rich in useful and dissolved minerals (as sodium (Na), potassium (K), magnesium (Mg) and Calcium (Ca) and etc..), whose recovery can increase the environmental and economical sustainability of the industrial [72]. Among the cations

presented in the industrial waste brines, magnesium is the one of the most abundant along with the sodium and calcium. Therefore, interest is rising towards waste industrial brines in order to exploit them as alternative sources of minerals and ,at the same time, reducing/avoiding the discharge of industrial waste brines into a water body and, then, reducing their environmental impact [86,87].

Already at the end of the 80s, Al-Mutaz [88] considered the brines as a source of minerals and not a waste. As matter of fact, he analysed the feasibility of recovering minerals from the brines produced by the desalination plants in Gulf countries. Considering that the concentration of minerals in the brines is higher than seawater, he proposed conceptual process schemes for the recovery of sodium chloride, potassium salts, bromine and magnesium. With his work, he highlighted the possibility to reduce the supply risk of minerals in the Gulf countries and, then, the strategic relevance of minerals recovery for the Gulf market. In 1996, Ericsson et al [89] proposed an integrated process for the valorisation of brines produced by coal mines. This process scheme allowed the recovery of fresh water and different kinds of minerals such as calcium sulphate and sodium chloride. The integrated process processed about 4570 m^3/d recovering about 12.5 ton/h of minerals at purity higher than 99.6%. More recently, Ahmed et al [90] proposed three different treatment chains for the valorisation of the industrial waste brines produced by an inland reverse osmosis (RO) desalination plant in Oman. In particular, Ahmed highlighted that it is possible to recover different kinds of minerals, such as gypsum, sodium chloride, magnesium hydroxide, calcium carbonate and sodium sulphate, at high purity by mean of choosing a suitable treatment chain. In 2004, Drioli et al [91] developed a system in order to recover calcium carbonate, sodium chloride and magnesium sulphate from waste brines. The authors demonstrated that their integrated system allowed recovering about 35.5 kg/h of sodium chloride, 2.95 kg/h of calcium carbonate and 8.4 kg/h of magnesium sulphate treating about 1 m^3/h of waste brine. Moreover, the integrated system allowed increasing the recovery of the fresh water from 64% up to 95% of the desalination unit. In 2006, the University of South Carolina [92] carried out several laboratory tests using different treatments chains for the production of magnesium hydroxide, sodium chloride, bromine, road salts and fresh water using waste brine produced by reverse osmosis. Moreover, they developed a mathematical model for each treatment chain proposed in order to evaluate the profitability of each treatment chain. The outcomes of the laboratory tests and model results highlighted that the recovery of high purity of sodium chloride (more than 95%) and magnesium hydroxide (more than 99%) made the

treatment chain very profitable and, moreover, allowed increasing the fresh water recovery of desalination plant up to 76% [92].

More recently in 2015, Wallace et al [85] patented a treatment chain in order to valorise the industrial waste brine recovering gypsum and magnesium hydroxide, and fresh water. The peculiarity of this treatment chain, respect to that presented above, was the self-production of all chemicals used for the recovery of minerals, such as sodium hydroxide and hydrochloric acid. The authors declared that it is possible to recovery until 70% of calcium as calcium sulphate and more than 95% of magnesium as magnesium hydroxide. Both minerals were recovered at high purity above 90%. At the same time, high grade of fresh water was recovered containing total dissolved solids (TDS) less than 1 g/l.

The integrated processes and treatment chains presented above allows increasing the environmental and economical sustainability and, also, the profitability of the industrial processes that produce brines. Moreover, the recovery of minerals, such as magnesium, it is important for the European countries because it has been defined as one of thirty critical raw material (CRW) by the European Commission, for the reason that will be explained in the following section [93].

5.3. Why recovery magnesium?

In light of the considerations previously reported, the industrial waste brine may be exploited as an alternative source for the mining of minerals, such as magnesium. In particular, the extraction of the magnesium has to be taken into account due to its high added value. Therefore, the recovery of magnesium from industrial waste brine is economically and industrially strategic due to its high risk of supply and high economical value in European countries. As a matter of fact, magnesium has been defined by the European Commission as one of thirty critical raw materials (CRW) [93], as shown in *Figure 5.3*.

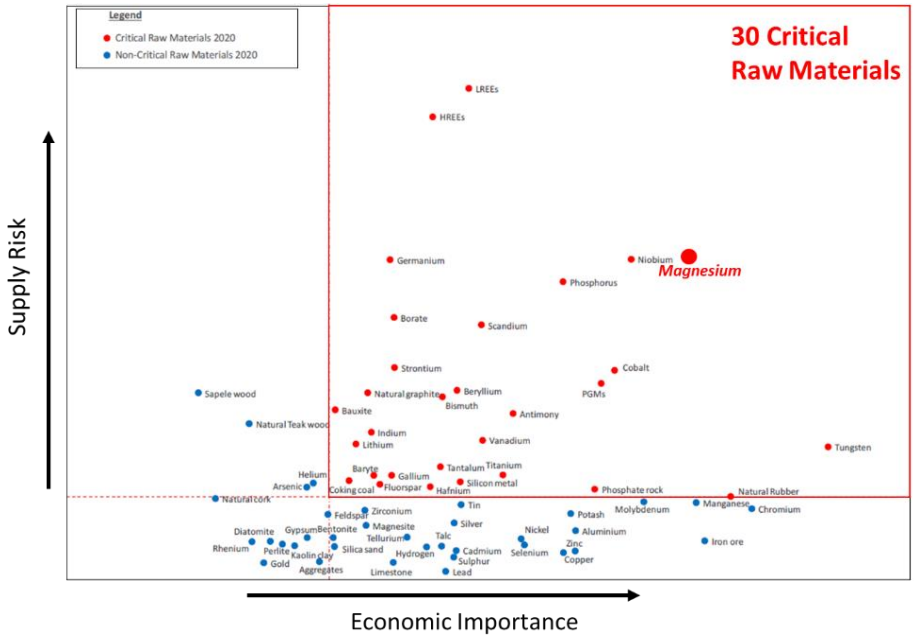

Figure 5.3. Critical raw material defined by European commission according the supply risk and economic importance [93].

Going to look at the European market of magnesium, the net import in the period between 2012 and 2016 was about 124 kton of magnesium as reported in *Figure 5.4* [94].

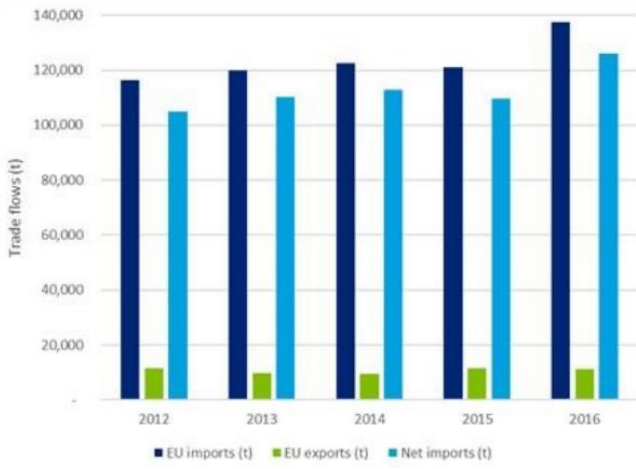

Figure 5.4. European trade flow of magnesium [94].

Now, going to analyse the worldwide production of magnesium compounds (*i.e.* magnesium hydroxide, magnesium oxide, magnesium metal, etc..), *Table 5.1* reports the ktons production of magnesium as equivalent of magnesium oxide in 2014 [95].

Table 5.1. Worldwide production of equivalent magnesium oxide in 2014 [95].

	Magnesite		Seawater or brines		
Country	**Caustic-Calcined**	**Dead-Burned**	**Caustic-Calcined**	**Dead-Burned**	**Tot**
Australia	218	110			328
Austria	76	325			401
Brazil	96	380	12		488
Canada	100				100
China	**1440**	**2740**			4180
France			30		30
Greece	90	110			200
India	20	202			222
Iran	25	40			65
Ireland				90	90
Israel			10	60	70
Italy	25				25
Japan			**50**	**70**	120
Jordan			10	50	60
North Korea	25	100			125
Republic of Korea				40	40
Mexico			15	95	110
Netherlands			**10**	**205**	215
Norway			30		30
Poland		10			10
Russia	**380**	**2500**			2880
Saudi Arabia	39	32			71
Serbia		35			35
Slovakia		465			465
South Africa	12				12
Spain	150	70			220
Turkey	**106**	**544**			650
Ukraine		170	20	80	270
United States	140		**191**	**195**	526
Total	2940	7730	378	885	12000

How it is possible to deduce from *Table 5.1*, the magnesium have minerals origin by the extraction of dolomite or magnesite or obtained from seawater or brine by mean of precipitation process. In particular, China, Turkey and Russia produce about 84% of worldwide production of equivalent magnesium oxide, and of 84%, only China produce about 67%. While, the Netherlands, US and Japan produce about 57% of the total equivalent magnesium oxide produced by precipitation process from brine or seawater. Thus, based on the consideration carried out previously, the countries in the Mediterranean basin have a high potential to become among the first worldwide producers of magnesium hydroxide extracted

by waste industrial brine. In order to give a rough idea of the potentiality of mining of the magnesium hydroxide from brines, some preliminary calculation has been made in order to estimate the quantity of magnesium obtainable from industrial waste brine.

As a starting point, it is necessary to consider that about 70 million m^3/day waste brine (about 50% of worldwide production) is placed in the Mediterranean basin with the magnesium concentration of about 3 kg/m^3 (two times higher than seawater concentration, about 1.5 kg/m^3). Considering a 100% recovery of $Mg(OH)_2$(s), it is possible to estimate a potential production of $Mg(OH)_2$(s) of about 504000 ton/day (184 Mton/year) (, (about 350000 ton/day (127 Mton/year) of MgO) equal to about 50% of the worldwide production of magnesium hydroxide produced from brine/seawater.

Magnesium, as magnesium hydroxide, have a lot of application in the different industrial sectors: (i) in the field of flame retardant, (ii) in pharmaceutical field, (iii) in environmental and protection as agent for desulphurisation and water treatment (iv) others application.

Considering the field of flame retardant and pharmaceutical one, it is important to use high purity of magnesium hydroxide because of the presence of impurities affecting the properties of the final product. For this reason, for this two application is required a magnesium hydroxide produced by the precipitation from brine due to the higher purity than the mineral one. Moreover, the selling price of magnesium hydroxide for the field of flame retards and pharmaceutical ones are about 2700$/ton and 2500 $/ton, respectively [95]. Thus, the production of magnesium hydroxide from industrial waste brine with the same characteristic required by the two sectors analysed is very attractive in terms of high potential profitability as well as the minimization of the detrimental impact on the marine environment. For this reason, the target specification chosen as reference is those of flame retardant and pharmaceutical sectors.

5.3.1 State of art of the recovery of the magnesium hydroxide

In literature, there are few works dealing with the recovery of magnesium from industrial waste brine. In 1990, Mutaz et al [84] focused their attention on the recovery of magnesium as hydroxide or chloride from the brine produced by the desalination plants in Arabian Gulf (about 9 million ton per year was produced and about 33% from seawater). The idea raised in the mind of authors to due to the fact that although 60% of world desalination plants were

installed in the Arabian Gulf, no magnesium production facilities were installed. Thus, the authors analysed several methods (chemical and physical) to recover magnesium from industrial waste brine. Afterwards, they carried out a preliminary economic evaluation considering a production about 2000 ton/year of metallic magnesium and all items needed for plant. Thus, a hypothetical selling price of the produced metallic magnesium equal to 2357 $/ton was estimated less than 3370 U$/ton, which was selling price of metallic magnesium in the United States in that year. Considering a different industrial process, *i.e.* the brine produced by the coal mine industry, Turek and Gnot studied the possibility to recover magnesium hydroxide (used for the refractories industries) as a by-product from a two-stage system that treated waste brines [96]. In order to produce magnesium hydroxide at industrial scale, calcined dolomite, burnt lime or ammonia is the common alkaline reactant used for the precipitation. However, burnt lime and calcined dolomite cannot be used for the precipitation of magnesium hydroxide due to the risk of calcium precipitation, while the use of ammonia as alkaline reactant could form explosive atmosphere during the electrolysis process. For this reason, sodium hydroxide was used as an alkaline reactant for the recovery of magnesium, although causing serious technological problems, such as low sedimentation rate, and, then, making difficult the filtration of the magnesium hydroxide slurry. The authors carried out a wide experimental campaign, results highlighted that the low temperature and slightly excess of hydroxyl ions than magnesium one during the precipitation allowed obtaining a product with a high sedimentation rate and high filterability. With reference to a similar case study, Micari et al [97] performed a theoretical techno-economic analysis demonstrating that an integrated treatment chain can effectively lead to the circular recovery and reuse of chemicals such as $Mg(OH)_2$(s), $CaCO_3$(s) and NaCl(s) in addition to fresh water. In 2007, Lee et al [98] carried out an experimental campaign via a multi-step reactive process in order to valorise the waste brine produced by salt purification plant. Before performing the precipitation of magnesium, the brine was mixed with a sulphuric acids in order to precipitate the calcium as calcium sulphate, because they may lead to low purity in the recovered magnesium. Afterwards, an alkaline solution (NaOH-water solution) was added to the brine for the precipitation of magnesium as magnesium hydroxide. Subsequently, carboxyl methyl cellulose was used in order to increase the sedimentation rate and make easier the washing step. Moreover, sodium stearate was added in order to inhibit and prevent the aggregation of the particle. Although the adding of foreign substances could affect the purity of magnesium hydroxide, they added them in small dosage in order to consider them as impurities. Thus,

the final products of magnesium hydroxide achieved a purity of about 99.5% with a mean crystal size equal to 0.5 μm.

In 2008, a fundamental study on the magnesium precipitation from sea bittern and artificial brine was carried by Alamdari et al [99]. The authors found that during the precipitation of magnesium hydroxide occurred three different phenomena, i.e. nucleation, growth and agglomeration. In particular, the nucleation was the dominant phenomenon than the growth due to the high supersaturation reached during the precipitation tests. The nucleation rate increased when real sea-bittern was used as well as the agglomeration phenomena. In particular, a high nucleation rate may cause the formation of very small crystal making difficult the filtration. On the contrary, the high agglomeration rate allows the formation of larger crystal making easier the filtration.

In 2011, Song et al [100] performed an experimental campaign with a batch reactor for the production of high purity of magnesium hydroxide using an artificial solution made up of magnesium chloride and sodium chloride. The authors analysed the process performance at different operative condition, such as concentration of sodium chloride, temperature, stirring rate etc. The optimal operation conditions were found when a spherical shape of magnesium hydroxide, purity higher than 99% and the particle size ranged between 6-30 μm was achieved. A few years later, the same authors [101] performed the precipitation of magnesium as magnesium hydroxide via continuous Mixed Suspension Mixed Product Removal (MS-MPR) crystallizer. Also, in this case, high purity of magnesium hydroxide was obtained. In particular, large size and uniform spherical structure particles, composted by $Mg(OH)_2(s)$ nanoparticles formed by agglomeration phenomenon, were precipitated. These aggregates of $Mg(OH)_2(s)$ forming gelatinous precipitate create some filtration difficulties, as already stressed in some previous works.

In 2012 Cipollina et all [86] investigated the possibility to recover magnesium from industrial waste brine produced by saltworks. They performed a wide experimental campaign in a laboratory scale batch reactor in order to demonstrate the feasibility to recover magnesium hydroxide at high purity and high conversion coupled with high filterability. Different operative condition was investigated, such as temperature, impeller speed and concentration of sodium hydroxide between others. The experimental outcomes highlighted that time required for a complete filtration increased reducing the speed of the impeller, and increasing the temperature and sodium hydroxide concentration. This is due to the dominance of the nucleation with respect to the growth that led to the formation of very tiny crystals. Moreover,

in all tests, the obtained a magnesium hydroxide purity higher than 90% along with a recovery of about 100%.

Two years later, the same authors [102] carried out a wide experimental campaign using a stirred tank crystallizer in two different configurations, semi-batch and continuous (CSTR) one. The experiments were performed using NaOH solution as an alkaline reactant and real industrial waste brine from saltworks for the precipitation of magnesium hydroxide. Different operative conditions were investigated in order to find the best one to obtain the desiderate crystal size distribution of the product. The results highlighted that in many tests the purity of the produced magnesium hydroxide was higher than 98%. Further, the higher concentration of alkaline reactant allowed the formation of the larger particles formed by the agglomeration of tiny crystals.

5.4. Zero Brine Project

The ZERO BRINE EU-2020 is a 4-years of innovative project coordinate by TU-Delft, and financed by European Commission providing the potential to implement circular economy solution for valorisation and reuse of industrial effluents, such as brines [103]. The project includes 22 European partners among these industrials, universities and research centres.

The aim of the project is the development of innovative technology for the recovery of salts, minerals, and clean water from industrial waste brine meeting the local market specifications and reusing them in other industries. In order to facilitate the implementation of the Circular Economy concept as a new industrial economic model, which may reduce the environmental impact of the disposal of industrial waste brines. In particular, the objectives of the projects are:

- Propose innovative solutions and technologies, economically and industrially valid for the recovery of minerals from industrial brines (water recovery > 90%, salt, mineral recovery > 90%);
- Minimize the disposal of solid in landfill (waste solid < 10% of the current volume);
- Encourage the industrial symbiosis through the recovery of waste heat to meet the thermal energy requirements (waste heat recovered >60%);
- Develop different treatment chain for the implementation of the circular economy concept in order to overcome the environmental issues due to disposal of waste brine

produced by different industrial process (involvement four different industrial sector for the implementation of treatment chain, these are: (i) water industry production, (ii) silica production, (iii) coal production and (iv) textile industry).

The project is structured in ten work packages (WPs). In particular, WP2 (implementation of treatment chains for the valorisation of brine produced by water industry) will be deeply analysed because a part of this PhD thesis is devoted to design and construction of a crystallizer at pilot scale installing within a treatment chain.

The WP2 focuses on the valorisation and reuse of the two waste brines produced in the Demi Water Plant (Evides, The Netherlands). The Demi Water Plant (*Figure 5.5*) consist of the following units: (i) dissolved air flotation, (ii) ion exchange resins (IEXs), (iii) reverse osmosis, (ii) mixed bed ion exchange. During the production of demi water, the water plant (*Figure 5.5*) produce two different brines, the first one is produced during the regeneration of IEXs for the reduction of water hardness removing magnesium and calcium, and the latter is produced by the reverse osmosis [103]. Thus, the aim of the WP2 is the implementation of two large scale treatment chains for the valorisation of the two industrial waste brines.

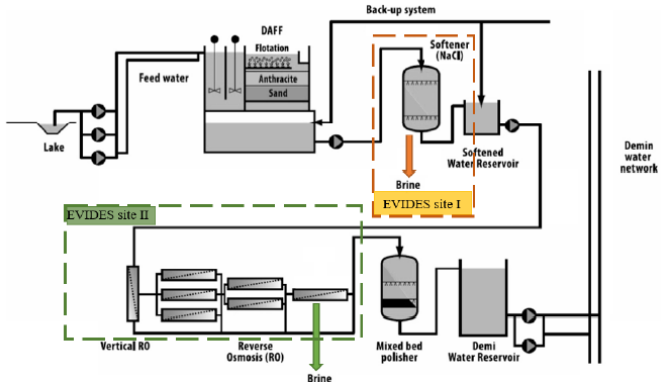

Figure 5.5.Treatment train of EVIDES demi water plant in the Botlek area. Illustration of the waste brine to be treated in ZERO BRINE PROJECT (Site One & Site Two) [103].

The first treatment chain will treat the waste brine produced by the regeneration of ion exchange resins (IEXs) (Evides Site 1, *Figure 5.5)* carried out by sodium chloride solution at high concentration (from 2 up to 5 g/l). The aim of the treatment chain is the regeneration of the spent brine by means of removing calcium and magnesium in order to reuse it again for the regeneration of IEXs. Magnesium and calcium were recovered in form of hydroxides,

and, moreover, the treatment chain allowed producing high-quality fresh water. On the other side, the second treatment chain will treat the waste brine produced by the reverse osmosis unit. This latter treatment chain aims to totally exploiting the waste brine recovering minerals, such as sodium bicarbonate ($NaHCO_3$) and sodium sulphate ($NaSO_4$), and, furthermore, fresh water in order to avoid any release in the environment.

As regards the EVIDES site I, a schematic representation of the treatment chain is shown in *Figure 5.6*.

In particular, a part of this PhD thesis is devoted on the development and testing of a reactive crystallisation pilot unit for the recovery of diivalent rare-earth metals (Mg^{2+} and Ca^{2+}) hydroxides implemented in the treatment chain (see *Figure 5.6*).

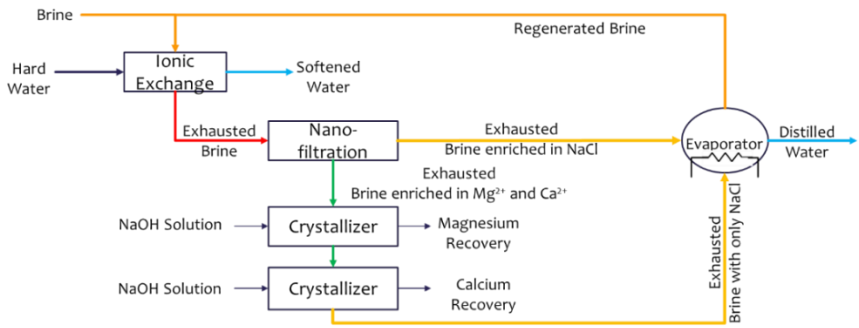

Figure 5.6. Schematics of the treatment chain proposed within the ZERO BRINE EU-H2020 project for the valorisation of brines from IX water softening plants.

The process consists of the following units: (i) nano-filtration (NF), (ii) Mg and Ca crystallizer and (iii) multi-effect distillation (MED). The waste brine from IEX is fed to the NF unit, which produces a retentate enriched in bivalent ions, e.g. magnesium and calcium, and a permeate enriched in monovalent ions, such as sodium chloride. Afterwards, the retentate is fed to a two-steps crystallizer for selective recovery of magnesium and calcium hydroxide, by chemical precipitation using an alkaline solution. After separating the hydroxides slurry within a continuous drum filter, the clarified (almost Ca- and Mg-free) brine is neutralized to pH=7 by addition of hydrochloric acid and mixed with the permeate from the NF. This stream is, eventually, fed to the MED in order to further concentrate the solution in sodium chloride, thus reaching the target value suitable for reuse in the IEX regeneration step.

5.5. Motivation and goal of this work

According to the idea to valorise waste brines by recovering minerals, this section of PhD thesis is devoted on the development and testing of a novel unconventional crystallizer for the recovery of magnesium and calcium by means of a fractionated crystallization. As said before, an alkaline solution, used as a chemical reactant, is mixed with the brine in order to firstly precipitate the magnesium as magnesium hydroxide due to its low solubility (solubility product (K_{so}) =$5.61*10^{-12}$ [104]). The Mg(OH)2(s) precipitation reaction is described by Eq. 5.1:

$$Mg^{2+} + 2OH^{-} \leftrightarrows Mg(OH)_{2(s)} \qquad (5.1)$$

Following the precipitation of magnesium, again, an alkaline reactant is mixed with the brine to recover calcium as calcium hydroxide due to its low solubility (solubility product (K_{so}) = $5.5*10^{-6}$ [104]) as it is described by Eq. 5.2:

$$Ca^{2+} + 2OH^{-} \leftrightarrows Ca(OH)_{2(s)} \qquad (5.2)$$

An unconventional pilot-scale crystallizer, Multiple Feed Plug Flow Reactor (MF-PFR), has been designed and assembled in order to recover magnesium and calcium, separately by means of accurate control of the reaction pH. Thus, a wide experimental campaign has been carried out in order to assess the effect of using of different types of brines, *i.e synthetic* brine, waste brine produced by water industry and saltworks, on stability and robustness of the reactor, and, further, on the capability of the reactor to recover the magnesium and calcium at high purity.

6 MF-PFR Technology, development and pilot construction

Chapter Outline

Part of this chapter has been published in:

F. Vassallo, D. La Corte, N. Cancilla, A. Tamburini, M. Bevacqua, A. Cipollina, G. Micale, « A pilot-plant for the selective recovery of magnesium and calcium from industrial waste brines», submitted to Desalination.

6.1 MF-PFR Development and Construction Crystallization fundamentals

The crystallization is one of the unit operations commonly used in chemical engineering. It consists of formation of solids particles within a homogeneous phase. Moreover, the formation of particles from the vapours, the solidification of liquid and the precipitation are contained within the crystallization. From an industrial point of views, the crystallization process allows producing/separating high purity of crystalline compounds, such as sugar, sodium chloride, etc [105–107]. As said previously, the crystallization process leads to produce a solid phase within a liquid solution, the two-phase mixture of mother liquid and crystals or aggregates form a suspension called magma. The formed crystals inside the solution are characterized by particles, which are formed by atoms or molecules or ions, arranged orderly in the space forming a crystal lattice, which is the most ordered inorganic matter.

In order to start with precipitation, it is necessary that the solution has been reached the saturation condition, which consists of equilibrium condition between crystal and the solution. However, the formation of the crystals consists of two important steps: (i) the birth of the new crystal (Nucleation), and (ii) the born crystals growth in order to form a macroscopic crystal. The driving force of the two steps is the supersaturation, because the formation and growth of crystals occur only when the solute concentration exceeds its solubility. Furthermore, solubility is a function of the temperature. As matter of fact, many species have a solubility that increases at the increasing of the temperature, such as potassium nitrate, while other species show an inverse solubility with temperature, such as the manganese sulphate dihydrate ($Mn(SO_4)\cdot 2H_2O$), finally, the third category of the chemical species show a solubility independent with the temperature such as the sodium chloride. In particular, the supersaturation can be achieved by three different way: (i) increasing/decreasing properly the temperature when the solubility of the species is very sensible with the temperature, (ii) evaporating a portion of the solvent, it is suitable when the solubility does not change with the temperature, and (iii) adding a third component in order to generate high supersaturation. Focusing the attention toward the latter way to create supersaturation, the third component can act physically, *i.e.* it forms with the solvent a mixed solvent, in which the solute has a lower solubility than the initial solvent. This process names salting. Otherwise, the third component may act chemically with the solute to create an

insoluble substance. This process is called precipitation. In particular in this PhD thesis, the so-called *common ion effect* is used. It is consists of adding a third component in the solution having a common ion with the interested compound has to be recovered.

As said previously, the supersaturation is the driving force of the crystallization process to lead the formation of the crystals that is defined as the difference of the current solute concentration and the equilibrium concentration as it is described by Eq. 6.1:

$$\Delta C = C - C^{sat} \qquad (6.1)$$

Another important parameter used in the crystallization process is the supersaturation concentration ratio (α) given by the ration the actual concentration and the equilibrium concentration, as it is described by Eq. 6.2:

$$\alpha = \frac{C}{C^{sat}} = 1 + \frac{\Delta C}{C^{sat}} = 1 + s \qquad (6.2)$$

in Eq. 6.2, a new parameter *s* (fractional supersaturation) is defined. In particular, the fractional supersaturation *s* is a relative supersaturation computed respect to the equilibrium concentration [105,107].

In the crystallization process, nucleation is the responsible phenomena allows generating very little crystals, named nuclei, which act as centre of growth. There are different types of nucleation, which may occur simultaneously during the crystallization. In particular, the first difference has to be made between the primary nucleation and secondary nucleation. With reference to primary nucleation, this takes place in absence of solute-own crystals, while the secondary nucleation occurs in presence of solute-own crystals, for example, because of adding of seeds. Focusing on the primary nucleation, it can be subdivided into homogenous or heterogeneous nucleation, depending on if the nuclei are formed by the influence or not of solid bodies (such as crystallizer wall, blade of impeller, foreign particle), which act as catalyser increasing the nucleation rate.

The homogeneous nucleation almost never happen in the crystallizer perhaps in some precipitation. However, the homogeneous nucleation is very important to understand the fundamental phenomena beyond the precipitation/crystallization process. The crystal can be formed by different types of particles, such as molecules, atoms or ions. In particular, the mechanism leads to the formation of a stable crystal in the solution. The homogeneous

nucleation is characterized, firstly by the formation of the cluster due to the association of small particle, which usually disappears quickly. Sometimes, the cluster continues to associate particle becoming an embryos, which has a lattice structure, but it has a short life get back to the cluster or individual particle, but if the supersaturation is large enough, the embryo can grow to form a stable size, called nucleus. The nucleus is a stable assemblage of particle that can grow to generate a crystal [105–108].

From the thermodynamic point of view, the difference of the small particle with the largest one is that the small particle has higher surface energy per unit mass than the large one, implying that the small particle has a higher solubility than a large particle. Thus, the solubility is affected by the size of the crystal, which is the key factor in the nucleation. The effect of the crystal size on the solubility is described by the *Kelvin equation (Eq. 6.3)*:

$$ln\frac{C_{sat}(L)}{C^*_{sat}} \propto \frac{1}{L} \qquad (6.3)$$

where L is the size of the particle with microscopic dimension that is in equilibrium in the solution with a concentration $C_{salt}(L)$ which is higher or equal than C^*_{sat} (conventional solubility).

At the contrary, the presence of physical bodies, such as solids particles, act as catalyser in the process according to the heterogeneous nucleation. In particular, the presence of the foreign bodies allows reducing the energy required for the formation of stable nuclei as a function of the wetting angle formed by the nucleus and foreign solid particle.

The secondary nucleation is due to the presence of the existing macroscopic crystals in the magma solution. The secondary nucleation is due to the presence of the existing macroscopic crystals in the magma solution. A cause of the secondary nucleation is the shear-stress of the liquid. This is due to the high velocity of the supersaturated solution that moves past the surface of growing crystals, and the shear stress may scrap away nuclei or embryos going to form new crystals. Overall, secondary nucleation is a phenomenon that can be deliberately desired if seeds are added. Generally speaking, secondary nucleation occurs spontaneously inside the crystallizer due to the presence of physical phenomena inside crystallizer, one of these is the shear-stress.

The last category of the nucleation phenomenon is the *spurious nucleation*. This occurs when large supersaturation or poor magma mixing lead to very fast growing of the crystals

obtaining a needle-like structure which easily break off generating new nuclei and, in the same time, giving crystals of a poor quality.

After the formation of a stable nucleus, this starts to grow becoming a crystal with a microscopic dimension. The crystal growth is based on mass transport. In particular, crystal growth consists of two consecutive steps. In the first step, the solute moves from the bulk of the solution to the surface of the crystal where the solute is accepted by the crystal and incorporated in the space lattice [105–108].

Rigorously speaking, the crystal growth is a function of the crystal size due to the terminal velocity that crystal with different dimension has inside the crystallizer. However, it is used an approximation which assumes a growth rate-independent with the crystal size. This hypothesis is known as ΔL law or McCabe law. However, the ΔL law has a limited range of applicability, in fact, a length size of crystals above 500 μm influence the flow dynamics around the particles, and, then, the mass transfers from the bulk to the crystal, at the contrary, the reduced size crystal allows the reduction of the equilibrium concentration (Kelvin law).

Another phenomenon occurring inside the crystallizer is the agglomeration. The agglomeration occurs when two particles collide and they can be disintegrated forming a crystal with a small size or they stick together forming a single large crystal. However, in order to stick together, the two crystals have to win the repulsive electrostatic force between them. For small particle, the agglomeration occurs by means of the Brownian motion, i.e. fluctuation in the solution, while for the larger crystals, a high velocity-gradient is required in order to allow the collision between the two particles. Thus, the agglomeration phenomenon mainly occurs between small particle because they easily collide thank to the Brown motion independently the flow-field of the crystallizer [109].

The crystallization phenomena involved during the crystallization process affect the final crystal size distribution. Thus the study and the knowledge of these phenomena, it is important in order to obtain a crystal product with a marketable crystal size distribution.

This brief description on the phenomena involved during the crystallization process it is important to understand the results obtained during the experimental campaign devote to develop and test of a pilot unit crystallizer for the recovery of magnesium by means of a precipitation process.

6.2 Fractionated crystallization for the recovery of Mg/Ca

The fractionated crystallization of the two hydroxides is achieved by an accurate control of the reaction pH. To this aim, a preliminary test has been performed using a laboratory semi-batch reactor and the following experimental procedure:

- an artificial solution, prepared using magnesium chloride hexahydrate (VWR, purity >99%), calcium chloride dehydrate (Honeywell, purity >99%) and sodium chloride (Sale di Volterra, purity >99%) in deionised water, was used to reproduce the typical composition of the IX spent brine (see *Table 6.1*);
- the artificial brine is put inside a magnetically stirred beaker, where the alkaline solution is slowly added via a syringe pump.

The pH is monitored by a portable pH-meter (WTW, mod. 3320) and the obtained pH trend over the time is shown in *Figure 6.1*.

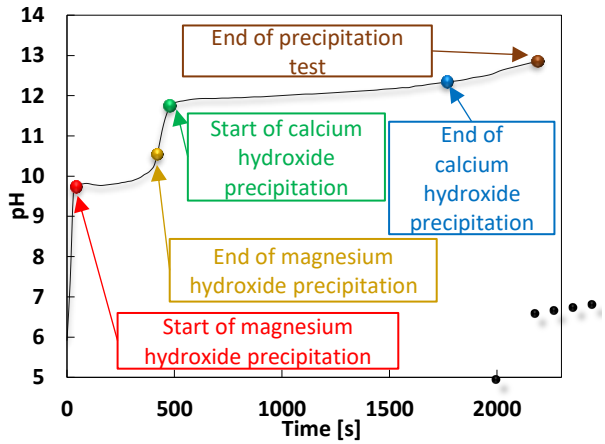

Figure 6.1. Evolution of rection pH as a function of time due to adding NaOH-water solution into a synthetic brine containing Mg^{2+} and Ca^{2+} (see Table 6.1)

Starting from a pH value around 6, the 1M NaOH-water solution is slowly injected at constant rate (60 ml/h) and the pH increases quickly until a value around 9.8 (red point in *Figure 6.1*) when the precipitation of magnesium hydroxide begins. Then, the pH increases very slowly until 10.4 (orange point in *Figure 6.1***Errore. L'origine riferimento non è stata trovata.**), where magnesium can be assumed to be quantitatively precipitated. The produced

magnesium hydroxide slurry is then filtered and the solids is dried and analysed, while the Mg-free filtered solution (after being analysed) is fed to a second precipitation where a 4M NaOH solution is used according to the same experimental procedure described above for the precipitation of $Ca(OH)_2$(s). Also, in this case, the pH starts to increase quickly until the value of 11.75 (green point *Figure 6.1*), where the precipitation of calcium hydroxide starts. Afterwards, the pH increases slowly reaching a value around 12.4 (blue point in *Figure 6.1*), where, theoretically, all calcium is precipitated as calcium hydroxide. The test is extended until a pH around 13 is reached (brown point in *Figure 6.1*) in order to be sure that Ca^{2+} is quantitatively precipitated. After this second precipitation step, the slurry is filtered to separate solids from liquid and, then, both analysed.

The cations composition of the initial brine and of two clarified solutions are reported in *Table 6.1* along with the purity of two solid hydroxides obtained. In particular, that shows a quantitative precipitation of both cations and a purity of the obtained solids above 98%, thus confirming the possibility to quantitatively recover magnesium and calcium hydroxide at high purity matching the specification required by the market.

Table 6.1. Fed batch test: pH, cation composition, purity and precipitation yield of magnesium and calcium hydroxides.

	Ca^{2+} [g/l]	Mg^{2+} [g/l]	pH
IEX Spent Brine	24.12	3.08	6
1° step (filtrate)	22.53	0.02	10.4
2° step (filtrate)	0	0	13
$Mg(OH)_2$(s)	Purity		>98%
	Precipitation yield		>99%
$Ca(OH)_2$(s)	Purity		>98%
	Precipitation yield		>99%

Following the results above, a conceptual scheme of a continuous system for fractionated precipitation of Mg and Ca hydroxides is shown in *Figure 6.2*.

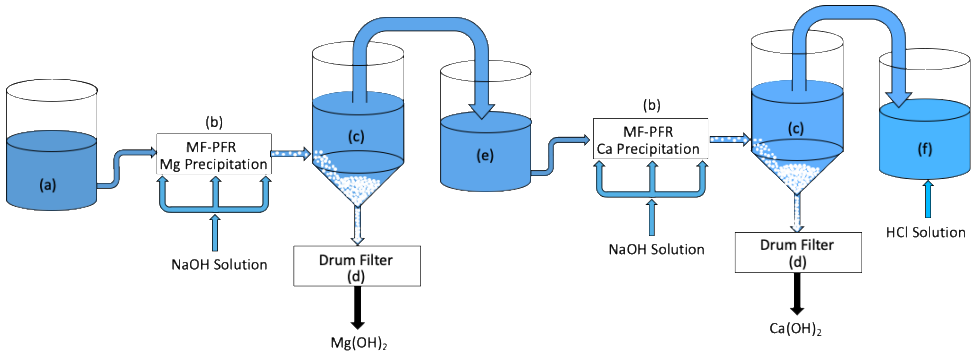

Figure 6.2.Conceptual scheme of the crystallisation pilot plant. (a) Storage tanks, (b) Precipitation Unit, (c) Settling tank, (d) Filtration unit, (e) Intermedia tank, (f) Neutralization unit

The pilot unit consists of the following main parts:

(a) brine storage tank;

(b) a precipitation unit where magnesium, first, and calcium, secondly, are precipitated from the brine by direct mixing with a sodium hydroxide solution ("precipitation unit"), represented as two separate blocks in the diagram, though being the same unit in practice;

(c) Magnesium and Calcium settling tanks, useful to collect and settle the produced slurry in order to prepare a concentrated slurry to be sent to the filtration unit.

(d) A filtration unit where crystals are separated from the slurry ("filtration unit").

(e) Interstage storage tank, where the first step clarified solution is stored before feeding the 2nd step precipitation for Calcium recovery;

(f) Neutralization unit, which allows for the neutralisation of the clarified solution exiting from the 2nd step settling tank and Ca-slurry filtration.

6.3 MF-PFR Development and Construction

The development and the construction of the MF-PFR crystallizer, which is the core unit for the recovery of the magnesium and calcium, was carried out through the followings steps: (i) 3D sketch and (ii) assembling.

Firstly, a 3D sketch of the MF-PFR was a crucial step for the assembling of the MF-PFR due to the following advantages:

- Allow the correct positioning of all instrumentations of the pilot;
- Allow correct assembling of the pipes;
- Allow easy changing the disposition of the instrumentations;
- Allow seeing the final appearance and dimension of the, MF-PFR.

Moreover, 3D drawing has allowed minimizing and avoiding human error during the assembling of the MF-PFR and to overcome the problems which could arise during the assembling. In this way, it was possible to construct the pilot in a short time and to save time and money due to the incorrect assembly of some part of the reactor. Thus, a 3D sketch of the MF-PFR was developed by using the drawing software, FUSION 360. The 3D sketch is shown in Figure 6.3.

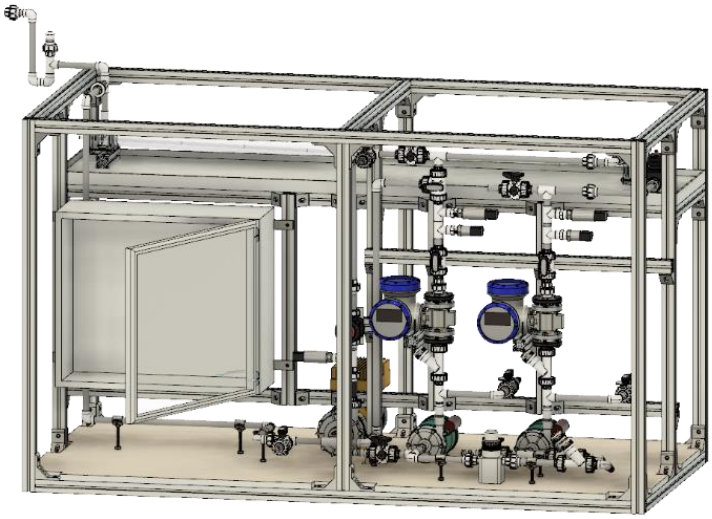

Figure 6.3. 3D CAD of the MF-PFR prototype

Following the 3D sketch, the MF-PFR was assembled. The main instruments that made up the MF-PFR are:

1 Magnetic drive centrifugal pump (IWAKI, mod. MD-40RZ-220) with high chemical resistant in order to feed the brine inside the reactor. The pump has maximum flow-rate equal to 22 L/min and maximum head of the pump of 10 meters. The electrical supply of the pump is 230 VAC.

2 Magnetic drive centrifugal pump (IWAKI, mod. MD-30RZ-220) with high chemical resistant in order to concentrate alkaline solution inside the reactor. The pump has maximum flow-rate equal to 15 L/min and maximum head of the pump of 8 meters. The electrical supply of the pump is 230 VAC.

3 Two electric-motorized valves (FIPNET, mod. VDK/CE) in order to control both flow rates, the brine and alkaline one.

4 Two magnetic inductive flow-meters (KHRONE, mod. OPTIFLUX 4300 C) calibrated for a measuring range of 0-8 l/min for the brine flow rate measures and 0-4 l/min for the measure of alkaline one.

5 Two pressure transducers (Krohne, mod. OPTIBAR P1010C and Vega, mod. VegaBar 14 respectively), in order to monitor the pressure drops of the brine and alkaline one.

6 Two resistance thermometer Pt100 sensors (KHRONE, mod. TRA-C20) in order to monitor the inlet temperature of both solutions.

7 A pH-meter (KHRONE, mod. PH 8320) to monitor the pH at the outlet section.

8 Two conductive meters (Krohne, PTSENS IND 1000) to measure the electrical conductivity of the alkaline and the brine solutions. The operational-range of measure is 0-2000 mS/cm, and also the sensors is provided by a resistance thermometer Pt1000.

9 A crystallizer, MF-PFR, in which the precipitation of the magnesium or calcium occurs.

10 An electrical cabinet, which contains all electrical devices for the management and control of the pilot unit.

All sensors have been electrically connected with chassis produced by *National Instrument*. Afterwards, the computer was linked with the chassis by means of software *NI Measurement & Automation Explorer (MAX)*.All sub-sections of the MF-PFR unit were connected using welded rigid PP-H (polypropylene homopolymer) pipes (ID 16 mm, thickness 2 mm) and fittings. Also, all valves are made of PP-H, in order to be perfectly resistant to the highly aggressive solutions of brine and sodium hydroxide solution [110] and, also, for the good mechanical properties possessed by the PP-H material [111].

Pipes and instrumentations are installed on a supporting structure built with corrosion-resistant materials (PVC sheets and aluminium-profiled bars). The supporting structure has a high of 116 cm, a width of 98 cm and a length of 198 cm.
A picture of the MF-PFR prototype is reported in Figure 6.4.

Figure 6.4. A picture of the MF-PFR prototype developed at the Brine Excellence Centre satellite laboratory of University of Palermo.

MF-PFR Crystallizer

The core of the pilot is the crystallizer Multiple Feed Plug Flow Reactor (MF-PFR). The unit consists of coaxial plexiglass tubes, with the brine flowing inside the internal tube and the alkaline solution flowing in the annular section. The brine is injected inside the annular section through distributed holes, whose position and orientation have been purposely selected in order to promote the fast mixing of reactants, (see *Figure 6.5*).

Figure 6.5. Schematic representation of the inner tube of the MF-PFR

Moreover, four pitch-blade shaped spacers were positioned along the length of the inner tube in order to give mechanical support avoiding deformation of internal tube, and, also, promoting the turbulence.

A picture of the MF-PFR crystallizer is reported in *Figure 6.6*.

Figure 6.6. Picture of the MF-PFR crystallizer.

7 MF-PFR, Pilot testing BEC-UNIPA

Chapter Outline

7.1 Experimental Methodologies

The experimental procedure used for all experiments carried out in the satellite laboratory BEC-UNIPA can be summarized in Figure 7.1. Each box refers to one (or multiple) operations, the solids line refers to the mass flow, while the dish lines refers to the obtained results from the analyses.

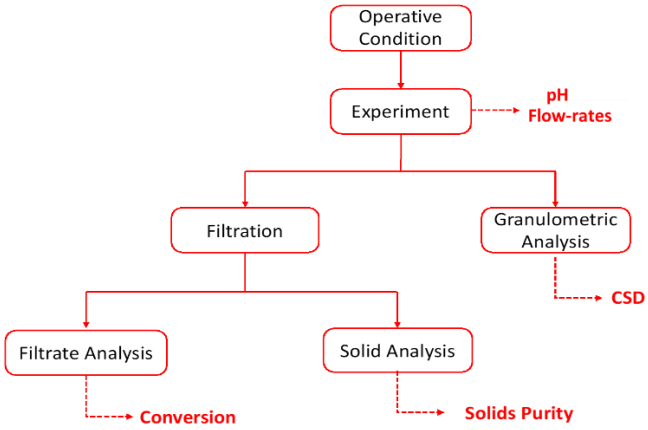

Figure 7.1. Experimental procedure for the recovery of Mg^{2+} and Ca^{2+} as hydroxides from waste brine

Operative Condition. The first step is the characterization of the reacting solution in terms of the need volume for the tests and the preparation of brine and alkaline solutions. For the first experimental campaign synthetic brine solution was used, for the second one a real waste industrial brine coming from saltworks located in Trapani. In the latter case, the brine was diluted in order to reduce the concentration of the Mg^{2+} to a value of 10 g/l, and 25 g/l. Moreover, further tests were carried out preparing an *ad-hoc* synthetic brine solution mimicking the composition of the retentate coming from the NF steps (see *Figure 5.6.* Schematics of the treatment chain proposed within the ZERO BRINE EU-H2020 project for the valorisation of brines from IX water softening plants.). Before each test, the brine solution was analysed via Ion Chromatography (IC 882 Compact Plus - Metrohm AG, Switzerland) in order to check composition of the prepared brine. Depending on what kind of brine and precipitation were performed, different concentration of alkaline solution was used and both

flow rates were calibrated in order to carry out the precipitation under stoichiometric condition.

Experiment. The experiment consisted of three parts: (i) start-up, (ii) stationary condition and (iii) cleaning. During the start-up, the brine and alkaline flow-rates were adjusted in order to reach the desired reaction pH (10.4 for the magnesium precipitation and more than 13 for the calcium one). Once the flow-rates were set, the reactor worked in the steady-state condition, where samples were collected at the outlet of the MF-PFR in order to avoid any disturbance on operational conditions. The volume collected for each sample was equal to 500 ml, necessary for the whole cycle of analysis. After the test, the reactor was cleaned using HCl solution (about 4M) in order to dissolve the fouling of $Mg(OH)_2(s)$ or $Ca(OH)_2(s)$ formed during the precipitation, and after flushed with tap water. During the precipitation and cleaning steps, the pH was measured by a pH-meter installed at the outlet of the crystallizer.

Stability analysis. During the experimental test, same key operative parameters, *i.e.* both flow rates and reaction pH, were recorded and analysed in order to assess the stability and the robustness of the MF-PFR, because the experiment test may be subjected to change as a result of variation of monitoring parameters. One of these is the pressure drop. The variation of the pressure drops can be due to the obstruction of the holes present in the internal pipe of the MF-PFR, caused by the fouling formation of the magnesium/calcium hydroxide. The variation of the pressure drop leads to the variation of both flow rates, *i.e.* the brine and the alkaline, causing the variation of the reaction pH, which in turn changes the recovery. Another cause is variation of the level inside the feeding tanks because the flow rates generated by the two feeding pumps are affected by the variation of liquid height.

*Granulometric Analysis***.** The produced slurry was analysed by Laser Granulometer (Malvern Mastersizer 2000 with Hydro 2000MU as sample dispersion system) in order to obtain the crystal size distribution (CSD) of crystal agglomerates.

Filtration. The samples were filtered in order to separate the produced solid from brine. A Büchner filter with a circular glass-fibre filter (General Electric, 110 mm) was used to separate the produced precipitate from the solution. The filtrate was collected and prepared for ion chromatography. The solid was washed two-time using deionized water in order to

remove any traces of brine and soluble salts. After the cleaning, the solid was dried in an oven for 24 hours at 120°C. About the produced slurry by the precipitation, it was collected in the tank about 500 l, in order to settle the produced crystal. Subsequently, the concentrate slurry was recovered and fed into a drum filter to recover the precipitate mineral. Both procedures were followed for magnesium and calcium precipitation.

*Filtrate Analyses***.** The filtrate was analysed via IC in order to compute the yield of the precipitation by determining the concentration of the magnesium or calcium ions inside the solution.

Solid Analysis. The solids were prepared for the IC analysis in order to estimate the purity of the precipitated crystals. Subsequently the drying, the solid was powdered and a small amount of powder (about 10 mg) was weighed. After, the weighed powder was dissolved using 1M of HCl solution and appropriately diluted in order to be ready of the IC analyses.

7.2 Performance Parameters

The following operating/performance parameters were chosen in order to evaluate the performance of the MF-PFR during the precipitation:

- *pH:* it gives a qualitative indication on the conversion degree, it mainly used during the fractionated precipitation of the $Mg(OH)_2(s)$, which stats at the pH equal to 9 and ends at pH equal to 10.4, and $Ca(OH)_2(s)$, which start at the pH value about 12 and ends at pH value more than 13.
- *Magma density:* it expresses the concentration of the produced solids, indirectly measured dividing the amount of the filtered solids (m_s) with the filtrate volume (V_f). The magma density is computed by using Eq. 7.1:

$$M_T = \frac{m_s}{V_f} \qquad (7.1)$$

- *Recovery (Y):* it expresses the efficiency of $Mg(OH)_2(s)$ (or $Ca(OH)_2(s)$) recovery in the crystallisation step. It is computed via the ratio of the quantity of precipitated Mg (or Ca) with respect to the total amount of magnesium (or calcium) present in the feed. It is defined for each precipitation step as defined by Eq. 7.2:

$$Y = \frac{N_i^o - N_i}{N_i^o} \qquad (7.2)$$

  Where *N* is the mole flow, the apex *o* refers to the initial mole-flow rate, while subscript *i* refers to the cations taking into account, *i.e.* Mg^{2+} or Ca^{2+}.

- Solid Purity: it expresses the amount of Mg^{2+} or Ca^{2+} respect to the total cation amount measured by IC analysis. The purity was calculated by using Eq. 7.3:

$$Purity = \frac{C_{Mg^{2+}(Ca^{2+})}}{\sum_{i=1}^{N} C} \qquad (7.3)$$

- *CSD:* it refers to the crystal size distribution measured by the laser granulometric analysis.

7.3 Description of the laboratory layout of the MF-PFR pilot-plant

Simplified Piping and Instrumentation Diagram (P&ID) of the pilot plant installed in the BEC-UNIPA is presented in *Figure 7.2*. The system is divided into three main sections:

1. Precipitation section, consisting of the MF-PFR crystallizer for the precipitation of the minerals and relevant auxiliary unit (*e.g.* pumps, tanks etc.)
2. Filtration section, consisting of a drum filter and relevant auxiliary units.

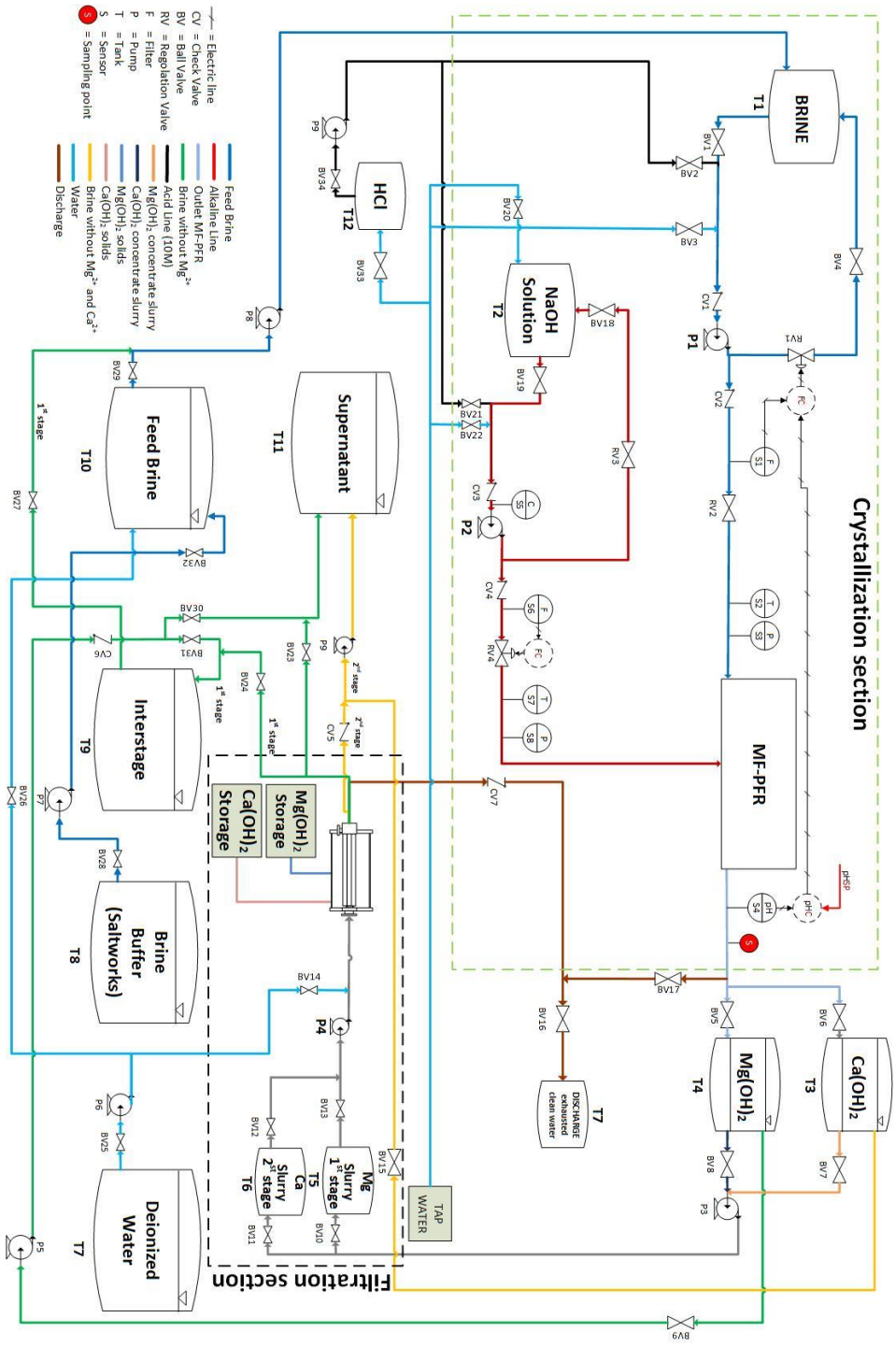

Figure 7.2. Simplified P&ID of the pilot plant installed in satellite BEC at UNIPA

A detailed description of the two sections is reported below.

Precipitation Section

With reference to the P&ID shown in *Figure 7.2*, the operation of the unit can be described as follows.

The tank T1 is filled with the brine coming from the *T10*, in which the brine either is prepared dissolving salts in deionized water (*T7*) (for the first, third, and fourth experimental campaign) or diluting the saltworks brine with deionized water (second experimental campaign). The tanks *T2* is filled with sodium hydroxide solutions used as reactant for the precipitation step of Mg^{2+} for all tested brine, while for the third and fourth tests was refilled with a sodium hydroxide solution with a molar concertation higher than previous one for the calcium precipitation. Brine and alkaline solutions are pumped by magnetic drive centrifugal pumps. Both pumps are equipped with a recycle loop to better control flow-rates via two electric-motorized valves. Flow rates are measured by magnetic induction flow-meters. Inlet pressure is measured by pressure transducers, in order to monitor the pressure drops inside the annular and internal sections of the reactor. Temperature is measured by Pt100 sensors.

The direct mixing of brine and alkaline solution inside the annular section of the MF-PFR reactor leads to the precipitation of $Mg(OH)_2(s)$ or $Ca(OH)_2(s)$ crystals in the form of agglomerates.

As discussed in the previous sub-chapter 6.2, it is crucial to control the pH of the slurry exiting from the MF-PFR for the third and fourth experimental campaign in order to precipitate only magnesium or calcium hydroxide.

Following the precipitation of magnesium hydroxide, the produced slurry is stored in a settling tank (*T4*). The settled slurry is sent to the storage tank (*T5*), ready for filtration, while the clarified solution is collect either to the intermedium tank (*T9*) and fed again to the feed tank (*T1*) to be further processed for the calcium precipitation or to the supernatant tank (*T11*) in which the clarified brine is neutralized and discharged.

Calcium hydroxide is precipitated according to the same steps, though a higher pH is maintained in this case, and a different settling tank is adopted (*T3*). From this, the clarified solution is sent to the supernatant tank (*T11*) for neutralization and disposal, while the settled slurry is sent to the storage tank (*T6*), ready for filtration.

The reactor is periodically cleaned using a hydrochloric acid solution, in order to dissolve residual scaling, and then flushed with water.

Filtration Section

The main unit of the filtration section is a vacuum drum Filter, *Figure 7.3.*

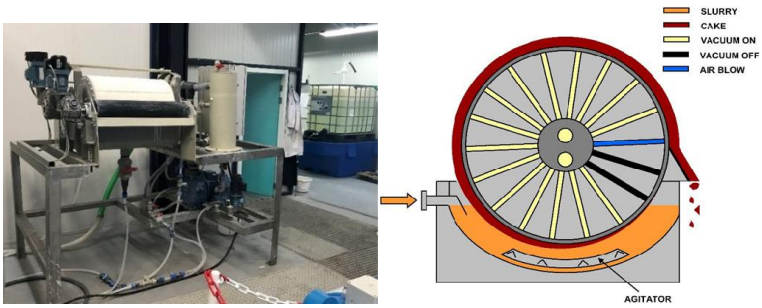

Figure 7.3.a) Picture of the drum filter installed and operated at the premises of Plant One (Botlek, Rotterdam, NL). a) Conceptualised scheme of operation of a drum filter [112].

The vacuum drum filter consists of the following parts:

- Feed tank, which is filled with the concentrated slurry. Inside the tank, there is an agitator necessary to maintain the solids in suspension.
- Rotating vacuum drum, with a filtration cloth of 1 m^2 filtration area. The vacuum drum is split in 12 sector, as shown in Figure 7.3-b, some of them kept under vacuum and others at atmospheric pressure. A part of the vacuum drum is submerged inside the slurry, allowing the submerged sectors to suck the concentrated slurry from feed tank. The unsubmerged sectors are used for washing the cake collected on the surface of the cloth, then, for drying the crystals and, finally, the last sectors in front of the secondary drum, from which the cake is detached.
- A secondary drum, rotating in opposite direction, is used to collect the solids cake from the cloth and discharge them through a knife.
- Two receiving tanks, one for collecting the sucked solution and the other for collecting the washing water. The two tanks are connected to the vacuum drum by the means of a tailored perforated Teflon plate, which allows connecting some sectors of the vacuum drum with a specific receiving tank. A vacuum pump (Robuschi, mod RVS-16/M-06) generates the vacuum inside the tank, while two peristaltic pumps (Ragazzini srl, mod. PSF2 and mod. PSF3) allow for the extraction of sucked solution and washing water from the tanks to the outlet collecting basins.

- Spray nozzle distributors, which spray the washing water on the top of the drum filter investing the whole surface of the cake.

After each precipitation step, the magnesium/calcium slurry was sent into the settling tank, *T3* and *T4,* respectively. The sedimentation of the produced slurry took about 16-18 hours. The concentrate slurry was sent into the feed tank of the drum filter (*T5* for magnesium slurry and *T6* for calcium) ready to feed into the drum filter.

The sedimentation, and the consequent increase of slurry concentration, is an important step for the correct operation of the drum filter. The filtration through the drum filter is based on the cake filtration principle [105,113]. In fact, during the filtration process, solids are retained onto the cloth surface forming a cake which is the filtration medium. Therefore, the function of the cloth is essentially that of a structural support. For this reason, it is important to have high solids concentration in the feed in order to promote a rapid formation of the cake onto the cloth surface [105,113].

Auxiliary units.

The external connections (brine tank, filtration unit and interstage buffer tank) have been constructed using semi-rigid PE (polyethylene) tube (ID 16mm, thickness 2mm), fittings and valves.

Information on all tanks adopted in the prototype is reported in *Table 7.1*.

Table 7.1. Tanks used in the pilot plant.

Tank n.	volume [l]	material	used for
T1	200	HDPE	Feed Brine
T2	200		Storing the NaOH aqueous solution for precipitation of $Mg(OH)_2$(s) or $Ca(OH)_2$(s)
T3	500	HDPE	Collecting and settling the $Mg(OH)_2$(s) slurry
T4			Collecting and settling the $Ca(OH)_2$(s) slurry
T5	125	PVC	Collecting the $Mg(OH)_2$(s) concentrated slurry
T6	125	PVC	Collecting the Ca(OH)2(s) concentrated slurry
T7	500	PE	Storing the deionized water
T8	2000	HDPE	Storing the saltworks brine
T9	1000	HDPE	Storing the brine after the precipitation of Mg^{2+}
T10	1000	HDPE	Buffer of feed brine
T11	1000	HDPE	Storing and neutralizing clarified brine for the disposal
T12	125	HDPE	Storing HCl solution

7.4 Results and discussion of the first experimental campaign with to precipitate $Mg(OH)_2$(s)

The first experimental campaign was carried out using an artificial brine mimicking the composition of the brine produced after the regeneration of the ion exchange resins considering only magnesium and sodium concentration. This experimental campaign aims to find the suitable operating condition of the MF-PFR in order to produce a precipitate of magnesium hydroxide easily filterable and plat hexagonal shape.

The experimental campaign was carried out fixing concentration of the magnesium (*i.e.* 4 g/l) and varying the concentration of the NaOH solution, *i.e.* 0.5 M, 1M, 2M and 4M. For each tested alkaline solution, two different configurations were used; the first was run feeding directly the two solutions in the MF-PFR, and the latter was run adding magnesium hydroxide seeds (20 g/l high purity of magnesium hydroxide [99] (ALBEMARLE®, Magnifin H10 [114])) in the alkaline solution. Magnifin H10 was used as seeds in order to promote the

growth than nucleation and to obtain a precipitate of magnesium hydroxide with the same distribution and morphology of the Magnifin.

The artificial brines were prepared using deionized water and dissolving NaCl (Sale di Volterra, purity >99%) and $MgCl_2*2(H_2O)$ (Honeywell, purity >99%), while the alkaline solution was made dissolving micro-pellet of NaOH (Inovyn, high-grade purity 99%) into the deionized water.

The main ion compositions of the brines and alkaline solution, and volumes of both solution are reported in *Table 7.2*.

Table 7.2.Main ion compositions of brine and alkaline solution.

Test	Inlet Brine				Alkaline solution		
	Composition [g/l]			Volume [l]	NaOH [mol/l]		Volume [l]
	Na^+	Mg^{2+}	Cl^-		No Seed	Seed	
A	4.3	4	12.5	100	0.5		50
B					1		
C					2		
D					4		

During the experimental tests, the flow rate of the alkaline solution was kept fixed at the value equal to 0.30 l/min, while the brine flow rate was adjusted until the reaction pH was about 10.4 in order to precipitate magnesium hydroxide under stoichiometric condition. The operative conditions of the MF-PFR are reported in *Table 7.3*.

Table 7.3. Operative condition for the precipitation of $Mg(OH)_2(s)$.

Tests		pH	Operative Condition of system	
			Brine Flow Rate [l/min]	NaOH Flow Rate [l/min]
A	No Seed	10.35	0.48	0.30
	Seed	10.4		
B	No Seed	10.45	0.91	0.30
	Seed	10.4		
C	No Seed	10.4	1.9	0.30
	Seed	10.35		
D	No Seed	10.4	3.9	0.33
	Seed	10.35		

During the experiment, some samples of the produced slurry were taken and stored in tanks (20/30 l) in order to settle the magnesium hydroxide produced for about 18-24 hours.

7.4.1 Filterability

Subsequently the settling, the concentrate magnesium hydroxide slurry was filtered via a Büchner filter with the same filtration cloth used for the drum filter in order to characterize the produced slurry in term of filterability.

The filterability of the produced concentrate slurry was assessed by measuring the time required for the filtration and thickness of the cake formed onto the filtration cloth surface. Results of the filtration are listed in *Table 7.4*.

Table 7.4. Results of filtration using filtration cloth of drum filter.

	Tests	NaOH M	Time [s]	thickness [mm]	cake weight [g]	M_T [g/l]
A	NO SEED	0.5	125	8	5.0	50.2
A_S	SEED		155	6.7	6.2	62.5
B	NO SEED	1	176	6.9	3.9	39.2
B_S	SEED		300	9	10	100.0
C	NO SEED	2	195	5.7	2.3	23.1
C_S	SEED		270	9.5	7.0	70.0
D	NO SEED	4	360	8.2	2.4	23.9
D_S	SEED		460	7.8	5.3	53.3

In *Figure 7.4*, the specific filtration time computed dividing the filtration time and the thickness of cake is reported.

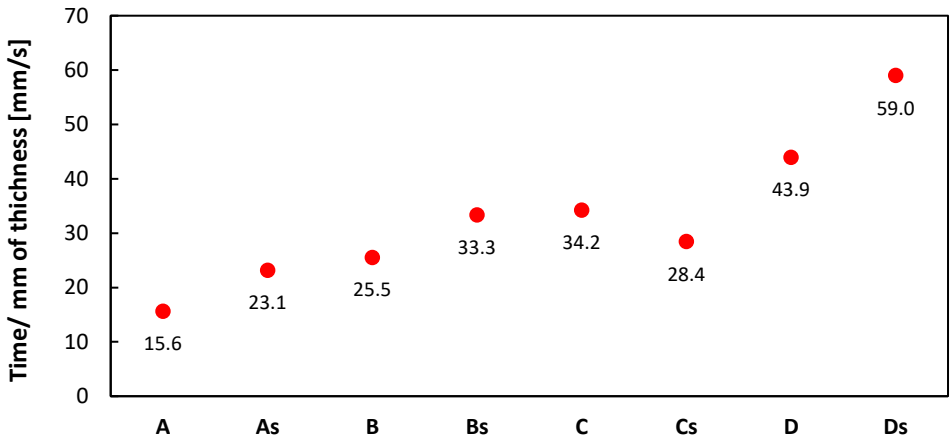

Figure 7.4. Specific filtration time.

As shown in *Figure 7.4*, an increase in the molar concentration of the alkaline solution produces an increase in the filtration time. A possible phenomenological explanation for this result may be related to the high nucleation rate along with the high agglomeration rate. Based on this consideration, when the precipitation occurs at a high concentration of the alkaline solution (Case D and D_S), it was necessary to increase the flow rates of the brine causing a reduction in the residence time inside the MF-PFR. As the residence time inside the reactor decreases, nucleation is favoured with respect to growth causing the formation of an enormous number of microcrystals favouring the formation of large agglomerate due to the closeness of crystallizing particles [99–101]. At the contrary, when the precipitation occurs at low concentration of the alkaline solution (Case A and A_S), the brine flow-rate is the lowest, this leads to an increase of residence time favouring the growth of the crystals respect to the nucleation and, at the same time, reducing the agglomeration phenomenon.

7.4.2 Morphology

Another aspect under investigation is the morphology of the obtained magnesium hydroxide at the different precipitation conditions.

In addition to CSD, another widely method used for describing particle size distribution is the d values. Then, d10, d50 and d90 are the d values used to represent the midpoint and the range of the particle size. These values can be calculated from the CSD as the diameter at the intercepts at the 10%, 50% and 90% of cumulative volume curve.

Firstly, a particle size distribution was carried out for three samples (case A, case B and case Ds) in order to compare the particle size with the one obtained by Magnifin H10. In *Figure 7.5*, the particle size distribution of the three samples (case A, case B and case Ds) and Magnifin H10 are reported.

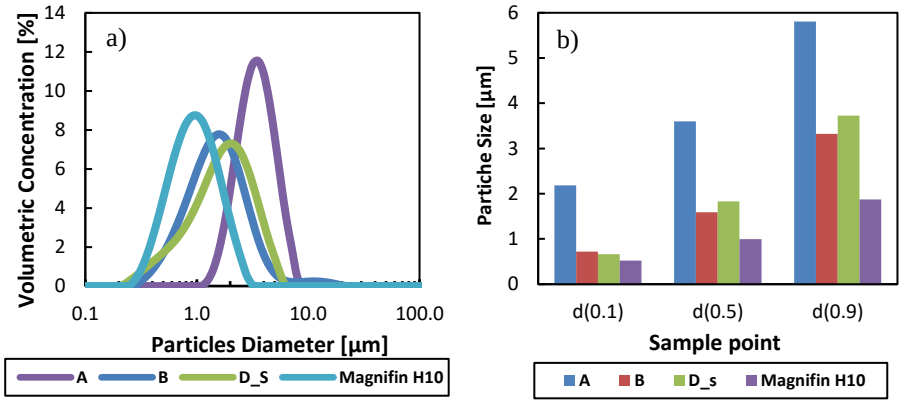

Figure 7.5. Comparison of particle size distribution between the test A, B D_S and the flame retardant reference (Magnifing H10).

With reference at the *Figure 7.5*, the particle size distribution obtained in the tests B and D_S are slightly different from the one of the flame retardant benchmark (Magnifin H10). Thus, results highlight that the produced magnesium hydroxide in tests B and D_S could be suitable for the flame retardant market. At the contrary, the magnesium hydroxide obtained in test A is formed by crystal with larger dimension than ones obtained in tests B, D_S and Magnifin H10. These preliminary results suggest that using the lowest molar concentration of NaOH solution (0.5 M) allows obtaining an easily filterable product, but, also, a product, apparently, formed by large crystals.

Thus, at the light of the considerations about the crystal size distribution, a morphological analysis via scanning electron microscope (SEM) was carried out in order to see the structure of the three samples (case A, case B and case Ds) and compare them with the morphology of the Magnifin H10. Images of three samples and Magnifin H10 at different magnifications are shown in *Figure 7.6*.

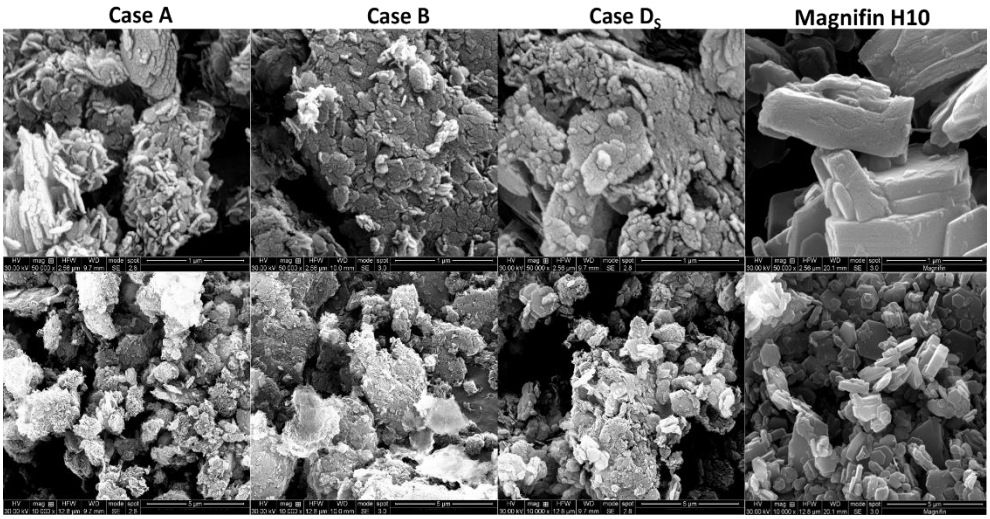

Figure 7.6.SEM images at different magnifications (10000X and 50000X) of the three samples of magnesium hydroxide (Case A, Case B and Case D_S) and Magnifin H10.

It is clear from *Figure 7.6* that the magnesium hydroxide produced during the test Ds is formed by agglomerates of very small crystals (less than 100 nm), which form themselves and agglomerate around the seeds of Magnifin H10. Indeed, the magnesium hydroxide obtained from the tests A and B is also formed by agglomerates of small crystals, which are larger than case D_S because the operative conditions improve the growth respect the nucleation, although the nucleation remains the dominant phenomena. Whereas, the Magnifin H10 is formed by single crystal with dimension about 1-5 µm, about 10-50 times larger than the size crystals produced with the MF-PFR. Moreover, the SEM pictures of the produced crystals explain because the specific filtration time increases at the increase of the NaOH molar concentration solution. In addition, in order to produce a magnesium hydroxide product suitable for the use of flame retardant, some researcher proposed the use of thermal process, such as hydrothermal treatment, that exploiting temperature, pressure and different promoter (*e.g.* NaOH solution, Triethanolamine, Diethanolamine, etc..) in order to modify the morphology and the crystal size distribution [115,116].

7.4.3 Conclusion

According to these tests, potential and limitation have been highlighted, indicating two different concentration of sodium hydroxide, i.e. 0.5M and 1M, allowed obtaining a filterable magnesium hydroxide. Moreover, the alkaline concentration equal to 0.5M is suitable for the magnesium precipitation by means of a fractionated crystallization because it allows to accurate control the reaction pH. While the alkaline concentration equal to 1M is suitable for the magnesium precipitation from brine without calcium, such as brines of saltworks, allowing achieving a higher pH and obtaining a complete recovery of magnesium. Thus, an alkaline solution equal to 1M was used for the second experimental campaign, while 0.5M for the third and fourth experimental campaign.

SEM pictures showed that the precipitate magnesium hydroxide shape is spherical, like cauliflower, formed by the agglomeration of nanoparticles not matching the shape of Magnifin H10.

7.5 Results and discussion of the second experimental campaign to precipitate $Mg(OH)_2(s)$

The second experimental campaign was carried out using two different concentration of magnesium in the inlet brine, analysing the stability and robustness of the pilot in terms of inlet flow rates, reaction pH and system's performance parameters. Each test was performed twice. The brine was prepared diluting the waste brine (WB) from the real Trapani's saltworks (composition reported in *Table 7.5*), while the alkaline solution was made dissolving micro-pellet of NaOH (Inovyn, high grade purity 99%) into the deionized water.

Mean anions composition of the brine, alkaline composition and volume of the solution are reported in *Table 7.5*.

Table 7.5. Main composition of brine and alkaline solution

	Brine							Alkaline solution	
Test	Composition [g/l]						Volume [l]	Composition [mol/l]	Volume [l]
	Na^+	K^+	Mg^{2+}	Cl^-	SO_4^{2-}	Br^-		NaOH	
WB*	48.1	12.7	50.4	179.0	64.5	2.0	-	-	-
A	8.6	2.6	9.6	34.3	12.4	0.9	750	1	500
B	23.5	6.1	24.5	87.2	31.4	0.4	200		250

** waste brine from real Trapani's saltworks*

7.5.1 Analysis of the system stability in terms of reaction pH and flow rates.

Firstly, the reactor was tested in order to analyse the stability. During the experiment, relevant operative conditions, *i.e.* brine and alkaline flow-rates and reaction pH, were recorded by means of the *software LabVIEW* in order to assess the behaviour of the pilot at different magnesium concentration.

Operative parameters set are reported in *Figure 7.7-a* for the tests A1 and in *Figure 7.7-b* for the test B1.

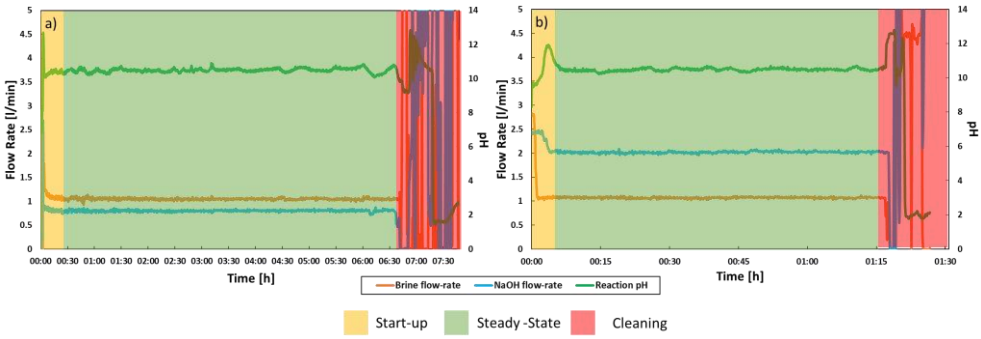

Figure 7.7. Variation of the outlet pH and both inlet flow rates vs the experimental time. a) Test A, and b) Test B.

With referring to *Figure 7.7*, both flow rates are stable, which highlights the stability of the MF-PFR once the steady-state condition was reached, while the pH was almost stable. The reaction pH is strongly affected by the variation of both flow rates. In fact, small variations of one of two flow rates caused a noticeable fluctuation in the reaction pH. The steady-state condition of both flow rates and the reaction pH throughout the experimental test may be subjected to change as a result of the variation of one or more of key operating parameters. One of these is the pressure drop. The variation of the pressure drops can be due to the obstruction of the holes present in the internal pipe of the MF-PFR, caused by the fouling formation of the magnesium hydroxide. In fact, the MF-PFR was stable during the experimental tests demonstrating that an increase of the concentration of the magnesium in the feed brine from 9 g/l (case A) up to 25 g/l (case B) did not cause obstruction of the holes, highlighting the flexibility of the MF-PFR to process brines with a wide range of magnesium

concentration. Moreover, the pressure drop variation could lead to the reduction/increase of both flow rates, i.e. the brine and the alkaline, causing the variation of the outlet pH, which in turn changes the recovery. Another cause is the variation of the level inside the feeding tanks because the flow rates generated by the two feeding pumps are affected by the variation of liquid height. Thus, in order to avoid the instability caused by the variation of the brine level, two control valves were properly adjusted in order to keep constant both flow rates.
Operative conditions of both experimental tests for the recovery of $Mg(OH)_2(s)$ is listed in *Table 7.6*.

Table 7.6.Operative condition for the $Mg(OH)_2(s)$ recovery.

Tests	Operative Condition of system			
	pH	Brine Flow Rate [l/min]	NaOH Flow Rate [l/min]	Worked Hours [h]
A1 A2	10.5	1	0.8	8
B1 B2	10.5	1.1	2	1.5

7.5.2 Performance of the $Mg(OH)_2(s)$ recovery.

To evaluate the quality of the recovered crystals, samples were analysed, following the procedure above reported, in order to evaluate the above defined performance parameters.
In *Figure 7.8*, the purity, conversion, magma density and magnesium concentration in the feed brine are reported.

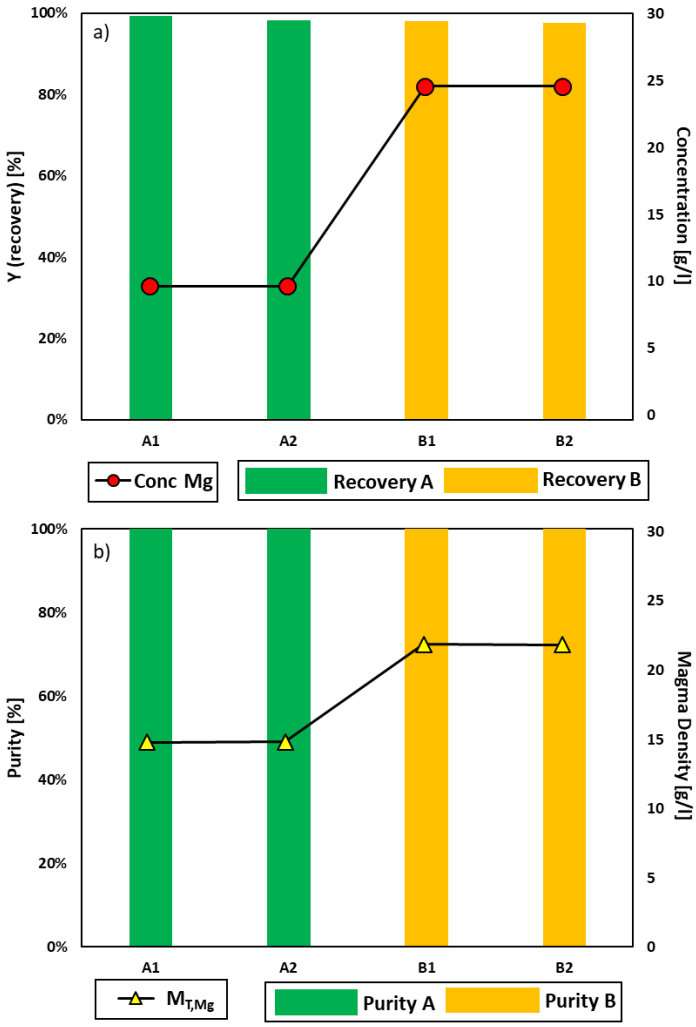

Figure 7.8.Purity of the $Mg(OH)_2$(s) produced, concentration of magnesium (black line with red marker) in the feed brine, conversion in magnesium hydroxide and magma density (black line with yellow marker

Regarding the purity of the produced $Mg(OH)_2$(s), the IC analyses highlighted that only Mg is present in the $Mg(OH)_2$(s) samples, obtaining a purity of 100%. Similar results were achieved in works of by Cipollina et al [86,102]. As regards the recovery of the $Mg(OH)_2$(s), the IC analysis of the inlet brine and the clarified solution allowed computing the recovery, which is about 98% for both tests. As expected, the magma density of the produced slurry

increases from case A to case B, due to the increase of the inlet concentration of magnesium compound.

Afterwards, the collected samples were analysed with the laser granulometer. The particle size of both tests are reported in *Figure 7.9*.

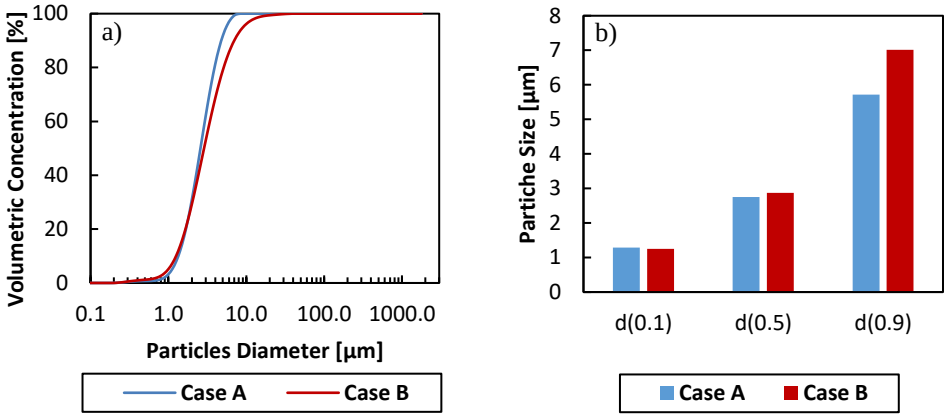

Figure 7.9. Comparison of particle size for case A and case B, a) cumulative size distribution and b) d values for $Mg(OH)_2(s)$

Clearly shown in *Figure 7.9*, d10 for both tests is quite similar, however, the amount of crystals with dimension below 1 µm is higher for test B than test A. This is due to the higher supersaturation reached by test B than test A causing a high nucleation rate and then a high formation of tiny crystals. At the contrary, the larger crystals were obtained, also in this case, for test B. In fact, the high supersaturation causes high agglomeration rate and then, the formation of large particles.

7.6 Results and discussion of the third experimental campaign for the recovery of $Mg(OH)_2(s)$ and $Ca(OH)_2(s)$

In the third experimental campaign, three different experiments were performed using three different concentration of the inlet brine. Brines solution were prepared in order to mimic the retentate produced by NF, which was fed by three different spent brines in terms of total dissolved solids (TDS). Brine solutions were prepared dissolving the following salts: $NaHCO_3$ (Natural products, purity 99%), $CaCl_22(H_2O)$ (Ciech, purity 99%), Na_2SO_4 (Fluka, purity 99%), $MgCl_26(H_2O)$ (purity 99%) and KCl (Honeywell Fluka, purity 99%), while the alkaline solution was made dissolving micro-pellet of NaOH (Inovyn, high grade purity 99%) into the deionized water.

Mean compositions of the three brines and alkaline solution are reported *Table 7.7*.

Table 7.7.Main composition of inlet brine and alkaline solution

	Inlet Brine								Alkaline solution			
	Composition [g/l]							Volume [l]	Composition [mol/l]		Volume [l]	
Test	Na^+	K^+	Mg^{2+}	Ca^{2+}	Cl^-	SO_4^{2-}	HCO_3^-		Mg Step NaOH	Ca Step NaOH	Mg Step	Ca Step
A	9.67	0.55	1.87	14.77	46.75	0.16	0.43					
B	8.96	0.54	1.74	13.39	42.71	0.43	0.11	200	0.5	2	200	
C	10.74	0.73	2.44	16.84	53.70	0.65	0.17					

7.6.1 Analysis of system stability in terms of reaction pH and flow rates.

Firstly, also in this case, the stability of MF-PFR was tested.

For the sake of brevity, the trend of the operative condition for test B are reported in *Figure 7.10-a* for the precipitation of magnesium hydroxide and in *Figure 7.10-b* for the precipitation of the calcium hydroxide.

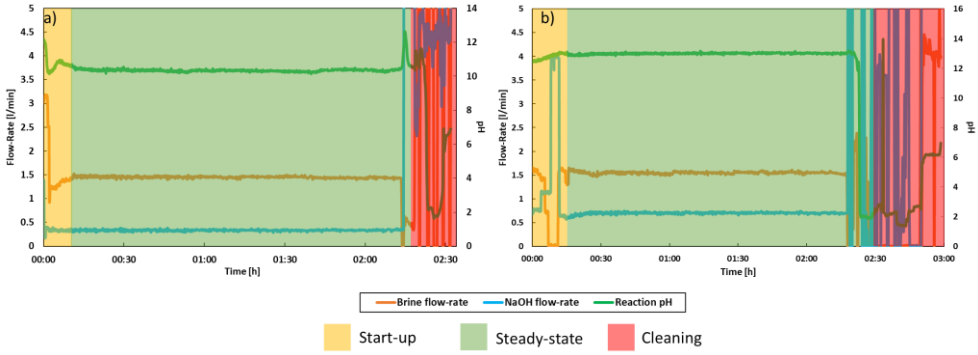

Figure 7.10.Variation of the outlet pH and both inlet flow rates over the experimental time. a) Precipitation of the magnesium hydroxide, and b) precipitation of the calcium hydroxide

As shown in *Figure 7.10*, the reaction pH and both flow rates are stable when the MF-PFR reached the steady-state condition. The stability of both flow rates and pH throughout the experiment may be subjected to change as a result of the variation of some operating parameters. One of these is the pressure drop. As said in the previously, a variation of pressure drop could lead to the reduction/increase of the flow rate. As an example, the variation of the NaOH solution flow-rate may lead to an increase of the reaction pH, causing the precipitation of the calcium as calcium hydroxide affecting the purity of the recovered magnesium hydroxide. On overall, the fine control of the reaction pH allowed recovery of magnesium and calcium as hydroxides by means of fractionated precipitation.

Operative conditions of each experiment for the recovery of $Mg(OH)_2(s)$ and the $Ca(OH)_2(s)$ are reported in *Table 7.8* and *Table 7.9* ,respectively.

Table 7.8.Operative condition for the $Mg(OH)_2$(s) recovery

Tests	Operative Condition of system			
	pH	Brine Flow Rate [l/min]	NaOH Flow Rate [l/min]	Worked Hours [h]
A	10.3	1.71	0.44	2.0
B	10.35	1.46	0.33	2.5
C	10.4	1.0	0.38	3.5

Table 7.9.Operative condition for the $Ca(OH)_2$(s) recovery

Tests	Operative Condition of system			
	pH	Brine Flow Rate [l/min]	NaOH Flow Rate [l/min]	Worked Hours [h]
A	13.0	1.62	0.78	2
B	13.0	1.57	0.7	3
C	13.0	1.05	0.6	3.5

7.6.2 Performance of the reactive precipitation processes

To evaluate the quality of the recovered crystals, *i.e.* $Mg(OH)_2$(s) and $Ca(OH)_2$(s), the samples were analysed, following the analytical procedure above reported, to evaluate the reaction performance parameters.

7.6.2.1 Magnesium hydroxide precipitation step

In *Figure 7.11*, the purity, conversion are reported, supported by magma density and magnesium/calcium concentration in the inlet brines.

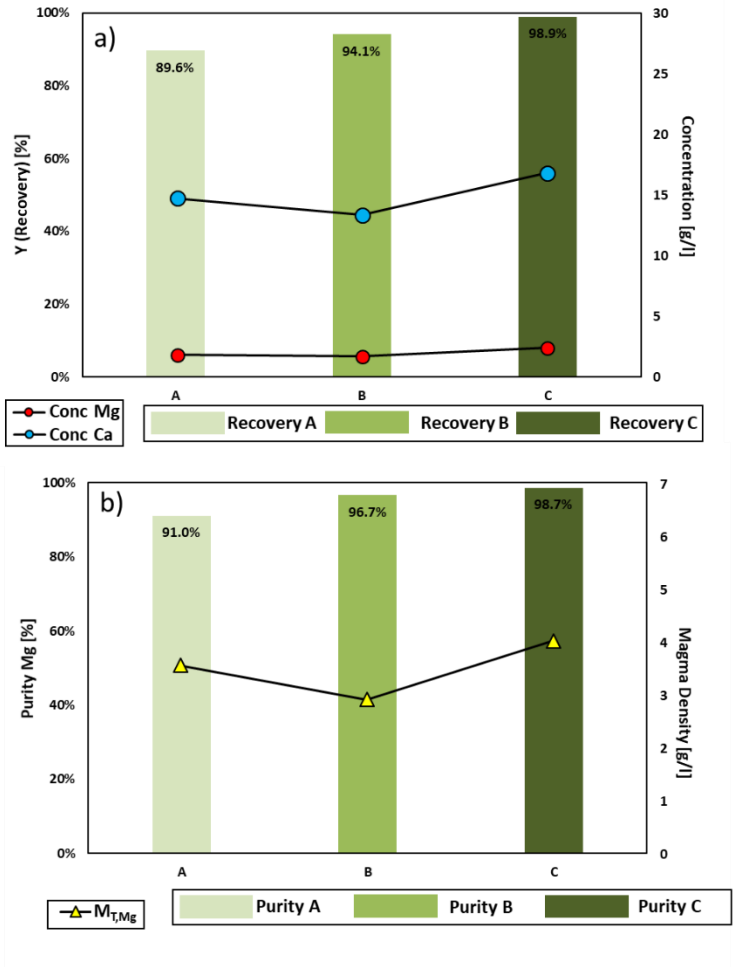

Figure 7.11. a) Mg recovery efficiency, b) Purity of $Mg(OH)_2(s)$ solids for all precipitation tests, accompanied by magnesium and calcium concentration in the feed brine; and magma density.

Regarding the purity of the produced magnesium hydroxide (see *Figure 7.11*) , the IC analyses highlighted that only Mg and Ca is present in the $Mg(OH)_2(s)$ precipitate, although the pH was kept below the 10.5 to avoid the precipitation of the calcium as calcium hydroxide. Nevertheless, the calcium affected the purity of produced crystals. The purity increases from the 91% (test A) up to 98.7% (test B). The precipitation of calcium in form of calcium carbonate during the reactive precipitation step of magnesium hydroxide was due to

the presence of the bicarbonate (HCO_3^-) in the feed brines. With reference to the bicarbonate ions, they are involved in chemical equilibrium reactions [117], as in Eq. 7.4-7.7:

$$CO_{2(g)} \Leftrightarrow CO_{2(l)} \quad (7.4)$$

$$CO_{2(l)} + H_2O \Leftrightarrow H_2CO_3 \quad (7.5)$$

$$H_2CO_3 \Leftrightarrow HCO_3^- + H^+ \quad (7.6)$$

$$HCO_3^- \Leftrightarrow CO_3^{2-} + H^+ \quad (7.7)$$

When the pH increased up to about 10.4, all chemical equilibriums were shifted in order to convert CO_2 dissolved and bicarbonate ions into carbonates, which were the form more stable in the brine.

In order to better understand the presence of the $CaCO_3$ in the precipitated Mg(OH)2(s), and taking into account all chemical equilibriums involved during the precipitation, a numerical simulation has been carried out via the MEDUSA software [118], along with the hydro-chemical equilibrium-constant database (HYDRA). The main inputs required by the software are: (i) concentration of the cations and anions in the brine and (ii) temperature at which the magnesium precipitation occurs.

Figure 7.12 shows the results of the simulation carried out with the Medusa software for the case B.

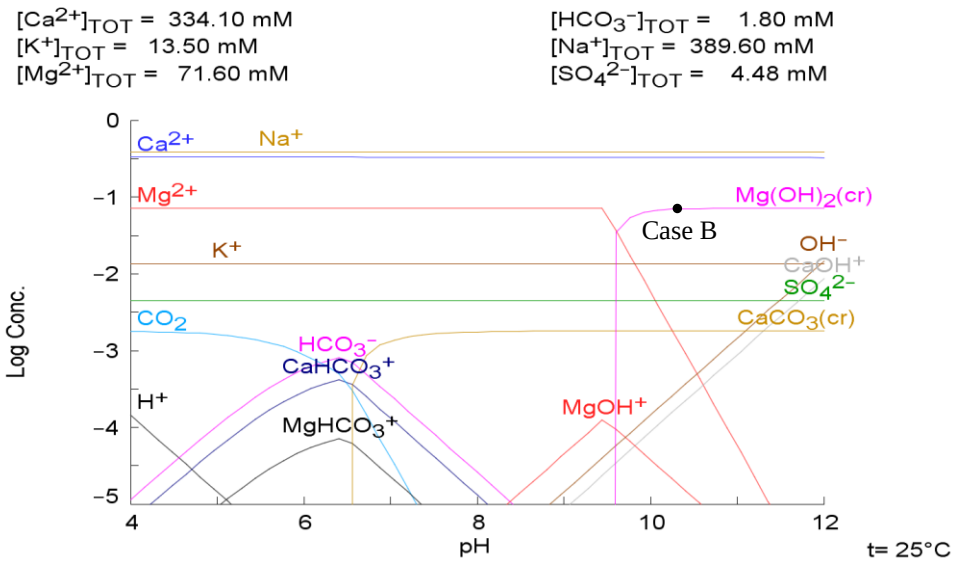

Figure 7.12.pH versus log concentration plot for the case A at 25°C, fixing the $[Na^+]$*=0.389M (8.96 g/l),*$[k^+]$*=0.0135M (0.54 g/l)* $[Mg^{2+}]$*=0.072M (1.74 g/l),* $[Ca^{2+}]$*=0.334M (13.39g/l),* $[HCO_3^-]$*= 0.0018M (0.110 g/l) and* $[SO_4^{2-}]$*=0.00448 (0.43g/l).*

As seen in *Figure 7.12*, the Medusa software predicts the precipitation of the magnesium, which starts at pH 9.5 and ends around pH 11. This latter value is higher than one measured during the laboratory precipitation test (final pH of total magnesium recovery equal to 10.4 *Figure 6.1*), due to the complexity of the brine composition could affect the solubility of magnesium hydroxide. Moreover, the software predicts the co-precipitation of the calcium in form of calcium carbonate.

As shown in *Figure 7.12*, the pH value of the tested brines, case B, was equal to 10.35. It is worth noting that the Medusa software predicted the variation of the amount of precipitated magnesium as a function of the pH. In fact, the recovery predicted by the software was 97.7% with a purity equal to 96.0%, while the experimental one was 94.1% and 96.7% respectively. Moreover, the results of XRD analysis, shown in *Figure 8.7*, highlighted that the recovered magnesium hydroxide, which refers to the tests run in the Netherlands, was precipitated as magnesium hydroxide (*Brucite*), while the calcium was precipitated as calcium carbonate. The $CaCO_3$(s) precipitated as *Calcite* (deduced by the XRD results shown in *Figure 8.7*) because it was the crystalline phase more stable at the operative condition of the MF-PFR, i.e. 25°C (room temperature of brine and alkaline solution during the spring in Palermo) and reaction pH equal to about 10.3 [119].

It is worth noting that the purity of the precipitate $Mg(OH)_2(s)$ depends on the amount of the recovered magnesium, as well as the bicarbonate concentration in the inlet brine. Indeed, looking at the tests A and B, which have similar magnesium concentration. The purity of the produced $Mg(OH)_2(s)$ increases from 91% (test A), up to 97% (test B), due to the reduction of the bicarbonate concentration along with the increase of the magnesium recover.
As regards the recovery of the magnesium, it ranged from about 90% (test A) up to almost 90% (test C) implying partial recovery.
As said previously, the recovery of the magnesium is affected by the value of the pH. Indeed, the lower recovery is obtained due to the outlet pH equal to 10.3, while the higher value of the recovery is obtained at pH equal to 10.4.

7.6.2.2 Calcium hydroxide precipitation step

After the first precipitation step, the produced slurry was stored in the tank *T4* in order to settle the precipitated crystals. After that, the crystals were sent to tank *T5* ready for the filtration, while the clarified brine was collect in the Ca tank, *T9*, and then re-sent into the feed tank, *T1*, in order to re-feed the brine into the MF-PFR for the calcium recovery.
In *Figure 7.13*, the purity, conversion of magnesium and calcium are reported, supported by magnesium and calcium concentration in the feed brine and magma density of the calcium hydroxide for the second precipitation step.

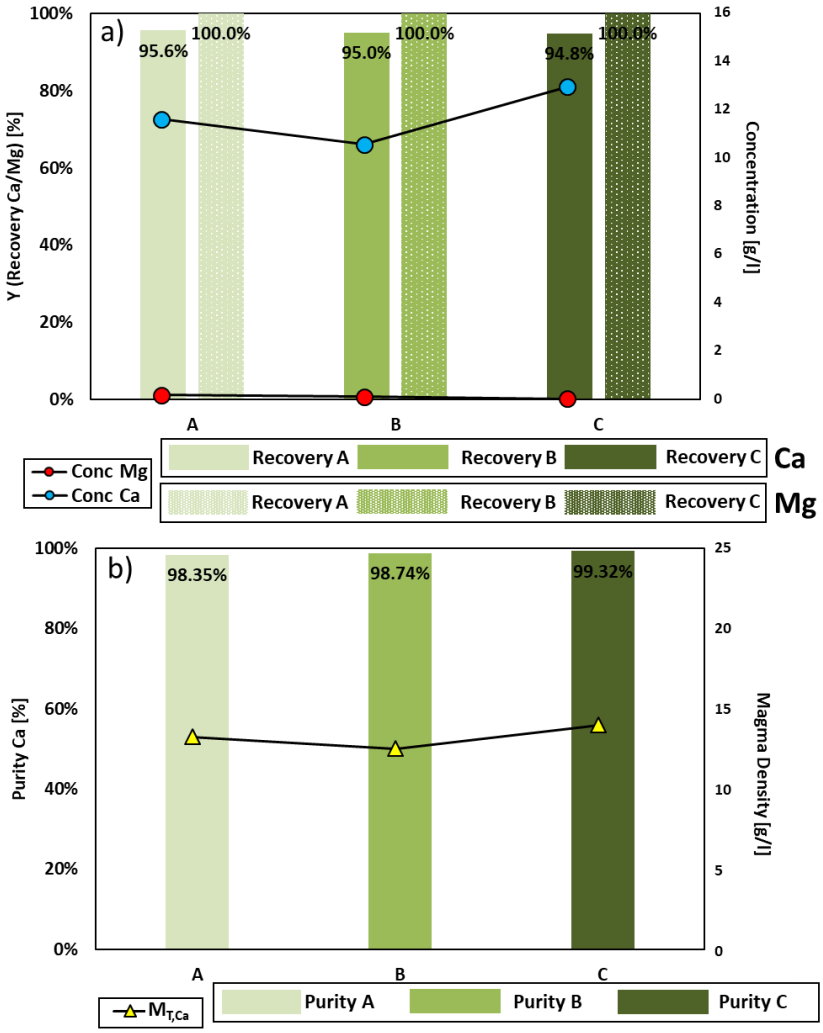

Figure 7.13. a) Ca and Mg recovery efficiency, b) Purity of $Ca(OH)_2$(s) solids, accompanied by magnesium and calcium concentration in the feed brine; and magma density.

The purity of the produced $Ca(OH)_2$(s) was determined by the same procedure described above. The IC analyses highlighted that only Mg and Ca are present in the $Ca(OH)_2$(s) precipitate. As reported, the purity of the $Ca(OH)_2$(s) increases from about 98%, (test A), up to almost 99% (test C) because the magnesium concentration in the interstage brine decreases from 155 mg/l (test A) down to about 2 mg/l (test C).

As regards the recovery of the calcium, it ranged from about 96% (test A) down to 95% (test C). Nevertheless, the outlet pH was kept equal to 13, which allows the complete precipitation of the calcium according to the precipitation path shown in *Figure 6.1*. However, tested brines required a reaction pH higher than 13 due to the high calcium concentration in the inlet brine. Moreover, the recovery of the magnesium was equal to 100% in all tests.

7.7 Results and discussion of the fourth experimental campaign for the recovery of $Mg(OH)_2$(s) and $Ca(OH)_2$(s)

Following the analysing the purity of magnesium hydroxide obtained within the third experimental campaign, the obtained results highlighted the needed of a pre-treatment step in order to minimize/avoid the precipitation of the calcium as calcium carbonate during the magnesium precipitation step. For this reason, a fourth experimental campaign was carried out in order to assess the possibility to recover magnesium hydroxide and calcium at high purity. Thus, a fourth experimental campaign was carried out using a brine with a composition quite similar to the composition of the brines reported in *Table 7.7*.
Mean composition of tested brines and alkaline solution are reported in *Table 7.10*.

Table 7.10. Mean composition of inlet brine and alkaline solution.

	Inlet Brine								Alkaline solution			
	Composition [g/l]							Volume [lt]	Composition [mol/l]		Volume [lt]	
Test	Na^+	K^+	Mg^{2+}	Ca^{2+}	Cl^-	SO_4^{2-}	HCO_3^-		Mg Step NaOH	Ca Step NaOH	Mg Step	Ca Step
A	9.59	0.93	1.80	15.25	47.64	0.16	0.43					
B	9.38	0.75	1.78	13.83	44.53	0.43	0.11	200	0.5	2	200	
C	11.20	0.92	2.41	17.15	55.05	0.17	0.65					

7.7.1 Pre-treatment section of the inlet-brine.

The pre-treatment step of the inlet brine consists of removing the bicarbonate ions. Exploiting the chemical equilibrium reactions involved in the brine solution (Eq 7.4 – 7.7), the pre-treatment step consists of the following:

1. Acidification of the inlet brine in order to shift the chemical equilibrium reactions towards the formation of carbon dioxide ($CO_{2(l)}$), as shown in *Figure 7.14.*
2. Removing carbon dioxide through a stripping process.

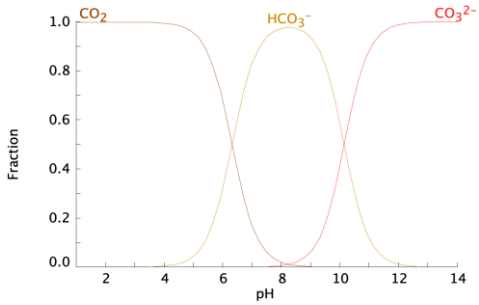

Figure 7.14. The distribution of carbonate species as function of solution pH obtained via MEDUSA numerical code [118].

Thus, the pre-treatment step of the inlet brine consists of two main sections: (i) *acidification section*, where an acid solution is added in the brine in order to convert bicarbonate/carbonate ions into carbon dioxide and (ii) *removal section*, where the brine is de-gassed by means of a stripping process. The process scheme of the pre-treatment step is reported in *Figure 7.15*.

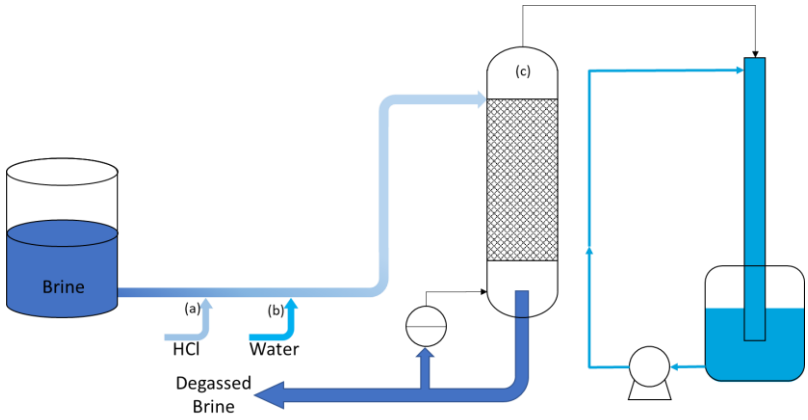

Figure 7.15.Process scheme of the pre-treatment section.

The pre-treatment step can be described as follow:

(a) Acidification. The inlet brine is mixed with a 1M of hydrochloric acid solution. The amount of the acid is equal to the moles of bicarbonate/carbonate in the inlet brine plus a small excess in order to reach a final pH value less than 4.

(b) Water Rebalance. Before entering in the stripping column, a small amount of water is added in order to restore the water content in the brine due to the water losses in the stripping column.

(c) Stripping section. Following the water rebalancing, the brine is preheated and feed in the top of the stripping column, where it is distributed over the packing material and put in contact with the rising vapour. The stripping vapour is produced in the reboiler, which is in the bottom of the column, vaporizing of a part of the brine. The enthalpy and mass exchange between the liquid and vapour promoting the stripping of the carbon dioxide, and, then, reducing its concentration in the brine.

The degassed brine, exiting from the bottom of the column, is cooled down to 25°C and stored in the tank, *T1*, ready for feeding into the MF-PFR.

The vapour is extracted from the top of the column through a barometric condenser. The barometric condenser produces the vacuum in order to operate the column at a temperature lower than 100°C and improve the removing of the carbon dioxide. The barometric condenser is operated by recirculating water from bottom to top of the column.

7.7.1.1 Developing a simulation platform for the pre-treatment step

Firstly, the pre-treatment step was implemented in Aspen Plus® to find amount of acids and water to add and the operative condition of the stripping column. A critical aspect in the implementation in the process simulator is the selection of the thermodynamic package, which describes the interactions between all different species in the brine. As matter of fact, the solution properties of the liquid streams and the behaviour of the column were modelled using the thermodynamic package *E-NRTL-RK* [120].

An model was developed on Aspen Plus® to simulate the behaviour of the packing column by using a rigorous method, namely *Rad Frac*. In addition, in order to take into account the involved chemical reactions and hydrodynamics of the column, as well as the heat and mass transfer occurring the inside the column, a *rate-based* model were chosen for all simulations. The simulations were performed in order to find the amount of acid, water to add and the thermal power required in order to remove at least 90% of the carbon dioxide from the brine. The column was set as in the following. The temperature of the boiling solution was equal to 80°C ($T_{Reboiler}$) and the column operated at a pressure equal to 0.4 bar (P_{column}). While, geometrical features and packing material of vapour stripping column were set equal to lab-scale vapour stripping column (*i.e. Koch-Glitsch® Flexipac 700Y* as packing material, column diameter equal to 50mm and a packing height of 1.8 m).

The Aspen flow sheet of the pre-treatment step is reported in *Figure 7.16*.

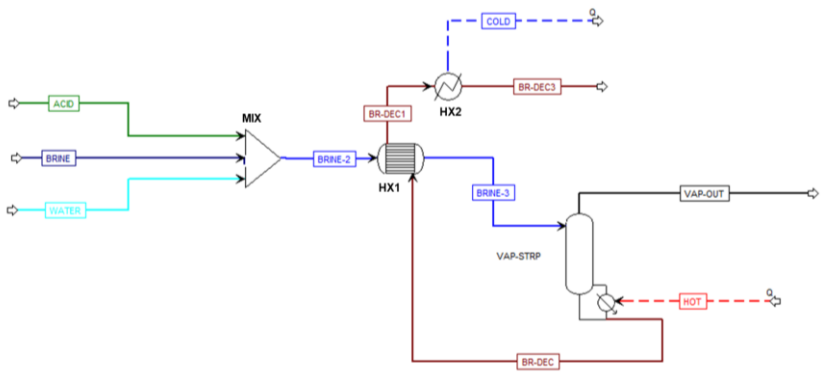

Figure 7.16.Aspen flow-sheet of the pre-treatment section. The flow-sheet consists of: (i)VAP-STRIP, vapour stripping tower, (ii) HX, thermal exchange and (iii) MIX, mixing unit between brine, acid and water.

The results of the simulation are reported in *Table 7.11*.

Table 7.11.Main simulation results and operative condition of the vapour stripping column

Tests	Brine	HCl-Water Solution		Water	Vapour Stripping column			
	Volume [l]	Volume [l]	Concentration [M]	Volume [l]	Flow-rate [l/min]	P_{column} [bar]	$T_{Reboiler}$ [°C]	Thermal duty [W]
A	200	1.5		1.0	1.03	0.4	80	741
B	200	0.46	1	1.0	1.03	0.4	80	652
C	200	0.64		1.35	1.03	0.4	80	840

7.7.1.2 Experimental set-up of pre-treatment step

In *Figure 7.17*, a simplified P&ID diagram of the pre-treatment step is reported.
The brine mixed with the hydrochloric acid solution and water is store in the plastic tank (*T1*) and fed to the top of the vapour stripping column by mean of a gear pump (fluid-o-tech FG204). Thus, the brine was spread over the packing material and it was put in contact with the rising vapour. The degassed brine was withdrawn from the bottom of the column by means of a gear pump (fluid-o-tech FG204), cooled down to 25°C and collected in a plastic tank (*T2*) ready for the precipitation steps.

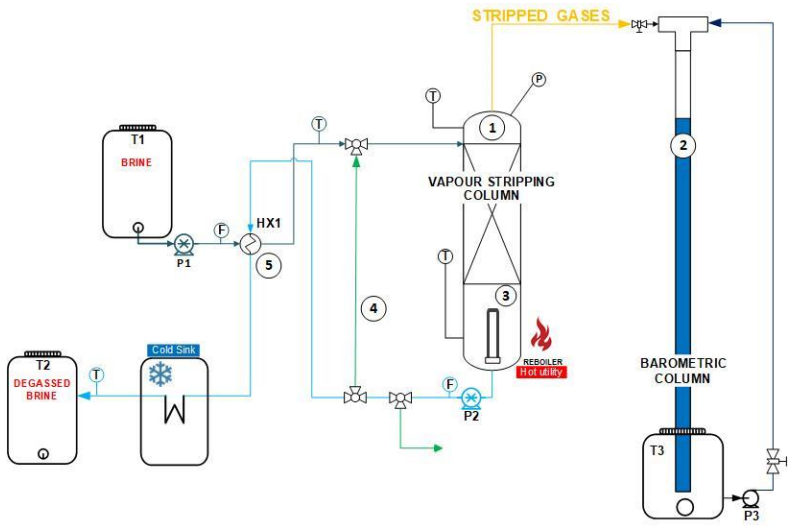

Figure 7.17.Simplified P&ID diagram of pre-treatment step. The main items are: (1) vapour stripping column, (2) barometric column circuit, (3) Reboiler, (4) auxiliary, (5) thermal integration exchange.

The vapour stripping column (1) is a Plexiglas tube of a height of 2m and an internal diameter equal to 50 mm, filled with structured packing material (*Flexipac® 700Y, Koch-Glitsch*). The packing material height is equal to 1.6m. The bottom of the vapour stripping column is connected to a reboiler (3) (ID 100mm), where a part of brine is vaporized in order to produce the stripping vapour. The heat is supplied by an electrical resistance, and it is fixed by regulating the intensity of the electrical current. The temperature of the brine in the reboiler is monitored via a T-type thermocouple.

The pressure and temperature of the column are monitored by an absolute pressure transducer (VEGA - VEGAbar 14) and a T-type thermocouple placed in the top of the column, respectively. The barometric condenser (2) is made up of a 15 m tube (inner diameter of ½") with the bottom end immersed water (*T3*).

The hot gases exiting from the top are sent to the top of the barometric column.

A hair-pin exchanger (5) is used for the thermal integration in order to recover a part of the heat exiting with the degassed brine from the bottom of the column and to pre-heat the feeding brine. The internal tube of the heat exchanger is made up of stainless steel (AISI 316) tube with an internal diameter of 6 mm and thickness 1.5 mm inserted within a Plexiglas tube (ID 12mm, thickness 2mm), with the cold brine flowing in the annular section. Moreover, to

reduce the thermal dissipation of hair-pin exchange, the Plexiglas tube is inserted inside an insulating tube of expanded neoprene.

Moreover, a thermal bath is used as cold seek in order to cool down to 25°C the degassed brine after thermal integration.

During the start-up, an auxiliary circuit (4) is used to recirculate the hot solution form the bottom to the top in order to speed up the heating-up of the packing material.

The specification of the sensors installed in the prototype are listed in *Table 7.12.* Specification of the sensors installed in the prototype..

All sensors in the laboratory pre-treatment system have been electrically connected with chassis NI cDAQ-9189 produced by *National Instrument*. Afterwards, the computer was linked with the chassis by means of software *NI Measurement & Automation Explorer (MAX)*. Eventually, an interface panel has been implemented in the software LabVIEW in order to monitor and control the desiderate parameters of the prototype.

Table 7.12. Specification of the sensors installed in the prototype.

Component	Specification
Pressure transducer	VEGA-14 range: 0-100kPa accuracy: 0.3% FS
Thermocouple	TC direct mineral insulated thermocouple, range:200-400 accuracy: ± 1°C
Multimeters	FLUKE 175 True RMS, range:0.1mV-1000V and 0.01 mA-10A, accuracy: V DC ±(0.15% + 2 counts) A DC ± (.0% + 3 counts).
Data logger for Thermocouples	TC resolution: 0.1°C accuracy:0.1 % of reading
Flowmeters	Riels VMZ 030 DN 3, Range: 0.05-2 l/min accuracy:1% reading
Reboiler level sensors	VEGADIF 65 Range: 0-10 kPa accuracy ±0,065% FS

7.7.1.3 Results of the pre-treatment step

Following the acidification and water rebalancing of the brine, the brine was sent to the top of the vapour stripping column working with the operative conditions listed in *Table 7.13*

Table 7.13.Operative condition of the vapour stripping column.

Test	Vapour Stripping column			
	Flow-rate [l/min]	P_{column} [bar]	$T_{Reboiler}$ [°C]	Thermal duty [W]
A	1.0	0.4	78	1500
B	1.0	0.4	77	1400
C	1.0	0.4	79	1600

During the continuous operation of the vapour stripping column, the flow rate of the degassed brine extracted from the bottom of the column was adjusted in order to control the liquid level inside the reboiler. Moreover, in order to guarantee an operative pressure column equal to 0.4 bar and, then, a bottom temperature of 80°C, it has been needed to supply a thermal power around two times higher than obtained by the simulations because an accurate control of the column pressure was not achievable by means of a needle valve installed along vapour line. After the pre-treatment step, the degassed brine was analysed.
Mean ions concentrations of the degassed brines are listed in *Table 7.14*.

Table 7.14. Mean compositions of degassed brine and removal efficiency of bicarbonate/carbonate ions

Test	Degassed Brine							
	Composition [g/l]							Removal efficiency [%]
	Na^+	K^+	Mg^{2+}	Ca^{2+}	Cl^-	SO_4^{2-}	HCO_3^-	
A	9.59	0.93	1.80	15.25	47.86	0.16	0.05	89
B	9.38	0.75	1.78	13.83	44.56	0.11	0.05	55
C	11.20	0.92	2.41	17.15	55.12	0.65	0.05	71

The brine exiting from the pre-treatment step contains a very low amount of bicarbonate ions. Nevertheless, the thermal power supplied into the reboiler was two times higher than one

predicted by the simulation platform, the ion concentrations don't change respect to the composition of the initial brine (*Table 7.10*).

7.7.2 Analysis of the system stability in terms of reaction pH and flow rates.

Also in this last experimental campaign carried out in BEC, the stability of the MF-PFR performance has been tested.

For the sake of brevity, the trend of the operative condition for the test B is reported in *Figure 7.18-a* for the precipitation of magnesium and in *Figure 7.18-b* for the precipitation of the calcium.

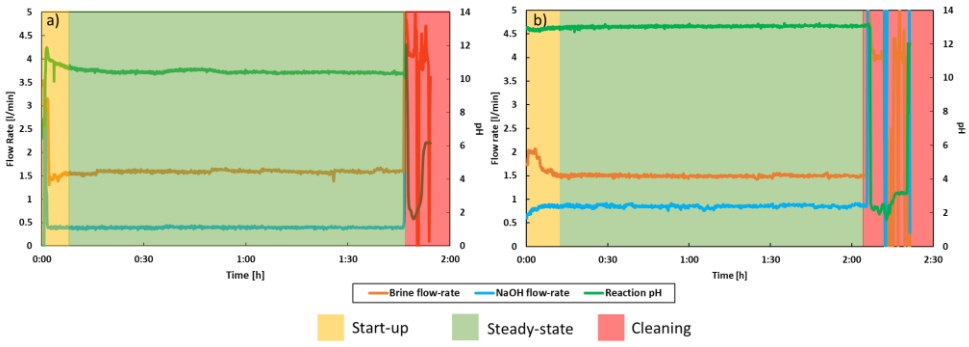

Figure 7.18.Variation of the outlet pH and both inlet flow rates over the experimental time. a) Precipitation of the magnesium hydroxide, and b) precipitation of the calcium hydroxide

As shown in *Figure 7.18*, also in this experimental campaign, the MF-PFR is very stable, *i.e.* both flow rates and reaction pH are almost stable, once reached the stationary condition.

The operative conditions of each experiment for the recovery of $Mg(OH)_2(s)$ and the $Ca(OH)_2(s)$ are reported in *Table 7.15* and *Table 7.16* ,respectively.

Table 7.15.Operative condition for the $Mg(OH)_2(s)$ recovery

Tests	Operative Condition of system			
	pH	Brine Flow Rate [l/min]	NaOH Flow Rate [l/min]	Worked Hours [h]
A	10.45	1.4	0.35	2
B	10.4	1.6	0.4	1.9
C	10.5	1.3	0.46	2.5

Table 7.16.Operative condition for the $Ca(OH)_2(s)$ recovery

Tests	Operative Condition of system			
	pH	Brine Flow Rate [l/min]	NaOH Flow Rate [l/min]	Worked Hours [h]
A	13.00	1.28	0.68	2
B	13.00	1.5	0.86	2.3
C	13.00	1.6	0.80	2

7.7.3 Performance of the Recovery

To evaluate the quality of the recovered crystals, *i.e*. $Mg(OH)_2(s)$ and $Ca(OH)_2(s)$, the samples were analysed, following the analytical procedure above reported, to evaluate the reaction performances parameters.

7.7.3.1 Magnesium hydroxide precipitation step

In *Figure 7.19*, the purity, conversion are reported, supported by magma density and magnesium/calcium concentration in each inlet brine.

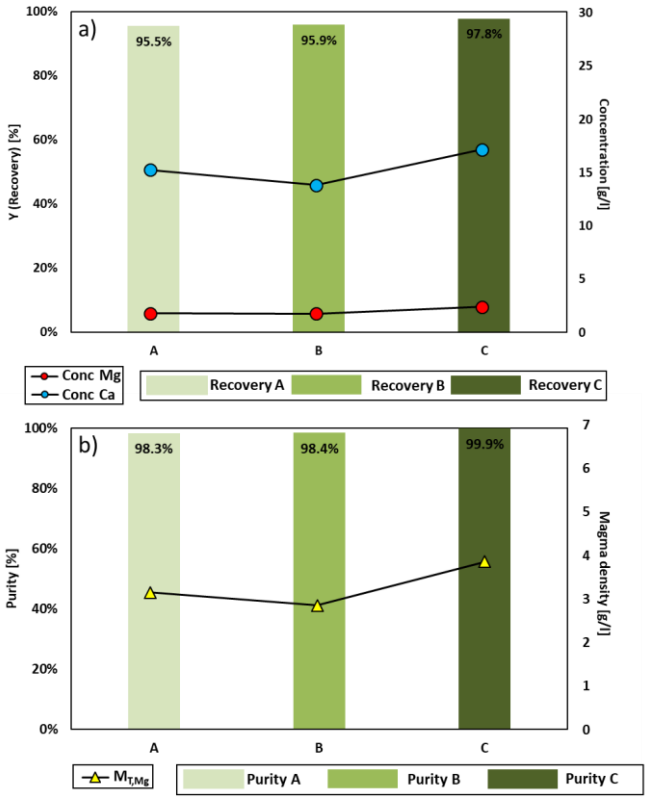

Figure 7.19. a) Mg recovery efficiency, b) Purity of $Mg(OH)_2$(s) solids for all precipitation tests, accompanied by magnesium and calcium concentration in the feed brine; and magma density.

Also in this case, the IC analyses highlighted that only Mg and Ca are present in the $Mg(OH)_2$(s) precipitate. Nevertheless the presence of the calcium in the precipitated magnesium hydroxide, the purity of the recovered magnesium hydroxide crystals increase from about 98% (test A) up to almost 100% (test C). These results highlight that the pre-treatment step allows achieving a magnesium hydroxide product at high purity. In fact, comparing these results with the one obtained in the third experimental campaign, the purity for test A increases from about 91% up to 98%, while for the highest one, test C, the purity increases from 99% up to almost 100%. Furthermore, the pre-treatment step allows operating a reaction pH value higher than one achieved in the third experimental campaign, thus obtaining a recovery of magnesium larger than one obtained during the previous experiment.

In *Figure 7.20*, a comparison of the magma density obtained in the third and fourth experimental campaign is reported.

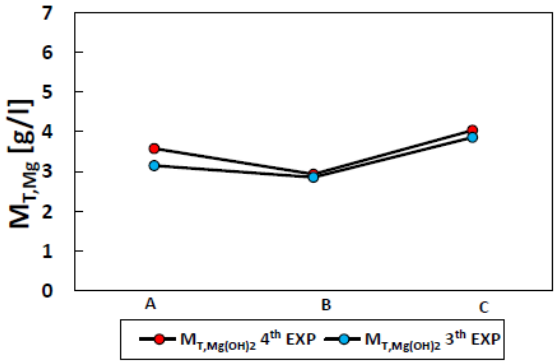

Figure 7.20. Comparison of the magma density obtained in the third (black line and red marker) and fourth (black line and sky-blue marker) experimental campaign.

As shown in *Figure 7.20*, the magma density obtained in the fourth experimental campaign is lower than one obtained in the third experimental although the recovery reached in the 4th experimental campaign was higher than the 3th one. This is due to two aspects: (i) lower content of calcium carbonate and (ii) the calcium carbonate have a molecular weight higher than one of magnesium hydroxide.

Moreover, a further comparison of the 4th experimental campaign with the 3th one was performed through the crystal size distribution shown in *Figure 7.21*.

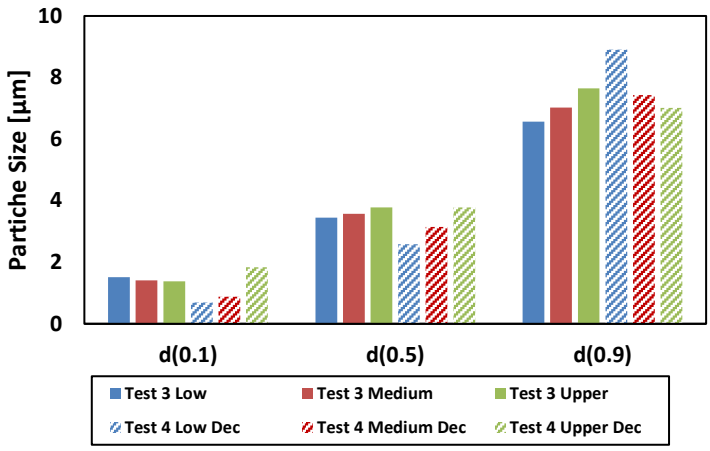

Figure 7.21. Comparison of d10, d50 and d90 between the 3th test and 4th test.

As shown in *Figure 7.21*, the pre-treatment step for the removal of carbonates/ bicarbonates, allowed to obtain crystals with a d90 higher than in test 3, as well as to allow an increase in purity and recovery. This could be caused due to the higher tendency of crystals of magnesium hydroxide to agglomerate in the absence of those of calcium carbonate. At the contrary, the d10 and d50 is higher in test 4 than in test 3. This is probably due to fact that the dimension of the particle is given by the dimension of calcium carbonate crystals which allow obtaining larger particle size than one obtained from particles formed by only hydroxide magnesium.

7.7.3.2 Calcium hydroxide precipitation step

After the first precipitation step, the produced slurry was stored in the tank *T4* in order to settle the precipitated crystals. After that, the crystals were sent to tank *T5* ready for the filtration, while the clarified brine was collected in the tank *T9*, and, then, re-sent into the feed tank, *T1*, in order to re-feed the brine into the MF-PFR for the calcium recovery.
In *Figure 7.22*, the purity, conversion of magnesium and calcium are reported, supported by magnesium and calcium concentration in the feed brine and magma density of the magnesium precipitation step.

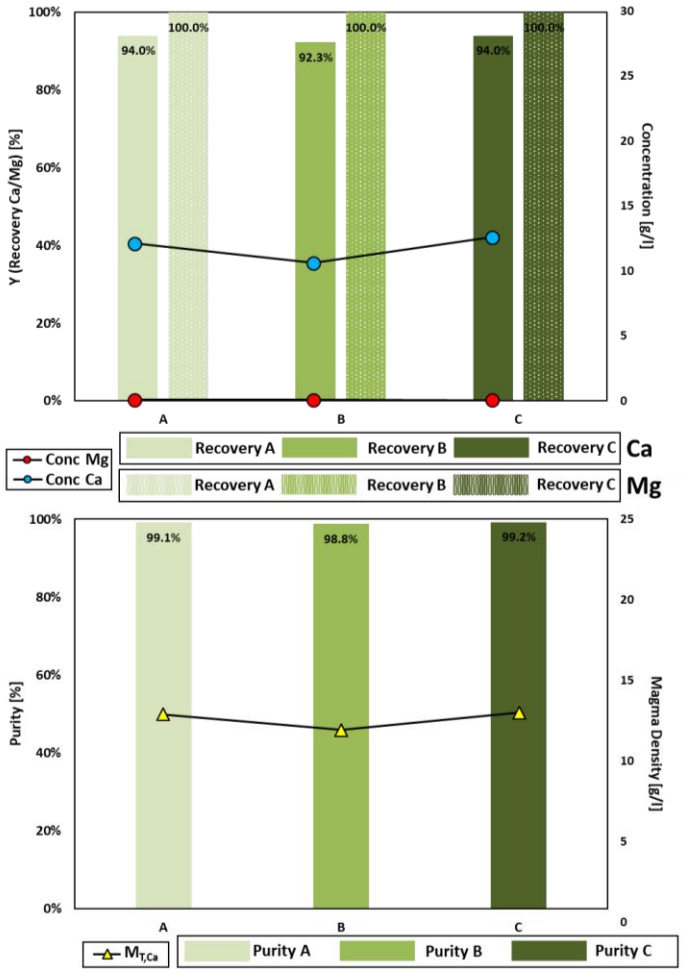

Figure 7.22. a) Ca and Mg recovery efficiency, b) Purity of $Ca(OH)_2$(s) solids, accompanied by magnesium/calcium concentration in the feed brine; and magma density.

As shown in *Figure 7.22*, the IC analyses highlighted that only Mg and Ca are again present in the $Ca(OH)_2$(s) precipitate. As reported, the purity of the $Ca(OH)_2$(s) is around 99% for all tested brine tanks to the high recovery of magnesium in the first precipitation step. As regards the recovery of the calcium, it increases from 92% (test B) up to 94% (tests A and C). Nevertheless, the outlet pH was kept around 13, which should allow a complete precipitation of calcium according to the precipitation path shown in *Figure 6.1*, the tested brine had to be led to a pH value higher than 13 due to the high calcium concentration in the inlet brine. At the contrary, the recovery of the magnesium was equal to 100% in all tested brines.

8. MF-PFR, Pilot testing in Plant One, The Netherlands

Chapter Outline

Part of this chapter has been published in:

F. Vassallo, D. La Corte, N. Cancilla, A. Tamburini, M. Bevacqua, A. Cipollina, G. Micale, « A pilot-plant for the selective recovery of magnesium and calcium from industrial waste brines», submitted to Desalination.

8.1. Introduction

As reported in sub-chapter 5.4, the MF-PFR is the core of a treatment chain for the regeneration of spent brine produced by regeneration of IEXs removing divalent ions (Mg^{2+} and Ca^{2+}) in the form of hydroxide. In fact, one of the main goals of the European project ZeroBrine is the real implementation of a treatment chain for the regeneration of spent brine in a real industrial contest (Plant One, port of Rottherdam, The Netherland) for the regeneration of spent brine produced by Evides Industriewater B.V., in Rotterdam (The Netherlands) based on the circular approach.

As matter of fact, the MF-PFR was shipped in Plant One B.V. (Rotterdam, The Netherlands) and, then, installed within a treatment chain along with the other involved units, i.e. nanofiltration and multi-effect distillation. After the installation of all units that required almost one month, the spent brine produced by the regeneration of IEXs was fed to the treatment chain for its regeneration. A wide experimental campaign was carried out using three different real industrial spent brines taken at different moments of ion exchange resins regeneration. The experimental campaign was performed for almost 5 months.

The aim of this experimental campaign is to assess the possibility to regenerate the industrial spent brine producing high purity (more than 90%) of precipitated minerals (*i.e.* $Mg(OH)_2(s)$ and $Ca(OH)_2(s)$) and high grade of fresh water.

This chapter is devoted to the installation and testing of the MF-PFR crystallizer in Plant One with the aim of assessing the possibility to recover Mg^{2+} and Ca^{2+} as hydroxides at high purity by means of a fractionated precipitation. In particular, simplified P&ID (process and instrumentation diagram) of the MF-PFR pilot plant installed is reported. The MF-PFR pilot unit consists of three main sections:

1. Crystallization section, consisting of MF-PFR unit described in chapter 6;
2. Filtration section, consisting of a drum filter;
3. Neutralization section.

The main MF-PFR's results, *i.e.* purity of the two recovered hydroxides and the recovery/removal of Mg^{2+} /Ca^{2+} from feed brines, are reported and deeply described as well as the stability and robustness of the MF-PFR operating using different real industrial spent brines. Moreover, the average purity of the magnesium and calcium hydroxide solids recovered by a drum filter was obtained and compared with the one obtained by MF-PFR.

8.2. Experimental methodologies

Also in this case, the experimental procedure used for all experiments carried out in Plant One (Rotterdam, The Netherlands) is shown in *Figure 8.1*.

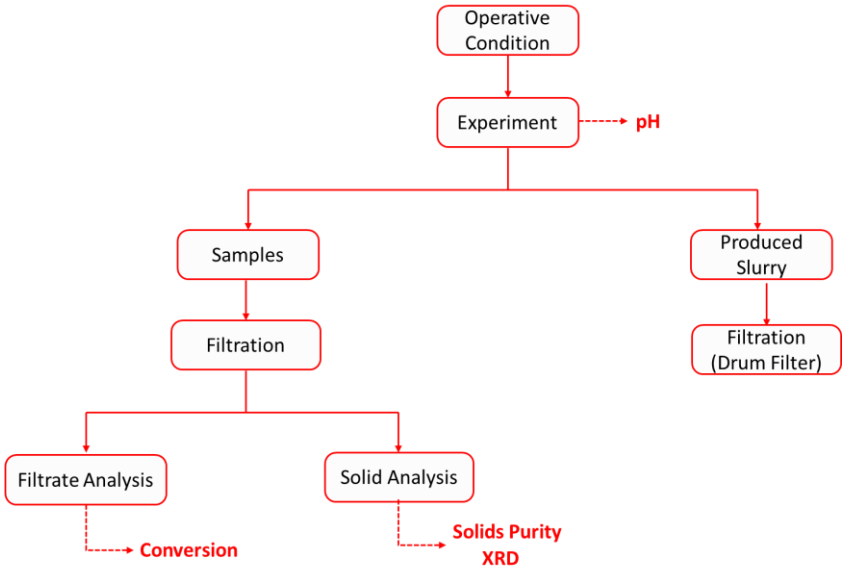

Figure 8.1. Experimental procedure for the recovery of the minerals from waste brine carried out in Plant one.

Operative Condition. The first step was to collect the retentate, exiting from the NF, in the feed tank. Subsequently, the brine was fed inside the reactor together with the alkaline solution in order to recovery, first, the magnesium and, after, calcium. Depending on the precipitation step, two different concentrations of alkaline solution were used and the flow rates were calibrated in order to precipitate magnesium, or calcium, under stoichiometric condition.

Experiment. Also in this case, the experiments followed the same procedure describe in subchapter *7.1*. The volume collected of the samples was equal to 1000 ml, necessary for the analyses. After the test, the reactor was cleaned with HCl solution (about 10M) in order to dissolve the fouling of $Mg(OH)_2(s)$ or $Ca(OH)_2(s)$ formed during the precipitation, and, after,

flushed with tap water. During the precipitation and cleaning steps, the pH was measured by a pH-meter installed at the outlet of the crystallizer.

Laboratory Filtration. The filtration of the samples were carried out by Büchner filter equipped with a glass-fibre filter. Also in this case, the filtrate was collected and prepared for ionic chromatographic analysis. The solid was washed twice using deionized water in order to remove any traces of brine and soluble salts. After the precipitation, the solid was dried in an oven for 24 hours at 120°C. Regarding the produced slurry during the precipitation, it was collected in the tank about 1000 l, in order to settle the produced crystal. Subsequently, the concentrate slurry was recovered and fed into the drum filter to recover the magnesium hydroxide or calcium one.

Filtrate Analyses. Also in this case, the filtrate was analysed via IC in order to assess the yield of the precipitation.

Solid Analysis. A part of the solids was prepared for the IC analysis in order to estimate the purity of the precipitated crystals. The preparation of the sample followed the same procedure described in subchapter *7.1*. While, the remaining part of the solids was analysed by X-Ray Diffractometry (XRD, Pan Analytical Empyrean, using a CuKα radiation with a wave length equal to 0.15405 nm) allowed determining which types of solids form the precipitated crystals under a qualitative point of view.

8.3. Process Description

Piping & Instrumentation Diagram (P&ID) of the pilot unit is presented in Figure 8.2. The system can be divided into three main sections:

1. Precipitation section, consisting of the Multiple-Feed Plug Flow Reactor (MF-PFR) and relevant auxiliary devices (e.g. pumps, tanks and sensors);
2. Filtration section, consisting of a drum filter and relevant auxiliary devices;
3. Neutralization section, consisting of a pH control loop with relevant pumps, sensors and tanks.

A detailed description of the three sections is reported in Figure 8.2.

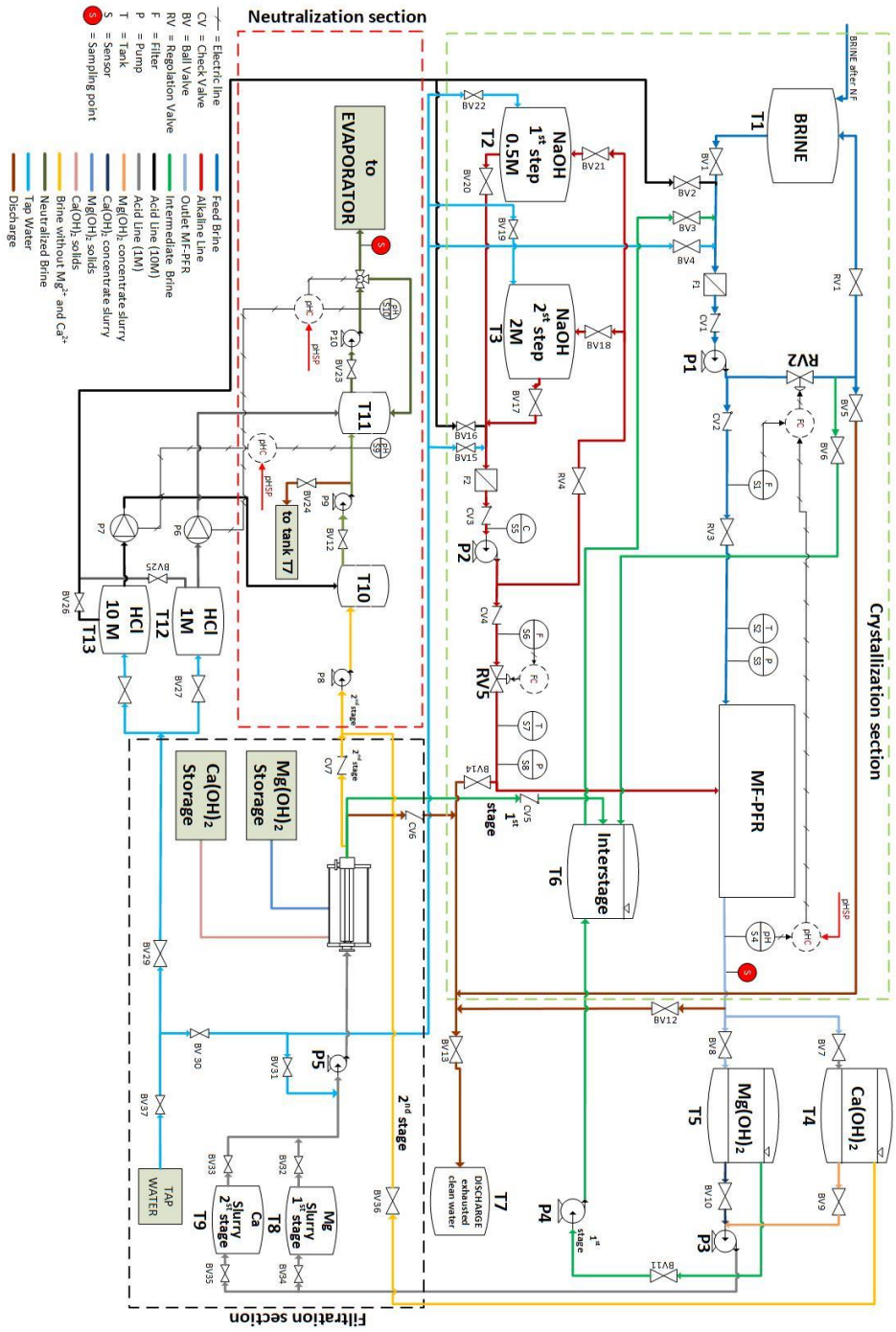

Figure 8.2.Simplified P&I Diagram of the pilot plant.

With reference to the P&ID shown in Figure 8.2, the operation of the unit can be described as follows.

Precipitation Section

The tank *T1* is filled with brine from the nanofiltration (NF) unit, while tanks *T2* and *T3*, are filled with sodium hydroxide solutions used as a reactant for the two steps of Mg^{2+} and Ca^{2+} precipitation. Brine and alkaline solutions are pumped by two different magnetic drive centrifugal pumps. Both pumps are equipped with a recycle loop to better control flow rates, using two electric-motorized valves. Flow rates are measured by magnetic induction flow-meters. Inlet pressure is measured by pressure transducers, in order to monitor the pressure drops inside the annular and internal sections of the reactor.

The direct mixing of brine and alkaline solution inside the annular section of the MF-PFR reactor leads to the precipitation of $Mg(OH)_2(s)$ crystals in the form of agglomerates, which exit from the reactor with the outlet slurry.

As discussed in the previous in sub-chapter 6.2, it is crucial to control the pH of the slurry exiting from the MF-PFR in order to precipitate only magnesium hydroxide or calcium.

A picture of the MF-PFR prototype is reported in *Figure 8.3.* A picture of the MF-PFR prototype installed and operated at the premises of Plant One (Botlek, Rotterdam, NL)..

Figure 8.3. A picture of the MF-PFR prototype installed and operated at the premises of Plant One (Botlek, Rotterdam, NL).

Following the precipitation of magnesium hydroxide, the produced slurry is stored in a settling tank (*T5*). The settled slurry is sent to the storage tank (*T8*), ready for filtration, while the clarified solution is sent to the interstage storage tank (*T6*) to be further processed for the precipitation of Ca^{2+}.

Calcium hydroxide is precipitated according to the same steps, but with higher pH value. Moreover, different settling tank is used (*T4*). From this, the clarified solution is sent to the tank (*T10*) for neutralization, while the settled slurry is sent to the storage tank (*T9*) for the filtration.

The reactor can be periodically cleaned using a $10\%_{w/w}$ hydrochloric acid solution, in order to dissolve residual scaling, and, after, flushed with tap water.

Filtration Section

The main unit of the filtration section is a vacuum drum Filter, which is widely discussed in the subchapter 7.3.

The concentrated slurry feeding the filtration unit is stored in tanks *T8* and *T9* and is circulated by the means of a membrane pump (SHURFLO, mod. SH-2088-594-444).

After the filtration takes place, the filtered solution is directed to the intermedium storage tank (*T6*), in case this has still to be processed for the calcium precipitation step, or to the neutralization section when all bivalent ions have been precipitated.

Neutralization section

The neutralization of clarified and filtered brines (arriving from tank *T4* and from the second step filtration, respectively) is carried out via two subsequent steps, which allow having a finely tuned control of pH [121]: (i) the brine is mixed with a 10M hydrochloric acid solution in order to neutralize the 90% of hydroxide ions, and, finally, (ii) the brine is mixed with a 1M acid solution to finalize the neutralization.

The neutralised brine pH is measured by means of an inline pH-meter (KHRONE, mod. PH 8320).

Auxiliary units

The external connections (brine tanks, filtration unit and intermediate buffer tanks) have been made up by semi-rigid PE (polyethylene) tube (ID 16mm, thickness 2mm) along with fittings and valves.

Information on all tanks adopted in the prototype is reported in *Table 8.1*.

Table 8.1. Tanks used in the pilot plant.

Tank n.	volume [lt]	material	used for
T1	5000	LLPE	Collecting the Brine from Nano-filtration step
T2	1000		Storing the NaOH aqueous solution for precipitation of $Mg(OH)_2(s)$
T3			Storing the NaOH aqueous solution for precipitation of $Ca(OH)_2(s)$
T4	1000	HDPE	Collecting and settling the $Mg(OH)_2(s)$ slurry
T5			Collecting and settling the $Ca(OH)_2(s)$ slurry
T6	3000	LLPE	Collecting the free Mg brine for the second step
T7			Collecting the waste effluents of the MF-PFR and the drum filter
T8	300	PE	Collecting the $Mg(OH)_2(s)$ concentrated slurry
T9	300	PE	Collecting the $Ca(OH)_2(s)$ concentrated slurry
T10	1000	HDPE	First step of neutralization
T11	5000	LLPE	Second step of neutralization
T12	200	HDPE	Storing 1 M of hydrochloric acid
T13			Storing 1 M of hydrochloric acid

8.4. Experimental tests

Long-run experimental tests (8 hours for each experiment) were carried out with 3 different feed brines resulting from three different phases of IEXs regeneration: i) High, resulting from the peak phase of releasing bivalent ions in the spent regenerant; ii) Low, resulting from the final phase of IEXs regeneration (lower bivalent concentration); and iii) Std, resulting from the averaging effect of the buffering storage tank, where spent regenerant is stored. This last condition was the most adopted in the experimental campaign and it was characterised by a large variability of ions concentration. In *Table 8.2*, the average composition of three different tested brines are reported. Worth noting that 9 long run tests were conducted with

the nominal brine composition, while 2 spot tests were conducted with the Low and High feed brine

Table 8.2. Average composition of feed brines adopted for the precipitation tests.

Brine coming from NF	pH	σ [mS/cm]	Concentration of main cations in solution [g/l]				Concentration of main anions in solution [g/l]		
			Na^+	K^+	Ca^{2+}	Mg^{2+}	HCO_3^-	Cl^-	SO_4^{-2}
A	7.23	62.87	8.80	0.21	10.8	1.34	0.33	30.46	0.11
B	7.03	74.24	8.29	0.24	12.6	1.76	0.11	41.21	0.55
C	7.00	91.40	11.49	0.24	15.8	2.51	0.14	46.38	0.65

Figure 8.4 reports the concentration of the main cations and anions in the tested brines, also indicating the range of variability of concentration for the nominal brine composition.

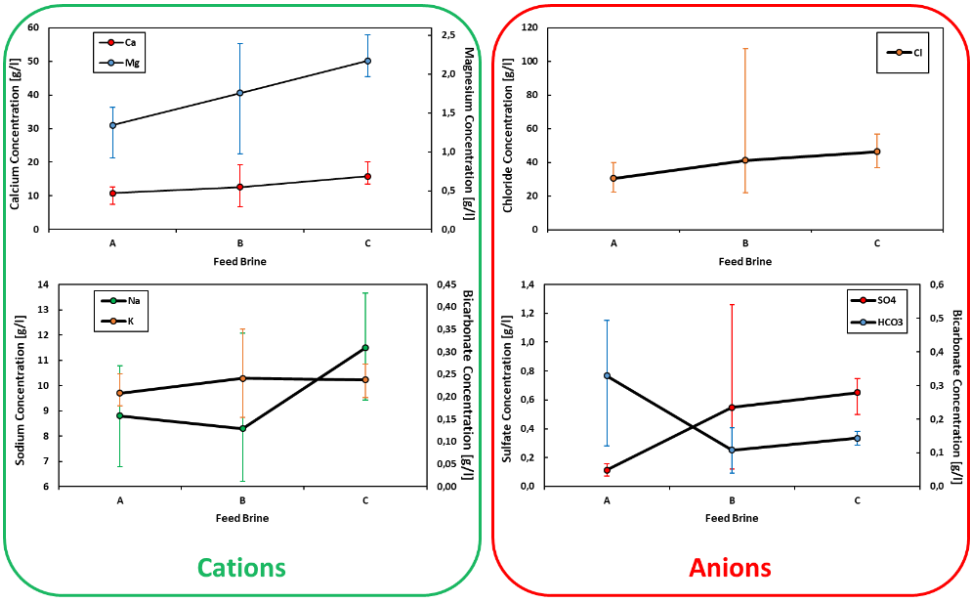

Figure 8.4. Cations and anions composition of the three different feed brines

All long run experiments were performed with the aim of analysing the stability and robustness of the reactor in terms of inlet flow-rate, outlet pH and system's performance parameters, as discussed in section *7.2. Table 8.3* and *Table 8.4* details of operative conditions for all the experiments are reported.

Table 8.3. Operative conditions for the $Mg(OH)_2(s)$ crystallisation experiments.

Test run ID	*Operative Condition of system*					
	pH	*Brine Flow Rate [l/min]*	*NaOH Flow Rate [l/min]*	*NaOH Conc. [mol/l]*	*Prouced slurry [l]*	*Worked Hours [h]*
A (Low TDS 12/02/2020)	*10.5*	*2.45*	*0.17*	*0.5*	*1000*	*6.5*
B1 (Std TDS 19/11/2019)	*10.6*	*2.0*	*0.41*	*0.4*	*900*	*7*
B2 (Nominal 21/11/2019)	*10.6*	*2.1*	*0.4*	*0.4*	*500*	*3.3*
B3 (Nominal 26/11/2019)	*10.7*	*2*	*0.37*	*0.4*	*550*	*4*
B4 (Nominal 28/11/2019)	*10.7*	*2*	*0.37*	*0.4*	*450*	*3.3*
B5 (Nominal 11/12/2019)	*10.6*	*1.2*	*0.45*	*0.4*	*800*	*8.5*
B6 (Nominal 13/12/2020)	*10.5*	*1.31*	*0.46*	*0.4*	*900*	*8.7*
B7 (Nominal 17/12/2019)	*10.5*	*1.25*	*0.42*	*0.4*	*800*	*8.5*
B8 (Nominal 18/02/2020)	*10.35*	*2.66*	*0.38*	*0.5*	*700*	*4*
B9 (Nominal 20/02/2020)	*10.8*	*1.6*	*0.4*	*0.5*	*1000*	*8.5*
C (High TDS 28/02/2020)	*10.25*	*6.1*	*0.34*	*1*	*500*	*1.5*

Table 8.4. Operative conditions for the $Ca(OH)_2(s)$ crystallisation experiments.

Test run ID	*Operative Condition of system*					
	pH	*Brine Flow Rate [l/min]*	*NaOH Flow Rate [l/min]*	*NaOH Conc. [mol/l]*	*Produced slurry [l]*	*Worked Hours [h]*
A (Low 13/02/2020)	*13.2*	*1.36*	*0.33*	*4*	*750*	*7.5*
B1 (Nominal 20/11/2019)	*13.0*	*1.4*	*0.36*	*2*	*650*	*6.2*
B3 (Nominal 27/11/2019)	*13.1*	*1.4*	*0.38*	*2*	*900*	*8.5*
B5 (Nominal 12/12/2019)	*13.1*	*1.3*	*0.42*	*2*	*800*	*8*
B7 (Nominal 18/12/2019)	*13.0*	*1.2*	*0.45*	*2*	*850*	*8.5*
B8 (Nominal 19/02/2020)	*13.1*	*1.56*	*0.36*	*4*	*800*	*6*
B9 (Nominal 21/02/2020)	*13.33*	*1.21*	*0.3*	*4*	*550*	*6.2*
C (Upper 28/02/2020)	*13.1*	*1.45*	*0.32*	*4*	*500*	*5*

8.5. Results and discussion

8.5.1. Analysis of system stability in the long-run operation.

The long-rung pilot tests aimed at analysing the robustness and the stability of the plant. During the test, all relevant operative parameters were recorded and plotted against time to assess the system's stability.

For the sake of brevity, only results relevant to the case B5 are shown in Figure 8.5.*a* for magnesium precipitation and Figure 8.5.*b* for calcium precipitation, being the plots for all the other tests performed very similar to these ones.

The test-run can be divided in three main phases: (i) start-up, (ii) steady state operation, and (iii) cleaning. During the start-up, brine and the alkaline flow-rates are smoothly adjusted in order to reach the required optimal reaction pH. Once this condition is reached, the pilot worked at steady-state for about 7-8 hours. At the end of the run, the reactor is cleaned using

10%$_{w/w}$ hydrochloric acid solution for a few minutes in order to dissolve the magnesium or calcium hydroxide scaling formed inside the reactor, and, subsequently, flushed with tap water for about 10 minutes.

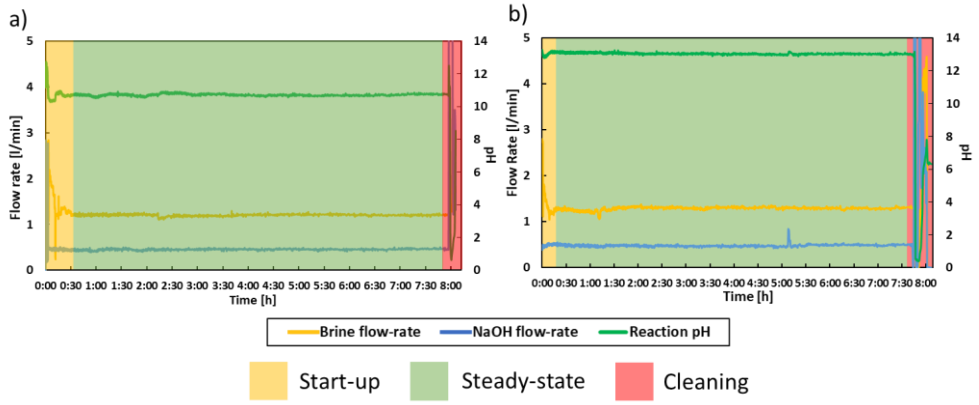

Figure 8.5.Variation of the outlet pH and both inlet flow rates over the experimental time. a) Precipitation of the magnesium hydroxide, and b) precipitation of the calcium hydroxide.

As shown in Figure 8.5, the outlet reaction pH and both flow rates are very stable during steady-state operation, which highlights the stability of the MF-PFR once the stationary-condition is reached.

Worth mentioning that stable operations were maintained also thanks to some control actions required in order to minimise the effects of disturbances, such as increase of pressure drops due to nozzles scaling, or variation of feed tanks level. However, control actions were always smooth and perfectly feasible within the nominal operations of the system.

In addition, some small control actions were needed in order to compensate slight variations in Mg^{2+} and Ca^{2+} feed brine concentration, likely caused by time-dependent stratification phenomena within the feed tanks (*T1* for the feed brine tank and *T6* for the interstage storage brine tank).

8.5.2. Performance of the reactive precipitation processes

To evaluate the quality of the recovered crystals of $Mg(OH)_2(s)$ and $Ca(OH)_2(s)$, and the recovery performance, solids and liquid samples from each test-run were analysed, following the analytical procedure reported above. Results for all tests are reported below, classified according to the first and second precipitation step

8.5.2.1 Magnesium hydroxide precipitation step

Solid purity and recovery efficiency for the tests conducted to precipitate $Mg(OH)_2(s)$ are reported in *Figure 8.6*. Magnesium and calcium concentration in the feed brine and magma density are also reported to support the results' interpretation.

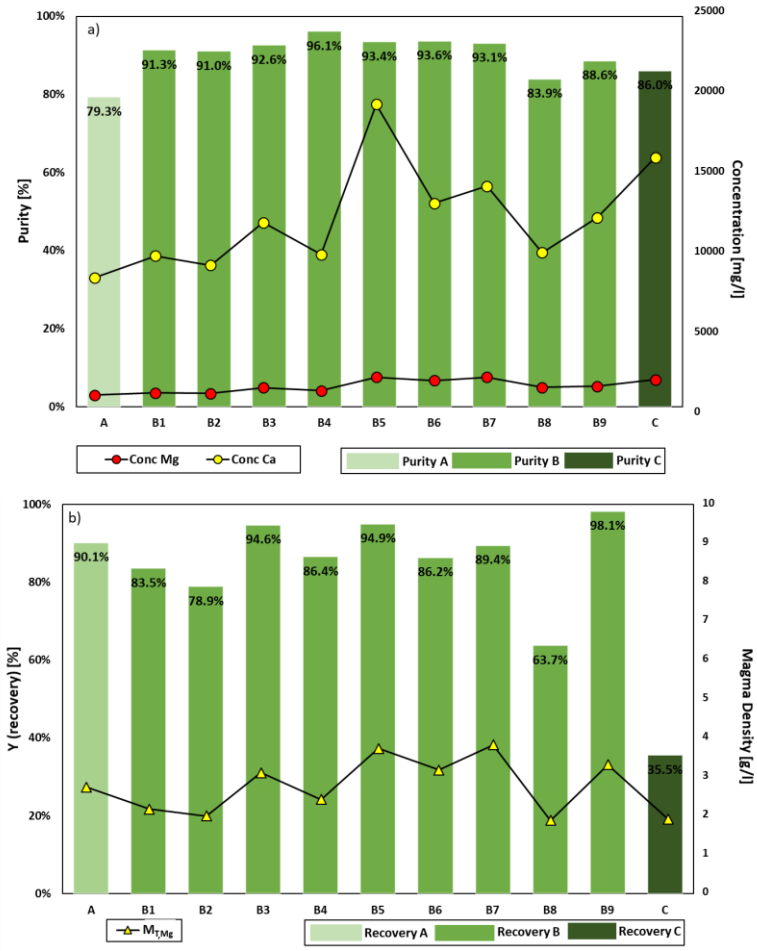

Figure 8.6. a) Purity of $Mg(OH)_2(s)$ solids for all precipitation tests, accompanied by magnesium and calcium concentration in the feed brine; b) Mg recovery efficiency and magma density

Concerning the purity of $Mg(OH)_2(s)$ solids, IC analyses have shown that only Mg and Ca cations were present in the $Mg(OH)_2(s)$ precipitate. The purity was typically higher than 90% for most of the tested brines with a peak of 96% for test B4, though for some tests values below 90% were found with a minimum of 79% for test A. In all cases, the purity was affected by the co-precipitation of calcium carbonate, as indicated by XRD analysis reported in. *Figure 8.7.*

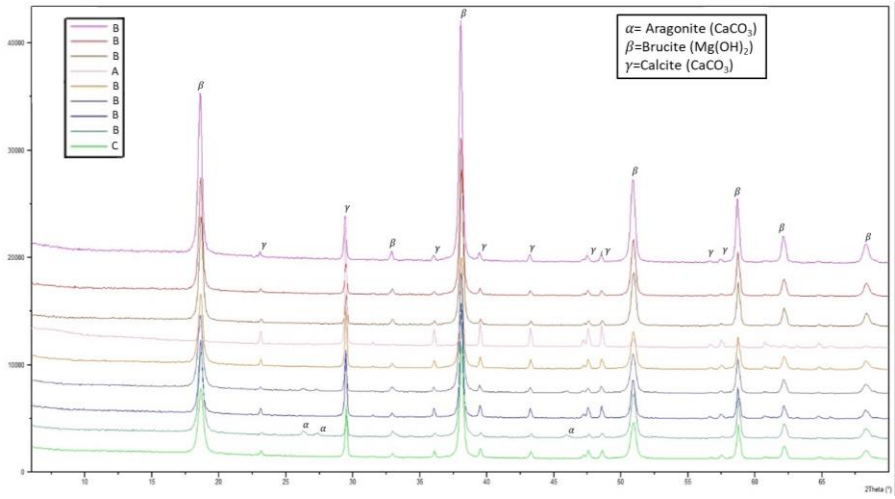

Figure 8.7. Cumulative XRD patterns for magnesium hydroxides samples from all different test-runs.

In particular, calcium was found in the form of *calcite* as the most stable species at the operating conditions (10-15°C and pH of 10.5 [119]). The precipitation of calcium carbonate during the reactive precipitation step of magnesium hydroxide was due to the presence of the bicarbonate (HCO_3^-) in the feed brines.

Also in this case, the MEDUSA software [118] was used to investigate the chemical equilibrium involved during the precipitation.

Figure 8.8 shows the results of the simulation carried out with the Medusa software for test B.

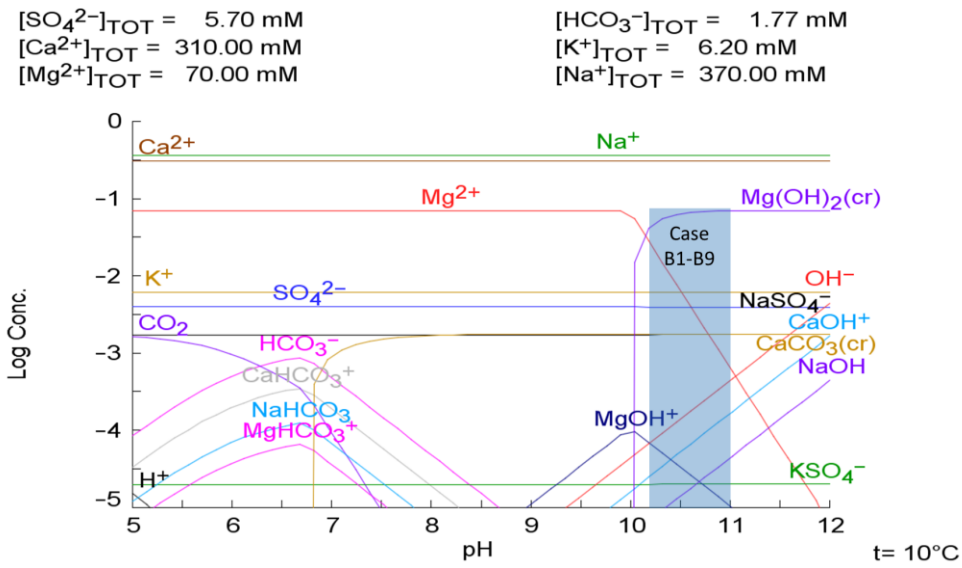

Figure 8.8. pH versus log concentration plot for the case A at 10°C, fixing the $[Na^+]$=0.36M (8.2g/l), [k+]=0.0062M (0.24g/l) $[Mg^{2+}]$=0.7M (1.76g/l), $[Ca^{2+}]$=0.31M(12.6/l), $[SO_4^{2-}]$=0.0057M (0.55g/l) and $[HCO_3^-]$= 0.0018M (0.108g/l).

As seen *Figure 8.8*, the Medusa software predicts the precipitation of the magnesium, which starts at pH 10.04 and ends around pH 11. This latter value is higher than that measured during the fractionated precipitation test (final pH of magnesium precipitation equal to 10.4, *Figure 6.1*) due to the complex composition of the brine that could affect the solubility of magnesium hydroxide. Moreover, the results of the software predict the co-precipitation of the calcium carbonate. On overall, the results obtained by the Medusa were in agreement with the experimental findings with particular reference to the composition of the precipitated phase.

As shown in *Figure 8.8*, the pH value of the tested brines grouped in test B varied between 10.35 and 10.8. It is worth noting that the Medusa software predicted the variation of the amount of precipitated magnesium as a function of the pH. In fact, the recovery increases from 80% at pH equal to 10.35 (test B8, conversion equal to 84%), up to 98% at value pH of 10.8 (test B9, conversion equal to 98%), which are very close to the experimental results.

In light of the results obtained by IC, XRD analyses and the Medusa software, the purity of the precipitated magnesium hydroxide is affected by the amount of the bicarbonate present in the inlet brine and the amount of the magnesium recovered. For this reason, it is important to look at the recovery of the magnesium, since a higher value of the Mg recovery increases

the ratio between Mg and Ca at fixed inlet brine concentration, thus resulting in a higher degree of purity of the produced crystals.

The recovery efficiency of magnesium in the form of $Mg(OH)_2(s)$ was for most cases equal or above 80%, with peaks above 95%. The lowest values (35 % and 65%), however, represent tests in which lower pH values were maintained due to non-optimal control of system operation for tests B8 and C.

The magma density of the produced slurry is strictly dependent on the amount of the magnesium and bicarbonates in the feed brines and can be related also magnesium recovery efficiency.

Considering only the dependence on (i) the recovery and (ii) the magnesium concentration in the inlet brine, the magma density can be computed by using Eq. 8.1:

$$M_T = Y_{Mg} \frac{C_{Brine}^{Mg} F_{in}^{Brine}}{F_{in}^{Brine} + F_{in}^{NaOH}} \frac{M_W^{Mg(OH)_2}}{M_w^{Mg}} \qquad (8.1)$$

where Y_{Mg} is the recovery of the magnesium, C_{Brine}^{Mg} is the magnesium concentration in the inlet brine [g/l], F_{in}^{Brine} and F_{in}^{NaOH} are the flow-rate of brine and sodium hydroxide solution [l/min], respectively, $M_W^{Mg(OH)_2}$ and M_w^{Mg} are the molecular weight of magnesium hydroxide and magnesium [g/mol], respectively. Based on the available collected experimental information on (i) recovery and (ii) magnesium concentration, the magma density was computed by eq.4.1 for each tested brine. *Figure 8.9* shows the computed and the experimental magma densities together with the inlet concentration of magnesium (*Figure 8.9-A*) and the recovery (*Figure 8.9-B*).

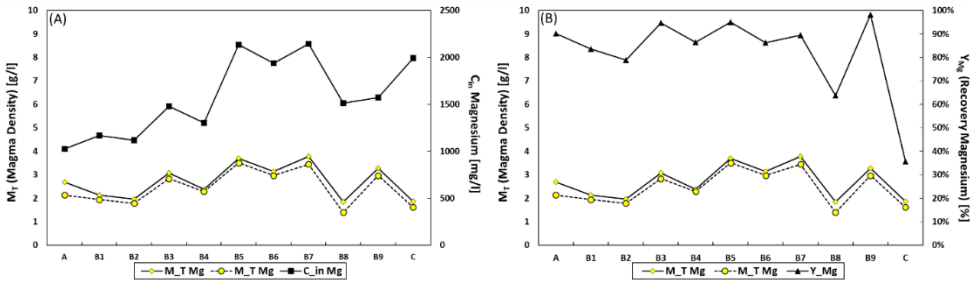

Figure 8.9. (A)Magma density and inlet magnesium concentration. (B) Magma density and recovery of magnesium. Solid line (black lined and square yellow marker) indicates the experimental magma density, while the dashed line (black lined and circle yellow marker) the computed one by mass balance.

Figure 8.9 show that the computed magma density has the same trend as the experimental one, the only difference between the two trends is due to the amount of the calcium carbonate co-precipitate during the magnesium precipitation. As shown in *Figure 8.9-A*, the magma density does not strictly follow the trend of the inlet magnesium concentration, thus indicating that is not strictly dependent upon the inlet magnesium concentration due to the influence of the recovery. In fact, as shown in *Figure 8.9-B*, both the computed and the experimental magma density follows the trend of the recovery. Taking test C as an example, the concentration of magnesium in the inlet brine is greater than in case B9 so that one would expect the magma density to increase as well, but, instead, it decreases due to the reduction of the recovery from 98.1% for test B9 down to 35.5% for test C.

8.5.2.2 Calcium hydroxide precipitation step

After the first precipitation step, the produced slurry was stored in the tank *T5* in order to settle and separate the produced magnesium hydroxide crystals. After the settling, the concentrate slurry was sent to tank *T8* and then feed to the drum filter to separate magnesium hydroxide crystals. Then, the clarified brine and the filtrate were sent to the interstage tank *T6*, and then fed to the crystallizer for the calcium precipitation step. It is worth mentioning that this second precipitation step aims at the quantitative removal of all bivalent cations from the brine, in order to make it suitable for NaCl-solution valorisation in the flowing steps of the treatment chain described in *Figure 5.6*. Thus, a part from the purity of recovered solids,

the major performance parameter for this precipitation step will be the recovery efficiency of Mg^{2+} and Ca^{2+}, which indicates the removal efficiency of bivalent cations from the brine. Solid purity and recovery efficiency for both Mg^{2+} and Ca^{2+} are reported in *Figure 8.10*, where also magnesium and calcium concentration in the feed brine and magma density are reported to support the results' interpretation.

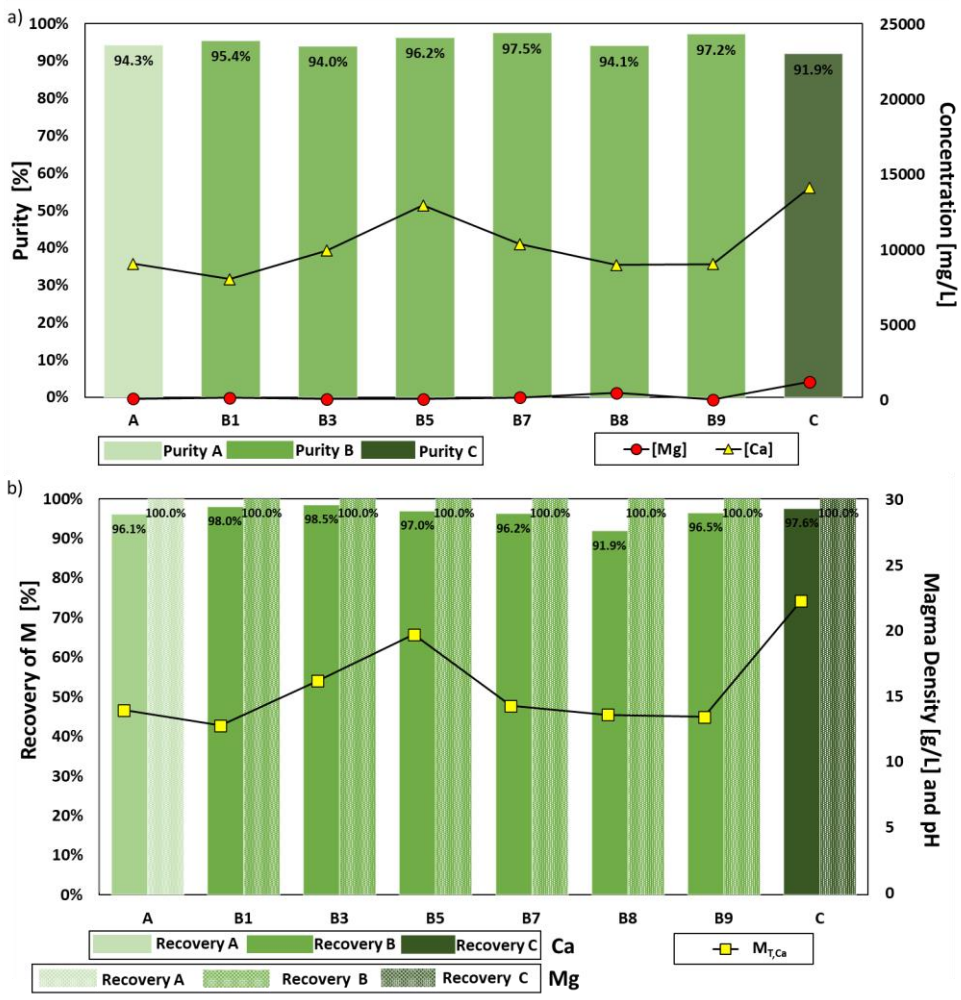

Figure 8.10. a) Purity of $Ca(OH)_2$(s) solids, accompanied by magnesium and calcium concentration in the feed brine; b) Ca and Mg recovery efficiency magma density.

The purity of the produced $Ca(OH)_2$(s) was determined by the same procedure describe above. The IC analyses highlighted that only Mg and Ca were present in the Ca(OH)2(s)

precipitate. Also in this case, IC analyses confirmed that only Mg and Ca were present in the Ca(OH)2(s) precipitate. The purity was around 95% for the all the tests, with maximum value of about 97% for the test B7 and a minimum value of about 92% for the test B3. In this case, the purity was affected by the co-precipitation of magnesium hydroxide, especially for tests with a lower Mg recovery efficiency in the first precipitation stage.

However, it is worth noting that, higher values of purity were expected (C_{Mg} in the feed brine is very low in most cases and this would affect the solid purity by about 1-2% maximum in all tests but the B8 and C, for which a very low recovery of Mg was observed in the first precipitation step), thus indicating that a problem of entrainment of magnesium hydroxide fine particles in the clarified and filtered solution used to feed the 2nd precipitation step.

Calcium recovery in the form of $Ca(OH)_2$(s) presented efficiency ranging from about 92% to almost 98%, while magnesium was totally removed by precipitation, thanks to the very high pH values (more than> 13). Thus, an overall removal efficiency of bivalent cations above 97% was reached in most cases.

Finally, the magma density of the produced slurry mostly followed the calcium concentration in the inlet feed brine, being calcium the major bivalent cation in the salt mixture and the recovery efficiency quite stable around the value of 95%.

Also in the present case, the magma density was computed taking into account (i) the calcium recovery and (ii) the calcium concentration in the inlet brine, by Eq. 8.2:

$$M_T = Y_{Ca} \frac{C_{Brine}^{Ca} F_{in}^{Brine}}{F_{in}^{Brine} + F_{in}^{NaOH}} \frac{M_W^{Ca(OH)_2}}{M_w^{Ca}} \qquad (8.2)$$

where Y_{Ca} is the recovery of the calcium, C_{Brine}^{Ca} is the calcium concentration in the inlet brine [g/l], F_{in}^{Brine} and F_{in}^{NaOH} are the flow-rate of brine and sodium hydroxide solution [l/min], respectively, $M_W^{Ca(OH)_2}$ and M_w^{Ca} are the molecular weight of magnesium hydroxide and magnesium [g/mol], respectively. Both the computed and experimental magma densities are shown in *Figure 8.11* together with the inlet magnesium concentration (*Figure 8.11-A*) and the recovery (*Figure 8.11-B*).

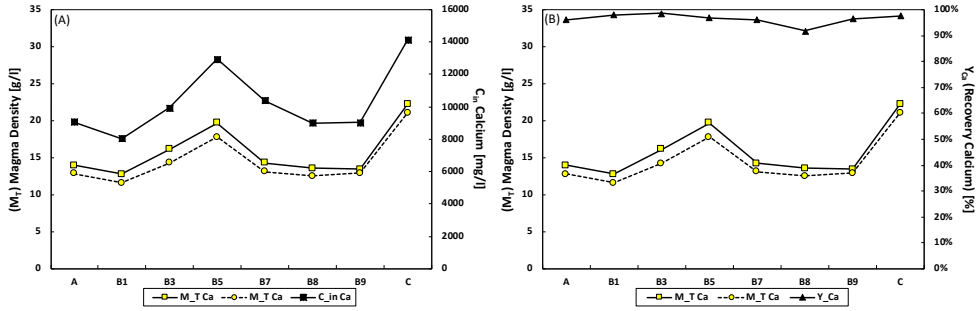

Figure 8.11. (A)Magma density and inlet calcium concentration. (B) Magma density and recovery of calcium. Solid line (black lined and square yellow marker) indicates the experimental magma density, while the dashed line (black lined and circle yellow) indicates the computed one.

Differently from the magnesium precipitation, in this case the magma density is affected by the calcium concentration in the inlet brine, rather than the calcium recovery. This behaviour of the magma density is explained because in all tested brines the obtained calcium recovery was about 95 %, and, thus, the magma density was slightly affected by the calcium recovery. On the other side, the difference between the computed magma densities with respect to the experimental one is due to the amount of magnesium hydroxide in the precipitated crystals. In fact, in some case, such as B9 and B7, the computed magma density is very close to the experimental one since the produced crystals are mainly composed by calcium hydroxide, with purity about 97% and 98%, respectively.

8.5.3. Drum filter solids separation

Optimal operation of the drum filter requires a feed slurry with a minimum volume of about 100 l and a particles concentration ranging from 60 to 100 g/l, thus much higher than that obtained in the precipitation steps. In fact, based on the cake filtration mechanism [105,113] adopted, high solids concentration in the feed promote a rapid formation of the cake onto the cloth surface [105,113] which allows for the effective filtration of solid particles.

In order to fulfil these requirements, after each precipitation step, the produced slurry was sent into the settling tanks, *T5* and *T4* respectively, in order to obtain a more concentrate slurry and a clarified brine. The settling phase required about 16-18 hours in order to effectively obtain a well separated clarified phase with a volume ranging from 80% to 95%

of the initial brine volume (larger values refer to the settling of magnesium hydroxide slurry). The concentrate slurry was sent to the inlet tank of the drum filter (*T8* for magnesium slurry and *T9* for calcium one) and accumulated for several tests, in order to reach a minimum volume of 100 litres, required to properly operate the drum filter.

In particular, the particle load of the magnesium hydroxide slurry was increased from 20 to 40 times, depending on the initial magma density. Lower concentration rate was required of the calcium hydroxide which passed from 15.0 g/l (average magma density of all tests B) up to 90 g/l of solids load.

Solids obtained from the filtration of the collected slurries were also analysed to measure the purity, finding a value close to the average observed in all tests, i.e. around 90% for $Mg(OH)_2(s)$ precipitate and 94% for $Ca(OH)_2(s)$.

.

8.5.4. Outlet brine neutralization

Following the sedimentation and filtration steps of the calcium hydroxide slurry, the clarified brine together with the filtrate undergo a final step for pH neutralization, which is propedeutical to the subsequent steps in the treatment chain for NaCl-solution valorisation (see *Figure 5.6*). As reported in paragraph 8.3, the neutralization section was carried out via two consecutive steps in order to better control the obtained pH along the typical shape of a neutralisation curve, see *Figure 8.12*.

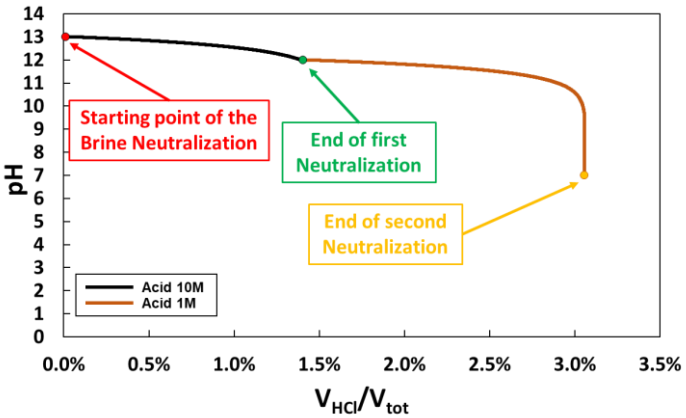

Figure 8.12. Neutralization steps reported on the pH vs V_{acid}/V_{tot} curve obtained adding a strong acid to an alkaline solution..

As shown in *Figure 8.12*, starting from a pH value around 13 (red point), an aqueous solution of 10M hydrochloric acid (HCl) was mixed with the brine in order to neutralize about 90% of hydroxyl ions reaching a pH around 12. After the first neutralization step, a 1M HCl solution was added in order to complete the neutralization reaching the equilibrium point (pH=7). Such step required a fine control of the acid solution volume added due to the dramatic sensitivity of pH to strong acid addition in pH-neutral solutions. Very small volumes (see *Figure 8.12*) of acid solution were needed for the neutralization of the brine volume, thus resulting in a final brine composition very similar to that obtained after the second precipitation step.

The average composition of the neutralised brine for each class of tests is reported in Table 8.5.

Table 8.5. Average composition of the neutralized brine.

Case ID	Cation composition [g/l]				Anion composition [g/l]	
	Na^+	K^+	Ca^{2+}	Mg^{2+}	Cl^-	SO_4^{-2}
A	24.2	0.07	0.28	0.0	15.2	0.12
B	19.3 (±4.1)	0.13 (±0.04)	0.27 (±0.23)	0.0	26.7 (±6.1)	0.33 (±0.3)
C	25.4	0.18	0.28	0.0	43.5	0.50

Interestingly, the brines produced by the pilot unit were essentially free of magnesium, while calcium concentration was reduced by 97-98%, thus achieving overall a very good efficiency bivalent cations removal, suitable for further processing in the NaCl-solution valorisation treatment chain.

Conclusion Section 2

Part of the thesis work, described in **Section 2**, was devoted to design, assembling, and testing an unconventional crystallizer, namely Multiple Feed Plug Flow Reactor (MF-PFR), for the recovery of minerals, such as magnesium and calcium, from industrial waste brines. Firstly, a preliminary laboratory test was carried out in order to assess the possibility to recover magnesium and calcium hydroxide in a fractionated way through accurate control of the reaction pH. The results of the laboratory tests showed that the quantitative recovery of both bivalent cations was achievable, recovering more than 99%, with a purity of the produced solids was above 99%. Afterwards, a pilot reactor for the selective recovery of Mg and Ca was designed and assembled. The MF-PFR (consists of two coaxial tubes where the brine, flowing in the inner tube, is injected through holes in the annular section where the alkaline solution flows. The particular position and orientation of the holes allow promoting the swirling turbulent motion favouring the fast mixing of the two reactants. Four different experimental campaigns were carried out in the Brine Excellence Center (BEC). The first experimental campaign was carried out using artificial brines. The precipitation was performed using four different concentrations of sodium hydroxide solution, with aims to finding the suitable operating conditions to precipitate a magnesium hydroxide easily filterable and plat hexagonal shape. The outcomes highlighted that two different concentration of sodium hydroxide, *i.e.* 0.5M and 1M, allowed obtaining a filterable magnesium hydroxide. Moreover, the alkaline concentration equal to 0.5M is suitable for the magnesium precipitation by means of a fractionated crystallization because it allowed to accurately control the reaction pH. While the latter alkaline concentration was suitable for the magnesium precipitation from industrial brine produced by saltworks. However, the SEM pictures showed that the precipitate magnesium hydroxide shape is spherical, like a cauliflower, not matching the form of Magnifim H10.

The second experimental campaign was carried out using waste brines produced by saltworks with two different magnesium concentration (10 and 25 g/l) in order to assess the stability and robustness of the reactor. The outcomes highlighted that very good stability along with very good robustness of the crystallizer in terms of brine and alkaline solution flow rates and reaction pH over the experimental duration. In particular, a magnesium hydroxide at high purity (almost 100%) was obtained with a recovery of about 98%.

In the third experimental campaign, three different experiments were performed using three different concentration of the inlet brines, which mimicked the composition of the retentate produced by NF fed by spent brines. Also in this case, the results highlighted that the MF-PFR was very stable and robustness during the precipitation of magnesium hydroxide and, also, for the calcium. As regards, the magnesium precipitation step, the recovered magnesium as $Mg(OH)_2(s)$ exhibited a purity of more than 90% in all tests. The value of the outlet pH was kept around 10.35 in order to avoid the precipitation of the calcium as calcium hydroxide. Nevertheless, the magnesium recovered was affected by the presence of the calcium as calcium carbonate due to the high concentration of carbonate/bicarbonate ions present in the brines. As regard the recovery of magnesium, it was between 89-99% due to the increase of the reaction pH from 10.3 up to 10.4. Regarding the calcium precipitation step, the recovered calcium as $Ca(OH)_2(s)$ exhibited a purity of more than 98% in all tested brines. Also, in this case, the purity of the produced $Ca(OH)_2(s)$ was affected by the co-precipitation of the $Mg(OH)_2(s)$ due to the partial recovery in the first precipitation step. While the recovery of the $Ca(OH)_2(s)$ was about 95% in all tested brines along with complete magnesium precipitation of the intermediate brine.

In order to increase the purity of the magnesium hydroxide, a fourth experimental campaign was carried out using the same composition of the brines tested in the third experimental one. In this case, a pre-treatment step was performed in order to remove the bicarbonate/carbonate ions from the brine. The pre-treatment step consisted of: (i) acidification step in order to convert bicarbonate/carbonate ions into carbon dioxide and (ii) stripping step in order to remove the carbon dioxide. After the pre-treatment step, the two precipitation steps were carried out. As regards the magnesium precipitation step, the outcomes highlighted that the purity of the magnesium ranged between from 98.3% up to about 100%. The purity achieved was higher than the ones obtained during the third experimental campaign. Moreover, the pre-treatment step allowed to achieve recovery higher, from 95% up to 98%, than the third experimental one. The purity of recovered calcium hydroxide was about 99% in all tested brines. While, the recovery of the $Ca(OH)_2(s)$ was about 94% coupled with complete magnesium precipitation from the inter-stage brine.

The MF-PFR was shipped at Plant One B.V in Botlek (Rotterdam, the Netherlands) and tested with real brines, demonstrating the possibility to recover magnesium and calcium hydroxide in a fractionated (two precipitation steps) way through an accurate control of the reaction pH. A drum filter, buffer tanks and a neutralisation unit complete the pilot

installation, which was installed within a larger treatment chain, aiming at the valorisation of spent brines, produced during the regeneration of IEXs resins for water softening, for the recovery of magnesium and calcium hydroxide and the regeneration of highly concentrated NaCl solutions.

Long-run tests were carried out feeding the pilot with real industrial brines and demonstrating the plant stability and robustness.

The recovered $Mg(OH)_2(s)$ solids exhibited a purity above 90% in most cases, with a peak of 96% and lower values around 80%. The major contaminant found was calcite, coprecipitated with magnesium hydroxide due to the high concentration of bicarbonates in the feed brine. This makes the recovered solids suitable for a number of market application of magnesium hydroxide, such as flame retardant, environmental and metallurgical sectors.

In the first precipitation step, a Mg recovery efficiency higher than 85% (pH around 10.5) was found in most tests.

Regarding the second precipitation step, the recovered $Ca(OH)_2(s)$ solids exhibited a purity above 94% in all tests, with the second component being, in this case, $Mg(OH)_2(s)$, which completed its precipitation in all cases where the first stage recovery was not quantitative.

A Ca recovery in the form of $Ca(OH)_2(s)$ above 95% was found, while quantitative magnesium removal was achieved in the second precipitation step, thus leading to an overall average removal efficiency of bivalent cations from the combined precipitation step well above 97%. This makes the brine suitable for the subsequent steps of the treatment chain for the NaCl solution valorisation of the spent brine.

Final Remarks

The present PhD thesis focused on the valorisation of industrial waste heat and effluents, such as brines, by means of a circular approach.

In this regard, the thesis is divided in two main sections:

- **Section 1**, titled "*Reverse electrodialysis heat engine: from waste heat to electrical energy*", focusing on the development of an integrated and validated modelling tool for the Reverse Electrodialysis Heat Engine (RED-HE) technology and on the experimental characterisation of the first world prototype of RED-HE;
- **Section 2,** titled "*Minerals recovery from industrial waste brine*", focusing on the design, construction and testing of an unconventional pilot crystallizer, namely the Multiple Feed Plug Flow Reactor (MF-PFR), for the recovery of minerals at high purity, such as magnesium and calcium hydroxide, from different types of industrial waste brines.

In **Section 1**, two different regeneration units, *i.e.* air and vapour stripping absorption/condensation processes, for the regeneration of thermolytic salts solutions were investigated. Two process models were implemented in Aspen Plus® and validated comparing model results with the experiments. The analysis showed that only the vapour stripping/absorption-condensation process was suitable for actual application. Thus, the simulation platform was extended to the whole RED-HE process, by integrating an existing and readapted model for the RED unit, and adopted for a thorough theoretical analysis. Results have indicated a maximum exergy efficiency achievable around 1.3%, considering actual membranes, and around 2% when considering enhanced membranes. Interestingly, a significantly higher exergy efficiency could be achieved using a multiple-column configuration (5 columns in series), leading to values up to 5.2% in the actual membranes scenario, or almost 10% with enhanced membranes. Such modest values of exergy efficiency compare poorly with alternative RED-HE schemes (*e.g.* MED-RED heat engine), achieving exergy efficiency around 28%, using NaCl-water solutions, and above 40%, using KAc (potassium acetate) solutions [15]. This highlights the limits of thermolytic salts solutions to efficiently convert low-grade waste heat into electrical energy.

The first world prototype RED-HE was tested under different operative conditions. Results showed very good stability and robustness during long-run experiments (55 h) in terms of thermal power consumption and produced electrical energy. A gross exergy efficiency equal

to 1% was achieved. However, space for improvements exists, as in the case of: (i) ion exchange membranes, which need to be specifically optimized for thermolytic solutions (*e.g.* ammonium bicarbonate) to increase the performance of RED unit; (ii) regeneration unit which need further optimization of the stripping column and the vacuum system to efficiently exploit the low-grade waste heat and, then, increase the exergy efficiency of the whole RED-HE unit.

Section 2 focused on the design and testing of an unconventional pilot crystallizer, namely Multiple Feed Plug Flow Reactor (MF-PFR), for the recovery of minerals, *i.e.* magnesium and calcium as hydroxides, at high purity from industrial waste brine. Four experimental campaigns were carried out in the Brine Excellence Center (BEC) at UNIPA. The first one was carried out in order to find the optimal sodium hydroxide concentration to recover magnesium hydroxide at high filterability and plate hexagonal shape. The results showed that 0.5M and 1M concentration of NaOH-water solutions were the one suitable to produce high filterability of magnesium hydroxide. The second experimental campaign was carried out using real industrial waste brine produced by saltworks aiming to assess the stability, robustness of the MF-PFR working with high magnesium concentration (9 g/l and 25 g/l) in the inlet brine. The outcomes showed that the MF-PFR was able to manage high magnesium concentration of waste brine achieving high recovery, about 98%, and high purity of magnesium hydroxide, almost 100%. The las two experimental campaigns were carried using an artificial brine mimicking the concentration of retentate produced by Nanofiltration, aiming to recover high purity of magnesium and calcium hydroxide. The results highlighted that purity of magnesium hydroxide increases from 94% (without pre-treatment) up to 99% (with the pre-treatment), and the recovery increases from 94% up to about 96, respectively. Meanwhile, the recovery of calcium was about 95% for both experimental campaigns and the purity increases from 98% up to 99%, respectively.

The MF-PFR was shipped at Plant One B.V in Botlek (Rotterdam, the Netherlands) and assembled within a treatment chain in order to demonstrate the possibility to recover magnesium and calcium hydroxide separately for the regeneration of a spent brine produced by ion exchange resins. The outcomes highlighted that the magnesium hydroxide recovered exhibited a purity above 90% with a peak of 96%. The main contaminant in the magnesium hydroxide solids was calcite due to the precipitation of calcium as calcium carbonate. The recovery was higher than 85%. Meanwhile for the calcium precipitation, the purity achieved was above 95% and a complete removal of the magnesium was achieved leading a global

removal efficiency of bivalents cations above 97%. Recovered calcium hydroxide purity exhibited a purity above 94%.

Future perspectives

For the case of Salinity Gradient Power Heat Engines (SGP-HE), results have shown that the RED-HE based on thermolytic salts is able to convert low-grade heat into electrical energy, although with significant limitation on the exergy efficiency thus preventing future industrial applications. A more promising alternative can be investigated in the future, developing RED-HEs based on other high performing, non-thermolytic, salts (*e.g.* potassium acetate, KAc). In fact, modelling results of such alternative HEs indicate that, by purposely selecting better performing salts in conjunction with a traditional thermal regeneration unit (e.g. Multiple-Effect Distillation, MED) based on solvent extraction, higher exergy efficiencies can be achieved.

For the case of minerals recovery from waste brines, the results obtained up to now are very promising, with magnesium and calcium as hydroxides recovered at high purity (above 98%) in a fractionated way. These results highlight the industrial application potential of the MF-PFR for the valorisation of waste brines in order to recover minerals. A future application of the MF-PFR is envisaged in the Sicilian minor islands, i.e. Lampedusa and Pantelleria, to valorise the SWRO brine producing high-quality magnesium hydroxide. As a matter of fact, the MF-PFR so far developed will be implemented in the island of Lampedusa for the production magnesium hydroxide at high purity (more than 90%), within the framework of the EU-H2020 “WATERMINING” project. This will push further forward improvements of the MF-PFR.

Nomenclature

Acronyms

AEM	Anionic exchange membrane
BEC	Brine Excellence Center
BECC	Brine evaporator cooler/concentrator
CC	Carbon carrier cycle
CEM	Cationic exchange membrane
CRW	Critical Raw Material
CSD	Crystal size distribution
CSTR	Continuous Stirred Tank Reactor
EDR	Electro dialysis reversal
E-NRTL-RK	Electrolyte Non Random Two Liquid Redlich-Kwong
EROI	Energy Return on Investment
FO-TRD	Forward Osmosis Thermally Re-generable Drawing solution
HDPE	High Density of Polyethylene
HT	High Temperature
IEX	Ionic Exchange Resins
IEMs	Ionic Exchange Membranes
KC	Kaline Cycle
LT	Low Temperature
MD	Membrane Distillation
MED	Multi-effect distillation
MF-PFR	Multiple Feed Plug Flow Reactor
MS-MPR	Mixed Suspension Mixed Product Removal
MSF	Multi stage flash
MT	Medium Temperature
NF	Nano Filtration
OC	Open Circuit
ORC	Organic Rankine Cycle
PE	Polyethylene
PEPG	Piezoelectric power generation with waste heat-powered expansion/compression cycle

PFC	Photocatalytic Fuel Cell
PP-H	Polypropylene Homopolymer
PRO-HE	Pressure Retarded Osmosis Heat Engine
PVC	Polyvinyl chloride
RED	Reverse Electrodialysis
RED-HE	Reverse Electrodialysis Heat Engine
RO	Reverse Osmosis
SEM	Scanning electron microscope
SGP-HE	Salinity Gradient Power Heat Engine
SRC	Steam Rankine Cycle
SC	Short circuit
STC	Specific Thermal Consumption [kWh/m^3]
TEG	Thermoelectric generation
TDS	Total Dissolved Solids
TMA-CO_2	Trimethylamine - carbon dioxide
T	Temperature (°C or K)
XRD	X-Ray Diffractometry
WAIV	Wind Aided Intensified eVaporation
WB	Waste Brine
WP	Work package
ZLD	Zero liquid discharge

Symbols

$\%R$	Recovery ratio
$\%\Delta G_{mix}$	Percentage of Gibbs free energy of mixing recovered in the SGP (%)
ΔC	Difference of the current solute concentration and the equilibrium concentration (mol/l)
$\Delta \dot{G}_{mix}$	Gibbs free power of mixing (W)
A_{cp}	Cell pair membrane area (m^2)
b	Membrane width
C	Molar concentration (mol/l)
C_H	Concentrate molar concentration (mol/l)
C_L	Dilute molar concentration (mol/l)

C^{sat}	Equilibrium concentration (mol/l)
D_{column}	Diameter of stripping column
$D_{packing}$	Diameter of packing materials
E_{cell}	Voltage generated by the cell pair (V)
E_{stack}	Voltage generated by the pile (V)
F	Volume flow rate (l/min)
F	Faraday Constant (C/mol)
F_{in}^{Brine}	Inlet volume flow-rate of brine (l/min)
F_{in}^{NaOH}	Inlet volume flow-rate of sodium hydroxide (l/min)
FO	Forward Osmosis
$\dot{G}_{mix}$	Gibbs free power of the resulting solution (W)
$\dot{G}_H, \dot{G}_L$	Gibbs free power of the inlet HIGH and LOW (W)
$\dot{G}_k$	Gibbs free power of the generic k^{th} stream (W)
i(k)	Electrical current of the generic k^{th} element (A)
I_{stack}	Total Electrical current (A)
k_{ps}	Product solubility
L	Size of particle
m	Molality (mol/kg)
m_s	Mass of crystals (g)
M_s	Salt molecular weight (kg/mol)
M_T	Magma Density (g/l)
M_w	Water molecular weight (kg/mol)
M_w^{Ca}	Molecular weight of calcium (kg/mol)
$M_W^{Ca(OH)_2}$	Molecular weight of calcium hydroxide (kg/mol)
M_w^{Mg}	Molecular weight of magnesium (kg/mol)
$M_W^{Mg(OH)_2}$	Molecular weight of magnesium hydroxide (kg/mol)
$N°$	Mole flow-rate of initial magnesium/calcium (mol/s)
N	Mole flow-rate of magnesium/calcium (mol/s)
N_{cp}	Number of cell pair
N_k	Number of discretization elements
N_{RED}^{C}	Number of the cycles of the solution in the RED unit
N_{REG}^{C}	Number of the cycles of the solution in the stripping column unit

$\dot{n}_{salt,k}$	Salt molar flow rate (mol/s)
$\dot{n}_{water,k}$	Water molar flow rate (mol/s)
P_{column}	Pressure of stripping column
P_d	Power density (W/m^2)
P_{RED}	Electrical power output from the RED unit (W)
P&ID	Piping and Instrumentation Diagram
Q	Volumetric flow rate (m^3/s)
R	Universal gas constant (J/(K mol))
R_{AEM}	Anionic membrane resistance (Ωm^2)
R_{blanck}	Electrical resistance of the electrodic compartment (Ω)
R_{cell}	Electrical resistance of cell pair (Ω)
R_{CEM}	Cationic membrane resistance (Ωm^2)
R_E	Load resistance (Ω)
R_H	Electrical resistance of concentrate (Ωm^2)
R_L	Electrical resistance of dilute (Ωm^2)
RR	Recovery ratio of the FO unit (%)
s	Supersaturation ratio
STC	Specific Thermal Consumption (kWh/m^3)
t_{RED}	Residence time in the RED unit [min]
t_{REG}	Residence time in the stripping column unit [min]
t_{test}	Duration of long run test [min]
V_f	Volume of the slurry (l)
VSEP	Vibratory shear enhanced processing
v	Velocity of the solutions (cm/s)
Y	Thermodynamic yield
Y	Recovery

Greek symbols

α	Supersaturation concentration ratio
α_{av}	Average ionic exchange membranes permselectivity
δ_m	Membrane thickness (m)
Δx	Calculation element length (m)

η_C	Carnot efficiency
η_{ex}	Exergy efficiency
$\eta_{ex,RED}$	Exergy efficiency of RED unit
η_{th}	Thermal efficiency
ϕ	Osmotic coefficient
$\Delta\pi_{out}$	Residual Osmotic Pressure difference between the outlet streams of the FO unit (bar)
γ	Salt activity coefficient (dimensionless)
ρ	Density (kg/m^3)
σ	Conductivity (mS/cm)
Λ	specific molar conductivity (mS l/(cm mol))
Λ_0	Equivalent conductivity of salt at infinite dilution (mS l/(cm mol))
A_Λ, B_Λ, C_Λ	Fitting parameters
$\mu_{salt,k}$	Chemical potential of salt (J/mol)
$\mu_{water,k}$	Chemical potential of water (J/mol)
ϑ	Purity of crystals

Subscripts

Brine	Related to the brine
Ca	Related to the calcium cation
H	Related to the concentrate stream
H-mix,1	Related to the part of the outlet concentration fed to he mix1
i	Related to magnesium or calcium cations
in	Related to the inlet solution from the RED
out	Related to the outlet solution from the RED
L	Related to the dilute stream
max	Related to the maximum value
mix	Related to the outlet from mixer 1
Mg	Related to the magnesium cation
RED	Related to the RED streams
REG	Related to the regenerated stream

References

[1] U. States., D. of Energy., O. of E.E. and R. Energy., U. States., D. of Energy., O. of S. and T. Information., Waste Heat Recovery : Technology and Opportunities in U.S. Industry., (2008).

[2] D.B. Gingerich, M.S. Mauter, Quantity, Quality, and Availability of Waste Heat from United States Thermal Power Generation, Environ. Sci. Technol. 49 (2015) 8297–8306. doi:10.1021/es5060989.

[3] L. Miró, S. Brückner, L.F. Cabeza, Mapping and discussing Industrial Waste Heat (IWH) potentials for different countries, Renew. Sustain. Energy Rev. 51 (2015) 847–855. doi:10.1016/j.rser.2015.06.035.

[4] H. Lu, L. Price, Q. Zhang, Capturing the invisible resource: Analysis of waste heat potential in Chinese industry, Appl. Energy. 161 (2016) 497–511. doi:10.1016/j.apenergy.2015.10.060.

[5] R. Law, A. Harvey, D. Reay, A knowledge-based system for low-grade waste heat recovery in the process industries, 94 (2016) 590–599. doi:10.1016/j.applthermaleng.2015.10.103.

[6] M. Papapetrou, G. Kosmadakis, A. Cipollina, U. LaCommare, G. Micalea, Industrial waste heat: Estimation of the technically available resource in the EU per industrial sector, temperature level and country, Appl. Therm. Eng. 138 (2018) 207–216. doi:10.1016/j.applthermaleng.2018.04.043.

[7] S. Brückner, S. Liu, L. Miró, M. Radspieler, L.F. Cabeza, E. Lävemann, Industrial waste heat recovery technologies: An economic analysis of heat transformation technologies, Appl. Energy. 151 (2015) 157–167. doi:10.1016/j.apenergy.2015.01.147.

[8] H. Chen, D.Y. Goswami, E.K. Stefanakos, A review of thermodynamic cycles and working fluids for the conversion of low-grade heat, Renew. Sustain. Energy Rev. 14 (2010) 3059–3067. doi:10.1016/j.rser.2010.07.006.

[9] Y. Wang, Q. Tang, M. Wang, X. Feng, Thermodynamic performance comparison between ORC and Kalina cycles for multi-stream waste heat recovery, Energy Convers. Manag. 143 (2017) 482–492. doi:10.1016/j.enconman.2017.04.026.

[10] M. Zebarjadi, K. Esfarjani, M.S. Dresselhaus, Z.F. Ren, G. Chen, Perspectives on thermoelectrics: From fundamentals to device applications, Energy Environ. Sci. 5 (2012) 5147–5162. doi:10.1039/c1ee02497c.

[11] T. Monin, A. Tessier-Poirier, E. Léveillé, A. Juneau-Fecteau, T. Skotnicki, F. Formosa, S. Monfray, L.G. Fréchette, First experimental demonstration of a Self-Oscillating Fluidic Heat Engine (SOFHE) with piezoelectric power generation, J. Phys. Conf. Ser. 773 (2016). doi:10.1088/1742-6596/773/1/012039.

[12] J. Karthauser, Energy generation from Waste Heat using the Carbon Carrier Thermodynamic Cycle, (2016).

[13] A. Tamburini, M. Tedesco, A. Cipollina, G. Micale, M. Ciofalo, M. Papapetrou, W. Van Baak, A. Piacentino, Reverse electrodialysis heat engine for sustainable power production, Appl. Energy. 206 (2017) 1334–1353. doi:10.1016/j.apenergy.2017.10.008.

[14] B.E. Logan, M. Elimelech, Membrane-based processes for sustainable power generation using water, Nature. 488 (2012) 313–319. doi:10.1038/nature11477.

[15] B. Ortega-Delgado, F. Giacalone, A. Cipollina, M. Papapetrou, G. Kosmadakis, A. Tamburini, G. Micale, Boosting the performance of a Reverse Electrodialysis – Multi-Effect Distillation Heat Engine by novel solutions and operating conditions, Appl. Energy. 253 (2019) 113489. doi:10.1016/j.apenergy.2019.113489.

[16] K.L. Hickenbottom, J. Vanneste, T.Y. Cath, Assessment of alternative draw solutions for optimized performance of a closed-loop osmotic heat engine, J. Memb. Sci. 504 (2016) 162–175. doi:10.1016/j.memsci.2016.01.001.

[17] J.B. Seale, Reverse electrodialysis for generation of hydrogen, United States Pat. (2006). https://patents.google.com/patent/US20060263646A1/en.

[18] R.A. Tufa, E. Rugiero, D. Chanda, J. Hnàt, W. van Baak, J. Veerman, E. Fontananova, G. Di Profio, E. Drioli, K. Bouzek, E. Curcio, Salinity gradient power-reverse electrodialysis and alkaline polymer electrolyte water electrolysis for hydrogen production, J. Memb. Sci. 514 (2016) 155–164. doi:10.1016/j.memsci.2016.04.067.

[19] H. Tian, Y. Wang, Y. Pei, J.C. Crittenden, Unique applications and improvements of reverse electrodialysis: A review and outlook, Appl. Energy. 262 (2020) 114482. doi:10.1016/j.apenergy.2019.114482.

[20] J.R. McCutcheon, R.L. McGinnis, M. Elimelech, Desalination by ammonia-carbon dioxide forward osmosis: Influence of draw and feed solution concentrations on process performance, J. Memb. Sci. 278 (2006) 114–123. doi:10.1016/j.memsci.2005.10.048.

[21] R.A. Neff, Solvent Extractor, (1964) 13–16.

[22] J.R. McCutcheon, R.L. McGinnis, M. Elimelech, A novel ammonia—carbon dioxide forward (direct) osmosis desalination process, Desalination. 174 (2005) 1–11. doi:10.1016/j.desal.2004.11.002.

[23] R.L. McGinnis, M. Elimelech, Energy requirements of ammonia-carbon dioxide forward osmosis desalination, Desalination. 207 (2007) 370–382. doi:10.1016/j.desal.2006.08.012.

[24] X. Zhou, D.B. Gingerich, M.S. Mauter, Water Treatment Capacity of Forward-

Osmosis Systems Utilizing Power-Plant Waste Heat, Ind. Eng. Chem. Res. 54 (2015) 6378–6389. doi:10.1021/acs.iecr.5b00460.

[25] H. Que, C.-C. Chen, Thermodynamic Modeling of the NH_3–CO_2–H_2O System with Electrolyte NRTL Model, Ind. Eng. Chem. Res. 50 (2011) 11406–11421. doi:10.1021/ie201276m.

[26] R.L. McGinnis, N.T. Hancock, M.S. Nowosielski-Slepowron, G.D. McGurgan, Pilot demonstration of the NH3/CO2forward osmosis desalination process on high salinity brines, Desalination. 312 (2013) 67–74. doi:10.1016/j.desal.2012.11.032.

[27] S. Shim, S. Lee, W. Kim, Experimental study on the performance evaluation of vacuum distillation process for NH4HCO3 removal, J. Mech. Sci. Technol. 27 (2013) 1171–1178. doi:10.1007/s12206-013-0304-7.

[28] Y. Kim, J.H. Lee, Y.C. Kim, K.H. Lee, I.S. Park, S.-J. Park, Operation and simulation of pilot-scale forward osmosis desalination with ammonium bicarbonate, Chem. Eng. Res. Des. 94 (2015) 390–395. doi:10.1016/j.cherd.2014.08.015.

[29] C. Boo, Y.F. Khalil, M. Elimelech, Performance evaluation of trimethylamine–carbon dioxide thermolytic draw solution for engineered osmosis, J. Memb. Sci. 473 (2015) 302–309. doi:10.1016/j.memsci.2014.09.026.

[30] S. Loeb, Method and apparatus for generating power utilizing Pressure-Retarded-Osmosis, (1974).

[31] S. Loeb, Method and apparatus for generating power utilizing Reverse Electrodialysis, (1978).

[32] X. Luo, X. Cao, Y. Mo, K. Xiao, X. Zhang, P. Liang, X. Huang, Power generation by coupling reverse electrodialysis and ammonium bicarbonate: Implication for recovery of waste heat, Electrochem. Commun. 19 (2012) 25–28. doi:10.1016/j.elecom.2012.03.004.

[33] R.D. Cusick, Y. Kim, B.E. Logan, Energy Capture from Thermolytic Solutions in Microbial Reverse-Electrodialysis Cells, Science (80-.). 335 (2012) 1474–1477. doi:10.1126/science.1219330.

[34] J.Y. Nam, R.D. Cusick, Y. Kim, B.E. Logan, Hydrogen generation in microbial reverse-electrodialysis electrolysis cells using a heat-regenerated salt solution, Environ. Sci. Technol. 46 (2012) 5240–5246. doi:10.1021/es300228m.

[35] M.C. Hatzell, I. Ivanov, R. D. Cusick, X. Zhu, B.E. Logan, Comparison of hydrogen production and electrical power generation for energy capture in closed-loop ammonium bicarbonate reverse electrodialysis systems, Phys. Chem. Chem. Phys. 16 (2014) 1632–1638. doi:10.1039/C3CP54351J.

[36] K. Kwon, B.H. Park, D.H. Kim, D. Kim, Parametric study of reverse electrodialysis using ammonium bicarbonate solution for low-grade waste heat recovery, Energy

Convers. Manag. 103 (2015) 104–110. doi:10.1016/j.enconman.2015.06.051.

[37] M. Bevacqua, A. Carubia, A. Cipollina, A. Tamburini, M. Tedesco, G. Micale, Performance of a RED system with ammonium hydrogen carbonate solutions, Desalin. Water Treat. 3994 (2016) 1–12. doi:10.1080/19443994.2015.1126410.

[38] H. Tian, Y. Wang, Y. Pei, Energy capture from thermolytic solutions and simulated sunlight coupled with hydrogen peroxide production and wastewater remediation, Water Res. 170 (2020) 115318. doi:10.1016/j.watres.2019.115318.

[39] D.H. Kim, B.H. Park, K. Kwon, L. Li, D. Kim, Modeling of power generation with thermolytic reverse electrodialysis for low-grade waste heat recovery, Appl. Energy. 189 (2017) 201–210. doi:10.1016/j.apenergy.2016.10.060.

[40] M. Bevacqua, A. Tamburini, M. Papapetrou, A. Cipollina, G. Micale, A. Piacentino, Reverse electrodialysis with NH4HCO3-water systems for heat-to-power conversion, Energy. (2017). doi:10.1016/j.energy.2017.07.012.

[41] R.L. McGinnis, J.R. McCutcheon, M. Elimelech, A novel ammonia-carbon dioxide osmotic heat engine for power generation, J. Memb. Sci. 305 (2007) 13–19. doi:10.1016/j.memsci.2007.08.027.

[42] X. Tong, S. Liu, J. Yan, O.A. Broesicke, Y. Chen, J. Crittenden, Thermolytic osmotic heat engine for low-grade heat harvesting: Thermodynamic investigation and potential application exploration, Appl. Energy. 259 (2020) 114192. doi:10.1016/j.apenergy.2019.114192.

[43] F. Giacalone, P. Catrini, A. Tamburini, A. Cipollina, A. Piacentino, G. Micale, Exergy analysis of reverse electrodialysis, Energy Convers. Manag. 164 (2018) 588–602. doi:10.1016/j.enconman.2018.03.014.

[44] T.Z. Fahidy, Activity coefficients in electrolyte solutions (second edition), edited by Kenneth S. Pitzer, 1991, 542 + vi pages, CRC Press, Boca Raton, FL; ISBN 0-8493-5415-3. Price: US$ 195.00, Can. J. Chem. Eng. 71 (1993) 494. doi:10.1002/cjce.5450710328.

[45] E.A.. C. Rashkovskaya E.I., Densities of ammonium bicarbonate, sodium bicarbonate, and ammonium chloride and ammonia salt solutions at 20-100°C, Zhurnal Prikl. Khimii. 40 (1967) 301.

[46] G. Jones, C.F. Bickford, The Conductance of Aqueous Solutions as a Function of the Concentration. I. Potassium Bromide and Lanthanum Chloride, J. Am. Chem. Soc. 56 (1934) 602–611. doi:10.1021/ja01318a021.

[47] M. Shahid, X. Xue, C. Fan, B.W. Ninham, R.M. Pashley, Study of a Novel Method for the Thermolysis of Solutes in Aqueous Solution Using a Low Temperature Bubble Column Evaporator, J. Phys. Chem. B. 119 (2015) 8072–8079. doi:10.1021/acs.jpcb.5b02808.

[48] A.M. Benneker, T. Rijnaarts, R.G.H. Lammertink, J.A. Wood, Effect of temperature gradients in (reverse) electrodialysis in the Ohmic regime, J. Memb. Sci. 548 (2018) 421–428. doi:10.1016/j.memsci.2017.11.029.

[49] Z. Meng, J.H. Seinfeld, P. Saxena, Y.P. Kim, Atmospheric Gas-Aerosol Equilibrium: IV. Thermodynamics of Carbonates, Aerosol Sci. Technol. 23 (1995) 131–154. doi:10.1080/02786829508965300.

[50] M. Vanoppen, E. Criel, G. Walpot, D.A. Vermaas, A. Verliefde, Assisted reverse electrodialysis—principles, mechanisms, and potential, Npj Clean Water. 1 (2018) 9. doi:10.1038/s41545-018-0010-1.

[51] R.A. Tufa, S. Pawlowski, J. Veerman, K. Bouzek, E. Fontananova, G. di Profio, S. Velizarov, J. Goulão Crespo, K. Nijmeijer, E. Curcio, Progress and prospects in reverse electrodialysis for salinity gradient energy conversion and storage, Appl. Energy. 225 (2018) 290–331. doi:10.1016/j.apenergy.2018.04.111.

[52] D.A. Vermaas, M. Saakes, K. Nijmeijer, Doubled power density from salinity gradients at reduced intermembrane distance, Environ. Sci. Technol. 45 (2011) 7089–7095. doi:10.1021/es2012758.

[53] F. Giacalone, C. Olkis, G. Santori, A. Cipollina, S. Brandani, G. Micale, Novel solutions for closed-loop reverse electrodialysis: Thermodynamic characterisation and perspective analysis, Energy. (2019). doi:10.1016/j.energy.2018.10.049.

[54] F. Giacalone, M. Papapetrou, G. Kosmadakis, A. Tamburini, G. Micale, A. Cipollina, Application of reverse electrodialysis to site-specific types of saline solutions: A techno-economic assessment, Energy. (2019). doi:10.1016/j.energy.2019.05.161.

[55] M.O. Mavukkandy, C.M. Chabib, I. Mustafa, A. Al Ghaferi, F. AlMarzooqi, Brine management in desalination industry: From waste to resources generation, Desalination. 472 (2019) 114187. doi:10.1016/j.desal.2019.114187.

[56] T. Mezher, H. Fath, Z. Abbas, A. Khaled, Techno-economic assessment and environmental impacts of desalination technologies, Desalination. 266 (2011) 263–273. doi:10.1016/j.desal.2010.08.035.

[57] E. Jones, M. Qadir, M.T.H. van Vliet, V. Smakhtin, S. mu Kang, The state of desalination and brine production: A global outlook, Sci. Total Environ. 657 (2019) 1343–1356. doi:10.1016/j.scitotenv.2018.12.076.

[58] D.A. Roberts, E.L. Johnston, N.A. Knott, Impacts of desalination plant discharges on the marine environment: A critical review of published studies, Water Res. 44 (2010) 5117–5128. doi:10.1016/j.watres.2010.04.036.

[59] I.S. Al-Mutaz, Environmental impact of seawater desalination plants, Environ. Monit. Assess. 16 (1991) 75–84. doi:10.1007/BF00399594.

[60] N. Voutchkov, Overview of seawater concentrate disposal alternatives, Desalination.

273 (2011) 205–219. doi:10.1016/j.desal.2010.10.018.

[61] T.M. Missimer, R.G. Maliva, Environmental issues in seawater reverse osmosis desalination: Intakes and outfalls, Desalination. 434 (2018) 198–215. doi:10.1016/j.desal.2017.07.012.

[62] P. Taylor, M. Tedesco, A. Cipollina, A. Tamburini, W. Van Baak, S. Ed, Desalination and Water Treatment Modelling the Reverse ElectroDialysis process with seawater and concentrated brines Modelling the Reverse ElectroDialysis process with seawater and concentrated brines, (n.d.) 37–41. doi:10.1080/19443994.2012.699355.

[63] T. Jeppesen, L. Shu, G. Keir, V. Jegatheesan, Metal recovery from reverse osmosis concentrate, J. Clean. Prod. 17 (2009) 703–707. doi:10.1016/j.jclepro.2008.11.013.

[64] G. Al Bazedi, R.S. Ettouney, S.R. Tewfik, M.H. Sorour, M.A. El-Rifai, Salt recovery from brine generated by large-scale seawater desalination plants, Desalin. Water Treat. 52 (2014) 4689–4697. doi:10.1080/19443994.2013.810381.

[65] R.G. Maliva, T.M. Missimer, R. Fontaine, Injection Well Options for Sustainable Disposal of Desalination Concentrate, IDA J. Desalin. Water Reuse. 3 (2011) 17–23. doi:10.1179/ida.2011.3.3.17.

[66] N. Afrasiabi, E. Shahbazali, Ro brine treatment and disposal methods, Desalin. Water Treat. 35 (2011) 39–53. doi:10.5004/dwt.2011.3128.

[67] S. Panta, P. Lane, R. Doyle, M. Hardie, G. Haros, S. Shabala, Halophytes as a Possible Alternative to Desalination Plants, Elsevier Inc., 2016. doi:10.1016/b978-0-12-801854-5.00019-4.

[68] A. Panagopoulos, K.J. Haralambous, M. Loizidou, Desalination brine disposal methods and treatment technologies - A review, Sci. Total Environ. 693 (2019) 133545. doi:10.1016/j.scitotenv.2019.07.351.

[69] P. Xu, T.Y. Cath, A.P. Robertson, M. Reinhard, J.O. Leckie, J.E. Drewes, Critical review of desalination concentrate management, treatment and beneficial use, Environ. Eng. Sci. 30 (2013) 502–514. doi:10.1089/ees.2012.0348.

[70] M. Ahmed, W.H. Shayya, D. Hoey, A. Mahendran, R. Morris, J. Al-Handaly, Use of evaporation ponds for brine disposal in desalination plants, Desalination. 130 (2000) 155–168. doi:10.1016/S0011-9164(00)00083-7.

[71] B.K. Pramanik, L. Shu, V. Jegatheesan, A review of the management and treatment of brine solutions, Environ. Sci. Water Res. Technol. 3 (2017) 625–658. doi:10.1039/c6ew00339g.

[72] A. Subramani, J.G. Jacangelo, Treatment technologies for reverse osmosis concentrate volume minimization: A review, Sep. Purif. Technol. 122 (2014) 472–489. doi:10.1016/j.seppur.2013.12.004.

[73] L. Chekli, S. Phuntsho, H.K. Shon, S. Vigneswaran, J. Kandasamy, A. Chanan, A review of draw solutes in forward osmosis process and their use in modern applications, Desalin. Water Treat. 43 (2012) 167–184. doi:10.1080/19443994.2012.672168.

[74] C.R. Martinetti, A.E. Childress, T.Y. Cath, High recovery of concentrated RO brines using forward osmosis and membrane distillation, J. Memb. Sci. 331 (2009) 31–39. doi:10.1016/j.memsci.2009.01.003.

[75] A. Subramani, J. DeCarolis, W. Pearce, J.G. Jacangelo, Vibratory shear enhanced process (VSEP) for treating brackish water reverse osmosis concentrate with high silica content, Desalination. 291 (2012) 15–22. doi:10.1016/j.desal.2012.01.020.

[76] O.K. J.Gilron, Y. Folkman, R. Savliev, M. Waisman, WAIV - wind aided intensified evaporation for reduction of desalination brine volume, Desalination. 158 (2003) 205–214.

[77] F. Macedonio, L. Katzir, N. Geisma, S. Simone, E. Drioli, J. Gilron, Wind-Aided Intensified eVaporation (WAIV) and Membrane Crystallizer (MCr) integrated brackish water desalination process: Advantages and drawbacks, Desalination. 273 (2011) 127–135. doi:10.1016/j.desal.2010.12.002.

[78] F. Laganà, G. Barbieri, E. Drioli, Direct contact membrane distillation: modelling and concentration experiments, J. Memb. Sci. 166 (2000) 1–11.

[79] D. Brogioli, F. La Mantia, N.Y. Yip, Thermodynamic analysis and energy efficiency of thermal desalination processes, Desalination. 428 (2018) 29–39. doi:10.1016/j.desal.2017.11.010.

[80] M. Micari, M. Moser, A. Cipollina, B. Fuchs, B. Ortega-Delgado, A. Tamburini, G. Micale, Techno-economic assessment of multi-effect distillation process for the treatment and recycling of ion exchange resin spent brines, Desalination. 456 (2019) 38–52. doi:10.1016/j.desal.2019.01.011.

[81] P. Palenzuela, A.S. Hassan, G. Zaragoza, D.-C. Alarcón-Padilla, Steady state model for multi-effect distillation case study: Plataforma Solar de Almería MED pilot plant, Desalination. 337 (2014) 31–42. doi:10.1016/j.desal.2013.12.029.

[82] H. Bamufleh, F. Abdelhady, H.M. Baaqeel, M.M. El-Halwagi, Optimization of multi-effect distillation with brine treatment via membrane distillation and process heat integration, Desalination. 408 (2017) 110–118. doi:10.1016/j.desal.2017.01.016.

[83] A. Cipollina, G. Micale, L. Rizzuti, A brine evaporative cooler/concentrator for autonomous thermal desalination units, Desalin. Water Treat. 31 (2011) 269–278. doi:10.5004/dwt.2011.2345.

[84] I.S. Al Mutaz, K.M. Wagialia, Production of magnesium from desalination brines, Resour. Conserv. Recycl. 3 (1990) 231–239. doi:10.1016/0921-3449(90)90020-5.

[85] P.S. Wallace, D4_WO2015077727A1.pdf, PCT/US2014/067176, n.d.

[86] A. Cipollina, A. Misseri, G.D.A. Staiti, A. Galia, G. Micale, O. Scialdone, Integrated production of fresh water, sea salt and magnesium from sea water, Desalin. Water Treat. 49 (2012) 390–403. doi:10.1080/19443994.2012.699340.

[87] S. Casas, C. Aladjem, E. Larrotcha, O. Gibert, C. Valderrama, J.L. Cortina, Valorisation of Ca and Mg by-products from mining and seawater desalination brines for water treatment applications, J. Chem. Technol. Biotechnol. 89 (2014) 872–883. doi:10.1002/jctb.4326.

[88] I.S. Al-mutaz, P.O. Box, By-product recovery from saudi desalination plants, Construction. 64 (1987) 97–110.

[89] B. Ericsson, B. Hallmans, Treatment of saline wastewater for zero discharge at the Debiensko coal mines in Poland, Desalination. 105 (1996) 115–123. doi:10.1016/0011-9164(96)00065-3.

[90] M. Ahmed, A. Arakel, D. Hoey, M.R. Thumarukudy, M.F.A. Goosen, M. Al-Haddabi, A. Al-Belushi, Feasibility of salt production from inland RO desalination plant reject brine: A case study, Desalination. 158 (2003) 109–117. doi:10.1016/S0011-9164(03)00441-7.

[91] E. Drioli, E. Curcio, A. Criscuoli, G. Di Di Profio, Integrated system for recovery of CaCO3, NaCl and MgSO 4·7H2O from nanofiltration retentate, J. Memb. Sci. 239 (2004) 27–38. doi:10.1016/j.memsci.2003.09.028.

[92] WHO, Desalination and Water Purification Research and Development Zero Discharge Seawater Desalination: Integrating the Production of Freshwater, Salt, Magnesium, and Bromine, (2006).

[93] European Commission, Study on the review of the list of Critical Raw Materials - Final Report, 2020. doi:10.2873/11619.

[94] European Commission, Study on the review of the list of Critical Raw Materials - Critical Raw Materials Factsheets, 2020. doi:10.2873/92480.

[95] QYR Chemical & Material Research Center, Europe Magnesium Hydroxide Industry 2016 Market Research Report, (2016) 65.

[96] M. Turek, W. Gnot, Precipitation of Magnesium Hydroxide from Brine, Ind. Eng. Chem. Res. 34 (1995) 244–250. doi:10.1021/ie00040a025.

[97] M. Micari, A. Cipollina, A. Tamburini, M. Moser, V. Bertsch, G. Micale, Techno-economic analysis of integrated processes for the treatment and valorisation of neutral coal mine effluents, J. Clean. Prod. 270 (2020) 122472. doi:10.1016/j.jclepro.2020.122472.

[98] S.W. Lee, J.H. Lim, Recovery of Magnesium Oxide and Magnesium Hydroxide from

the Waste Bittren, Adv. Mater. Res. 26–28 (2007) 1019–1022. doi:10.4028/www.scientific.net/amr.26-28.1019.

[99] A. Alamdari, M.R. Rahimpour, N. Esfandiari, E. Nourafkan, Kinetics of magnesium hydroxide precipitation from sea bittern, Chem. Eng. Process. Process Intensif. 47 (2008) 215–221. doi:10.1016/j.cep.2007.02.012.

[100] X. Song, S. Sun, D. Zhang, J. Wang, J. Yu, Synthesis and characterization of magnesium hydroxide by batch reaction crystallization, Front. Chem. Sci. Eng. 5 (2011) 416–421. doi:10.1007/s11705-011-1125-9.

[101] X. Song, K. Tong, S. Sun, Z. Sun, J. Yu, Preparation and crystallization kinetics of micron-sized Mg(OH)2 in a mixed suspension mixed product removal crystallizer, Front. Chem. Sci. Eng. 7 (2013) 130–138. doi:10.1007/s11705-013-1332-7.

[102] A. Cipollina, M. Bevacqua, P. Dolcimascolo, A. Tamburini, A. Brucato, H. Glade, L. Buether, G. Micale, Reactive crystallisation process for magnesium recovery from concentrated brines, Desalin. Water Treat. 55 (2015) 2377–2388. doi:10.1080/19443994.2014.947771.

[103] P.S. Forms, Horizon 2020 Call : H2020-IND-CE-2016-17 (Industry 2020 in the Circular Economy) Topic : CIRC-02-2016-2017 Type of action : IA (Innovation action) Proposal number : 730209-1 Proposal acronym : Renut Deadline Id : H2020-CIRC-2016TwoStage Table of conte, (2017). doi:10.1051/0004-6361:20021389.

[104] P. Bajpai, Introductory Chemistry Reviews, Biermann's Handb. Pulp Pap. (2018) 401–426. doi:10.1016/b978-0-12-814238-7.00020-9.

[105] H.P. McCabe W.L., Smith J.C., Unit Operations in Chemical Engineering, (1993). doi:10.1016/j.apenergy.2017.05.096.

[106] Allan S.Myerson, Handbook of Industrial Crystallization, 2002. doi:10.1051/matecconf/201711401016.

[107] J.W. MALLIN, CRYSTALLIZATION, 2001.

[108] A.D. Randolph, M.A. Larson, Particulate Processes, 1988. doi:10.1016/b978-0-12-579652-1.50007-7.

[109] W. Beckmann, Crystallization: Basic Concepts and Industrial Applications, 2013.

[110] P. Chemicals, M.C. Pvc, P.F.A. Epdm, Chemical resistance guide, (2008).

[111] A. Dasari, R.D.K. Misra, On the strain rate sensitivity of high density polyethylene and polypropylenes, Mater. Sci. Eng. A. 358 (2003) 356–371. doi:10.1016/S0921-5093(03)00330-7.

[112] WesTech, IO&M Manual Pilot Drum Filter, (n.d.).

[113] D. Grasso, D. Grasso, Bioprocess Engineering Principles, 2018. doi:10.1201/9780203752265-5.

[114] F. Street, Magnifin ® h-10, (2000).

[115] A.A. Pilarska, Ł. Klapiszewski, T. Jesionowski, Recent development in the synthesis, modification and application of Mg(OH)2 and MgO: A review, Powder Technol. 319 (2017) 373–407. doi:10.1016/j.powtec.2017.07.009.

[116] Y. Chen, T. Zhou, H. Fang, S. Li, Y. Yao, B. Fan, J. Wang, A novel preparation of nanosized hexagonal Mg(OH)2as a flame retardant, Particuology. 24 (2016) 177–182. doi:10.1016/j.partic.2015.01.007.

[117] B. Coto, C. Martos, J.L. Peña, R. Rodríguez, G. Pastor, Effects in the solubility of CaCO 3: Experimental study and model description, Fluid Phase Equilib. 324 (2012) 1–7. doi:10.1016/j.fluid.2012.03.020.

[118] https://www.kth.se/che/medusa/downloads-1.386254, (n.d.).

[119] C.Y. Tai, F.B. Chen, Polymorphism of CaCO3 precipitated in a constant-composition environment, AIChE J. 44 (1998) 1790–1798. doi:10.1002/aic.690440810.

[120] K.I.M. AL-MALAH, Aspen Plus Chemical Engineering Textbook, 2017.

[121] F. Buchholt, M. Kümmel, Self-tuning control of a pH-neutralization process, Automatica. 15 (1979) 665–671. doi:10.1016/0005-1098(79)90034-7.

LIST OF ISI PUBLICATIONS AND PRESENTATIONS AT INTERNATIONAL CONFERENCES

- F. Giacalone, **F. Vassallo**, L. Griffina,, , M.C. Ferrari, G. Micale, F. Scargiali, A. Tamburini, A.Cipollina," Thermolytic reverse electrodialysis heat engine: model development,integration and performance analysis", Energy Conversion and Management, Volume 189, 1 June 2019, Pages 1-13, doi: 10.1016/j.enconman.2019.03.045

- F. Giacalone, **F. Vassallo**, F. Scargiali, A. Tamburini, A. Cipollina , G. Micale , "The first operating thermolytic reverse electrodialysis heat engine", Journal of Membrane Science, Volume 595, 1 February 2020, Article number 117522,doi: 10.1016/j.memsci.2019.117522.

- Daniele La Corte, **Fabrizio Vassallo**, Andrea Cipollina, Marian Turek, Alessandro Tamburini and Giorgio Micale , «A novel ionic exchange membrane crystallizer to recover magnesium hydroxide from seawater and industrial brines », in press Membranes journal, 10, 303; doi:10.3390/membranes10110303.

- **F. Vassallo**, F. Giacalone, F. Scargiali, A. Cipollina, G. Micale," Regeneration Units for Thermolytic salts applications in water & power production: State of art, Experimental and Modelling assessments", Desalination, Volume 504, 15 May 2021, https://doi.org/10.1016/j.desal.2021.114965

IN PREPARATION AND/OR SUBMITTED

- **F. Vassallo**, D. La Corte, M. Bevacqua, A. Cipollina, G. Micale, «A novel ionic exchange membrane crystallizer to recover magnesium hydroxide from natural and industrial brine», in preparation.

- **F. Vassallo**, D. La Corte, A. Cipollina, A. Tamburini, G. Micale, « High purity recovery of magnesium and calcium hydroxides from waste brines», submitted in CHEMICAL ENGINEERING TRANSACTIONS.

- **F. Vassallo**, C.Morgante, G. Battaglia, D. La Cortea, M. Micari, A. Cipollina, A. Tamburinia, G. Micale , «A mathematical model of an ion exchange membrane crystallizer for the recovery of magnesium hydroxide from waste brine», in preparation.

- **F. Vassallo**, D. La Corte, A. Cipollina, A. Tamburini, G. Micale, High purity recovery of magnesium and calcium hydroxides from waste brines, submitted to Chemical engineering transactions

Presentation at international conference

- F. Giacalone, **F. Vassallo**, F. Scargiali, A. Tamburini, A. Cipollina, G. Micale, "Thermolytic RED- Heat Engine: first experimental assessment", 13th SDEWES Conference, Palermo, 30th of September – 4th of October 2018.

- F. Giacalone, **F. Vassallo**, L. Griffin, F. Scargiali, A. Tamburini, M.C. Ferrari, G. Micale, A. Cipollina, "Modelling analysis of Thermolytic RED-Heat Engine", 13th SDEWES Conference, Palermo, 30th of September – 4th of October 2018. **(Oral presentation)**

- F. Giacalone, **F. Vassallo**, F. Scargiali, A. Tamburini, A. Cipollina, G. Micale, "Experimental assessment of reverse electrodialysis in closed loop configuration fed byNH4HCO3-water solutions", Desalination for the Environment: Clean Water and Energy 3-6 September 2018, Athens, Greece.

- D. La Corte, C. Morgante**, F. Vassallo**, G. Battaglia, M. Micari, A. Cipollina, A. Tamburini, G.Micale "Ion exchange membrane crystallizer for magnesium recovery from seawater and industrial brine", SDEWES (1-5/09/2020).

- **F. Vassallo**, D. La Corte, A. Cipollina, A. Tamburini, G. Micale, High purity recovery of magnesium and calcium hydroxides from waste brines, ICheaP15, 23-26/05/2021, submitted for oral presentation.

- **F. Vassallo**, D. La Corte, N. Cancilla, M. Bevacqua, A. Tamburini, A. Cipollina, G. Micale, Selective crystallisation of magnesium and calcium hydroxides from industrial waste brines: a pilot study, Symposium 21st International Symposium on Industrial Crystallization, Potsdam, 30/08-2/09/2021, submitted for oral presentation.

- C. Morgante, **F. Vassallo**, D. Xevgenos, A. Cipollina, M. Micarie, A. Tamburini, G. Micale, Techno-economic analysis of a novel hybrid system for the valorisation of SWRO brines in a minor Sicilian island. 16th SDEWES 2021, Dubrovnik, 10-15/10/2021, submitted for oral presentation

Presentation at national conference

- "Cancilla Nunzio, **Vassallo Fabrizio**, La Corte Daniele, Cipollina Andrea, "Sviluppo di un impianto pilota per il recupero di idrossido di magnesio da salamoie di scarto", Poster, Convegno Gricu, Palermo, 1-3 Luglio 2019. (Poster)